To the Graduate Council:

I am submitting herewith a dissertation written by Man-Ho Kim
entitled "The Melting Behavior and Structure of Ethylene Copolymers from Metallocene Catalysts." I have examined the final copy of this dissertation for form and content and recommend that it be accepted in partial fulfillment of the requirements for the degree of Doctor of Philosophy, with a major in Polymer Engineering.

Paul J. Phillips, Major Professor

We have read this dissertation
and recommend its acceptance:

Accepted for the Council:

Associate Vice Chancellor and
Dean of The Graduate School

The Melting Behavior and Structure of Ethylene Copolymers from Metallocene Catalysts

A Dissertation
Presented for the
Doctor of Philosophy Degree
The University of Tennessee, Knoxville

Man-Ho Kim
May 1996

DEDICATION

This dissertation is dedicated

First, to God.

Second, to my parents

Mr. Ki-Ro Kim and Mrs. Sang-Bae Park

who have supported me through prayer.

Third, to my wife

Won-Sil Shin Kim

and

my son

Young-Wook Kim

who are the most important people in my life.

Copyright © Man-Ho Kim, 1996

All rights reserved

ACKNOWLEDGEMENTS

This research could not have been accomplished without the faculty, staff, and graduate students who have assisted me directly or indirectly in Department of Materials Science and Engineering. I am especially grateful to Dr. Paul. J. Phillips for serving as my advisor and committee chairman who guided me with enthusiastic discussions, helpful suggestions, and correction of the dissertation draft. Thanks must also be extended to Dr. J. S. Lin of Small Angle X-ray Scattering National Laboratory at Oak Ridge, Knoxville, who gave me the useful discussions and helped with the alignment of the SAXS equipment. Thanks also is owed to Dr. Brian Annis for his help with the SAXS alignment near the end of this research.

I can not overlook the suggestions given to me by the dissertation committee members, Dr. Joseph E. Spruiell, Dr. Edward. S. Clark and Dr. Mark Dadmun whose interest in this study provided me with many important questions, and whose advise increased the scientific accuracy of this dissertation. Especially, Dr. E. S. Clark whose final correction of this manuscript I sincerely appreciate.

Gratitude goes to the financial support from Electric Power Research Institute (EPRI) and National Science Foundation (NSF).

Eternally, I will remember my best friend and wife, Won-Sil, in my heart who has always been near me with encouragement, smiles, tenderness as well as our seven month old son, Young Wook, who has made us very happy with his crying, smiles and giggles.

ABSTRACT

Ethylene/1-octene copolymers produced using metallocene catalysts have a homogeneous comonomer content with respect to molecular weight. Two series of molecular weight having 1-octene content ranging from zero to thirty nine branches per 1000 carbon atoms, have been studied. The influence of branch content on structure and melting behavior as well as on isothermal and non-isothermal bulk crystallization has been studied. The principal techniques used have been thermal analysis and small angle x-ray scattering.

As branch (defect) content increases in olefin copolymers, non-isothermal and isothermal crystallization rates, melting temperature, and heat of fusion decrease. Melting temperatures of homogeneous random copolymers are always lower than those of fractions of heterogeneous copolymers, having approximately the same comonomer content and molecular weight. Hence, defect distribution in copolymer systems is a more important parameter rather than defect content.

The Hoffman-Weeks plot to obtain the equilibrium melting temperatures of ethylene/1-octene random copolymers results in a non-sensible, high value or no intercept at all. The equilibrium melting temperatures of linear polyethylenes and homogeneous ethylene/1-octene random copolymers were determined as a function of molecular weight and branch content, using Thompson-Gibbs plots involving lamellar thickness data. This systematic study makes it possible to evaluate two equilibrium melting temperature depression equations for the olefin type random copolymers, the Flory equation and the Sanchez-Eby equation, as a function of defect content and molecular weight. An empirical equation determined from this study for predicting the equilibrium melting point of linear polyethylene as a function of molecular weight is more sensitive to molecular weight than

the Flory-Vrij equation. The range over which the two equations can be applied depends on the defect content, after correcting the molecular weight effect on the equilibrium melting temperature. The $T_m^o(n \to \infty)$ of linear polyethylene at infinite molecular weight was found to be 144.4 ^oC.

The equilibrium melting temperature, $T_m^o(n, p_B)$, of ethylene/1-octene random copolymers was a function of the molecular weight and defect at low defect content ($p_B\% \leq 1.0\%$). The $T_m^o(n, p_B)$ was a weak function of molecular weight and a strong function of the defect content at high defect content ($p_B\% \geq 1.0\%$). The Flory copolymer equation could predict $T_m^o(n, p_B)$ at $p_B\% \leq 1.0\%$ when molecular weight was corrected. Sanchez-Eby's uniform inclusion model could predict $T_m^o(p_B)$ at high defect content, $1.6\% < p_B\% < 2.0\%$. It was observed that some defects were included in crystalline phase and the excess free energy (18 ~37 kJ/mole) estimated in this study were within the theoretical range.

A mathematical and graphical method was developed to estimate the phase boundary thickness. The calculated electron density profiles showed an intermediate profile between linear-gradient and semi-sigmoidal models. Background intensity showed a systematic positive deviation as a function of defect content. Electron density fluctuation component increased and electron density difference between amorphous and crystalline phase decreased with defect contents, reflecting defect inclusion. Interfacial layer thickness depended on defect content, defect distribution, crystallization temperature and time, and the temperature at which SAXS intensity is measured. The interfacial layer thickness of the homogeneous ethylene/1-octene copolymers decreased as a function of defect content while that of the heterogeneous copolymers increases. The interfacial layer thickness of LPE and EO copolymers at low in-situ temperature were

higher than those at ambient temperature. On increasing in-situ temperature, the phase boundary became thin and finally disappeared.

As a conclusion, the philosophy that defects can affect the thermodynamics properties and morphology was verified experimentally and theoretically through this study.

PREFACE

This study is reported in six chapters. Chapter 1 introduces the objectives and the importance of this research including a short explanation of the approach. Chapter 2 provides an extensive literature review: The metallocene catalysts are reviewed briefly to provide a basis regarding linear polyethylene, ethylene/α-olefin random copolymer and recent trends of catalysts for producing these polyolefins. The general thermodynamics for understanding melting and crystallization behavior, the isothermal bulk kinetics, the various methods to obtain equilibrium melting temperature and the fundamental theory of small angle X-ray scattering and its theoretical background for morphology study are described. Even though this chapter is titled as literature review, some explanations are modified and added and some equations are rearranged for more clear understanding of the concepts. Chapter 3 describes the experimental methods to reach the objectives of this research described in Chapter 1. The experimental results obtained in this study are shown in Chapter 4 and they are analyzed and discussed in Chapter 5 based on Chapter 2. Lastly, Chapter 6 summarizes the conclusions of this study.

TABLE OF CONTENTS

CHAPTER PAGE

1. INTRODUCTION 1

2. LITERATURE REVIEW 4

2.1. Catalysts for Polymerization of Olefins 4
2.1.1. Multi Site (Heterogeneous or Ziegler-Natta) Catalysts 4
2.1.2. Uniform Site (Homogeneous or Metallocene) Catalysts 5

2.2. Random Copolymers of Ethylene/ α-olefins 6

2.3. Thermodynamics of Melting and Crystallization 9

2.4. Kinetics of Isothermal Crystallization 13
2.4.1. Avrami Analysis 15
2.4.2. Bulk Isothermal Crystallization Kinetics 16

2.5. Equilibrium Melting Temperatures 17
2.5.1. Effect of Defects 18
2.5.1.1. Complete Exclusion of Defects 18
2.5.1.2. Uniform Inclusion of Defects 20
2.5.2. Equilibrium Melting Temperature from Hoffman-Weeks Plot 24
2.5.3. Effects of Chain Length (Molecular Weight) 27

2.6. Small Angle X-ray Scattering (SAXS) 28
2.6.1. Fundamental Theory of Small Angle X-ray Scattering 30
2.6.2. Theoretical Background to Obtain the Thickness of Long Range Order 35
2.6.2.1. Bragg's Law 35
2.6.2.2. Correlation Function 37
2.6.2.3. Interface Distribution Function 42
2.6.3. Distance Distribution Function 43
2.6.4. Radius of Gyration by Guinier Approximation 47

3. EXPERIMENTAL 53

3.1. Materials 53

3.2. Sample Preparations and Dimensions 56
3.3. Thermal Analysis 56
3.4. Bulk Crystallization and Melting by Polarized Light Transmission. 56
3.5. Isothermal Crystallization 57
3.6. Small Angle X-ray Scattering (SAXS) 58
3.7. Wide Angle X-ray Scattering (WAXS) 63
3.8. Density Gradient Column 64

4. RESULTS 65

4.1. Thermal Analysis 65
4.1.1. Non-isothermal Crystallization 65
4.1.1.1. Cooling Rate Effects 65
4.1.1.2. Branch Amount and Length Effects 69
4.1.2. Melting Behavior 72
4.1.2.1. As-received LLDPE 72
• Ethylene/1-octene Random Copolymers 72
• Ethylene/1-propene (EP) and ethylene/1-butene (EB) random copolymers 75
4.1.2.2. Isothermally Crystallized LLDPE 78
• Isothermal Crystallization Temperature Effect 78
• Isothermal Crystallization Time Effect 82
4.1.2.3. Degree of Crystallinity with Crystallization Temperature, Time and Branch Content 91

4.2. Crystallization Kinetics 96
4.2.1. Avrami Analysis 96
4.2.2. Rate of crystallization 103
• By Reciprocal Half-time, $1/t_{1/2}$ 103
• By Reciprocal Initial-time, $1/t_i$ 105
4.2.3. Secondary Nucleation 105

4.3. Equilibrium Melting Temperature (T_m^0) 105
4.3.1. Hoffman-Weeks Plots 107
4.3.2. Thompson-Gibbs Plots 107

4.4. Morphology Study using SAXS 118
4.4.1. Intensity Measured at Ambient and Crystallization Temperature 118
4.4.1.1. Quenched Samples 118
4.4.1.2. Measured at Crystallization Temperatures 120

4.4.1.3. Temperature Effect on SAXS Intensity for Linear

Polyethylene. 124
4.4.2. Tail Region Effect on SAXS Analysis 124
4.4.3. Theoretical Development for Estimation of Interfacial Layer Thickness Using SAXS 128
4.4.3.1. Theoretical Background for Transition Layer Thickness 128
4.4.3.2. Development of Mathematical Model and Analytical Approach 135
4.4.3.2.1. Slit Collimation 137
4.4.4. Interfacial Layer Thickness of LPE and EO copolymers 142

5. DISCUSSION 149

5.1. Thermal Analysis 149
5.1.1. EO, EB and EP Copolymers 149
5.1.2. Melting Temperatures of Homogeneous and Heterogeneous EO Copolymers. 151

5.2. Bulk Crystallization 155
5.2.1. Avrami Analysis 155
5.2.1.1 At Early Stage of Crystallization Process 158
• Crystallization Temperature Effect 158
• Branch content and Molecular Weight Effect 159
5.2.1.2 Crystallization Process at Middle Stage. 160
• Crystallization Temperature Effect 161
• Branch Content and Molecular Weight Effect 161
5.2.2. Rate of Crystallization 162
• Molecular weight Effect 162
• Branch effect 163
5.2.3. Secondary Nucleation Kinetics 165
5.2.3.1. by reciprocal Half-time ($1/t_{1/2}$) 166
• Input Parameter Effect 168
• Molecular Weight Effect 168
• Branch Effect 175
5.2.3.2. By Reciprocal Initial-time ($1/t_i$) 177

5.3. Equilibrium Melting Temperature, T_m^o 178
5.3.1. Hoffman-Weeks Plots 180
Overestimation and $T_m = T_c + c$ 180
Curvature 181
5.3.2. Thompson-Gibbs Plots 187
5.3.3. Molecular Weight Effect 191
5.3.3.1. Equilibrium Melting Temperatures of Linear

Polyethylenes from Literature 191

5.3.3.2. Determination of T_m^o's of Linear Polyethylenes as a Function of Molecular Weight 194
• Using the data of D. C. Bassett et. al 194
• From This Study 197
5.3.3.3. Empirical Estimation of T_m^os for Linear Polyethylenes 197
5.3.3.4. Modification of Flory-Vrij Equation 200
5.3.4. Defect (or Branch) Content Effect 209
5.3.5. Analysis of Defect Location and Content 219

5.4. Morphology Study Using Small Angle X-Ray Scattering 227
5.4.1. Room and High Temperature Behavior 227
5.4.2. Lamellar Thickness from 1-Dimensional Correlation Function. 228
5.4.3. Tail (Porod's) Region Intensity 232
• Extrapolated and Observed Intensity 235
5.4.4. Electron Density Fluctuation and Invariant 244
5.4.5. Interfacial Layer (Phase Diffuse Boundary or Transition Layer) Thickness 256
5.4.5.1. Effect of Background Correction 256
5.4.5.2. As a Function of Defects for Quenched Samples 258
5.4.5.3. As a Function of Crystallization Time 264
5.4.5.4. As a Function of Crystallization Temperature 269
5.4.6. Morphology of H-LPE ($T_c = 130\ ^oC$, $t_c = 17$ days) with Temperature 272

6. CONCLUSIONS 280
6.1. Thermal Analysis 280
6.2. Bulk Crystallization Kinetics 281
6.3. Equilibrium Melting Temperature 281
6.4. Morphology Study using SAXS 282

REFERENCES 284

VITA 291

LIST OF TABLES

TABLE PAGE

2.1.1. Uniform site(homogeneous) catalysts for poly(olefins) polymerization. 7

2.6.1. $p(r)$ −functions of the particles consisted of simple geometry.....45

2.6.2. Radius of gyration, R_g, of the particles with some simple geometry.....54

3.1.1. Characteristics of as-received linear polyethylene (LPE) and ethylene/1-octene random (EO) copolymers. 55

3.1.2. Characteristics of as-received ethylene/1-propene (EP) and ethylene/1-butene random (EB) copolymers. 102

4.2.1.1. Induction (t_i(sec)), half time ($t_{1/2}$(sec)) and Avrami index obtained from bulk crystallization using transmitted depolarized light intensity. 113

4.3.2.1. Peak melting temperatures and lamellar thicknesses of LPE and EO copolymers.....172

5.2.3.1. Analysis of regime slopes. ($T_\infty = -70\ ^\circ C$, $U^* = 1500\, cal/mole$) 173

5.2.3.2. Analysis of regime slopes. ($T_\infty = -155\ ^\circ C$, $U^* = 1500\, cal/mole$) 179

5.3.1. Equilibrium melting temperatures of the literatures determined from the plot of T_m versus $1/l$ for LPE.....183

5.3.1.1. Thermodynamics parameters and thickening coefficients of EO copolymers.....183

5.3.2.1. Equilibrium melting temperatures, $T_m^o(n, p_B)$, of LPE and EO copolymers.....190

5.3.3.1. Molecular weights and corresponding equilibrium melting temperatures. 195

5.3.3.2. Impurity (low molecular weight) influence on number and weight average molecular weight.....199

5.3.3.3. $T_m^o(n, p_B)$ calculated from the various conditions.....210

5.3.4.1. Analysis method for Figure 5.3.4.1 and 5.3.4.2 and T_m^o (^oC) of linear polyethylene used to calculate theoretical values. 213

5.3.5.1. Parameters relating to inclusion of defects for EO copolymers.....222

5.4.3.1. The treatment of background intensity and its effect on SAXS analysis (see **Figure 5.4.3.1** and **5.4.3.5**).....242

5.4.4.1.Electron and weight density of the crystalline and amorphous phase for the quenched LPE and EO copolymers.....252

5.4.5.1. Interfacial layer thickness and background effect due to the electron density fluctuation component for the quenched LPE, EO, EB, and EP copolymers.....257

5.4.6.1. Morphological parameters obtained from SAXS analysis for H-LPE (T_c = 130 °C, t_c = 17 days).....279

LIST OF FIGURES

FIGURE PAGE

2.3.1. Schematic diagram of thermodynamics behavior of polymer chains.....10

2.5.1. Exclusion and Inclusion Models.....19

2.6.1. General Small Angle X-ray Scattering Phenomena.....32

3.6.1. Schematic diagram of ORNL 10m small angle x-ray scattering spectrometer.....59

3.6.2. Accessories for mounting the samples at the room and the in-situ (T_c) temperatures.....60

4.1.1.1. Non-isothermal crystallization thermograms (a) of H6-O at the different cooling rate, 10, 20, 30, 40 $^{\circ}C$/min.....67

4.1.1.2. Exotherm peak temperatures as a function of cooling rate.....70

4.1.1.3. DSC exotherms of EO , EB, EP copolymers measured at cooling rate, 10 $^{\circ}C$/min.....71

4.1.2.1. DSC thermogram of as-received EO copolymers (high molecular weight).....73

4.1.2.2. DSC thermogram of as-received EO copolymrs (low molecular weight).....74

4.1.2.3. DSC thermogram of as-received EB and EP copolymers.....76

4.1.2.4. Plot of peak melting tmperatures as a function of branch content for EO, EB and EP copolymers quenched in room temperature.....77

4.1.2.5. DSC thermogram of L31-B crystallized at the indicated temperatures for 1 day.....79

4.1.2.6. DSC thermogram of L40-P crystallized at the indicated temperatures for 1 day.....80

4.1.2.7. DSC thermogram of L93-P crystallized at the indicated temperatures for 1 day.....81
4.1.2.8. Melting thermogram of H7-O crystallized at 113 °C (arrow) for indicated times.....83
4.1.2.9. Melting thermogram of H16-O crystallized at 100 °C (arrow) for indicated time (day).....84
4.1.2.10. Melting temperature, T1 above T_c and T2 just below T_c, of high molecular weight EO copolymers with crystallization time, at labeled temperatures. Open and closed symbols are T1 and T2, respectively. Square, circle, and triangle are H7-O, H10-O and H16-O, respectively.....86
4.1.2.11. Melting temperature difference (T1-T2) of high molecular weight EO copolymer as a function of crystallization time, t_c (day). Labeled numbers are isothermal crystallization temperatures (°C).....87
4.1.2.12. Heat of fusion, $\Delta H1$ above T_c and $\Delta H2$ just below T_c, of high molecular weight EO copolymers with crystallization time at labeled temperatures. Open and closed symbols are $\Delta H1$ and $\Delta H2$, respectively. Square, circle, and triangle mean H7-O, H10-O and H16-O, respectively.....89
4.1.2.13. Heat of fusion (ΔH, J/g), degree of volume ($v_c(\%),\mathrm{dsc}$) and weight crystallinity ($w_c(\%),\mathrm{dsc}$) obtained between T_c and base line return temperatures (T_{br}) as a function of T_c for low molecular weight EO copolymers. Labeled numbers are isothermal crystallization time, t_c (day).....92
4.1.2.14. Heat of fusion (ΔH, J/g), degree of volume ($v_c(\%),\mathrm{dsc}$) and weight crystallinity ($w_c(\%),\mathrm{dsc}$) obtained between T_c and base line return temperatures (T_{br}) as a function of T_c for high molecular weight EO copolymers. Labeled numbers are isothermal crystallization time, t_c (day).....93

4.1.2.15. Heat of fusion (ΔH, J/g), degree of volume ($v_c(\%),\mathrm{dsc}$) and weight crystallinity ($w_c(\%),\mathrm{dsc}$) obtained between T_c and base line return temperatures (T_{br}) as a function of T_c for low molecular weight EO copolymers. Labeled numbers are isothermal crystallization time, t_c (day).....94

4.1.2.16. Heat of fusion (ΔH, J/g) and weight crystallinity ($w_c(\%),\mathrm{dsc}$) of EO copolymers crystallized at various temperature and time with branch content. 95

4.2.1.1. Normalized intensity (a) and Avrami plot (b) of L10-O at the indicated temperature.....97

4.2.1.2. Normalized intensity (a) and Avrami plot (b) of L18-O at the indicated temperature.....98

4.2.1.3. Normalized intensity (a) and Avrami plot (b) of H7-O at the indicated temperature.....99

4.2.1.4. Normalized intensity (a) and Avrami plot (b) of H10-O at the indicated temperature.....100

4.2.1.5. Normalized intensity (a) and Avrami plot (b) of H16-O at the indicated temperature.....101

4.2.2.1. Plots of reciprocal half time ($1/t_{1/2}$, min^{-1}) as a function of crystallization temperature (a) and supercooling (b).....104

4.2.2.2. Plots of reciprocal initial time (min^{-1}) as a function of crystallization temperature (a) and supercooling (b).....106

4.3.1.1. Plot of melting temperatures against crystallization temperatures for the ethylene/1-octene random copolymers of high molecular weight. Labeled numbers are the crystallization time and the weight crystallinity.....108

4.3.1.2. Plot of melting temperatures against crystallization temperatures for the ethylene/1-octene random copolymers of low molecular weight. Labeled numbers are the crystallization time and the weight crystallinity from DSC.....109

4.3.2.1. Peak melting temperatures (°C) against reciprocal lamellar thickness ($\mathring{A}^{-1}$) for linear polyethylenes (LPE) of high and medium moleular weight.....110

4.3.2.2. Peak melting temperatures (°C) against reciprocal lamellar thickness ($\mathring{A}^{-1}$) of high moleular weight EO copolymers.....111

4.3.2.3. Peak melting temperatures (°C) against reciprocal lamellar thickness ($\mathring{A}^{-1}$) for low moleular weight EO copolymers.....112

4.4.1.1. SAXS intensity profiles for the quenched LPE and EO copolymres.....119

4.4.1.2 Lorentz corrected SAXS intensity profiles for quenched LPE and EO copolymers.....121

4.4.1.3. SAXS intensity profiles for H6-O with different melting temperatures.....122

4.4.1.4. Lorentz corrected SAXS intensity profiles for H6-O with different melting temperatures.....123

4.4.1.5. SAXS intensity profiles for H-LPE ($T_c = 130\ ^{\circ}C$, $t_c = 17$ days) measured at different temperatures.....125

4.4.1.6. Lorentz corrected SAXS intensity profiles for H-LPE ($T_c = 130\ ^{\circ}C$, $t_c = 17$ days) measured at different temperatures.....126

4.4.2.1. SAXS intensity profiles obtained from 5m and 1m geometry of L39-O quenched in ambient temperature.....127

4.4.3.1. Schematic diagram showing electron density fluctuation due to defects and interfacial layer in systems.....130

4.4.3.2. Electron density profiles obtained from the convolution product of an ideal electron density, $g(r)$, for two phase system and the various ghost functions, $h(r)$, where the x-axis was normalized. (see text for the detail condition of $h(r)$ functions).....138

4.4.3.3. Various modified Porod's law for the pin-hole collination with a scattering vector, $q = 4\pi \cdot \sin\theta/\lambda$.....139

4.4.4.1. Graphical demonstration ((a) for sigmoidal-gradient model, (b) for linear- and semi-sigmoidal-gradient models) showing the effect of background intensity correction on estimating interfacial layer thickness. (sample H16-O quenched at ambient temperature.....143

4.4.4.2. Graphical demonstration ((a) for sigmoidal-gradient model, (b) for linear- and semi-sigmoidal-gradient models) showing the effect of background intensity correction on estimating interfacial layer thickness. (sample L39-O quenched at ambient temperature.....144

4.4.4.3. Plot to estimate interfacial layer thickness of the quenched LPEs and EO copolymers, using linear and semi-sigmoidal electron density gradient model.....146

4.4.4.4. Plot to estimate interfacial layer thickness of the quenched LPEs and EO copolymers, using sigmoidal electron density gradient model.....147

4.4.4.5. One-dimensional correlation function showing invariant and transition layer variation as a function of defects.....148

5.1.2.1. Peak melting temperatures of the homogeneous and heterogeneous EO copolymers cooled fast as a function of branch content.....152

5.1.2.2. Schematic diagram for heterogeneous and homogeneous copolymers of extreme case.....154

5.2.1.1. Avrami index with crystallization temperature. (open and closed symbol: obtained by including initial point and except initial part, respectively).....156

5.2.1.2. Avrami index n (a) and n′ (b) as a function of branch content, obtained including initial point and except initial part, respectively.....157

5.2.3.1. Regime plots of the bulk crystallization kinetics analyzed with half time $t_{1/2}$ assuming a heterogeneous (a) and homogeneous (b) secondary nucleation ($T_\infty = -70\ ^\circ C,\ U^* = 1500\, cal/mole$).....167

5.2.3.2. Regime plots of the bulk crystallization kinetics analyzed with half time $t_{1/2}$ assuming a heterogeneous (a) and homogeneous (b) secondary nucleation ($T_\infty = -155\ ^\circ C,\ U^* = 1500\, cal/mole$) 169

5.2.3.3. Regime plots of the bulk crystallization kinetics analyzed with initial time t_i assuming a heterogeneous (a) and homogeneous (b) secondary nucleation ($T_\infty = -70\ ^\circ C,\ U^* = 1500\, cal/mole$) 170

5.2.3.4. Regime plots of the bulk crystallization kinetics analyzed with initial time t_i assuming a heterogeneous (a) and homogeneous (b) secondary nucleation ($T_\infty = -155\ ^\circ C,\ U^* = 1500\, cal/mole$) 171

5.3.1.1. Observed and calculated melting temperatures (°C) against crystallization temperatures (°C) for high molecular weight EO copolymers. 184

5.3.1.2. Observed and calculated melting temperatures (°C) against crystallization temperatures (°C) for low molecular weight EO copolymers. 185

5.3.2.1. Melting thermograms of H7-O fast cooled and crystallized at 113 °C for indicated times 188

5.3.3.1. Plot of peak melting points (°C) against reciprocal stem length (nm^{-1}) using the data by D. C. Bassett et. al., (Proc. R. Soc. Lond. A377, 39 (1981)) 193

5.3.3.2. Plot of melting temperatures against reciprocal stem length at indicated molecular weights, reanalyzing the data by D. C. Bassett *et. al.* 196

5.3.3.3. Equilibrium melting temperatures against reciprocal molecular weights. Solid and dotted lines are the values calculated with Flory-Vrij equation and modified equation (5.3.3.7), respectively 201

5.3.3.4. The observed and the calculated melting temperatures of n-alkanes. (dotted line; with 145.35 °C by Flory & Vrij, solid line; with 144.42 °C in this study) 206

5.3.3.5. Deviations between the calculated and the measured melting temperatures of n-alkanes. 208

5.3.4.1. Equilibrium melting temperatures of LPE (square) and EO copolymers (circle; high Mw, triangle; low Mw) as a function of branch point mole fraction at the indicated weight average molecular weight (k = 1000 g/mole; closed circle stands for T_m^o calculated with equation (5.3.3.1)). 211

5.3.4.2. Equilibrium melting temperatures of LPE (square) and EO copolymers of low Mw as a function of branch point mole fraction at the indicated weight average molecular weight (k = 1000 g/mole , closed circle stands for T_m^o calculated with equation (5.3.3.1)). 215

5.3.5.1. (a) Equilibrium melting temperature depression with defect content of EO copolymers. ($T_m^o(n \rightarrow \infty) = 144.4$ °C for infinite molecular weight). (open and closed symbols are $T_m^o(n, p_B)$ from SAXS (open symbol) and Hoffman-Weeks (closed symbol). 225

5.3.5.1. (continued) (b) Equilibrium melting temperature depression with defect content of EO copolymers.($T_m^o(n) = 142.1$ °C for finite molecular weight, $\overline{M}_w = 100k$) ($Tm^o(n, p_B)$ from SAXS (open symbol) and Hoffman-Weeks (closed symbol). 226

5.4.2.1. Comparison of one-, $\gamma 1(x)$, and three-dimensional correlation function, $\gamma 3(x)$, for H6-O quenched in ambient air. 229

5.4.2.2. Schematic diagram showing the dimension concepts for correlation function using ideal two phase system. 230

5.4.2.3. Normalized one-dimensional correlation function behavior of the quenched LPE and EO copolymers. 231

5.4.2.4. Normalized one-dimensional correlation function behavior of H-LPE with different melting temperatures. 233

5.4.2.5. Normalized one-dimensional correlation function behavior of H7-O with different melting temperatures. 234
5.4.3.1. An example (sample L39-O quenched in ambient air) of the observed and the extrapolated background intensity. (see Table 5.4.3.1 for symbols). 236
5.4.3.2. SAXS intensity profiles measured at room temperature and calculated background intensity of L39-O quenched in ambient temperature)....237
5.4.3.3. Plot to correct electron density fluctuation with Vonk's empirical equation (sample L39-O quenched in ambient temperature). 239
5.4.3.4. Plot to correct electron density fluctuation with Ruland's empirical equation (sample L39-O quenched in ambient temperature). 240
5.4.3.5. The effect of background intensity (sample; L39 quenched in ambient air) on an 1-dimensional correlation function. (see Table 5.4.3.1 for symbols). 243
5.4.4.1. The observed and the background intensity obtained using Vonk (broken line) and Ruland (solid line) empirical equation for M-LPE and EO copolymers. 246
5.4.4.2. Alternative plot to estimate electron density fluctuation component, Fl, for LPE and EO copolymers. 247
5.4.4.3. Electron density fluctuation components (Fl_e) of polymer systems by various empirical methods....248
5.4.4.4. Electron density fluctuation components for LPE and EO copolymers without and with subtraction of Fl_e of H-LPE. 249
5.4.4.5. Invariant, $Q(mole \cdot el^2/cm^6)$, as a function of defect content for quenched LPE and EO copolymers....251
5.4.4.6. Electron density ($mole\ el/cm^3$) of crystalline (ρ_c) and amorphous (ρ_a) phase for quenched LPE and EO copolymers as a function of defect content, assuming a two-phase model. Indicated arrows represent the corresponding theoretical values....254

5.4.4.7. Electron density fluctuation component as a function of temperature for H-LPE crystallized at various temperature.....255
5.4.5.1. The effect of background intensity (I_{Bg}) correction on the interfacial layer thickness $\Delta(\mathring{A})$ assuming sigmoidal-gradient model.....259
5.4.5.2. Interfacial layer thicknesses, Δ, T, E ($\mathring{A}$) obtained by using various models, sigmoidal-, semi-sigmoidal- and linear gradient models, as a function of defect content for LPE and EO copolymers quenched in ambient temperature.....260
5.4.5.3. Interfacial layer thickness for homogeneous (open circle) and heterogeneous (closed circle) EO copolymers assuming linear gradient of electron density.....262
5.4.5.4. Interfacial layer thickness (Δ) determined at ambient temperature as a function of crystallization time for EO copolymers crystallized at indicated T_c (closed symbol is the corresponding Δ quenched in ambient temperature).....265
5.4.5.5. Interfacial layer thickness (T) determined at ambient temperature as a function of crystallization time for EO copolymers crystallized at indicated T_c (closed symbol is the corresponding T quenched in ambient temperature).....266
5.4.5.6. Interfacial layer thickness (Δ) as a function of crystallization time. H7-O and H16-O were crystallized at 113 $^{o}C$and 100 ^{o}C, respectively. Open and closed symbols indicate the room and the in-situ measurement of SAXS intensity.....267
5.4.5.7. Interfacial layer thickness (T) as a function of crystallization time. H7-O and H16-O were crystallized at 113 $^{o}C$and 100 ^{o}C, respectively. Open and closed symbols indicate the room and the in-situ measurement of SAXS intensity.....268
5.4.5.8. Interfacial layer thickness (Δ ($\mathring{A}$) estimated from sigmoidal model) as a function of crystallization temperature (^{o}C). Open and closed symbols represent the measurement at room and crystallization temperature, respectively. Dotted horizontal line is the Δ for quenched EO copolymers.....270

5.4.5.9. Interfacial layer thickness (T (Å) estimated from the graphical method of this study) as a function of crystallization temperature (^{o}C). Open and closed symbols represent the measurement at room and crystallization temperature, respectively. Dotted horizontal line is the T for quenched EO copolymers.....273

5.4.6.1. One dimensional correlation function behavior of H-LPE ($T_c = 130\ ^{o}C$, $t_c = 17$ days) measured at different temperatures.....275

5.4.6.2. Ruland's plot to obtain Δ of H-LPE crystallized at 130 ^{o}C for 17days, using SAXS profiles measured at indicated temperature.....277

5.4.6.3. Interfacial Layer thickness (Δ) against temperature for H-LPE ($T_c = 130\ ^{o}C$, $t_c = 17$ days).....278

1. INTRODUCTION

Linear low density polyethylene (LLDPE) is a copolymer of ethylene with α-olefins such as propene (), 1-butene (), 1-hexene (), 1-octene (), or 4-methyl-1-pentene (). The α-olefin comonomers produce the corresponding branches (methyl, ethyl, *n*-butyl, *n*-hexyl, or *iso*-butyl) along the main chain backbone which consists of methylene ($-CH_2-$) linkages. These branches are named short chain branches (SCB) because of their uniform, short branch length, unlike the branches found in low density polyethylene (LDPE) that has long and short branches, and linear polyethylene (HDPE) with few branches in its main chain. The number and the length of SCB are controlled by the proper comonomer concentration and its concentration in the reaction medium. The sequence length-distributions are dependent on the catalyst and the reaction condition.[1]

Crystallization behavior and morphological phenomena are influenced by the type and number of branches, the molecular weight, and the inter- and intra-sequence length distribution. As one increases the SCB, one observes a decrease in degree of crystallinity, crystallite size, crystallization temperature, onset and peak melting temperatures, long periods and lamellar thickness.[2,3]

As a consequence, it is important to use the linear low density polyethylene where parameters such as chain length and branch distribution are precisely controlled, in order to study the melting behavior and the morphology. In the past, these parameters could not be controlled using the classical Ziegler/Natta catalysts, but in the present, the new catalysts make it possible to produce the linear polyethylenes and α-olefin type

copolymers with the narrow molecular weight distribution, (MWD, $Mw/Mn \approx 2.0$) and uniform distribution of comonomer in copolymer systems.

The underlying philosophy of this study came from the simple concept that the defects affect the morphological structure and crystallization behavior regardless of whether they enter into or are rejected from the crystal. The objectives of the present work based on this idea are to trace the relationships between structures and defects qualitatively and quantitatively through the systematic study of location of defects, equilibrium melting temperature, lamellar thickness, interfacial layer thickness and other miscellaneous morphological parameters. To achieve these objectives the two research techniques, (i) equilibrium melting temperature, (ii) small angle X-ray scattering behavior, have been used on ethylene/1-octene random copolymers with narrow molecular weight distribution and uniform distribution of comonomer along the main chain backbone.

The equilibrium melting temperature is a very important parameter reflecting the nature of the structure. It is also important to the analysis of secondary nucleation kinetics and the simulation of kinetics, and in other polymer physics fields. In spite of its fundamental nature, there has been no absolute systematic study aimed at obtaining this value accurately. The equilibrium melting point of linear polyethylene that has been a matter of controversy will be re-estimated as a function of molecular weight. It will then be used to test the validity of the Flory & Vrij equation, based on the their analysis. The equilibrium melting temperature of ethylene/1-octene random copolymers will be studied as a function of the defect content and the molecular weight (Section 4.3 and Section 5.3.).

The equilibrium melting temperatures will be obtained from the relation between lamellar thickness (from SAXS) and observed melting temperatures using the Thompson-

Gibbs concept. Data will then be used to evaluate the applicabilities of the rival Flory and Sanchez-Eby theories of equilibrium melting points in copolymers. In addition, the defect location in semi-crystalline polymers will be studied, and the application of the Hoffman-Weeks plot to obtain equilibrium melting temperature and the annotated problems will be demonstrated.

The morphology study using small angle X-ray scattering (SAXS) will be focused on morphological parameters such as periodicity, lamellar thickness (crystalline phase thickness) and interfacial layer (transition layer, phase diffuse boundary) thickness assuming a three-phase model. In this study, new analytical methods to estimate transition layer thickness will be introduced, based on mathematical concepts (**Section 4.4.3**). Especially, **Section 4.4.3** will be considered as an independent part concentrating on this analytical method although the concepts and values described and obtained in this section are connected to the results of Section 5.4. We will test the possibility, if SAXS supports the results of **Section 5.3.4** and **5.3.5**, that some defects are incorporated into the crystalline phase. Additionally, some miscellaneous morphological parameters such as electron density (or mass density) for each amorphous and crystalline phase, lamellar planarity and shapes of particles will be considered.

2. LITERATURE REVIEW

2.1. Catalysts for Polymerization of Olefins

2.1.1. Multi Site (Heterogeneous or Ziegler-Natta) Catalysts

The introduction of poly(olefins) originated with low density polyethylene (LDPE) produced at high pressure (124MPa, 18,000psi) and high temperature (100~300 ℃) in Imperial Chemical Industries, Ltd. (ICI) in 1933. Since Karl Ziegler *et al.* in Germany discovered that titanium tetrachloride ($TiCl_4$) or vanadium tetrachloride (VCl_4) / alkyl aluminum catalysts system can polymerize ethylene at room temperature and atmospheric pressure and simultaneously G. Natta *et al.* in Italy found that the polymer from these catalysts shows stereoregularity and crystalline properties, various vinyl polymers such as high density polyethylene (HDPE) or linear polyethylene (LPE), linear low density polyethylene (LLDPE) and isotactic polypropylene have been produced commercially. These catalysts (or initiator) systems are referred to as Ziegler-Natta catalysts and are composed of an organometallic compound of a Group I-III metal with a halide of a Group IV-VII of the periodic table.[4] Two main systems are titanium chloride with alkylaluminium (e.g., $Et_3Al/TiCl_3$) and chromium on silica. The catalyst systems are heterogeneous for some titanium-based systems and soluble for most vanadium-based catalysts. HDPE and LLDPE are produced using both titanium- and chromium-based systems and isotactic polypropylene (*iso*-PP) is polymerized with titanium-based catalyst.

In spite of their practical importance due to the commercial production of *iso*-PP, HDPE and LLDPE *et al.*, the Ziegler-Natta catalysts can't control molecular weight distribution and avoid the production of by-products of low molecular weight and low density due to their multi-site properties. The terminology, multi-site, came from the fact that a heterogeneous (transition metal) catalyst species has the various sites with different activity. Due to the different activity the polymers produced with multi-site (or heterogeneous Ziegler-Natta catalyst) catalysts consist of various chain lengths resulting in different physical properties. Especially, in the case of the random copolymers of ethylene/α-olefins (LLDPE), the narrow comonomer distribution as well as narrow molecular weight distribution is required. It is impossible to satisfy this requirement with heterogeneous catalysts since multiple active sites with different reactivity ratios for ethylene and comonomers cause polymers with broad MWD and broad SCB. New attempts to control polymer structure and properties have been concentrated on the preparation of catalysts with uniform activity.

2.1.2. Uniform Site (Homogeneous or Metallocene) Catalysts

The kinds of metallocene catalysts consisting a Group IV transition metal complex with methylaluminoxane (MAO) have uniform activity and allow the production of poly(olefins) with controlled molecular weight, narrow molecular weight distribution ($Mw/Mn \approx 2.0$) and stereoregular structures.[5] These uniform site catalysts are variously called (a) single site catalysts or homogeneous catalysts, due to their uniform activity compared to multi-site Ziegler-Natta catalysts with heterogeneous activity, (b) Kaminsky-type catalysts due to the contribution of Kaminsky *et al.* to improve activity of these catalysts, (c) metallocene catalysts and (d) constrained geometry catalysts (Dow

Chemical Co.). Although metallocene chemistry was started by Natta *et al.*, the activity of the catalysts was too low to be useful.[6] In 1980, Sinn and Kaminsky reported that the addition of a small amount of water increases the activity of these catalyst systems significantly.[7]

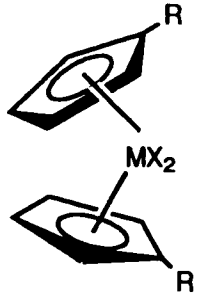
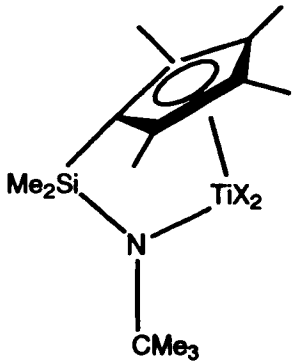
The most popular single site catalyst systems are a combination of bent metallocenes, which are a Ti, Zr or Hf complex with two cyclopentadienyl ligands and two halides or alkyl ligands (1 in **Table 2.1.1**), and excess MAO, which was discovered by Kaminsky *et al.*[5, 8] Furthermore the cyclopentadienyl-amide catalysts (2 in **Table 2.1.1**), named Constrained Geometry catalysts by Dow Chemical, have only a single cyclopentadienyl ligand and seem to have been used in the production of LLDPE. In 1990, Dow filed patents for these types of catalysts (European Patent Application 416 815) and 13 days later, Exxon did the same independently (European Patent Application 420 436).

The cyclopentadienyl-amide catalysts/excess MAO cocatalysts systems allow ethylene/1-octene copolymer of high molecular weight to be obtained. In these catalyst systems, molecular weight is controlled using hydrogen gas (H_2).

2.2. Random Copolymers of Ethylene/ α-olefins

To obtain narrow molecular weight distribution (MWD) from the poly(olefins) polymerized with heterogeneous catalysts, fractionation methods such as temperature rising elusion fractionation (TREF) for fractionation by crystallinity and composition of copolymer or solvent-gradient elusion fractionation (SGEF) and successive

Table 2.1.1. Uniform site (homogeneous) catalysts for poly(olefins) polymerization

Code	Structures	Poly(olefins)	Expected Process	Expected Company
1		HDPE LLDPE Atactic PP Ethylene/cycloalkene copolymer	-	Exxon
2		LLDPE(comonomer: 1-octene) Ethylene/styrene copolymer	High pressure, High temperature in solution	Dow

M=Zr, Hf, Ti : X=Cl or Me

reprecipitation fractionation for separation by the molecular weight have been used. However, it is not easy to provide a large volume of resin with narrow molecular weight to the market. Recent catalyst developments allow the production of a new type of LLDPE by controlling molecular weight, its distribution (MWD), comonomer incorporation, or homogeneous distribution of short chain branch, using single site (homogeneous) catalysts.

In industry, the first products using single site catalysts are copolymers of ethylene/α-olefins of Exxon that has produced 15kt of LLDPE/year from the demonstration plant since 1991. Following Exxon, Dow Chemical began producing 57kt of LLDPE/year using a titanium-based catalyst with a linked cyclopentadienyl-amide ligand in 1993.

The cyclopentadienyl-amide catalysts/excess MAO cocatalysts systems have the following characteristics: i) α-olefins (comonomers) randomly incorporate to the propagating ethylene chain, which will cause uniform SCB distribution, ii) comonomer content is independent of the chain length, iii) significant comonomer incorporation into the polymer is achieved without a large excess of comonomer, iv) very precise control of molecular weight is possible, v) narrow MWD ($\overline{M}_n/\overline{M}_w \approx 2.0$) is obtained, vi) these controlled molecular parameters will produce uniform morphology. On the other hand, classical multi site (heterogeneous) catalysts cause non-random copolymers with broad MWD and heterogeneous SCB distribution (i.e., shorter chains have a much higher -olefin contents than the longer chains). The LLDPE with narrow MWD shows sharper melting point, better hot tack and heat-seal properties, as well as higher clarity, better impact resistance and lower levels of alkan-soluble components.[5, 9] Resins prepared with single

site catalysts are being produced on a demonstration scale for niche markets and their cost remains high relative to competing resins.

Despite their unique advantages, there are practical processing problems with these new polymers. The narrow MWD makes the melt viscosity of polymers low shear sensitive. However, Dow can overcome this problem by incorporating long chain branches into the linear short chain branched structure, using cyclopentadienyl-amide catalysts. The final products show very high shear sensitivity and higher melt strength, allowing facile processing. This technology is called In-site technology and is different from common single-site catalysts technology at the point that Constrained Geometry Homogeneous Catalyst is used.[9] It is known that Dow produces copolymers having from 2~12%(w/w) 1-octene to a thermoplastic elastomer with up to 20%(w/w) comonomer.

2.3. Thermodynamics of Melting and Crystallization

The thermodynamic behavior of flexible polymer chains can be summarized as shown in **Figure 2.3.1**.[10] For spontaneous process to be possible the Gibbs free energy (or free enthalpy) should be negative. This spontaneous process will derive a system go to a lower energy state from a higher energy state. Thus the lowest energy state is most stable state. This most stable and lowest Gibbs free energy state can be obtained energetically in the most favorable conformation of polymer chains. The most favorable conformation of polymer chains depends on temperature and the phases present such as crystalline phase and amorphous phase. This thermodynamics will be explained based on the Gibbs free energy equation which shows the relation of free enthalpy (G), the enthalpy (H) and entropy (S) with thermodynamic temperature (T):

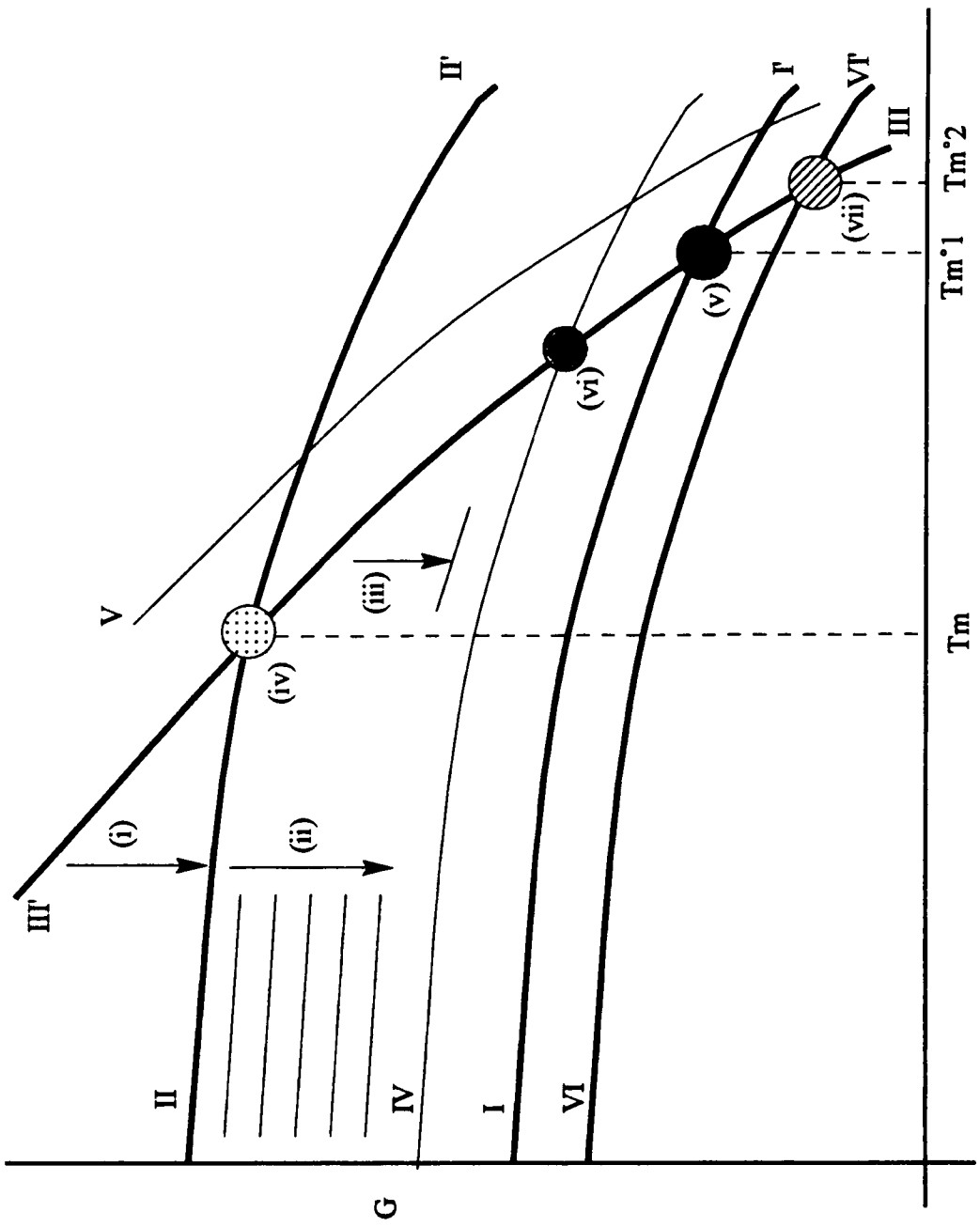


Figure 2.3.1. Schematic diagram of thermodynamics behavior of polymer chains.

$$G = H - TS \tag{2.3.1}$$

In the molten state the polymer chains will have many more possible conformations since the flexible polymer chains are coiled and entangled. It will cause entropy increase and hence, will lead the Gibbs free energy decrease of polymer chains as sharply as $-TS$. This means that there is a temperature above which the random coil state is more stable. This temperature is the melting temperature (T_m) and called first order transition by Ehrenfest due to the sharp discontinuity change of the slope, $\partial \Delta G / \partial T = -\Delta S$. These first order transition temperatures are (iv), (v), (vi) as shown in **Figure 2.3.1**. If the crystal is metastable, the first order transitions appear (iv) and if the crystal is the equilibrium crystal structure (fully extended chains), the first order transition is (v) and called the equilibrium melting temperature.

When, however, the melts are supercooled (III') to a temperature below the melting temperature, the long range ordering of polymer chains occurs due to crystallization. Clearly, this long range ordering leads to a reduction in entropy due to fewer available conformations than in the amorphous phase. This unfavorable entropy reduction that causes the increase of Gibbs free energy can be offset by a large reduction of enthalpy because of intermolecular forces such as van der Waals force or Hydrogen bonding. Thus, the relationship of magnitudes between the enthalpy change and the product of the melting temperature and the entropy change will determine whether crystallization is favorable or not. If the magnitude of enthalpy change, $|\Delta H| = H_{crystal} - H_{melt}$, is larger than that of the product of the melting temperature and the entropy change, $T|\Delta S| = T\left|S_{crystal} - S_{melt}\right|$, crystallization will be favored thermodynamically since the Gibbs free energy will be lowered (i).

It is worthwhile to note that the value of the T_m is dependent on the intermolecular interaction force between adjacent chains. Thus a single isolated fully extended chain will have highest free enthalpy and a relatively low melting point because of lack of interaction with the neighboring chains (IV). Usually, since fully extended chains pack well crystallographically generating intermolecular interaction, the Gibbs free energy will be lowered compared to a single isolated fully extended chain and thus T_m will shift to higher temperature ($IV \rightarrow I \sim I'$). This is also the reason why the equilibrium melting temperature (v) of polyethylene with weak van der Waals force between the chains has a lower value than that (vii) of polyamide with strong hydrogen bonding between adjacent chains.

In fact, the melting temperature of the crystal with the lamellar, fibrillar, and fringed micellar structures is a non-equilibrium melting temperature due to the metastability of the crystal. This metastable crystal can become more stable by controlling three variables, time, temperature and pressure, although its metastability can not be removed completely unless it changes to fully extended chains. As increasing the crystallization time at a crystallization temperature, the non-equilibrium crystal will approach to the lower free enthalpy and less metastable crystal due to the annealing effect (ii). Interestingly, the molten state has also metastability when the metastable crystal melts. In the metastable molten state that has the free energy of supercooled melt, recrystallization may occur (iii).

The difficulty in measuring melting temperature is to remove the effects of annealing, superheating and recrystallization on heating. As a whole these effects will cause higher temperature than zero entropy production melting, at which there is no reorganization process. There are three classical methods to obtain zero entropy melting

of polymer chain during heating: first, fast heating in which the crystal does not have enough time to reorganize; second, crosslinking of polymer chain in the amorphous region to prevent lamellar thickening due to annealing; third, removing of the fold and amorphous region by etching technique to make thickening impossible.

2.4. Kinetics of Isothermal Crystallization

The crystallization process is controlled by primary nucleation and growth (secondary nucleation). Primary nucleation is the process by which molten polymer chains become aligned to form nuclei when the polymer melt is cooled down below its equilibrium melting temperature. Growth is a step that the crystal nuclei grow through by the addition of polymer chains onto the nuclei surface. Primary nucleation is categorized as homogeneous and heterogeneous nucleation. Homogeneous nucleation occurs when the nuclei form spontaneously and heterogeneous (or instantaneous) nucleation takes place when the foreign surface such as impurity, motes, and wall of container are already present in the system. The characteristic behavior of these nucleations can be explained as a function of time. In homogeneous nucleation the number of nuclei increases with crystallization time and in heterogeneous one the number of nuclei is constant with time. The former is a kind of athermal nucleation and the latter is that of thermal nucleation.

The rate of nucleation is a function of temperature. The crystal growth process is governed by two competing terms, diffuse-control at low crystallization temperature and nucleation-control at high crystallization temperature.[11] This process is expressed in

$$G = G_o \exp(\frac{-\Delta F^*}{kT}) \exp(\frac{-\Delta U^*}{kT}) \qquad (2.4.1)$$

where G is the growth rate at a crystallization temperature T_c, G_o a pre-exponential factor, ΔF^* the free energy of formation of the critical nucleus and ΔU^* the activation energy of the elementary jump process. At high crystallization temperature, the rate of nucleation becomes slow whereas the mobility of chains is high and the viscosity becomes low. Thus this condition is nucleation-control. As temperature is lowered, the rate of nucleation (or rate of crystallization) is increased due to favorable thermodynamic driving force, keeping the favorable mobility of chains. As the temperature is lowered further toward the glass transition temperature, the motion of chains becomes restricted and the viscosity of the system is increased, whereas the rate of nucleation is increased. This slow molecular motion makes the transport of polymer chains difficult across the phase boundary to the crystal growth surface. Thus this condition is diffusion-control. Therefore, nucleation occurs between the equilibrium melting and glass transition temperature and the rate of crystal growth shows a maximum somewhere between the two temperatures.

The overall (or bulk) crystallization kinetics is a result of the nucleation and crystal growth processes. The first attempt at analysis of the crystallization kinetics is Avrami analysis. More advanced theory of crystallization kinetics is the introduction of secondary nucleation as a function of supercooling by Hoffman and Lauritzen.[12,13]

2.4.1. Avrami Analysis

The kinetics of isothermal crystallization can be quantitatively analyzed by Avrami equation :

$$X_t = 1 - \exp(-K \cdot t^n) \tag{2.4.2}$$

After rearranging and taking the double natural logarithms in both sides of **equation (2.4.2)**

$$Ln(-Ln(1 - X_t)) = Ln(K) + n \cdot Ln(t) \tag{2.4.3}$$

where K is the kinetic rate constant, that is temperature dependent, and n the Avrami exponent, can be obtained from slope and intercept in the plot of $Ln(-Ln(1 - X_t))$ versus $Ln(t)$, respectively. Alternatively, K can be calculated using the following relationship:

$$K = \frac{Ln2}{t_{0.5}^n} \tag{2.4.4}$$

The constant K contains the information relating nucleation, linear growth rate, and crystal geometry

The problems of Avrami analysis came from the assumption behind this theory. These assumptions are (i) the constant volume, which cannot be satisfied in real polymer systems since volume contraction takes place during crystallization by as much as 5~20%.[14] and (ii) the complete crystallization, which can not be achieved in polymer systems. When the volume change is corrected, the *n* values may change by one to two

tenths of a unit. The maximum crystallinity is around 90% in our experience. Additionally, Avrami exponents, n, do not show the integer values in experiment results unlike the theoretical estimation. An additional complication is that even the same n value is related to different crystallization and nucleation type. Thus, without detail morphological information, the Avrami analysis cannot be used correctly, although it is recommended to get rough sense of crystallization mechanism.

2.4.2. Bulk Isothermal Crystallization Kinetics

Bulk crystallization kinetics can be studied with assuming one of two nucleation types, homogeneous nucleation and heterogeneous nucleation. Homogeneous nucleation can be plotted using [15]

$$\ln(t_{1/2}) + U^*/2.3R(T_c - T_\infty) \text{ vs. } 1/T_c(\Delta T)^2 f^2 \qquad (2.4.5)$$

For heterogeneous nucleation,

$$\ln(t_{1/2}) + U^*/2.3R(T_c - T_\infty) \text{ vs. } 1/T_c(\Delta T) f \qquad (2.4.6)$$

where ΔU^* is the activation energy(J/mole) for chain motion, T_m is the temperature (generally, $T_\infty = T_g - 30K$) and R is gas constant (8.314J/moleK). The factor f is a correction term which is close to unity at high crystallization temperatures, but that is important at high supercooling where the heat of fusion varies significantly with temperature. This correction factor f is given empirically as:

$$f = 2T_c/(T_m^\circ + T_c) \qquad (2.4.7)$$

Usually, U^* and T_∞ are little importance in the kinetic analysis of polyethylene.

2.5. Equilibrium Melting Temperatures

The equilibrium melting temperature (T_m°), at which the infinitely large crystal melts, is an important parameter for studying crystallization kinetics that describes the crystal growth rate as a function of supercooling ($T_m^\circ - T_c$).[11] In spite of its importance, there has been no detailed study to determine the equilibrium melting temperature for the ethylene/α-olefin copolymer within the limit of our knowledge. The purpose of this study is, thus, to determine the equilibrium melting temperatures of the series of the ethylene/1-octene copolymers as a function of SCB contents and study the location of the defects in the system.

The equilibrium melting temperature of a polymer depends on the molecular weight, comonomer (or branching) contents, diluents, pressure and so on. A theoretical method to calculate T_m° of the copolymer as a function of B-counit contents in the polymer chain was developed by Flory under the assumption of eutectic separation of homopolymers and comonomer units.[16,17]. Other theoretical methods were developed under the consideration of the molecular weight effect[18], the lamellar thickness [13], and the location of the B-counits in the system[19,20] and the need to estimate the T_m° from the experimentally determined melting points. For homopolymers, the latter takes the form of an extrapolation from the observed melting temperature of the n-alkanes to infinite molecular weight of linear polyethylene, an extrapolation to infinite lamellar thickness in

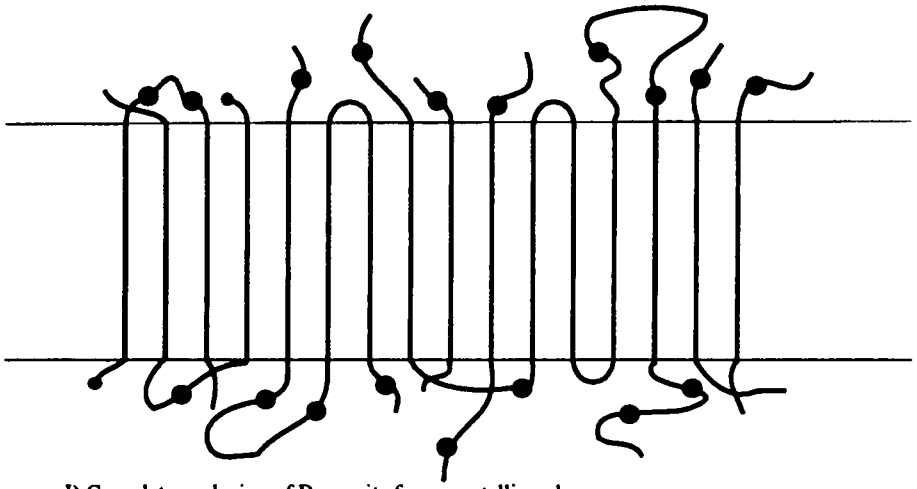
the plot of the melting temperature against the reciprocal lamellar thickness, or an extrapolation to the $T_c = T_m = T_m^\circ$ in the plot of melting temperature versus crystallization temperature. In the later section these theoretical and experimental methods will be compared and discussed with the experimental results from the ethylene/1-octene copolymer.

2.5.1. Effect of Defects

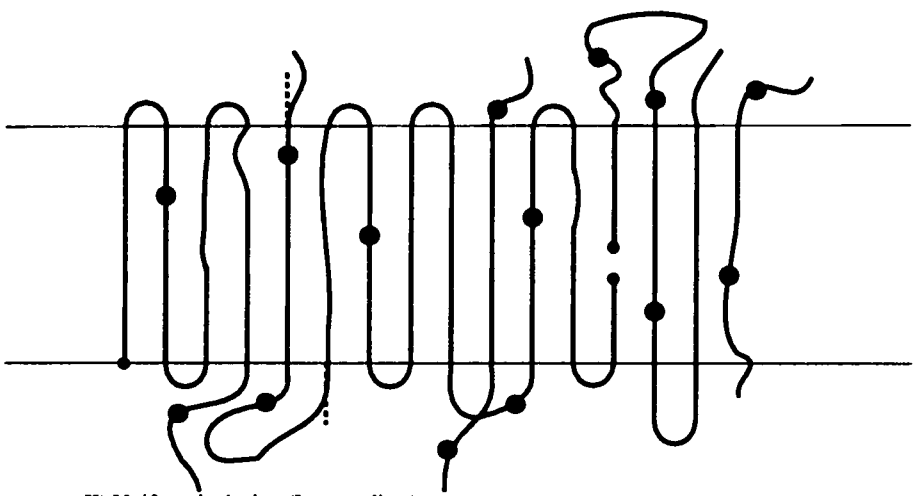
There are many well-known theoretical approaches to estimate the equilibrium melting temperature. These theoretical methods have been developed, focusing on the effects of the molecular weight and non-crystallizable B-counit content on the melting temperature. (Usually, the notation A, and B mean the crystallizable unit and the non-crystallizable counit as chosen by Flory.[16] The equilibrium melting point depression equations of the random copolymers with B counits were derived from two different models that are based on the location of B-counits in the system. One is the case of complete exclusion of B counit from the lattice solid solution formation, eutectic separation, and the other is that of uniform inclusion of B counit in the crystalline phase. The following sections introduces of the models shown in **Figure 2.5.1**.

2.5.1.1. Complete Exclusion of Defects

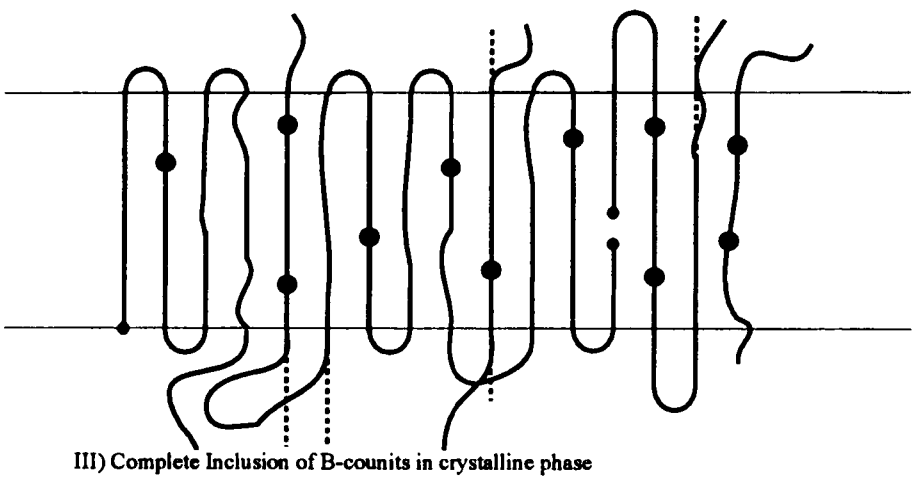
Flory's equilibrium melting point depression equation of a non-polar copolymer was developed assuming the exclusion of all the B co-units(defects including chain ends) from the crystalline lattice. The equilibrium melting temperature, melting end, liquid's line



I) Complete exclusion of B-counits from crystalline phase



II) Uniform inclusion (Intermediate)



III) Complete Inclusion of B-counits in crystalline phase

Figure 2.5.1. Exclusion and Inclusion Models.

of the copolymer $T_m^\circ(X_B)$ is expressed by the relationship of the equilibrium melting point of homopolymer T_m°, the enthalpy of fusion ΔH_u per crystallizable repeating A unit, and the sequence perpetuation probability p

$$\frac{1}{T_m^\circ} - \frac{1}{T_m^\circ(X_B)} = \left(\frac{R}{\Delta H_u}\right) \ln p \qquad (2.5.1)$$

or

$$\frac{1}{T_m^\circ} - \frac{1}{T_m^\circ(X_B)} = -\frac{R}{\Delta H_u} X_B \qquad (2.5.2)$$

where R is the universal gas constant, and for a random copolymer p is the mole fraction of crystallizable unit A, and X_B is the mole fraction of noncrystallizable B-counit. As p approaches unity, it reduces the melting point depression to zero.

2.5.1.2. Uniform Inclusion of Defects

On the other hand, using Helfand and Lauritzen's equilibrium theory of B counits in the crystal [19], Sanchez and Eby derived the equilibrium melting point depression equation of a random copolymer for the case of the uniform inclusion of defects into the crystal lattice [20]

$$\frac{1}{T_m^\circ} - \frac{1}{T_m^\circ(X_B)} = -\frac{R}{\Delta H_u}\left\{\frac{\varepsilon \cdot X_{B,C}}{RT_m^\circ(X_B)} + (1 - X_{B,C}) \ln\left[\frac{1 - X_{B,C}}{1 - X_B}\right] + X_{B,C} \ln\left[\frac{X_{B,C}}{X_B}\right]\right\} \qquad (2.5.3)$$

where T_m° and $T_m^\circ(X_B)$ are the equilibrium melting temperatures of the infinitely large crystal of a homopolymer consisting of A units and that of a copolymer with B-counits in the crystalline lattice, respectively. The mole fraction of all B-counits in the whole polymer and the mole fraction of the B-counits incorporated into the crystalline phase are X_B and $X_{B,C}$, and. ε is the excess free energy created by incorporating a B-unit in the crystalline phase. Finally, ΔH_u is the enthalpy of fusion of the homopolymer (i.e. for $X_B = 0$). **Equation (2.5.3)** can be rearranged to evaluate the degree of defect inclusion in the lattice or the excess free energy by introducing the term $\beta = X_{B,C}/X_B$, the degree of incorporation of the B-counit.[21]

$$\frac{1}{T_m^\circ} - \frac{1}{T_m^\circ(X_B)} = -\frac{R}{\Delta H_u}\left\{\frac{\varepsilon \cdot \beta X_{B,C}}{RT_m^\circ(X_B)} + (1-\beta X_B)\ln\left[\frac{1-\beta X_B}{1-X_B}\right] + \beta X_B \ln\beta\right\} \qquad (2.5.4)$$

Since the mole fractions of B-counits (i.e. hexyl branch in case of ethylene/1-octene copolymer) in the whole polymer of the ethylene-1-octene copolymers are $X_B << 1.0$, **equation (2.5.4)** can be changed to a more tractable form by expanding the first logarithm term in the parentheses to first term

$$\frac{1}{T_m^\circ} - \frac{1}{T_m^\circ(X_B)} = -\frac{RX_B}{\Delta H_u}\left\{\frac{\varepsilon \cdot \beta}{RT_m^\circ(X_B)} + (1-\beta) + \beta\ln\beta\right\} \qquad (2.5.5)$$

Equation (2.5.5) shows the linear relation between equilibrium melting point depression and mole fraction of B-counit. If we know the values of $T_m^\circ(X_B)$ and ε, the degree of incorporation β can be determined from the plot $1/T_m^\circ - 1/T_m^\circ(X_B)$ vs. X_B. Here $\beta = 0$ (i.e. $X_{B,C} = 0$) means the perfect exclusion of B-counit from the crystalline lattice and equation (2.5.5) reduced to Flory's equilibrium melting point depression **equation (2.5.2)**

(the expanded form of **equation (2.5.1)**). For the complete inclusion of all B-counits into the crystalline lattice, $\beta = 1$(i.e. $X_{B,C} = X_B$), **equation (2.5.3)** or **(2.5.4)** becomes

$$\frac{1}{T_m^\circ} - \frac{1}{T_m^\circ(X_{B,C} = X_B)} = -\frac{\varepsilon \cdot X_B}{\Delta H_u T_m^\circ(X_{B,C} = X_B)} \tag{2.5.6}$$

where the heat of fusion ΔH_u of the homopolymer has a relation with the observed heat of fusion $\Delta H_u(T, X_B)$ that is assumed as the linear function of the number of comonomer units entering the crystal and the temperature independence.

$$\Delta H_u = \Delta H(T, X_B) + \varepsilon \cdot X_{B,C} \approx \Delta H(X_B) + \varepsilon \cdot X_{B,C} \tag{2.5.7}$$

By combining **equation (2.5.6)** and **(2.5.7)** we obtains :

$$\frac{1}{T_m^\circ} - \frac{1}{T_m^\circ(X_{B,C} = X_B)} = -\frac{\varepsilon \cdot X_B}{(\Delta H(X_B) + \varepsilon \cdot X_B) \cdot T_m^\circ(X_{B,C} = X_B)} \tag{2.5.8}$$

As the crystallization temperature decreases, the driving force for crystallization, the so-called supercooling $T_m^\circ - T_C$ for the homopolymer and $T_m^\circ(X_B) - T_C$ for the copolymer, increases and it will make the rate of the addition of a stem larger than the rate of detachment during the crystallization process. This will provide enough excess energy for the B-counit to be incorporated into the crystal lattice.[19] As the supercooling decreases, however, the crystal growth rate slows, both the rate of addition and detachment of stems on the substrate are nearly equal, and the defect concentration will approach equilibrium. Clearly, the respective equilibrium melting temperatures of the copolymer evaluated at large supercooling and at low supercooling will be different based on the derived equations.

For the case of the equilibrium, an expression for the defect (B-counit) concentration in the crystal has been suggested by the Helfand and Lauritzen.[19] According to Helfand and Lauritzen, for the polymer composed of a fraction X_B of B-counits and a fraction $X_A = 1 - X_B$ of A-units, the ratio of B-counits in the crystal to A-units is given by equilibrium statistical mechanics as follows

$$\frac{X_B e^{-\varepsilon/RT}}{1 - X_B} \tag{2.5.9}$$

and the fraction of B-counit in the crystal, $X_{B,C}$, under the equilibrium condition (i.e. $T_m^\circ(X_B)$ is given by

$$X_{B,C} = X_{eq} = \frac{X_B e^{\varepsilon/RT}}{1 - X_B + X_B e^{-\varepsilon/RT}} \tag{2.5.10}$$

Equation. (2.5.3) for $X_{B,C} = X_B$ becomes then :

$$\frac{1}{T_m^\circ} - \frac{1}{T_m^\circ(X_{B,C} = X_{eq})} = -\frac{R}{\Delta H(X_B) + \varepsilon \cdot X_{eq}} \ln\left[1 - X_B + X_B e^{-\varepsilon/RT_m(X_{B,C} = X_{eq})}\right] \tag{2.5.11}$$

The relation between $T_m^\circ(X_{B,C} = X_B)$ *and $T_m^\circ(X_{B,C} = X_{eq})$ is given by[22]

$$\frac{1}{T_m^\circ(X_{B,C} = X_B)} - \frac{1}{T_m^\circ(X_{B,C} = X_{eq})} = \frac{\varepsilon \cdot X_B}{(\Delta H(X_B) + \varepsilon X_B) \cdot T_m^\circ(X_B)} + \frac{R \ln(1 - X_B + X_B e^{-\varepsilon/RT_m^\circ(X_{B,C} = X_{eq})}}{\Delta H(X_B) + \frac{\varepsilon \cdot X_B e^{-\varepsilon/RT_m^\circ(X_{B,C} = X_{eq})}}{1 - X_B + X_B e^{-\varepsilon/RT_m^\circ(X_{B,C} = X_{eq})}}} \tag{2.5.12}$$

Equation. (2.5.12) seems to be cumbersome but we can calculate the excess free energy due to the defect incorporation in the crystal if we know the respective equilibrium melting temperatures of the copolymer crystallized at low and high

crystallization temperature region since we already know the composition X_B of B-counit in copolymer and the observed enthalpy of fusion $\Delta H(X_B)$.

2.5.2. Equilibrium Melting Temperature from Hoffman-Weeks Plot

So far we have mentioned the Flory's equilibrium melting point depression equation of the copolymer in the case of complete exclusion of B-counits from crystalline phase, the Sanchez-Eby's equilibrium melting point depression for the case of uniform inclusion of B-counits into the crystalline phase, and the equilibrium melting temperature determination for the perfect inclusion of all B-counits into the crystalline phase from the plot of T_m vs. T_c. As will be shown in the preliminary results of the Hoffman-Weeks plot in later **section 4.3.1**, one cannot find, however, the T_m° in the low supercooling region of crystallization that is sufficiently close to equilibrium. Therefore, it is necessary to understand the background of the Hoffman-Weeks plot. The well-known Thompson-Gibbs equation can be derived from the thermodynamics of the single chain folded thin lamella consisted of the thickness, l, and the lateral dimension, x.

$$\Delta\phi_{crystal} = -x^2 l\Delta G_f + 4xl\sigma + 2x^2\sigma_e \qquad (2.5.13)$$

where $\Delta\phi_{crystal}$ is the free energy of formation of a crystal, ΔG_f is the bulk free energy of fusion, σ_e is the surface interfacial free energy of the lamellar basal plane, σ is the lateral surface interfacial energy. Using the conditions that lateral dimension of crystal is much bigger than its thickness, $x >> l$, the fold surface energy contribution normal to chain direction is much larger than the lateral surface free energy, $\sigma_e >> \sigma$, and that $\Delta\phi_{crystal} = 0$ at the melting point, ΔG_f from **equation(2.5.13)** is equal to $2\sigma_e/l(= \Delta H_f(T_m^\circ - T)/T_m^\circ)$.

Thus, the relationship between the lamellar thickness and the melting temperature can be expressed in a well-known Thompson-Gibbs equation form.

$$T_m = T_m^\circ(1 - \frac{2\sigma_e}{\Delta H_f l}) \qquad (2.5.14)$$

where T_m is the melting temperature with a certain lamellar thickness l, ΔH_f is the heat of fusion. **Equation (2.5.14)** requires the condition of no recrystallization, reorganization, or superheating.(ref.10) The lamellar thickness l in **equation (2.5.14)** is the essential key point for understanding the Hoffman-Weeks plot.

If the lamellar thickness l is equal to the initial lamellar thickness l_g^* (**equation (2.5.15)**) of a chain folded lamella, although this assumption is not quite realistic,

$$l_g^* = \frac{2\sigma_e}{\Delta G_f} + \delta l = \frac{2\sigma_e T_m^\circ}{\Delta H_f \Delta T} + \delta l \qquad (2.5.15)$$

Equation (2.5.14) becomes

$$T_m = T_c + \Delta T\left\{1 - \frac{1}{\delta l(\Delta H_f)(\Delta T)/2\sigma_e T_m^\circ}\right\} \qquad (2.5.16)^{23}$$

where the ΔT is the supercooling and δl is a quantity related to very small thickening and only a weak function of supercooling. δl is $kT/b\sigma$ for the case of $\Delta G_f = 0$ and can be considered as constant.[13] **Equation (2.5.16)** means that the melting temperature is the same as the crystallization temperature for the case of $\delta l = 0$. Thus, it is required that δl must be larger than zero for the crystal to grow. The melting point with negligible isothermal thickening is slightly above the crystallization temperature. Also **equation**

(2.5.17) shows the non-linear relationship between the melting temperature and the crystallization temperature.

If l is the lamellar thickness of the finally thickened crystal and it reaches a lamellar thickness γ times larger than the initial lamellar thickness l_g^* as shown in the relationship

$$l = \gamma \cdot l_g^* \tag{2.5.17}$$

by inserting **equation (2.5.15)** and **equation (2.5.17)** into **equation (2.5.14)** we can have a more general formula

$$T_m = T_m^\circ - \frac{\Delta T}{\gamma}\left\{\frac{1}{1+\delta l(\Delta H_f)(\Delta T)/2\sigma_e T_m^\circ}\right\} \tag{2.5.18}$$

where for $\gamma = 1$ (i.e. $l = l_g^*$) **equation (2.5.18)** reduces to **equation (2.5.16)**. Under the condition of the $l(=2\sigma_e/\Delta G) >> \delta l$ at low supercooling, $\delta l(\Delta H_f)(\Delta T)/2\sigma_e T_m^\circ$ approaches zero, and **equation (2.5.18)** reduces to the well-known equation for the Hoffman-Weeks plot as follows:

$$T_m = T_m^\circ(1-1/\gamma) + T_c/\gamma \tag{2.5.19}$$

From the slope of the linear relationship in the plot of the observed melting temperature against the crystallization temperature of **equation (2.5.19)** the thickening parameter γ can be obtained. The T_m° can be obtained at the intersection of $T_m = T_c$. However, as shown in the **Figure 4.3.1.1** and **4.3.1.2**, the experimental result does not follow the linear

relationship but shows the curvature between the low and the high crystallization temperature. In order to estimate the defect free energy ε in the earlier section, this curvature was assumed to be caused by the inclusion of B-counits into the lattice at low T_c and the exclusion of B-counits from the crystalline phase at high T_c.

2.5.3. Effects of Chain Length (Molecular Weight)

Flory and Vrij suggested an equation to predict the equilibrium melting temperature of linear polyethylene with infinitely large chain length from the melting temperatures of the *n*-alkane molecular crystals of uniform length, considering the entropy contribution, $R\ln(cn)$ to the molar free energy of fusion.[18, 24] The molar free energy of fusion, $n\Delta G_n$ of a chain with n repeating unit at a temperature T is given by

$$n\Delta G_n = n\Delta G(T) + \Delta G_e(T) - RT\ln n \qquad (2.5.20)$$

where $\Delta G(T)$ is the free energy of fusion per repeating unit at the temperature T, $\Delta G_e(T)$ independent of n is an excess free energy change due to the destruction of the pairing terminal unit during the melting process. These two terms are the temperature dependence function and can be expanded in a Taylor series about the equilibrium melting temperature T_m° for $n \to \infty$

$$\Delta G(T) = \Delta G(T_m^\circ) + \left.\frac{\partial G(T)}{\partial T}\right|_{T=T_m^\circ} (T - T_m^\circ) + \left.\frac{\partial^2 G(T)}{\partial T^2}\right|_{T=T_m^\circ} \frac{(T - T_m^\circ)^2}{2!} + \left.\frac{\partial^3 G(T)}{\partial T^3}\right|_{T=T_m^\circ} \frac{(T - T_m^\circ)^3}{3!} + \cdots \qquad (2.5.21)$$

where $\Delta S = \Delta H_u / T_m^\circ$ at $\Delta G(T_m^\circ) = 0$ and **equation (2.5.21)** becomes

$$\Delta G(T) = (T_m^\circ - T)\frac{\Delta H_u}{T_m^\circ} - \frac{(T_m^\circ - T)^2}{2}\cdot\frac{C_p}{T_m^\circ} - \frac{(T_m^\circ - T)^3}{6}\frac{1}{T_m^{\circ 2}}(\Delta C_p - \Delta C_p' T_m^\circ) - \cdots \quad (2.5.22)$$

Similarly, the second term of **equation (2.5.20)** can be expanded using the $\Delta G_e(T_m^\circ) = \Delta H_e - T_m^\circ \Delta S_e$

$$\Delta G_e = \Delta H_e - T_m^\circ \Delta S_e - (T_m^\circ - T)\frac{C_{p,e}}{2}\frac{1}{T_m^\circ} - \cdots \quad (2.5.23)$$

After substituting **equation (2.5.20)** with **equation**. **(2.5.22)** and **(2.5.23)**, Flory and Vrij derived **equation (2.5.24)** using the condition of $\Delta G_n = 0$ at the melting temperature (i.e. $T = T_m = T_m(n)$ of a *n*-alkane,

$$n\left\{\Delta H(T_m^\circ - T_m) - \frac{\Delta C_p}{2}(T_m^\circ - T_m)^2 - \cdots\right\} - RT_m T_m^\circ \ln(n) = T_m T_m^\circ \Delta S_e - \Delta H_e + \frac{\Delta C_{p,e}}{2T_m^\circ}(T_m^\circ - T_m)^2 + \cdots \quad (2.5.24)$$

and obtained the T_m° of the linear polyethylene by analyzing the plot of left-hand-side of **equation (2.5.24)** against $T_m^\circ - T_m$.

2.6. Small Angle X-ray Scattering (SAXS)

In small angle X-ray scattering, we will consider the scattered beam as elastic scattering since the Compton effect is small enough to be neglected. Small angle X-ray scattering can be used to obtain the following information for polymeric materials:

i) Morphological parameters:

- determination of phase

  crystalline, interfacial (transition layer), amorphous phase
- periodicity of phases

  shape of particle

  rod, disk, lamellar, cylinder, spherical, ellipsoidal, hollow geometry etc.
- dimension of each phase

  lamellar (crystallite layer), amorphous layer, transition
- layer(interfacial layer) thickness
- size of particles (geometrical parameters)

  radius of gyration for spherical particle

  thickness factor for plate-like particle

  cross-section factor for rod-like particles
- electron density difference between two phases
- inner surface (surface/volume)

ii) Molecular weight (molar mass) of particle

iii) Degree of coiling

iv) Void, craze, interfacial area, and surface topography of reflective surface

(v) fractal geometry

Those parameters can be obtained from the relative intensity and absolutely intensity, depending on the properties of the parameters. The geometric parameters such as length, area, and volume of a system can be obtained from the relative intensity as well as absolute intensity. The parameters related to mass such as the molecular weight and the electron density fluctuation require the measurement of the absolute intensity.[25, 26]

To measure the absolute intensity needs much time. The simultaneous measurement of the intensity of the primary beam with scattered intensity is difficult because the primary energy exceeds that of the scattered X-ray by several orders of magnitude. Three methods have been suggested to measure the absolute intensity: attenuation of primary beam using (i) Nickel filter or (ii) a perforated Rotor, (iii) correction of that of the unknowns with the absolute intensity of the standard samples such as PES3-STD or Vitreous Carbon. In this research, method (iii) was used.

2.6.1. Fundamental Theory of Small Angle X-ray Scattering.

X-rays have dual natures of electromagnetic wave and particle behavior. When X-rays pass through matter, they interact with electrons, depending on these two natures. On the basis of wave-like properties of X-rays, if scattered waves have no change of wavelength (i.e., no energy loss) this scattering is called Thomson scattering (or elastic, coherent scattering). On the other hand, the particle properties of X-rays will cause the transfer of momentum when X-ray particles collide with electrons. This is called Compton scattering (incoherent scattering). The fundamental theory of X-rays will be reviewed under the following assumptions: (i) The wavelengths of the incident and scattered beams are constant (Thomson scattering). (ii) Only primary scattering will be considered and secondary scattering will be neglected. In other words, scattered beams interfere with other scattered X-rays, but they do not interact with other atoms, although X-rays from a given atom spread out over all space and certainly have a enough chance to collide with other atoms in the vicinity. (iii) All the scattered X-rays arriving at a given observation point (detector) are parallel, just as the incident beams are taken to be parallel (Fraunhofer approximation) if the detector position is far enough and the distance

between point O and P is short enough (**Figure 2.6.1**). (iv) In small angle range, the polarization effect can be neglected due to the small 2θ values.

Scattering from One Electron

To understand X-ray diffraction, let's start with a single electron. In the case of the elastic scattering from a single electron, Thomson intensity is given

$$I_e = I_o(\frac{e^2}{m_e c^2 R})^2(\frac{1+\cos^2 2\theta}{2}) \qquad (2.6.1)$$

where I_e is the incident beam intensity, e is the charge of electron ($1.602177\times10^{-19}C$), m_e the electron mass ($9.10939\times10^{-31}Kg$), R is the distance from the sample to the detector (or observation), c the velocity of light ($2.99792458\times10^{8}m/\text{sec}$), 2θ the scattering angle. With proper conversion unit, Thomson's number $(e^2/mc^2)^2 = 7.940\times10^{-26}cm^2$.[27] Therfore, Thomson intensity becomes

$$I_e = I_o(7.94030\times10^{-26}cm^2)\frac{1}{R^2}(\frac{1+\cos^2 2\theta}{2}) \qquad (2.6.2)$$

where, $(1+\cos^2 2\theta/2)$ is the polarization factor. As assumed earlier, in small 2θ range, $\cos 2\theta \cong 1$. The polarization factor is approximately equal to unity, and the correction of the polarization effect can be ignored.

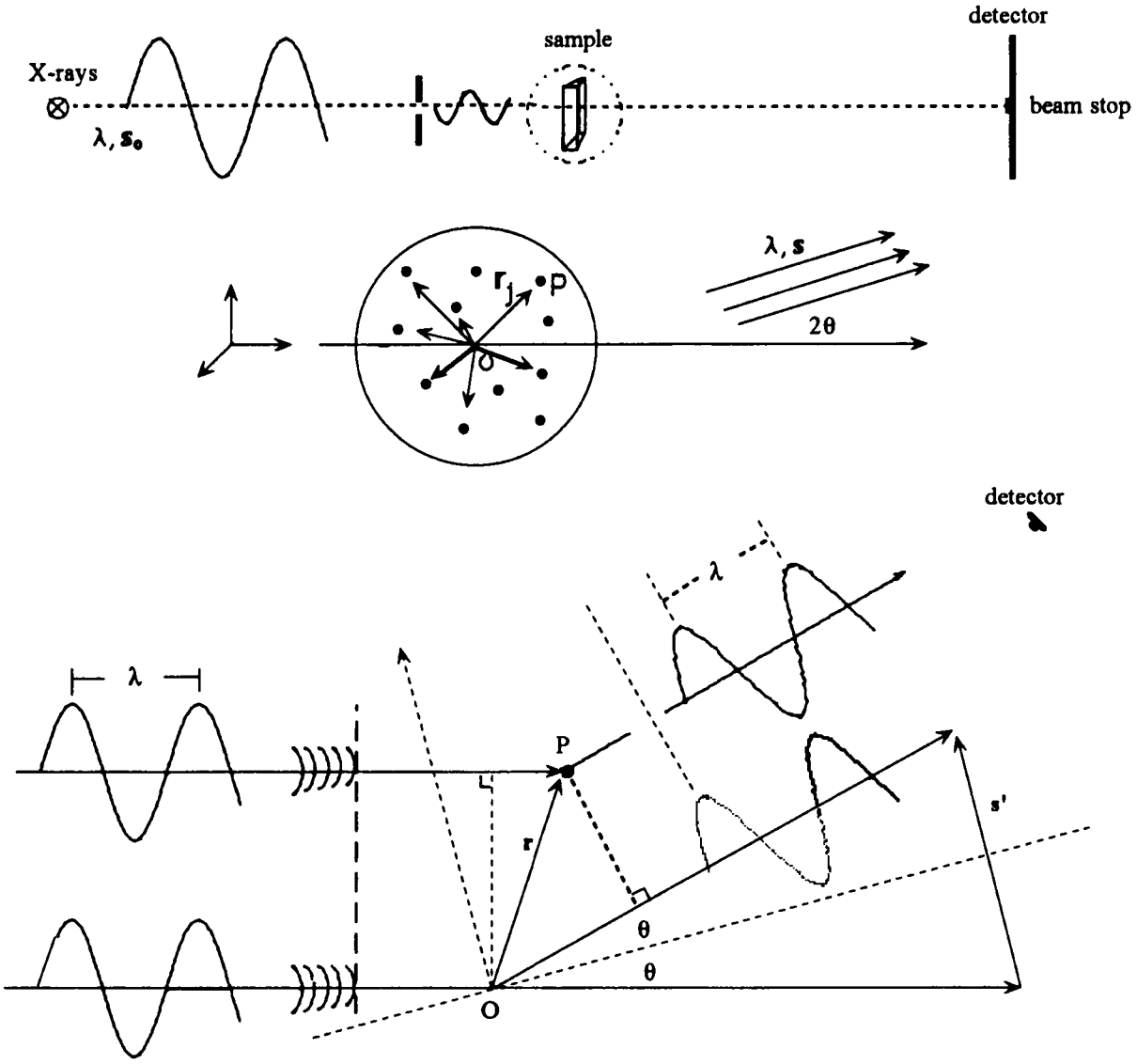


Figure 2.6.1. General Small Angle X-ray Scattering Phenemena.

Scattering from more than One Electron

The general X-ray scattering theory for more than one electron can be understood with the interference among the scattered waves of the individual electrons. Here, let's imagine an incident beam of wavelength and unit vector $\mathbf{s}_o$. For coherent scattering, $\mathbf{r}_j$ represents the vector distances from origin to the j-th scatters (**Figure 2.6.1**). The path difference of the scattering between an origin O and an arbitrary point P is given $-\mathbf{r}\cdot(\mathbf{s}-\mathbf{s}_o)$. Thus the phase is

$$\varphi = -(\frac{2\pi}{\lambda})\cdot\mathbf{r}(\mathbf{s}-\mathbf{s}_o) \tag{2.6.3}$$

The magnitude of the scattering vector s'

$$|\mathbf{s}'| = \frac{|\mathbf{s}-\mathbf{s}_o|}{\lambda} = 2\frac{\sin 2\theta}{\lambda} \tag{2.6.4}$$

For convenience, the different form of scattering vector can be defined in

$$\mathbf{q} = 2\pi\mathbf{s}' \tag{2.6.5}$$

In this case, the phase lag is $\varphi = -\mathbf{q}\cdot\mathbf{r}$ and the absolute magnitude of **q** becomes[28]

$$q = |\mathbf{q}|\frac{4\pi\sin 2\theta}{\lambda} \tag{2.6.6}$$

The amplitude is given in the Fourier transform of the electron density over the irradiated volume of X-rays

$$F(\mathbf{q}) = \int_{v} \rho(\mathbf{r}) \exp(i\mathbf{q} \cdot \mathbf{r}) dv_{\mathbf{r}} \tag{2.6.7}$$

For a system where a center of symmetry exists in the electron distribution, the intensity is a result of the interference for various scattered X-rays of the individual electrons in the materials. The intensity in this case is given by the product of the structure factor $F(\mathbf{q})$, which is the ratio of the total scattering amplitude to the amplitude of radiation scattering by one electron, and its complex conjugate $F^*(\mathbf{q})$:[29]

$$\begin{aligned} I(\mathbf{q}) = I_e(\mathbf{q})\left|F \cdot F^*\right| &= I_e(q) \int_{v} \rho(\mathbf{r}) e^{i\mathbf{q}\cdot\mathbf{r}} dv_{\mathbf{r}} \int_{v} \rho(\mathbf{r}') e^{i\mathbf{q}\cdot\mathbf{r}'} dv_{\mathbf{r}'} \\ &= I_e(q) \iint_{v} \rho(\mathbf{r}) \rho(\mathbf{r}') e^{i\mathbf{q}\cdot(\mathbf{r}-\mathbf{r}')} dv_{\mathbf{r}} dv_{\mathbf{r}'} \end{aligned} \tag{2.6.8}$$

Equation (2.6.8) shows that the scattering intensity is a function of the square of the electron density $\rho(\mathbf{r})$ and the scattering vector $\mathbf{q}$. Since the scattering vector has the reciprocal dimension $[\mathrm{L}]^{-1}$ of wavelength, in fact, the measured intensity shows the real morphology of a material in reciprocal space. Thus, in order to get any morphological information from the measured intensity, as mentioned earlier, it is required to switch from the reciprocal domain to the physical (real) space, using the Fourier transform, or to compare theoretical intensity based on a model to measured intensity profile.

One of the fundamental parameters in morphology study of a crystalline polymer is crystallite thickness. The following section will show the theoretical background to get crystalline phase thickness.

2.6.2. Theoretical Background to Obtain the Thickness of Long Range Order

Here the long range order reflecs to the crystalline phase in a material. The morphological shapes of this crystalline phase may be rod, disk, lamella, cylinder, crystal bundle, and hard segment domain in block copolymers. The thickness of those crystalline phases can be obtained from the SAXS.

There are two approaches to determine the lamellar thickness of semi-crystalline polymer using the SAXS. The one is the reciprocal space approach by Bragg's law assumption, and the other is the real space in which reciprocal domain is changed by the Fourier transform.

2.6.2.1. Bragg's Law

The reciprocal space method has been the most commonly used to get thickness of crystalline phase. By assuming the Bragg's law for a two-phase system, the average one-dimensional period (so-called long period, L) can be obtained. The term one-dimensional means that the electron density within a system varies with only one-direction which implies the length (for the system with lamellar structure, the electron density varies with only the normal direction to the lamellar plane). When collimated X-rays encounter a crystal, they are diffracted by the electrons of atoms arranged "periodically." These diffracted X-rays produce the sharp spot on a photographic film or maximum intensity at SAXS curve. Therefore, in order to apply Bragg's law to the semi-crystalline polymer, the polymer should consist of parallel lamellae and have a sharp phase boundary between the amorphous and the crystalline phases. The Bragg's law relation can be expressed as follows:

$$n\lambda = 2d \cdot \sin 2\theta \tag{2.6.9}$$

where, d is the distance between the crystalline planes (for semi-crystalline polymer d is Long period) and, 2θ, is the scattering angle, λ is the wavelength of X-ray. From **equatio (2.6.6)** and **(2.6.9)**, $d = L$ (long periodicity) for $n = 1$ (first-order) is given as follows:

$$L = \frac{2\pi}{q_{max}} \tag{2.6.10}$$

where q_{max} corresponds to the maximum in the intensity profile. If the value of q_{max} is obtained from the $I(q)$ versus q plot, it would yield the long periodicity in real space. The semicrystalline polymer, however, cannot satisfy Bragg's law that assumes the regular repeat of planes in only one direction. The repeating plane would not align parallel and has a different reflection condition. In this case the Lorentz correction can be applied, which requires the intensity corrected by the multiplication factor q^2.[30,31] The long periodicity can be obtained from the maximum in the plot of $I(q) \cdot q^2$ against q.

The lamellar thickness (l) can be obtained from the long period multiplied by volume crystallinity.

$$l = L \cdot \phi_v \tag{2.6.11}$$

where ϕ_v is the volume fraction of crystalline portion in the system, which is determined from the DSC, density measurement, or using the WAXS and density measurement.

2.6.2.2. Correlation Function

The method for obtaining crystallite thickness from real space is based on the correlation function, originally developed by Debye and Bueche for the case of inhomogeneous solid materials with voids.[32,33] When we introduce the concept of electron density variation into **equation (2.6.8)**, the scattered intensity becomes [29]

$$I(q) = I_e(q)\iint_v [\overline{\rho} + \eta(\mathbf{r})][\overline{\rho} + \eta(\mathbf{r}')]e^{-i\mathbf{q}\cdot(\mathbf{r}-\mathbf{r}')}dv_r dv_{r'} \qquad (2.6.12)$$

where $\overline{\rho}$ is the average density of the substance, $\eta(\mathbf{r})$ is electron density difference between the mean electron density ($\overline{\rho}$) and that $\rho(\mathbf{r})$ at a point **r**. It is defined as

$$\eta(\mathbf{r}) = \rho(\mathbf{r}) - \overline{\rho} \qquad (2.6.13)$$

The integration result is given by Guinier *et.al*,[29]

$$I(\mathbf{q}) = I_e(\mathbf{q})\overline{\eta^2}V\int_v \gamma_3(\mathbf{r})e^{i\mathbf{q}\cdot\mathbf{r}}dv_r \qquad (2.6.14)$$

where $\overline{\eta^2}$, so called mean square electron density fluctuation, is the average value of η^2, and $\gamma_3(\mathbf{r})$ is the three dimensional (or spatial) correlation function given by

$$< \eta_1\eta_2 >_{avg} = \gamma_3(\mathbf{r})\overline{\eta^2} \qquad (2.6.15)$$

where the local deviations of the electron density of each point 1 and 2 from the average density are given in $\eta_1 = \rho_1 - \overline{\rho}$ and $\eta_2 = \rho_2 - \overline{\rho}$.

The reason that is named in three dimensions is because the electron density is considered in the volume domain. In other words, this function connects the mean electron density fluctuation between two points as a function of **r**. To understand this function, let's consider the following two extreme conditions.

$$\begin{cases} \lim_{r\to\infty} \gamma_3(\mathbf{r}) \to 0 \quad : \quad \gamma_3(\mathbf{r}) \to < \eta_1 \eta_2 >_{avg} = 0 \\ \lim_{r\to 0} \gamma_3(\mathbf{r}) \to 1 \quad : \quad \gamma_3(0) \to < \eta_1 \eta_2 >_{avg} = \overline{\eta^2} \end{cases} \tag{2.6.16}$$

In the first case there is no relation between the fluctuations of point 1 and 2 for large **r**. In this case $\gamma_3(\mathbf{r})$ goes to zero as the distance **r** increases to the infinite region. Thus the average product of each electron density fluctuation will be zero, since η_1 and η_2 will vary quite independently. Second is the case of small **r**, in which two points overlap, or the distance of two points is so close that the electron density fluctuation between the two points cannot be distinguished. Thus $\gamma_3(\mathbf{r})$ goes to unity as the distance **r** decreases to the infinitesimal region.

Here $\gamma_3(\mathbf{r})$ depends only on the distance r and not on the direction in this vector space, the integration of **equation (2.6.14)** over all directions in space can be expressed as follows:

$$I(q) = 4\pi I_e(q)\overline{\eta^2}V \int_{r=0}^{\infty}\int_{\phi=0}^{\pi}\int_{\theta=0}^{2\pi} \gamma_3(r) e^{-iqr\cos\phi} r^2 \sin\phi \, d\theta \, d\phi \, dr \tag{2.6.17}$$

The result of **equation (2.6.17)** becomes

$$I(q) = 4\pi I_e(q)\overline{\eta^2}V \int_0^{\infty} r^2 \gamma_3(r) \frac{\sin qr}{qr} dr \tag{2.6.18}$$

Taking the inverse Fourier transform of **equation (2.6.18)**, we can get the spatial correlation function:

$$\gamma_3(r) = \frac{1}{2\pi^2 \overline{\eta^2}} \int_0^{\infty} I_{abs}(q) \cdot q^2 \frac{\sin qr}{qr} dq \qquad (2.6.19)$$

An important physical quantity can be derived using the relation $\gamma_3(0) = 1$. For $r = 0$, the term $\frac{\sin qr}{qr}$ in **equation (2.6.19)** goes to unity and equation becomes

$$\gamma_3(0) = \frac{1}{2\pi^2 I_e(q) \overline{\eta^2} V} \int_0^{\infty} I(q) \cdot q^2 dq = 1 \qquad (2.6.20)$$

Equation (2.6.20) shows that the integration of the Lorentz corrected intensity over reciprocal space is directly related to the mean square fluctuation of electron density , irrespective of the special features of the structure. In other words, the integration in **equation (2.6.20)** remains invariant, and represents the scattering power of the system. Thus the equation is the so called invariant Q ($= \overline{\eta^2}$).

$$Q = \overline{\eta^2} = \frac{1}{2\pi^2 I_e(q) V} \int_0^{\infty} I(q) \cdot q^2 dq \qquad (2.6.21)$$

If the intensity is measured absolutely, $I_{abs}(q)$, that is the ratio of scattered intensity to the intensity of primary beam (or that of the intensity of single electron) per unit volume

$$I_{abs}(q) = \frac{I(q)}{I_e(q) V} \qquad (2.6.22)$$

the 3-dimensional correlation function and invariant can be simplified

$$\gamma_3(r) = \frac{1}{2\pi^2 \overline{\eta^2}} \int_0^{\infty} I_{abs}(q) \cdot q^2 \frac{\sin qr}{qr} dq \tag{2.6.23}$$

$$Q = \gamma_3(0) = \frac{1}{2\pi^2} \int_0^{\infty} I_{abs}(q) \cdot q^2 dq = \overline{\eta^2} \tag{2.6.24}$$

With the combination of **equation (2.6.19)** and **(2.6.21)** (or **equation (2.6.23)** and **(2.6.21)**), the final spatial correlation function can be expressed by

$$\gamma_3(r) = \frac{\int_0^{\infty} I(q) \cdot q^2 \frac{\sin qr}{qr} dq}{\int_0^{\infty} I(q) \cdot q^2 dq} \tag{2.6.25}$$

where this spatial correlation function is not sensitive to the intensity type when it is normalized with the invariant. As mentioned earlier, the three dimensional correlation function has been derived on the assumption of spherical symmetry and that there is no concept of direction, since the electron density between two points depends only on the distance from the center of a given region or phase. On the other hand, if the system has electron density change in only one direction, we can project the scattering vector **q** on a line in reciprocal space parallel to the distribution. Vonk and Kortleve developed the method to measure the crystalline thickness in real space by the Fourier transform of the scattering intensity, which is called one-dimensional correlation function.[34]

The application of 3-dimensional correlation function that is derived for the case of the spherical symmetry of electron density deals the electron density of all the

directions from the center of a given origin or phase. To obtain the one-dimensional correlation function from the 3-dimensional scattering intensity due to all orientation of lamellar stacks, the observed intensity was corrected by multiplying the *I(q)* with q^2. The $\gamma_1(x)$ can be obtained by the Fourier transform of the Lorentz corrected scattering curve

$$\gamma_1(x) = \frac{1}{2\pi^2} \cdot \int_{q=0}^{\infty} I_{abs}(q) \cdot q^2 \cos(qx) dq \qquad (2.6.27)$$

and the correlation function normalized by invariant is [34]

$$\gamma_1(r) = \frac{\int_{q=0}^{\infty} I_{abs}(q) \cdot q^2 \cos(qx) dq}{\int_{q=0}^{\infty} I_{abs}(q) \cdot q^2 dq} \qquad (2.6.28)$$

Equation (2.6.28) is the one-dimensional correlation function normalized by the invariant. The invariant, Q, is the total scattering power of the sample and is defined for pinhole-collimation in the case of an ideal two-phase system as follows:

$$Q = \frac{1}{2\pi^2} \int_{q=0}^{\infty} I_{abs}(q) \cdot q^2 dq = \phi_v(1-\phi_v) \cdot (\rho_c - \rho_a)^2 \qquad (2.6.29)$$

where, ϕ_v is vol ume fraction of crystalline phase and ρ_c and ρ_a are the corresponding electron densities.

There is a relation between one-dimensional and three-dimensional correlation functions

$$\left(\frac{d\gamma_1(x)}{dx}\right)_{x=0} = 2\left(\frac{d\gamma_3(r)}{dr}\right)_{r=0} \quad \text{and} \quad \frac{1}{3}\left(\frac{d^2\gamma_1(x)}{dx^2}\right)_{x=0} = \left(\frac{d^2\gamma_3(r)}{dr^2}\right)_{r=0} \qquad (2.6.30)$$

When we consider the inside of lamellae, the direction along the chain direction perpendicular to the surface plane is more important than other directions. Thus the one-dimensional correlation function approach is more reasonable than the three-dimensional correlation function to obtain crystallite thickness.

Since the one dimensional correlation function should be integrated from $q = 0$ to $q = \infty$ and the scattering data from the 5 m geometry were only measured at 0.040 $\leq q(nm^{-1}) \leq$ 1.060 region, it is necessary to have the data of near zero q and of $q = \infty$ region. The scattering vector of the near zero region was obtained from fitting the low scattering angle region with the second order power equation. The infinite q region was obtained from plot of the $\log I(q)$ versus $\log 1/q^4$. This extrapolation of the tail region contributed to the smoothness of the curve shape of the one-dimensional correlation function, and that of the low q region didnot show any particular effect on the shape of the one dimensional correlation function.

The number average lamellar thickness was obtained from the intersection of the slope in the self-correlation triangle and the baseline corrected with volume crystallinity.

2.6.2.3. Interface Distribution Function

A similar function to the one-dimensional correlation function was developed by Ruland.[35,36,37], and is called the interface distribution function , which describes the

distribution of the lengths of all chords that can be drawn between the interfaces in two a phase system. The interface distribution function $g_1(x)$ is the second derivative of **equation (2.6.28)**.

$$g_1(x) = -4\pi^2 \int_0^{\infty} I(q) \cdot q^4 \cos(qx) dq \Big/ Q \qquad (2.6.31)$$

The integration of **equation (2.6.31)** is a Fourier transform of $I(q) \cdot q^4$. The $\lim_{q \to \infty} I(q) \cdot q^4$ is a constant if this tail region obeys Porod's law and this term can be separated to a δ-function in the origin of $g_1(x)$, which may be ignored in the calculation of $g_1(x)$. Thus the remaining part becomes

$$g_1(x) = -4\pi^2 \int_0^{\infty} [\lim_{q \to \infty}(I(q) \cdot q^4) - I(q) \cdot q^4] \cos(qx) dq \Big/ Q \qquad (2.6.32)$$

An important procedure required for using this function is the determination of $\lim_{q \to \infty} I(q) \cdot q^4$. If there is good separations of multiple peaks, the distribution of amorphous and crystalline phase as well as the crystallinity can be directly obtained from the interface distribution function.

2.6.3. Distance Distribution Function

Distance distribution function, $p(r)$, represents the number of distances within the particle for homogeneous particles, i.e. the number of lines with length r which are found in the combination of any small volume element *i* with any other volume element *j*.[38] For inhomogeneous particles the electron density difference at the volume element

must be considered. In this case $p(r)$ function is proportional to the number of different electrons separated by the distance r which are found in the combination of any volume element *i* with any other volume element *k* of the same particle.

The $p(r)$ function can be defined as a product of the three-dimensional correlation function and the distance r between two element volumes.

$$p(r) = \gamma_3(r) \cdot r^2 \tag{2.6.33}$$

From **equation (2.6.19)** and **(2.6.33)**, the $p(r)$ can be given

$$p(r) = \frac{1}{2\pi^2 \overline{\eta}^2} \int_0^{\infty} I_{abs}(q) \cdot q \cdot r \sin(qr) dq \tag{2.6.34}$$

Information on the particle shape and its internal structure from the $p(r)$ function can be obtained.[38, 39] For homogeneous particles consisting of constant electron density difference, $p(r)$ function is summarized in **Table 2.6.1**.

The deviation from spherical shape can be expressed as the ratio, r_{max}/D. As the ratio decreases, changes of the geometry will appear from globular particles (three dimension) to flat particles (two dimension) and then rod-like particles (one dimension) in sequence.[38, 39]

For a planar particle, let's take a point in the center of the lamella and imagine the following conditions: (i) if $r << d$, $p(r)$ will increase with the second power of r if no boundary loss, since the number of distance is proportional to the surface of a sphere

Table 2.6.1. $p(r)$-functions of the particles consisted of simple geometry.

Shape	$p(r)$ function	Comments
sphere	$p(r) = 12x^2(2-3x+x^3)$	$r_{max} = D/2$ at $x \approx 0.525$ D : diameter of sphere
flat particle (e.g., disk, flat prism, lamellar)	$p(r) = \frac{16}{\pi} x\left(\arccos x - x\sqrt{1-x^2}\right)$	$x = r/D$ d : thickness of lamellar
rod-like particle (e.g. long cylinder, prism)	$p(r) = \frac{1}{2\pi}\rho_c^2 \cdot A^2(L-r)$	A : cross-section with maximum dimension d L : length of the whole particle $d << L,\ L = \sqrt{D^2-d^2} \approx D$

with radius r. However actually, even very small r, there is boundary loss, $p(r)$ will increase a quadratically. (ii) if $r > d$, $p(r)$ will increase roughly linearly, since the intersecting plane between lamella and sphere approximates a circular cylinder. (iii) if $r \geq D$, $p(r)$ will drop to zero since the point of center will be place outside of the lamella.

These transitions of geometry cannot be seen clearly some cases like $r = d$. If we introduce $f(r)$ function as defined in **equation (2.6.35)**, more clear shape of the plot can be obtained.

$$f(r) = \gamma_3(r) \cdot r = \frac{p(r)}{r} \tag{2.6.35}$$

This $f(r)$ function can be applied for lamellar particles. The curve increases linearly and at the point $r = d$ the curve becomes almost linear. It is possible to calculate the area of the basal plane of the lamellar from the extrapolation of the quasi linear part of $f(r)$ function toward $r = 0$.

$$A = f(r)\big|_{r \to 0} = \frac{\rho_c \cdot V \cdot d}{2} \tag{2.6.36}$$

For a rod-like particle satisfying $A << L$ of the whole particle, $p(r)$ will increase linearly as r decreases, starting from $r = L$. In principle, the cross-section area A can be obtained from the slope of the linear part of $p(r)$ if the electron density, ρ_c, of a particle is known

$$p(r) = \frac{1}{2\pi} \cdot \rho_c^2 \cdot A^2 \cdot (L - r) \tag{2.6.37}$$

and

$$slope = -\frac{dp(r)}{dr} = \frac{A^2 \cdot \rho_c^2}{2} \tag{2.6.38}$$

In order to use **equation (2.6.32) ~ (2.6.37)** as well as other Fourier transform functions the whole range of small angle scattering must be measured. Since the background range, however, is usually beyond the measurable small angle limit and intensities scatter, accurate intensity measurements are required. The termination effect on integrating will cause such strong artificial oscillation (so called "Fourier ripples") in one-, three-dimensional correlation function, interface distribution function, and distance distribution function, as to make the analysis by these functions unreliable. These termination effects can be severely reduced by applying appropriate extrapolation techniques in Porod's region and the Guinier region. This effect will be shown in this research.

2.6.4. Radius of Gyration by Guinier Approximation

Other structural parameters such as particle size can be obtained in terms of the root-mean-square radius of gyration from the intensity profile, based on the Guinier approximation that assumes a dilute system of monodisperse particles. The amplitude of scattering for a space is given by **equation (2.6.7)**

$$F(\mathbf{q}) = \int_v \rho(\mathbf{r}) \exp(i\mathbf{q} \cdot \mathbf{r}) dv_r \tag{2.6.7}$$

At the point **r** in (θ , ϕ ,r) space, the amplitude can be written in

$$F(\mathbf{q}) = 4\pi\eta \int_{r=0}^{r=R} \int_{\phi=0}^{\pi} \int_{\theta=0}^{2\pi} e^{i\mathbf{q}\cdot\mathbf{r}} \sin\phi d\theta d\phi dr \tag{2.6.39}$$

Taking integration over and , one can have

$$F(\mathbf{q}) = 4\pi\eta \int_{r=0}^{r=R} r^2 \frac{\sin qr}{qr} dr \tag{2.6.40}$$

If $qr << 1$

$$\frac{\sin qr}{qr} = 1 - \frac{(qr)^2}{3!} + \frac{(qr)^4}{5!} - \cdots \tag{2.6.41}$$

By considering first two terms of **equation (2.6.41)** and inserting it into **equation (2.6.40)**

$$F(\mathbf{q}) = F_e(q) 4\pi\eta \int_{r=0}^{r=R} r^2 (1 - \frac{(qr)^2}{3!}) dr \tag{2.6.42}$$

we can have

$$F(\mathbf{q}) = F_e(q) \frac{4}{3} \pi\eta R^3 (1 - \frac{1}{10} q^2 R^2) \tag{2.6.43}$$

Using the relation $e^x = 1 - x$ for small arguments

$$F(q) = F_e(q) \frac{4}{3} \pi\eta R^3 e^{-\frac{1}{10} q^2 R^2} \tag{2.6.44}$$

The relative intensity can be expressed

$$I(q) = I_e(q) V_{particle}^2 \eta^2 e^{-\frac{1}{5} q^2 \cdot R^2} \tag{2.6.45}$$

where $V_{particle}$ is the volume of the particle as $4\pi R^3/3$, and $I_e(q)$ is essentially independent of q and can be considered as a constant. If the intensity is absolute intensity $I_{abs}(q)$

$$I_{abs}(q) = V_{particle}^2 \eta^2 e^{-\frac{i}{5} q^2 \cdot R^2} \tag{2.6.46}$$

The natural logarithm of **equation (2.6.45)** or **(2.6.46)**

$$\log I_{abs}(q) (= I(q)) = \log(K) - \frac{1}{5} q^2 R^2 \tag{2.6.47}$$

allows us to get the radius of a particle. The radius of a particle can be obtained from the slope of the linear part in the plot of $\log I(q)$ versus q^2

$$R = \sqrt{5 \cdot slope} \tag{2.6.48}$$

In order to get radius of gyration, R_g, the shape of a particle should be considered. As shown in the **Table 2.6.2**, the radius of gyration depends on the shape of particle. For example, the radius of gyration of a sphere is $R_g = \sqrt{3/5} R$, **equation (2.6.45)** becomes the Guinier equation [40]

$$I(q) = I_e(q) V_{particle} \eta^2 e^{-\frac{1}{3} q^2 R_g^2} \tag{2.6.49}$$

and the natural logarithm of both side in **equation (2.6.49)** make it possible to estimate the R_g directly by the Guinier plot . If we know the shape of a particle, it is more convenient to get the R of a particle using the plot based on **equation (2.6.45)** and convert the R into the R_g For reference for the further work the relations among the radius of gyration, the intensity and the simple geometrical shapes of particles are summarized in **Table 2.6.2**.

Whereas the Guinier approach uses reciprocal space to evaluate the radius of gyration, the real space can be used to get the R_g. This is related to the distance distribution function. The starting point is to substitute **equation (2.6.18)** with **equation (2.6.41)**

$$I(q) = 4\pi I_e(q)\overline{\eta^2}\int_0^\infty r^2\gamma(r)[1-(qr)^2/3!]dr \tag{2.6.50}$$

$$= 4\pi I_e(q)\overline{\eta}V\int_0^\infty r^2\gamma_3(r)\left[1-\frac{q^2}{3!}\cdot\frac{\int_0^\infty r^4\gamma_3(r)dr}{\int_0^\infty r^2\gamma_3(r)dr}\right] \tag{2.6.51}$$

where at $q=0$, the intensity becomes from **equation (2.6.18)**

$$I(0) = 4\pi I_e(q)\overline{\eta^2}V\int_0^\infty r^2\gamma_3(r)dr \tag{2.6.52}$$

and

$$R_g^2 = \int_0^\infty r^4\gamma(r)dr \Big/ 2\int_0^\infty r^2\gamma(r)dr \tag{2.6.53}$$

Table 2.6.2. Radius of gyration, R_g, of the particles with some simple geometry.*)

Shape	R_g	Intensity $I(q)/V^2$
Sphere of radius R	$\sqrt{\frac{3}{5}}\cdot R$	$\Phi^2(qR) = \left[\frac{3(\sin qr - qr\cos qr)}{(qr)^3}\right]^2 = \frac{9\pi}{2}\left[\frac{J_{3/2}(qR)}{(qR)^{3/2}}\right]^2$
Spherical shell of exterior radius R and interior radius cR	$\sqrt{\frac{3}{5}}\cdot R\cdot\sqrt{\frac{1-c^5}{1-c^3}}$	$\frac{[R^3\Phi(qR)-(cR)^3\Phi(qcR)]^2}{[R^3-(cR)^3]^2}$
Ellipsoid of semi-axes, a, a, ka	$a\cdot\sqrt{\frac{2+k^2}{5}}$	$\int_0^1 \Phi^2\left[qa\sqrt{1+x^2(k^2-1)}\right]dx$
Cylinder of length 2H and diameter 2R	$\sqrt{\frac{R^2}{2}+\frac{H^2}{3}}$	$\int_0^{\pi/2}\frac{\sin^2(qH\cos\theta)}{q^2H^2\cos^2\theta}\cdot\frac{4J_1^2(qR\sin\theta)}{q^2R^2\sin^2\theta}\sin\theta d\theta$
Thin circular disk of radius R	$\frac{R}{\sqrt{2}}$	$\frac{1}{q^2R^2}\left[2-\frac{2J_1(2qR)}{qR}\right]$
Fiber of length 2H and extremely small radius $R\to 0$	$\frac{H}{\sqrt{3}}$	$\frac{Si(2qH)}{qH}-\frac{\sin^2(qH)}{q^2H^2}$, where $Si(x)=\int_0^x\frac{\sin x}{x}dt$
Parallelepiped of edges 2a, 2b, 2c	$\sqrt{\frac{a^2+b^2+c^2}{3}}$	
Cube of edge 2a	a	

*) International Table of X-ray Crystallography.
J. M. Schultz, Diffraction for Materials Scientist, Chapter 7, Prentice-Hall, New Jersey, 1982.
L.A. Feigin and D.I. Svergun, Structure Analysis by Small-Angle X-ray and Neutron Scattering, Chapter 3, Plenum Press, NY, (1987).

Thus **equation (2.6.51)** can be expressed as

$$I(q) = I(0)\left[1 - \frac{q^2 R_g^2}{3!}\right] \tag{2.6.54}$$

Since the approximations neglect the higher orders of qR, the application can be reliable in the range about $qR < 1.0$. Therefore to obtain the accurate R_g (around 1%), it is necessary to redefine R_g by trial-and-error procedure, after estimating this value roughly and then checking if the range satisfy $q < 1/R$.

The disadvantages of using the Guinier approximation to estimate R_g that determines the behavior of the scattering intensity near the $q = 0$ come from the facts that (i) the q_{min} depends on the geometrical set-up of the SAXS experimental condition, (ii) there are not enough points of the value of q_{min}, to satisfy statistical confidence, (iii) the points of the scattering intensity due to the primary beam around the beam stop can be detected and can affect to the slope behavior although we have to remove these points. Thus it is convenient to use **equation (2.6.52)** if the condition of $q_{min} < n/D$ is satisfied, although it has the difficulty of integrating from zero scattering vector to infinite scattering vector, whose range is hard to be obtained experimentally. Extrapolation techniques can be applied to get integration intervals, thus this extrapolation procedures can affect the value of R_g. If Guinier region shows non-linear behavior, it can be approximated by using a polynomial of second order.[41]

3. EXPERIMENTAL

3.1. Materials

The ethylene/1-octene random copolymers with branch content, molecular weight and polydispersity($\overline{M}_w/\overline{M}_n$) controlled by homogeneous catalyst of methallocene type and two linear polyethylenes were supplied by the Dow Chemical Co. The details of as-received samples are listed in **Table 3.1.1**. Here, the code H, L, number and O stand for the high molecular weight, low molecular weight, methyl groups per 1000 carbon (i.e. branch content) and octene comonomer, respectively.

The ethylene/1-propene and ethylene/1-butene copolymers were provided by Exxon chemical company. Specifications of these materials are in **Table 3.1.2**, where the code P and B represent 1-propene and 1-butene comonomer, respectively. Melting point data were measured at a heating rate 10 $^{\circ}C$/min using DSC under the conditions described in later thermal analysis **section 3.3**.

In this study, we used the CH_3/1000C to calculate the mole fraction of branching points, assuming a branch as a point defect.

Table 3.1.1. Characteristics of as-received linear polyethylenes (LPE) and ethylene/1-octene random (EO) copolymers.

Code [a]	$\overline{M}_w$ (g/mole)	$\overline{M}_n$ (g/mole)	$\overline{M}_w/\overline{M}_n$	Density (g/cm^3)	CH_3/1000C	T_m (°C)
H-LPE	101,300	53,900	1.88	0.9540	0.00 [b]	132.25
M-LPE	77,600	38,200	2.03	0.9510	0.00 [c]	131.43
H7-O	-	43,600	-	0.9180	6.84	113.19 [e]
H7'-O	98,400	44,800	2.2	0.9180	7.32	113.25
H10-O	-	48,800	-	0.9126	9.50	107.54 [e]
H16-O	-	45,200	-	0.9003	16.34	94.54 [e]
H17-O	102,700	48,700	2.11	0.9003	16.92	96.19
L4-O	59,900	27,300	2.19	0.9365	3.98	118.81
L10-O	-	23,700	-	0.9195	9.83	109.21 [e]
L13-O	51,800	25,000	2.07	0.9110	12.93 [d]	105.00
L18-O	-	24,900	-	0.9027	18.17	94.46 [e]
L24-O	46,900	21,800	2.15	0.8975	24.04	90.24
L39-O	48,000	22,800	2.11	0.8700	38.62	48.23 [e]

a) H, M, L ; high, medium, and low molecular weight
LPE ; linear polyethylene
Numbers ; branch content
O ; octene comonomer
b) Trans/1000C = 0.003, vinyls/1000C = 0.135, vinylidenes/1000C = 0.013
c) Trans/1000C = 0.027, vinyls/1000C = 0.128, vinylidenes/1000C = 0.023
d) Trans/1000C = 0.298, vinyls/1000C = 0.045
e) measured at DSC heating rate 10 °C/min in this work.

Table 3.1.2. Characteristics of as-received ethylene/1-propene (EP) and ethylene/1-butene random (EB) copolymers.

Code [a]	$\overline{M}_w$ (g/mole)	$\overline{M}_n$ (g/mole)	$\overline{M}_w/\overline{M}_n$	Density (g/cm^3)	CH_3/1000C	T_m (°C) [b]
L40-P	58,400	26,800	2.20	0.9046	40.10	92.04
L93-P	59,100	29,100	2.00	0.8849	92.60	49.45
L31-B	55,400	25,400	2.20	0.9048	31.00	94.46

a) L ; low molecular weight
Numbers ; branch content
P ; propene comonomer
B ; butene comonomer

b) measured at DSC heating rate 10 °C/min in this work

3.2. Sample Preparations and Dimensions

The films were prepared using a hydraulic press. The thickness of the samples was 0.15 - 0.3 mm for SAXS, and 0.1 mm for DSC experiments. The films were stacked together to make a total thickness about 1.0 mm for SAXS measurement.

3.3. Thermal Analysis

Thermal analysis was performed under a nitrogen atmosphere using a Perkin-Elmer Series 7 differential scanning calorimeter (DSC) attached with a cooling accessory. The calibration of the DSC with indium ($T_{onset} = 156.60^{\circ}C$, $\Delta H_f = 28.45 J/g$) was carried out several times until deviation from the known onset temperature (T_{onset}) of indium was within $\pm 0.05^{\circ}C$. After completing study, the T_{onset} of indium was re-measured and the deviation from the known T_{onset} of indium was always within $\pm 0.15^{\circ}C$. In all melting experiments, the DSC heating rate was $10^{\circ}C/min$. The peak temperature in the DSC thermogram was chosen as the melting temperature.

3.4. Bulk Crystallization and Melting by Polarized Light Transmission.

Bulk crystallization kinetics were studied by measuring the intensity of transmitted polarized light.[42, 43, 44] The equipment used in this study are a polarized optical microscope (OLYMPUS BH-2) consisting of light source, a light detector (photomultiplier tube) and radiometer (IL 700 Research Radiometer) for tracing the light

intensity, together with two hot stages (Mettler-82) for melting and crystallization. Isothermal crystallization was done in two steps under dry nitrogen gas. The first step was to melt samples at 160 $^{\circ}C$ in one hot stage and hold for 10 min to remove thermal history. The second step was to transfer the samples quickly into another hot stage, having a fixed crystallization temperature, mounted on the microscope. As polarized light passes through a sample crystallizing isothermally in the Mettler-82 hot stage, the intensity changed and was measured as a function of time on XY chart paper and then it was digitized for Avrami, half time, and induction time analysis.

After light intensity leveled-off, melting temperatures for Hoffman-Weeks plots were measured as the disappearance of birefringence under the microscope attached to a Mettler-82 hot stage with a heating rate of 10 $^{\circ}C/\min$ (uncorrected for instrument lag).

3.5. Isothermal Crystallization

The isothermal crystallizations were carried out in a silicone oil bath. In order to avoid contact of oil and sample, the sample was placed between the two cover glasses, placed in a thin copper jacket and then sealed in an aluminum bag coated with a thin plastic film, under nitrogen gas. The sealed samples were melted at 150°C for 10 minutes to remove the thermal history and then transferred to the oil bath, pre-set at the crystallization temperature. The isothermal crystallization studies were carried out as a function of crystallization temperature and time. In order to avoid thickening phenomena during small angle X-ray scattering(SAXS) at the crystallization temperature, all the materials were crystallized for at least 24 h. After crystallization, the samples were rapidly quenched in liquid nitrogen to room temperature. By this quenching process, it

was hoped to separate the isothermally crystallized fraction from the fraction that crystallized on quenching.

3.6. Small Angle X-ray Scattering (SAXS)

To study the morphological parameters of the polymers, the 10m Small Angle X-Ray Scattering Spectrometer (SAXS) of Oak Ridge National laboratory (ORNL) was used. A schematic diagram is shown in **Figure 3.6.1**.[45] The ORNL-SAXS allows the measurement of a true scattering pattern, which is free from the procedures of collimation (desmearing) correction.[46] The X-ray generator was a 12 kW Rigaku-Denki rotating anode and only $CuK\alpha$ radiation (=1.54 Å) was used at an accelerating voltage 40 kV and a current 100 mA. The monochromator was a pyrolytic graphite crystal. The detector was a 2-dimensional position-sensitive proportional counter with resistance wire mesh of a dimension 20 cm × 20 cm. The X-ray source-to-sample distance was 3.5 m and sample-to-detector distance (SDD) was 5.115 m that provides the highest resolution at room temperature (RT) and was 5.065 m for measurement at crystallization temperature (T_c). The reason for using different geometry between RT and T_c is that different sample holders (see **Figure 3.6.2**) for T_c experiments were used at fixed geometry, SDD = 5.115 m. Both geometries will be described as 5 m geometry for simplicity.

The wheel with twelve holes was used for room temperature experiments. Each sample disk or film was attached to the center of each hole. A stepping motor controlled the automatic revolution with a programmed time. On the other hand, high temperature experiments were performed manually. The samples were placed on a Kapton film in the sample cell, which was inserted into the cell holder at a chosen temperature. The sample

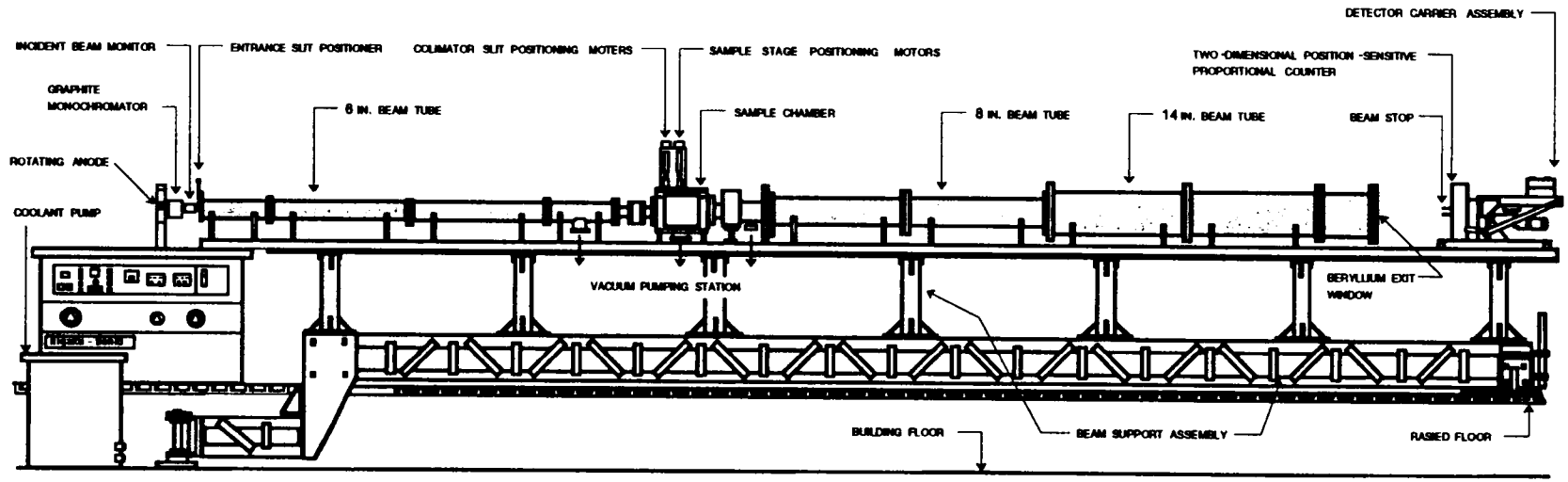


Figure 3.6.1. Schematic diagram of ORNL 10m small angle X-ray scattering spectrometer.

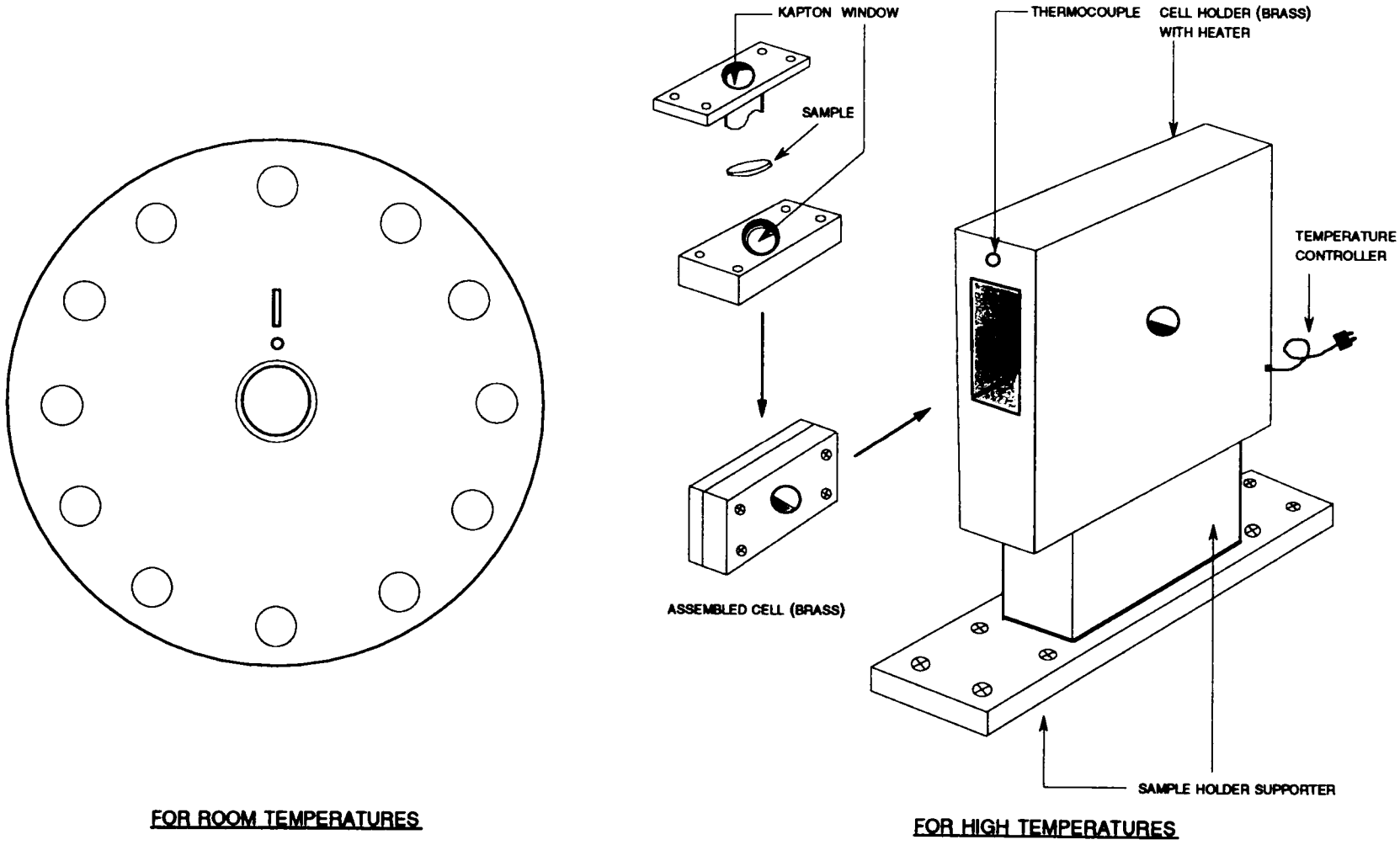


Figure 3.6.2. Accessories for mounting samples at the room and the in-situ (Tc) temperatures.

cell and cell holder were made of brass for fast thermal equilibrium. Intensity was measured for at least 40 ~ 60 min, depending on the total count rate of photons, after waiting about 5 or 10 min or so until the temperature of the sample cell reached the programmed temperature.

The scattering vector, q (nm^{-1}), at SDD = 5 m was about 0.040 ~ 1.060 nm^{-1}. Also, for the purpose of obtaining high scattering vector q, necessary to correct for the thermal density fluctuation of the sample itself, SDD=1.119 m whose q range is 0.9160 ~ 4.8620 nm^{-1} was used at both ambient and crystallization temperature.

The proper corrections (such as thickness of sample, detector sensitivity, dark current, background scattering, and absolute intensity factor) to obtain the net corrected absolute scattering intensity (cm^2/cm^3) were carried out for all scattering measurements. First, in order to correct the non-uniform detecting efficiency of the detector, a radioactive isotope, Fe-55, which emits γ-rays uniformly was placed in the sample position and monitored by detector without X-rays for more than 4 hours. This sensitivity run was used to correct the possible non-uniform performance of each detector element. Second, the dark current related to environmental radiation such as cosmic radiation and electronic noise was measured by detector for at least 30 minutes with X-rays was blocked from the radiation source. Third, background intensity was measured in the empty sample chamber for more than 30 minutes. Fourth, the absolute intensity factor (AIF) used for absolute units of scattering intensity was obtained as follows: in the case of 5 m geometry, the maximum intensity of secondary standard material, so called PES3-STD (thickness; 0.72 mm, transmission; 0.768) with a pre-calibrated absolute scattering cross-section, was obtained from the number average of only the symmetrical region around the peaks of the scattering pattern and **equations (3.6.1)** and **(3.6.2)**.

$$\left(\frac{d\Sigma}{d\Omega}\right)_{peak} = 24.5 \pm 1 \ (\mathrm{cm}^{-1}) \tag{3.6.1}$$

$$AIF = \frac{\sum_{i=1}^{n} I_i(q)}{24.5} \tag{3.6.2}$$

where, the $(d\Sigma/d\Omega)_{peak}$ is the scattering cross-section per unit volume obtained by calibration against the primary standard. In the case of 1 m geometry (SDD=1.119 m), a Vitreous-Carbon-STD (thickness: 1.29 mm ; transmission: 0.0422) was used as the secondary standard. The AIF was obtained from the ratio of the intercept of linear region ($0.2\ \mathring{A}^{-2} < q^2 \le 1.0\ \mathring{A}^{-2}$) in the Debye-Bueche plot ($1/\sqrt{I(q)}$ versus q^2) to the known $I_{q=0} = 32.1\ cm^{-1}$.

The transmission of each sample was calculated by **equation (3.6.3)**:

$$Transmission\ of\ sample\ (T_s) = \frac{(I_{GCS} - I_{DC}) - 0.686 \times (I_S - I_{DC})}{(I_{GC} - I_{DC}) - 0.686 \times (I_{MT} - I_{DC})} \tag{3.6.3}$$

where, I_{GCS}, I_{DC}, I_S, $I_{GC}$and I_{MT} are the intensity of glassy carbon and sample, dark current, sample alone, glassy carbon alone, and nothing in the beam, respectively. The 0.686 is the transmission of the glassy carbon used in the ORNL-SAXS system.

Finally the net corrected absolute scattering intensity that had been used for data analysis was calculated as shown in Equation (3.6.4):

$$I_{NCAI}(q) = \frac{1000.0}{C_{M,S}}\left[\left(I_S - \frac{t_S}{t_{DC}} \cdot I_{DC}\right) - \frac{T_S}{T_{MT}} \cdot \left(I_{MT} \cdot \frac{C_{M,S}}{C_{M,MT}} - \frac{t_S}{t_D} \cdot I_{DC}\right)\right] \cdot \frac{1.0}{T_S \cdot h \cdot f_{sensitivity}(i,j) \cdot f_{abs,I}} \tag{3.6.4}$$

where, $C_{M,S}$ and $C_{M,MT}$ are the monitor counts for the sample run and for the empty background run and t_S, t_{DC}, are the measuring time for the sample run and for the dark current run, respectively. h is the thickness of sample, $f_{sensitivity}(i,j)$ sensitivity factor, and $f_{abs.I}$ absolute intensity factor. The $f_{sensitivity}(i,j)$ means 64×64 data array which is related to detector resolution.

The total photon flux from the X-ray generator at ambient and Tc experiments were more than 1.0×10^6 and $5.0\times10^5 \sim 1.0\times10^6$ photons / $(\sec\cdot mm^2)$, respectively. The SAXS data were in the form of net corrected absolute intensity *I(q)* versus scattering vector $q(nm^{-1})$.

3.7. Wide Angle X-ray Scattering (WAXS)

Wide angle X-ray scattering studies were carried out using the Rigaku diffractometer at reflection mode which connected to the Digital pdp-11/34 computer and a XY-chart recorder. WAXS was calibrated using the silicon standard ($2\theta = 24.465°$). The unit cell parameters were calculated using the digitized data and the weight degree of crystallinity was obtained by the deconvolution method[47] using the planimeter. $CuK\alpha$ radiation (=1.54 Å) was used at 35 kV and 20 mA. The scan range of 2θ was $10°\sim 40°$, the step size was $0.05°$, and normally the run time was 45 min.

3.8. Density Gradient Column

The density was measured with a density gradient column (DGC) which contains mixtures of isopropanol and ethylene glycol. DGC was calibrated with standard beads and a linear gradient (correlation coefficient = 0.999) was obtained and the density range was $0.8800 \sim 0.9400 g/cm^3$.

Weight (w_c) and volume (v_c) average crystallinity were calculated from the following equation.

$$v_c = \frac{\rho - \rho_a}{\rho_c - \rho_a} \tag{3.8.1}$$

$$w_c = \frac{\rho_c}{\rho} \cdot v_c \tag{3.8.2}$$

where $\rho_c = 1.002$ and $\rho_a = 0.855$ (g/cm^3) are the density of the unit cell and that of the amorphous phase of polyethylene, respectively. ρ is the density measured of the sample obtained from the calibration plot of density versus height of standard beads.

4. RESULTS

4.1. Thermal Analysis

Thermal analysis deals with heat capacity, enthalpy, and temperature changes. The study of these parameters can guide us to obtain thermal and morphological information of the polymer. Crystallization, and first order (melting temperature) and second order transitions (glass transition temperature) of polymer are related to enthalpy change. A crystallization process causes the release of heat (exothermic), a first order transition the absorption of heat (endothermic), and a second order transition the discontinuity of heat capacity and volume.

In this chapter, crystallization and melting behavior of ethylene/1-octene (EO), ethylene/1-butene (EB), and ethylene/propene (EP) random copolymers are studied as a function of branch content, branch length and crystallization conditions.

4.1.1. Non-isothermal Crystallization

4.1.1.1. Cooling Rate Effects

Before studying isothermal crystallization of ethylene/1-octene random (EO) copolymers, it is necessary to find the crystallization temperature range; this was done using non-isothermal crystallization in the DSC. Usually, the isothermal crystallization

should be carried out above the non-isothermal crystallization temperature. **Figure 4.1.1.1 (a)** and **(b)** show exotherms of H7-O and H16-O, which are of similar molecular weight but different hexyl branching content, with different cooling rates. As cooling rate increases, the areas of the exotherms increase and the maximum peak temperatures shift to lower temperatures.

There are two different crystallization exotherms. The first is a large exotherm at high temperature(LEHT) and the other a small one at low temperature(SELT). LEHT is known to be due to the crystallization of polymer chains with high molecular weight and low branching content while SELT is caused by polymer chains with low molecular weight and high branching content.[48] This tells us that segregation of polymer molecules by molecular weight can occur. In other words, there is enough time for molecular fractionation, even during non-isothermal crystallization at a cooling rate of 40 $^{\circ}C$ / min. Molecular weight is not the only factor to cause different crystallization temperature. The low molecular weight chains tend to be more branched. According to D. Wilfong *et al.*[2] temperature rising elusion fractionation (TREF) shows the high molecular weight chains to have fewer branches. Therefore, segregation during crystallization is controlled by branching content as well as molecular weight.

When we consider that the EO copolymers were polymerized using metallocene catalysts (uniform site catalyst) of Dow Chemical Co., the branching distribution should be quite random without localization of branching along the main chain as well as narrow molecular weight distribution. However experimental results show there is still the possibility of branching heterogeneity or of low molecular weight molecules.

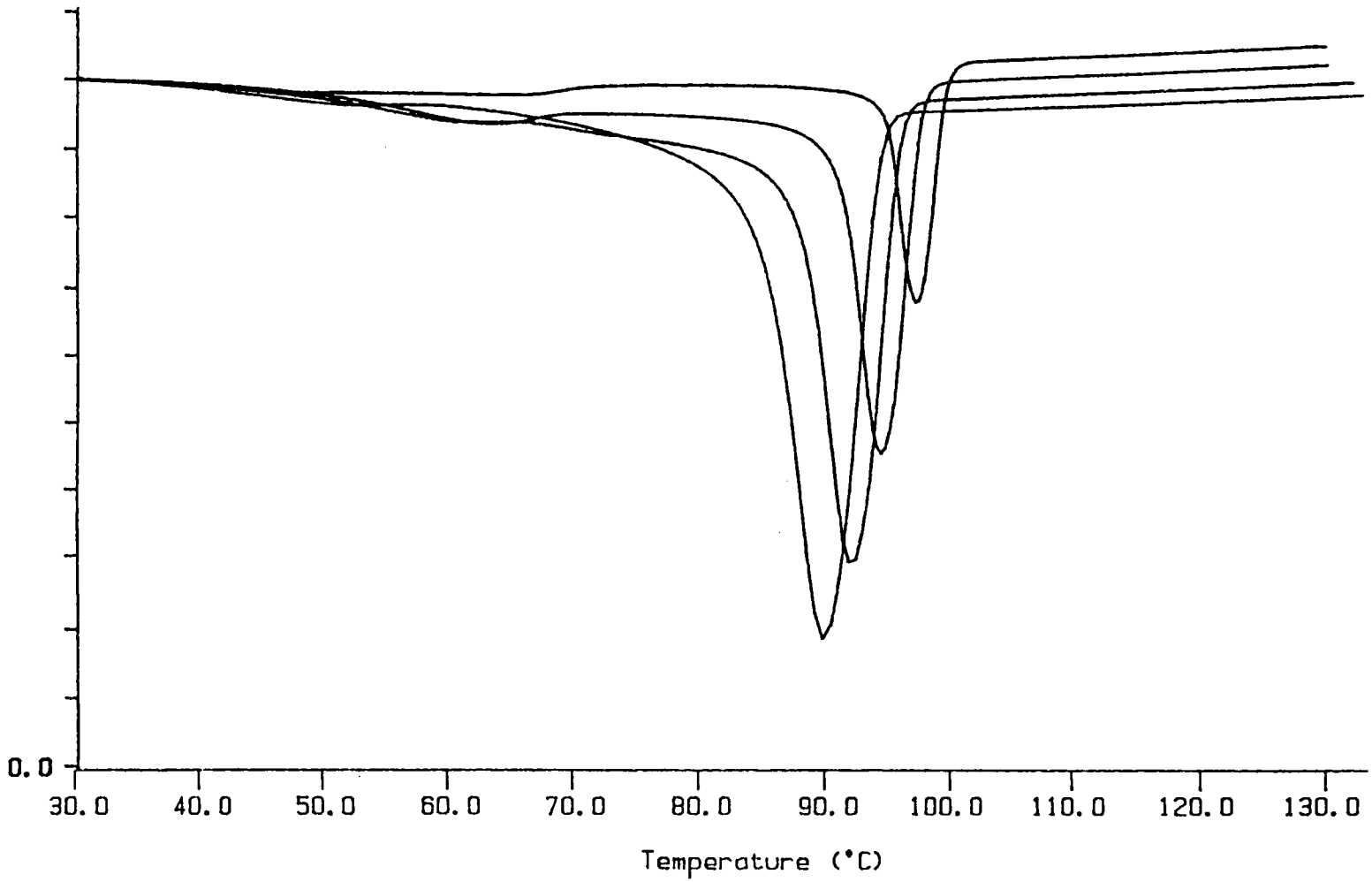


Figure 4.1.1.1. Non-isothermal crystallization thermograms (a) of H6-O at the different cooling rate, 10, 20, 30, 40 °C/min.

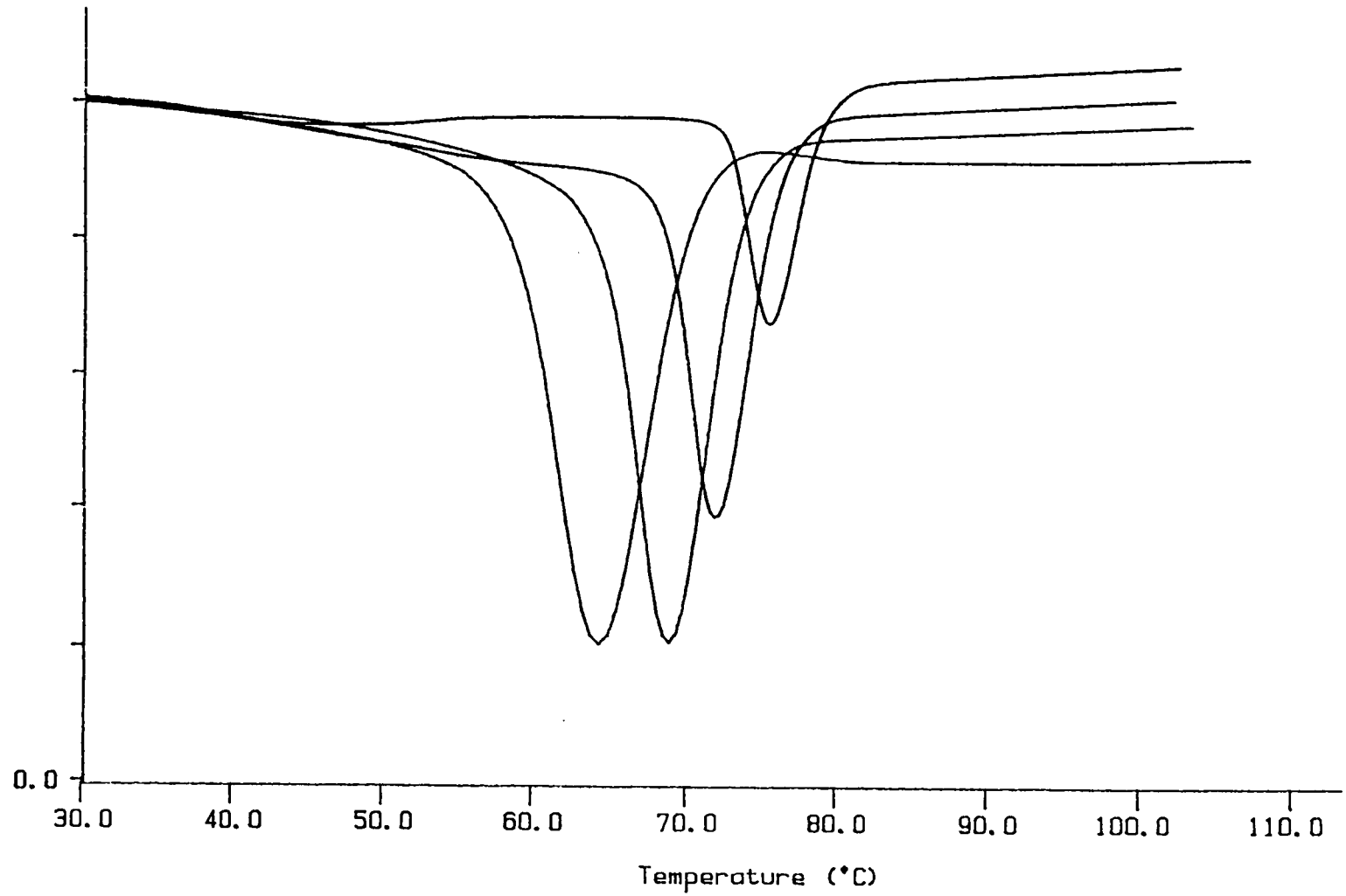


Figure 4.1.1.1. (continued) (b) of H16-O

Figure 4.1.1.2 is the plot of the exothermic peak temperatures (non-isothermal crystallization temperature) as a function of cooling rate. Non-isothermal crystallization temperature decreases linearly with cooling rate and that of the highly branched polymers is lower than that of less branched polymers.

4.1.1.2. Branch Amount and Length Effects

At a constant cooling rate 10°C / min, the exotherms as a function of branch content are shown in **Figure 4.1.1.3**. As branch content increases, the non-isothermal crystallization temperature decreases. Two samples with different molecular weight but the same branch length and content, H10-O (high molecular weight) and L10-O (low molecular weight), show similar crystallization temperature occurs. Non-isothermal crystallization temperatures are dominated by branch content rather than molecular weight in the case of branched polyethylene.

The olefin copolymers with different branch lengths such as hexyl, ethyl and methyl show different non-isothermal crystallization temperatures. Non-isothermal crystallization temperature of L93-P that has methyl branch as much as 93 SCB is higher than that of L39-O with hexyl branch as much as 39 SCB and the one of L40-P is higher than that of L24-O. In the same manner, the crystallization temperature of L31-B that has ethyl branch as much as 31 SCB is higher than that of H16-O. In other words, increasing branch length causes a lowering of non-isothermal crystallization temperature. Longer branches will have more chance of inhibiting the ordering of polymer chains during crystallization due to the increase of effective radius. Since the crystal structure becomes poorer and less stable as branches get longer, the polymer stays in molten state at high

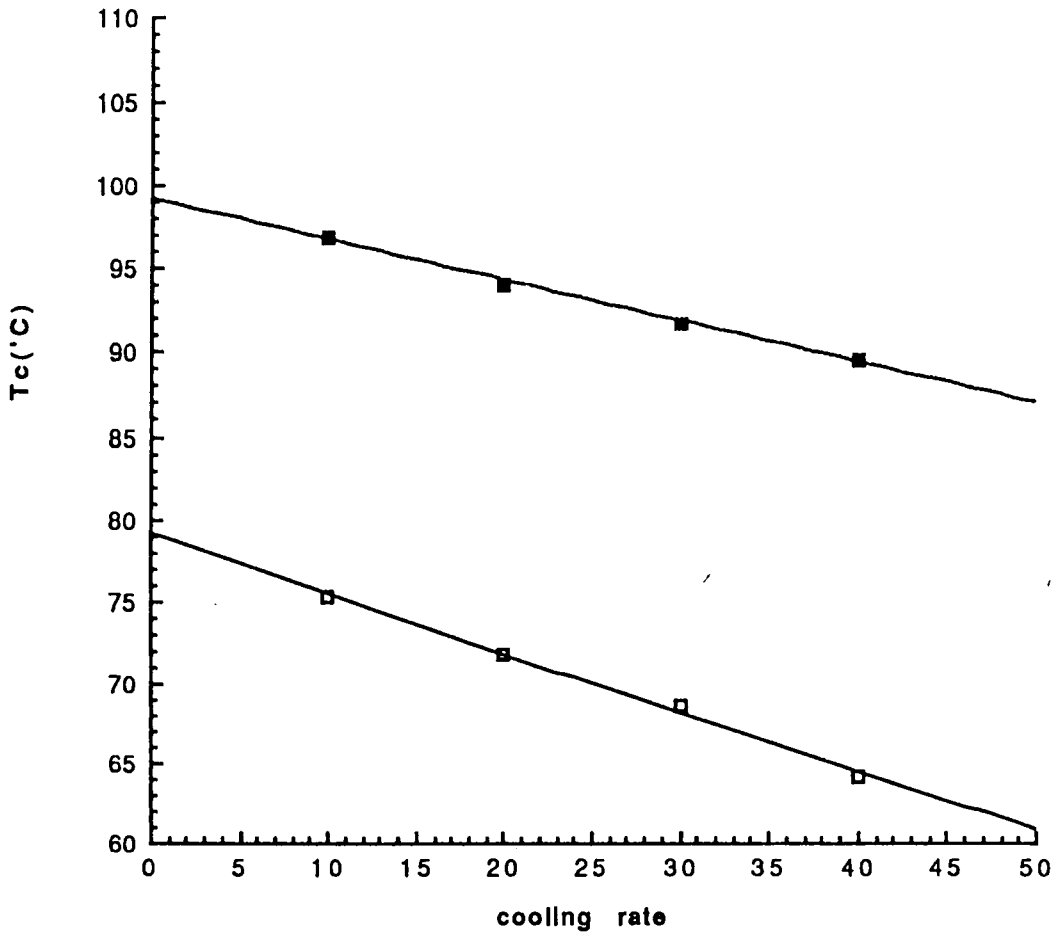


Figure 4.1.1.2. Exotherm peak temperatures as a function of cooling rate.

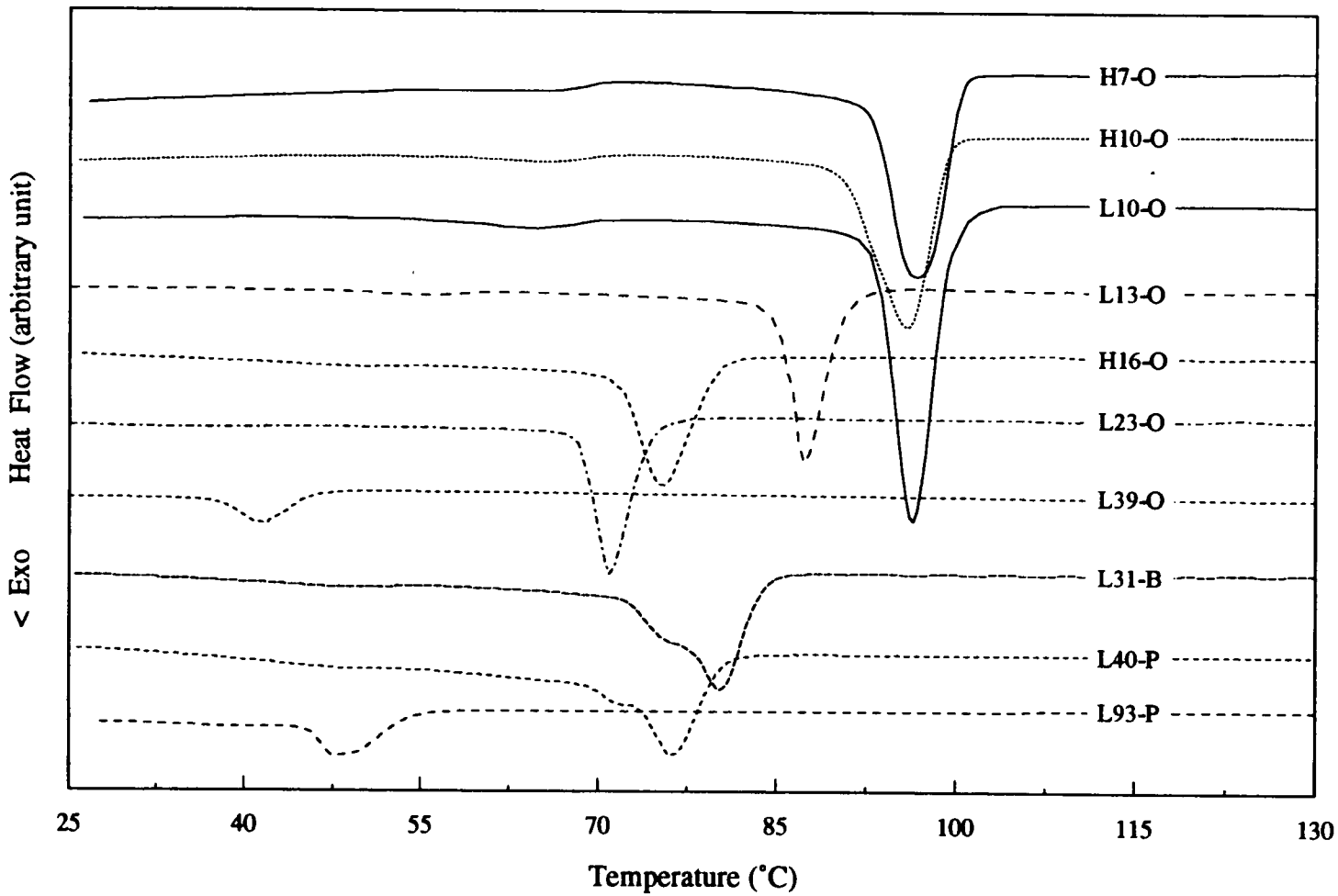


Figure 4.1.1.3. DSC exotherms of EO, EB, and EP copolymers measured at cooling rate, 10 °C/min.

crystallization temperature. Therefore, for polymer chains having long side chains to be crystallized, lower crystallization temperatures are required. **Figure 4.1.1.3** demonstrates this physical explanation.

4.1.2. Melting Behavior

The melting behavior of semi-crystalline material is as important as non-isothermal crystallization behavior for understanding the effect of the polymer structure on the phase transform process.

4.1.2.1. As-received LLDPE

- Ethylene/1-octene Random Copolymers

The melting behaviors of as-received ethylene/1-octene random copolymers are shown in **Figure 4.1.2.1 and 4.1.2.2** for the high and low molecular weight series, respectively. Peak temperature (at which most probable crystals in system melt) was chosen as melting temperature rather than onset temperature at which melting of crystals starts by definition, or baseline return point, at which the last trace of crystal melts. The peak melting temperature decreased as branch content increased. Because melting point is a function of crystal thickness based on the Thompson-Gibbs concept if surface energy and heat of fusion are constant, melting point depression with branch content means that the branches restrict the thickness of lamellae. Therefore, lamellar thickness decreases with branch content and melting point shifts toward lower temperature.

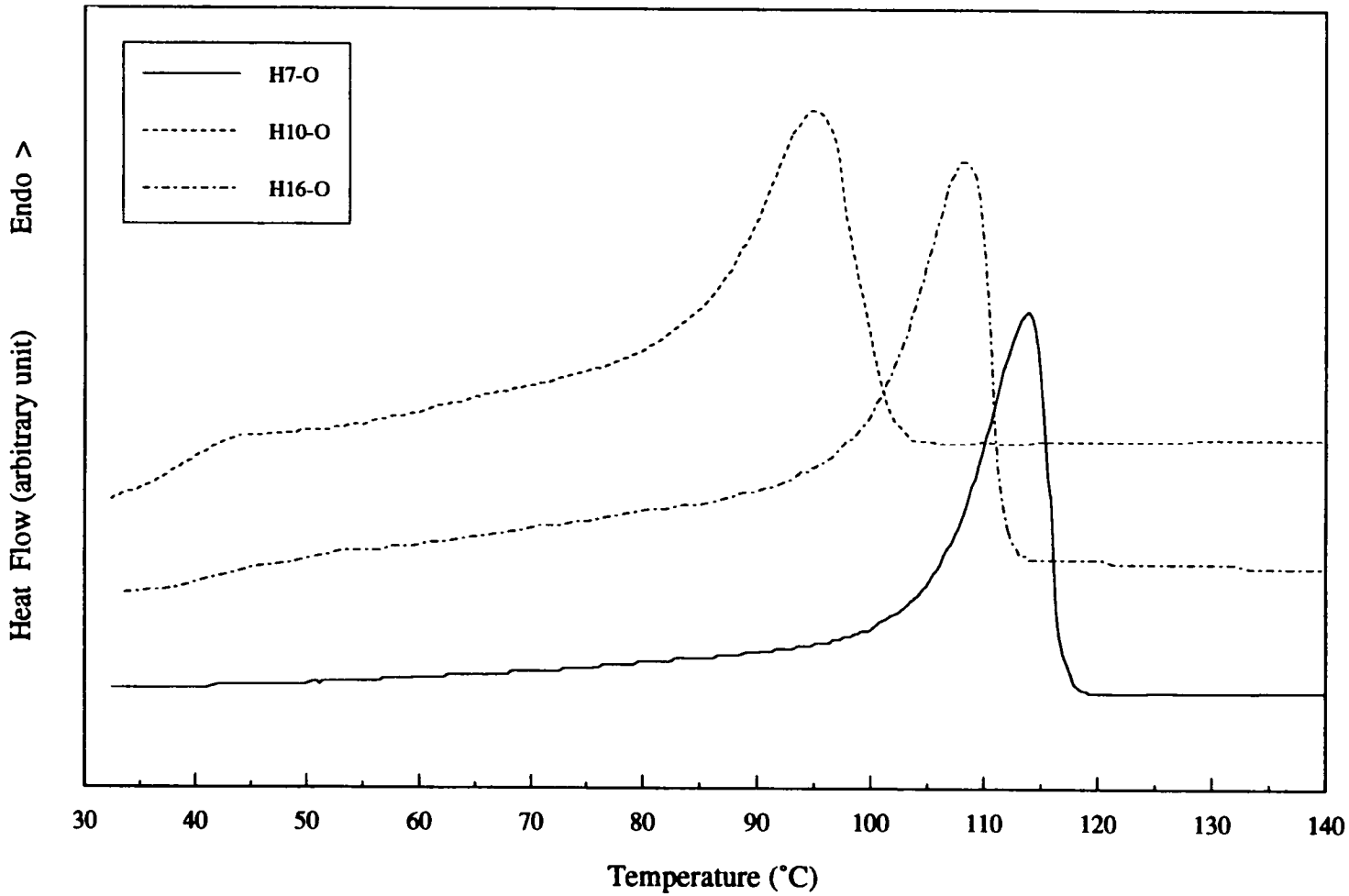


Figure 4.1.2.1. DSC thermogram of as-received EO copolymers (high molecular weight).

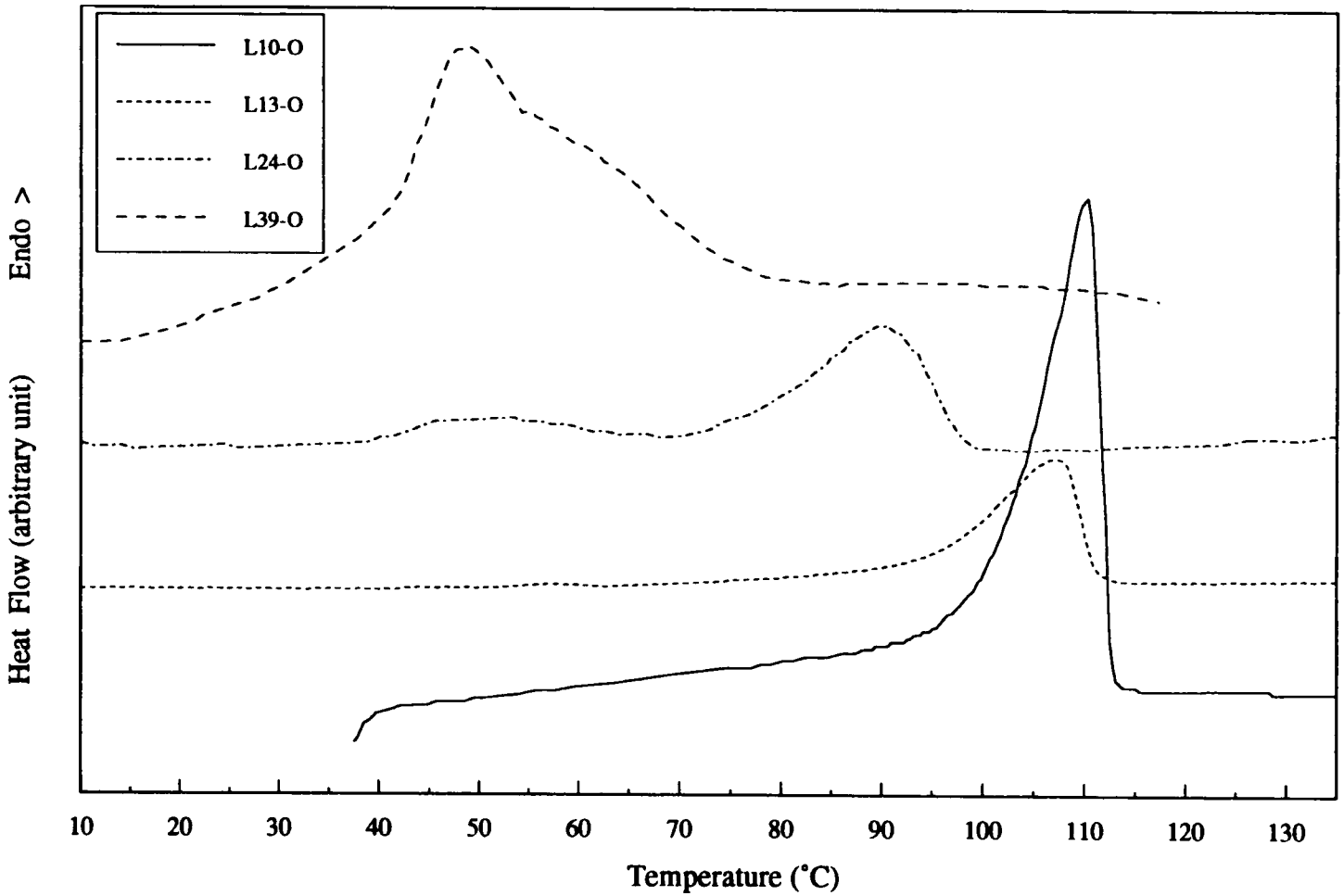


Figure 4.1.2.2. DSC thermogram of as-received EO copolymers (low molecular weight).

The shape of melting thermogram becomes broader with branching content. This means crystal thickness (or lamellar thickness) distributions become broader as branching content increases. In more detail, increasing branching content decreases the distance between branch points and results in thin lamellar thickness. As mentioned in **section 4.1.1.1**, if there is still heterogeneity of branch distribution, it will cause the crystals to have a broader range of lamellar thickness.

• Ethylene/1-propene (EP) and ethylene/1-butene (EB) random copolymers

Melting behavior of L31-B, L40-P and L93-P are shown in **Figure 4.1.2.3**. The shape of melting thermograms is similar to that of EO random copolymers. As branch content increases, the width of the melting curve broadens and peak temperatures shift to lower temperatures. The humps arou[redacted]45 ℃ of L31-B and L40-P are at the same position as the peak temperature of highly branched L93-P. Because their molecular weights are similar to each other and the molecular weight distributions are narrow, the branch distribution is probably the main factor in producing these small humps. On cooling, segregation and crystallization of highly branched parts occurs. This certainly means that there is an unevenness of branch distribution for L31-B and L40-P. In more detail, a localized branch distribution exists for L31-B and L40-P and the distance between branch points in this localized area must be similar to the distance between two branch points in the randomly distributed area of L93-P. In the same sense, the humps of EO copolymer probably reflect the heterogeneity of the branch distribution

Comonomers of propene, 1-butene and 1-octene produce methyl, ethyl and hexyl branches. It is of interest to learn if there is a branch length effect on thermal properties. The comparison of melting temperatures in **Figure 4.1.2.4** shows L31-B ($T_m = 94.46°C$)

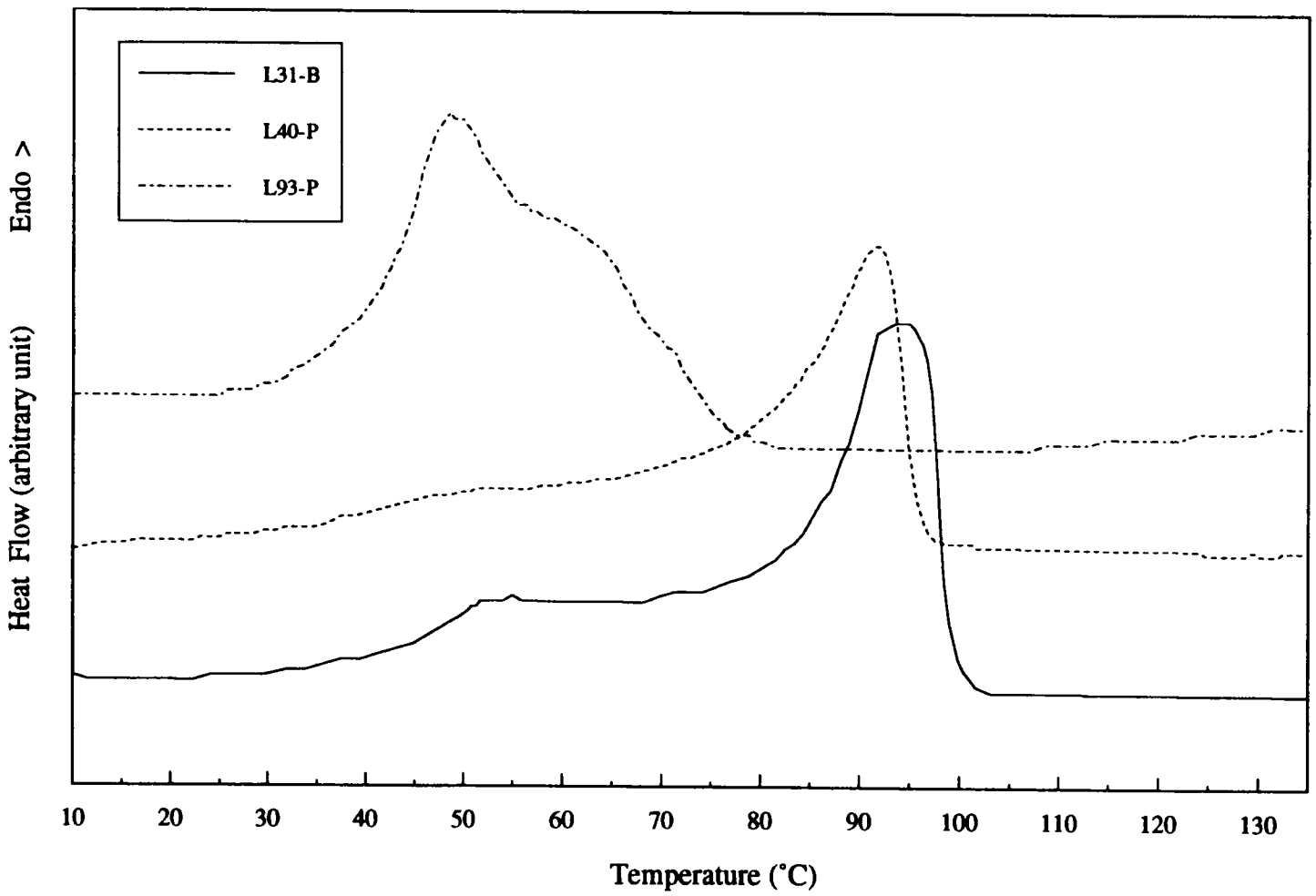


Figure 4.1.2.3. DSC thermogram of as-received EB and EP copolymers.

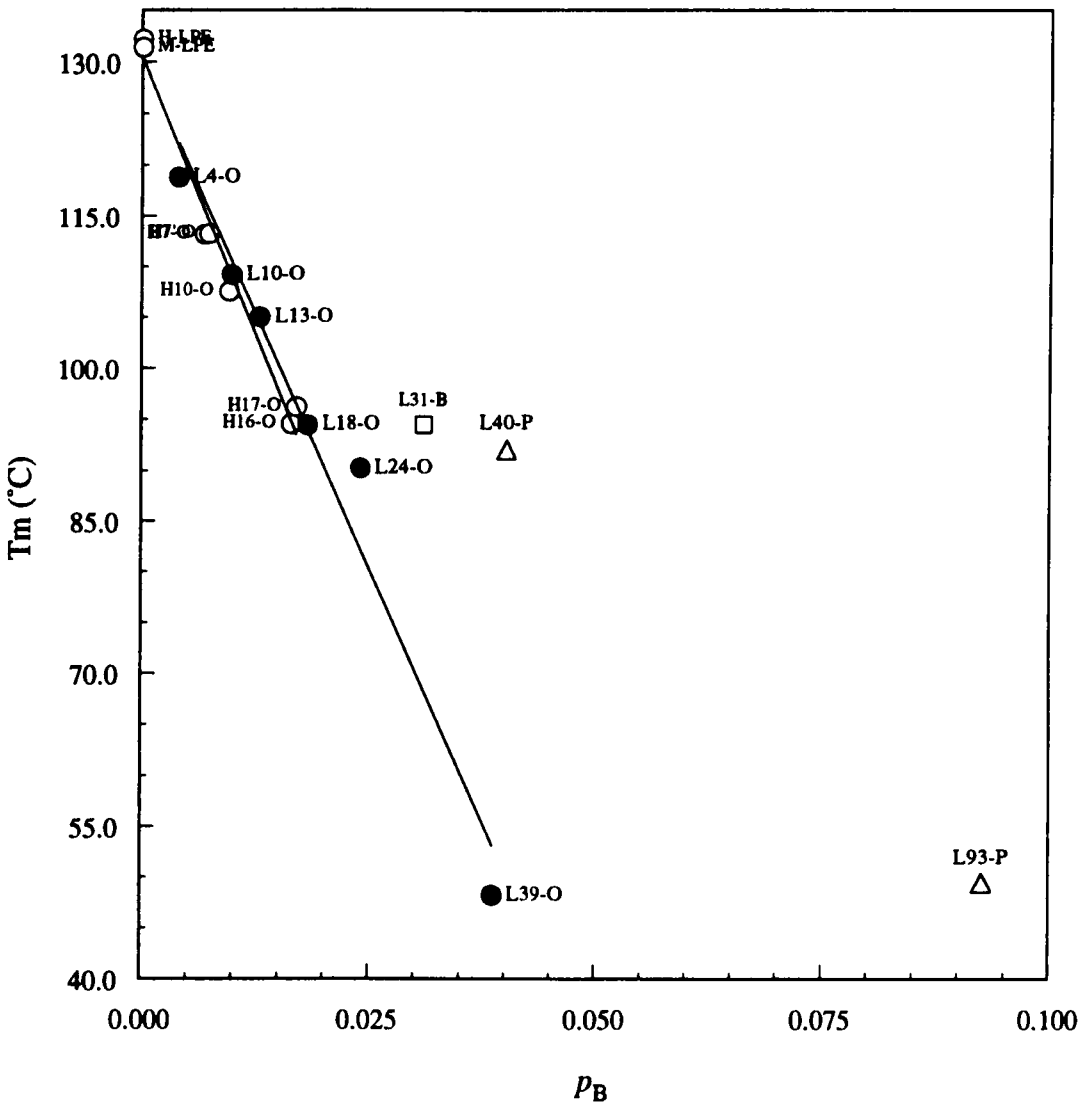


Figure 4.1.2.4. Plot of peak melting temperatures as a function of branch content for EO, EB, and EP copolymers quenched in room temperature.

= L18-O($T_m = 94.46°C$) ≈ H16-O($T_m = 94.54°C$), L40-P($T_m = 92.04°C$) > L24-O($T_m = 90.24°C$), and L93-P($T_m = 49.45°C$) > L39-O($T_m = 48.23°C$) and this is the same tendency as the branch effect on non-isothermal crystallization temperature(see **section 4.1.1.2**). This result is an expected one because the crystals formed at higher crystallization temperature will have higher melting temperatures than those formed at lower temperatures. It is important to know that branch length affects the melting temperature and the crystallization temperature in a consistent manner. The melting temperature of a polymer having a small amount of long side branches corresponds to that of a polymer having a large amount of short branches. In other words, the melting point depression of a copolymer with long side branches is bigger than that of a copolymer with short chain branches. Of course, this does not mean they have the same thermal, mechanical, and rheological properties. In fact the isothermal crystallization behavior and the ability to crystallize are quite different. A long branch copolymer showed poorer crystal structure than a short branch copolymer. (Here EP and EB copolymers are assumed homogeneous copolymers.)

4.1.2.2. Isothermally Crystallized LLDPE

• Isothermal Crystallization Temperature Effect

The effect of crystallization temperature at a fixed crystallization time of 1 day is shown in **Figure 4.1.2.5, Figure 4.1.2.6, and Figure 4.1.2.7** for L31-B, L40-P and L93-P. The broad single melting peak of the quenched sample was separated into three discrete melting peaks, except for the L31-B crystallized at 90°C. The first peak (T1) appears at a higher temperature than the isothermal crystallization temperature (T_c), and results from

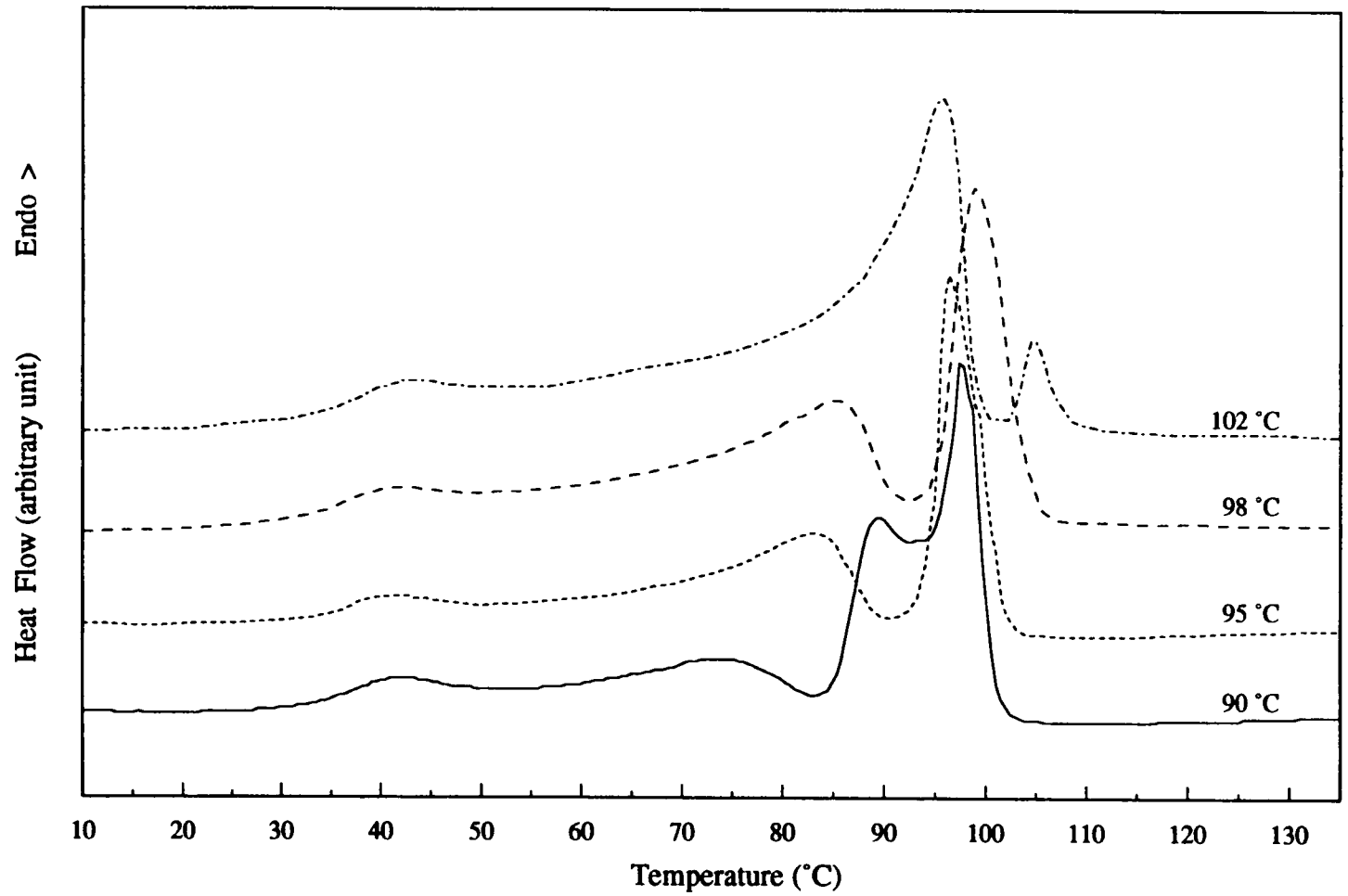


Figure 4.1.2.5. DSC thermogram of L31-B crystallized at the indicated temperatures for 1 day.

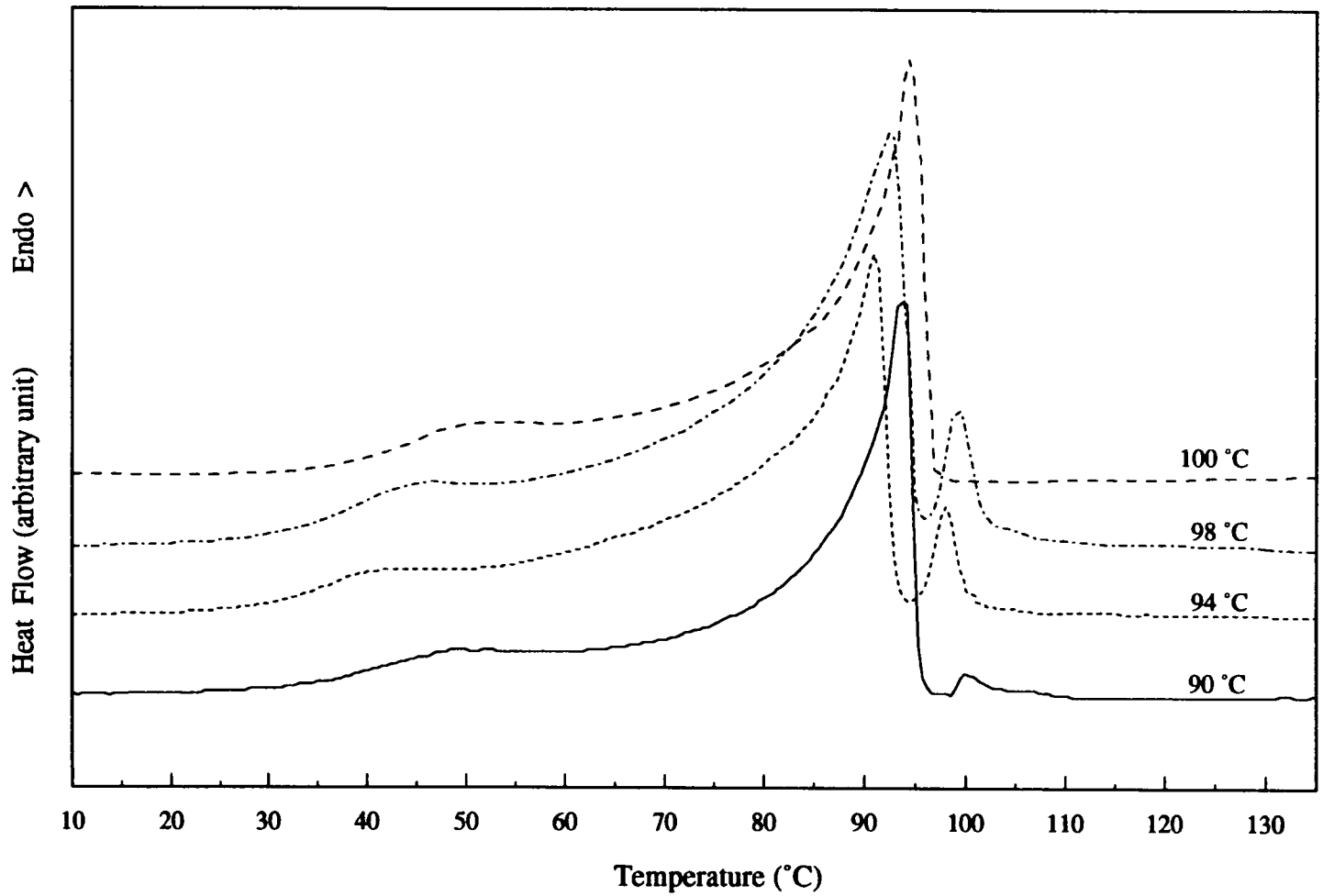


Figure 4.1.2.6. DSC thermogram of L40-P crystallized at the indicated temperatures for 1 day.

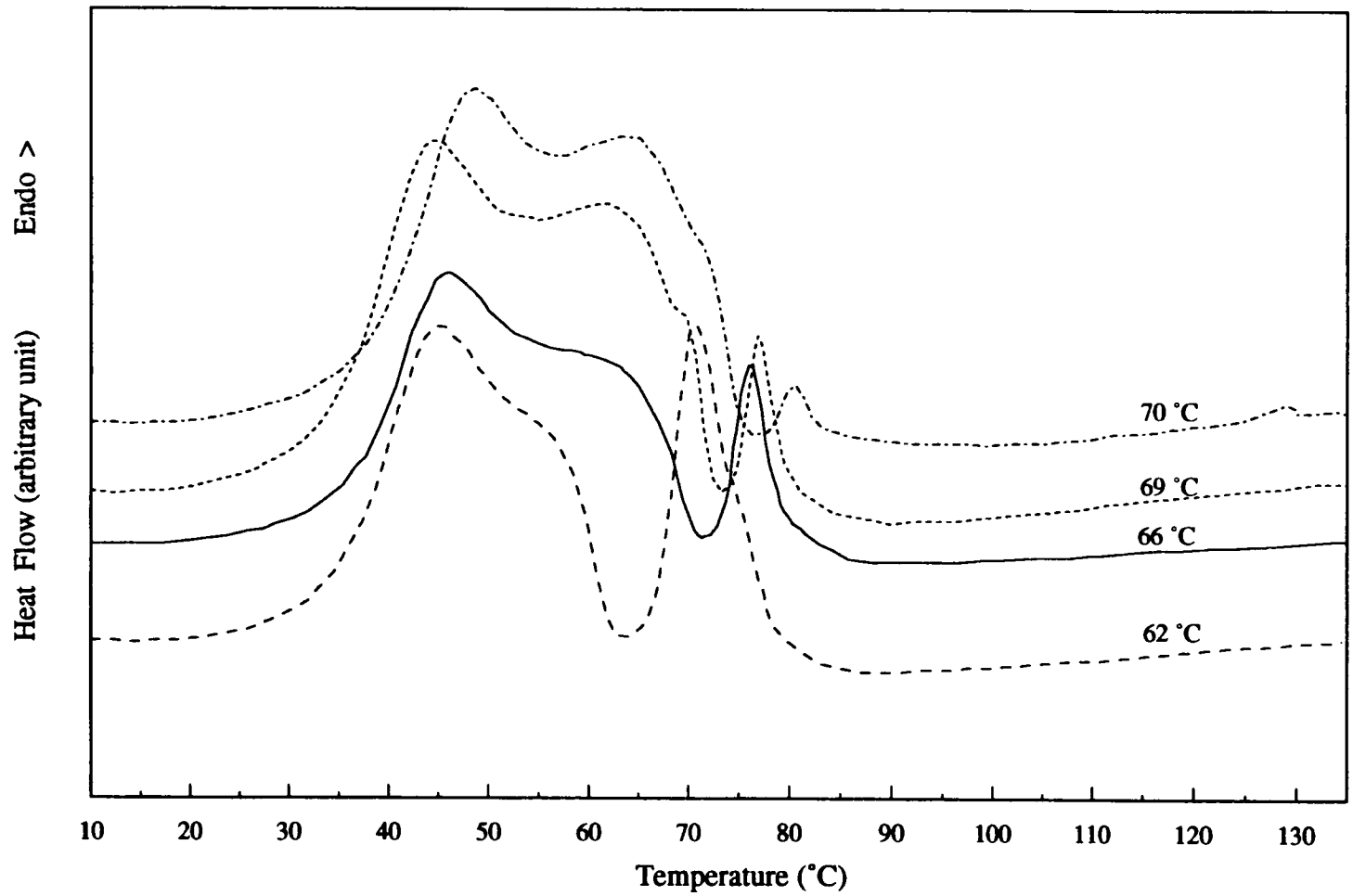


Figure 4.1.2.7. DSC thermogram of L93-P crystallized at the indicated temperatures for 1 day.

the isothermal crystallization process. The second peak (T2) just below T_c and the last peak (T3) around 45 $^{\circ}C$ (far away from T_c) are due to the quenching process. The value of T1 shifts to a higher temperature with increasing crystallization temperature. Evidently, this may be due to the crystallization of molecules capable of thick lamellae at a particular temperature. The first peak area of L31-B crystallized at 102 $^{\circ}C$ is much smaller than for samples crystallized below 102 $^{\circ}C$. This indicates that some molecules can be crystallized at this temperature even though most molecules are in the molten state. The latter will crystallize, generating the second and third peaks during cooling. All molecules have a particular crystallization temperature depending on branch content and molecular weight. Molecules are segregated as a function of branch distribution in the random copolymer even during the fast cooling process resulting in the two endotherms, T2 and T3, below the crystallization temperature.

• Isothermal Crystallization Time Effect

Crystallization is controlled by time as well as temperature. A demonstration on the melting behavior with crystallization time is shown in **Figure 4.1.2.8 and Figure 4.1.2.9** for H7-O and H16-O, respectively. The quenched sample of H16-O shows a single broad melting peak around 94.0 $^{\circ}C$ in **Figure 4.1.2.9** with a weak shoulder around 40 $^{\circ}C$. As isothermal crystallization proceeds, the single broad peak is separated into multiple peaks. The first peak (T1) appears above the isothermal crystallization temperature(T_c), the second peak (T2) below T_c and the last peak (T3) around 45 $^{\circ}C$, far away from T_c. The last two peaks are caused by the quenching process.

In **Figure 4.1.2.8** and **Figure 4.1.2.9**, the T1 just above the crystallization temperature (T_c) grows larger at the cost of the T2 peak and shifts to higher temperatures

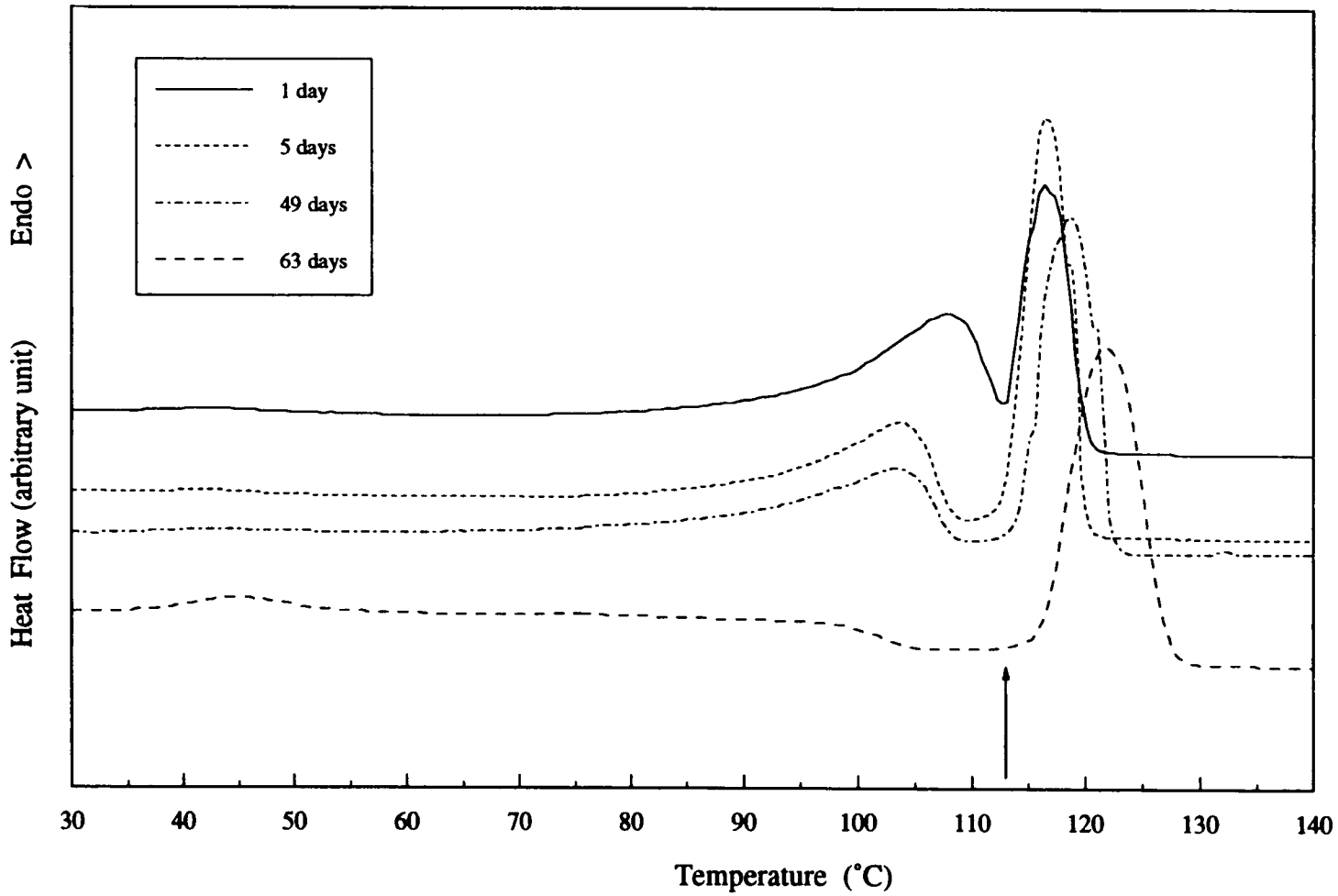


Figure 4.1.2.8. Melting thermograms of H7-O crystallized at 113 °C (arrow) for indicated times.

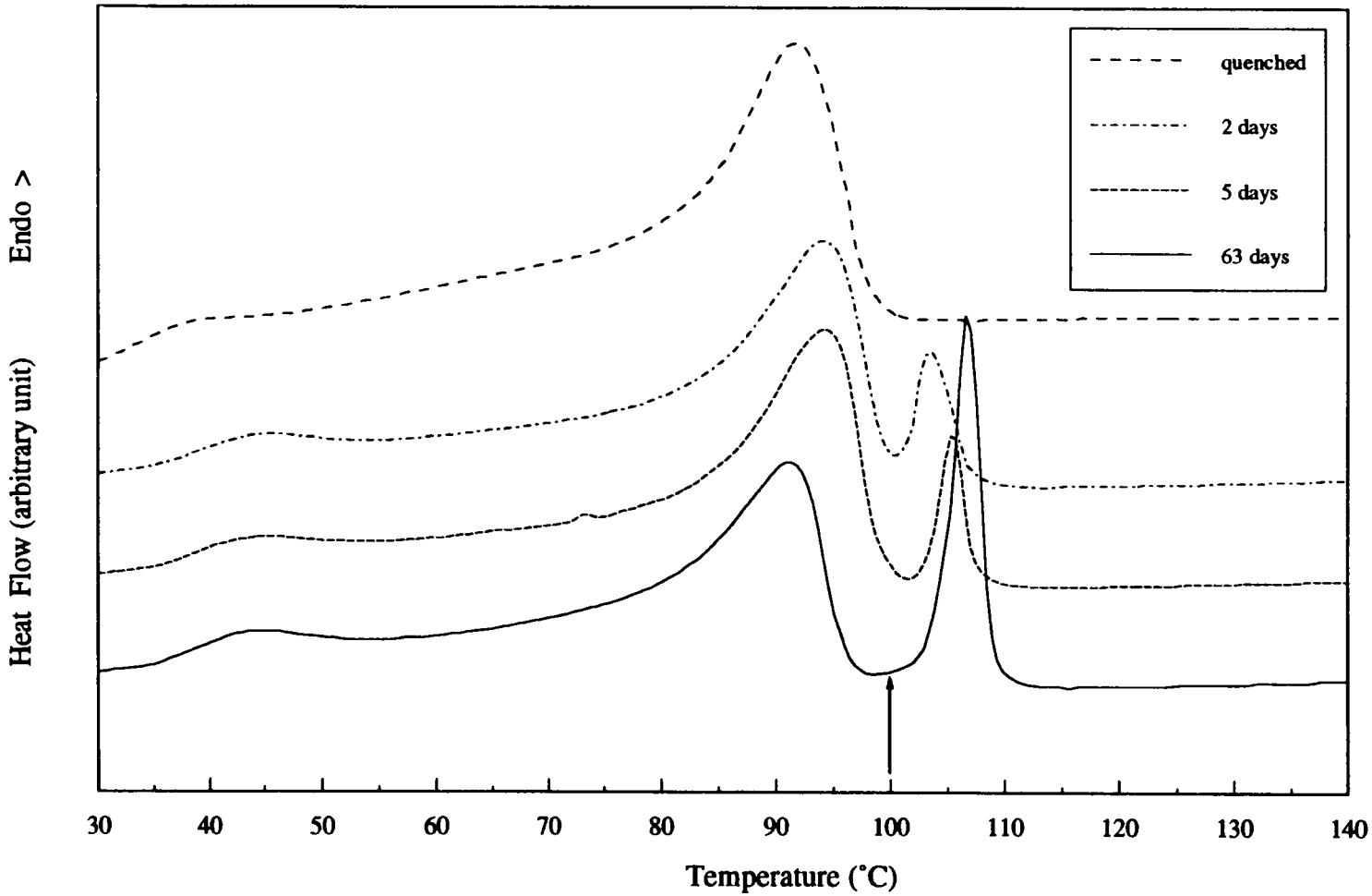


Figure 4.1.2.9. Melting thermograms of H16-O crystallized at 100 °C (arrow) for indicated times.

with crystallization time. Further the T2 peak shifts to a lower temperature and the gap between the first and second peaks increases as crystallization time increases. **Figure 4.1.2.10** and **Figure 4.1.2.11** show that T1 increases rapidly for short crystallization time and then increases slowly as time is increased. Simultaneously, T2 decreases steeply for short crystallization times and then decreases slowly. Long crystallization times are known to result in the crystal becoming more stable by annealing and reorganization. As crystallization time becomes longer the increase of the T1 temperature levels off. The reason for the increasing of T1 with crystallization time can be explained. The polymer chains that form the most stable crystals at a certain temperature will crystallize first, while other polymer chains form unstable crystals or remain in the molten state. The crystallized polymers will thicken by depleting such features as folded chains, loops, loose chains, cilia and tie molecules connected to crystalline phase, and be reorganized to lower the free energy and be more stable. Thickening and stabilization of the crystal will cause the increase of melting temperature, since melting point is a function of lamellar thickness and heat of fusion based on the Thompson-Gibbs equation.

The reasons for decrease of the T2 temperature are complex. One way to understand this behavior is to consider the effect of molecular weight distribution on the crystallization process. If the crystallization follows the order of chain length, lower molecular weight will be incorporated after longer chains are consumed. If this happens, under the assumption that annealing effect is small, the peak melting temperature (T1) should be decreased because most probable crystal thicknesses are decreased statistically as the chain of low molecular weight participates in crystallization. However, the tendency in **Figure 4.1.2.10 and Figure 4.1.2.11** contradicts the above expectation. To explain this, we need to borrow the secondary nucleation idea.

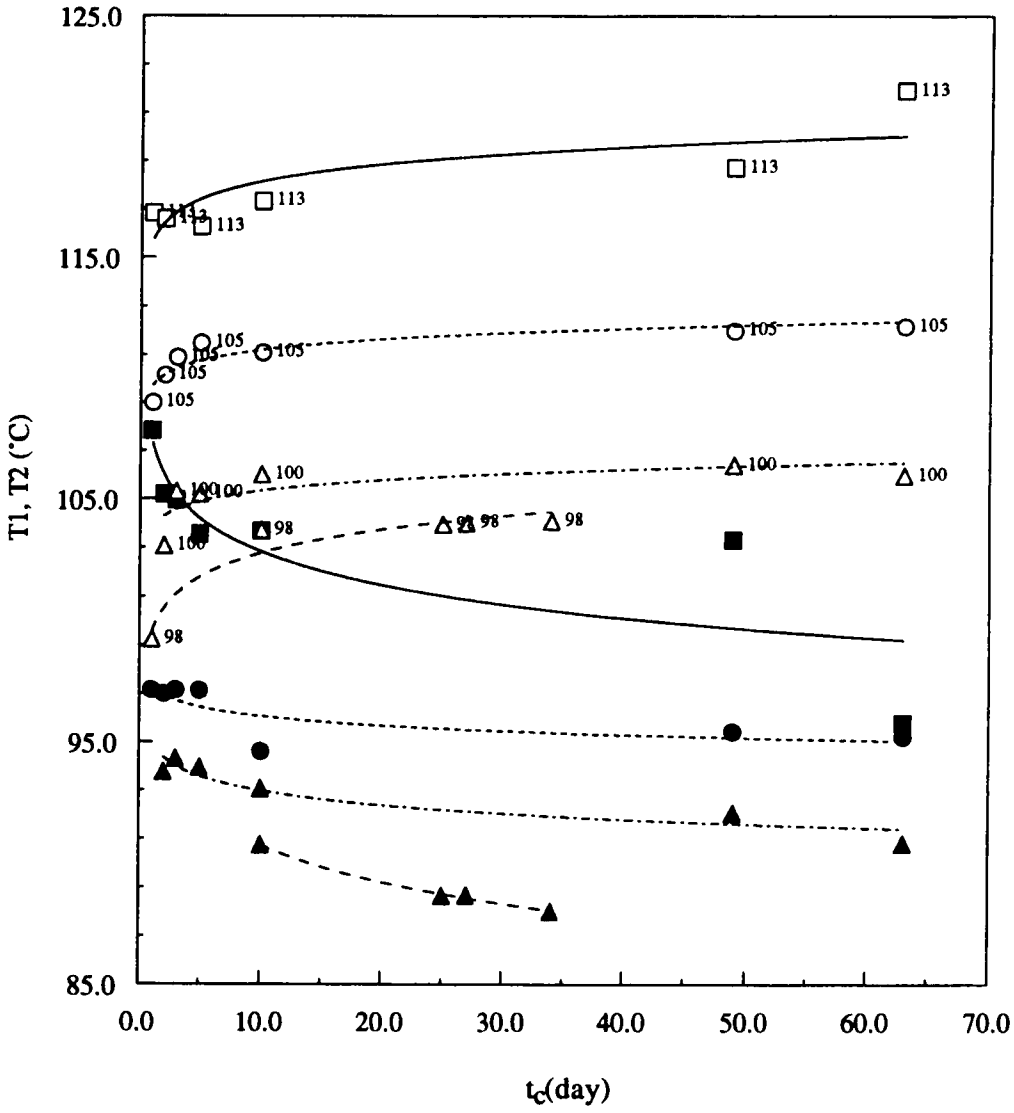


Figure 4.1.2.10. Melting temperature, T1 above T_c and T2 just below T_c, of high molecular weight EO copolymers with crystallization time at labeled temperatures. Open and closed symbols are T1 and T2, respectively. Square, circle, and triangle are H7-O, H10-O, and H16-O, respectively.

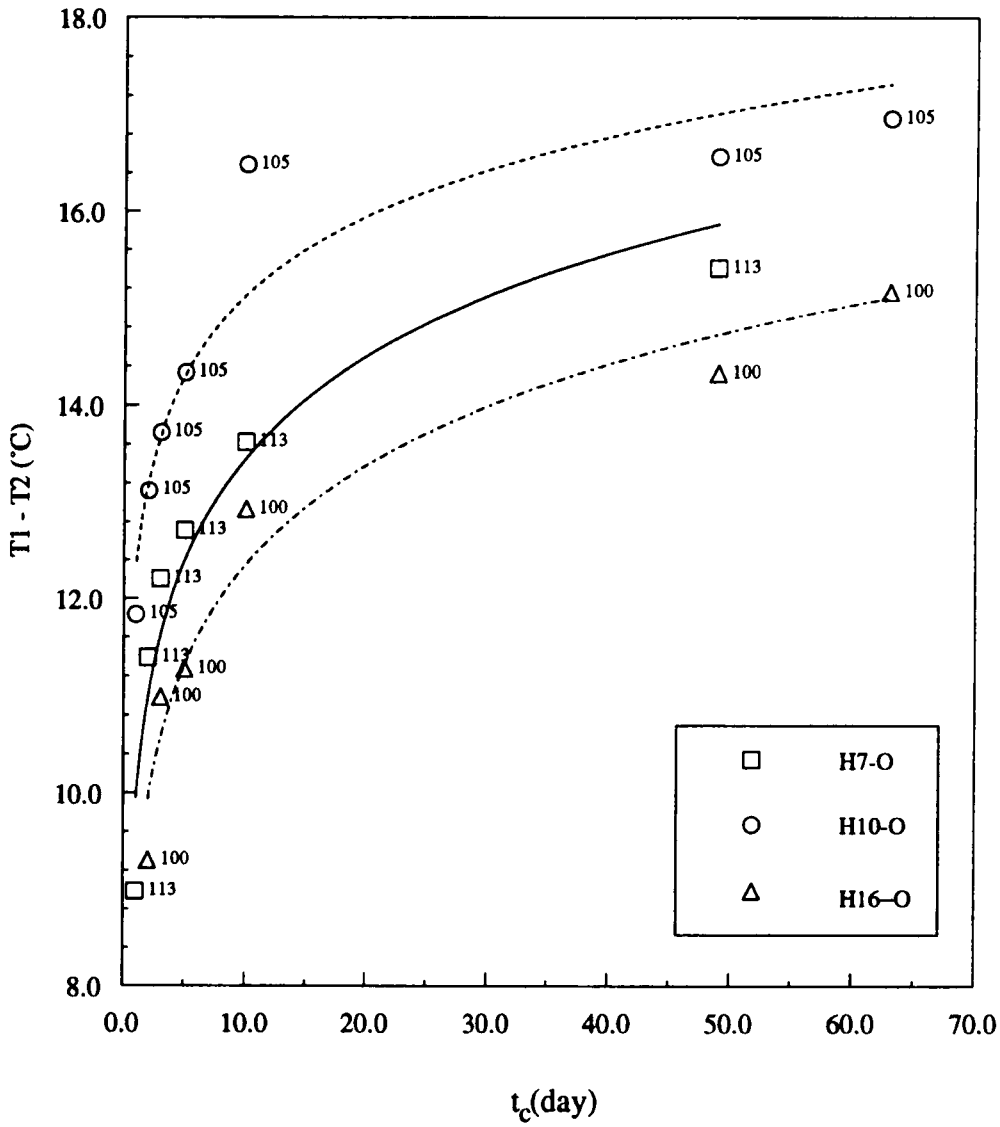


Figure 4.1.2.11. Melting temperature difference (T1-T2) of high molecular weight EO copolymer as a function of crystallization time. Labeled numbers are isothermal crystallization temperatures.

The starting point is the crystal surface with some niches. The chains of low molecular weight are unstable at the temperature at which long chains crystallize. For short polymer chains to overcome this thermodynamic barrier, it is necessary to reduce their surface energy. The only place for this to occur is the niche of the growing crystal surrounded by two and three surfaces. As short polymer chains are registered on niches, the crystal surface becomes smooth, the crystal becomes more perfect and shorter chains remain in the amorphous state. As the crystal becomes perfect, the peak melting temperature (T1) is increased. Shorter chains remaining in the amorphous state will be crystallized on cooling, resulting in shifting the second peak(T2) to lower temperature. The reduced amount of low molecular weight chains will cause the decreasing heat of fusion shown in **Figure 4.1.2.12**.

Consider now the relationship between heat of fusion and crystallization time. The heat of fusion (the area under melting curve) is the amount of energy required to break intermolecular forces in transforming the crystalline phase into the amorphous phase. This heat of fusion is directly related to the degree of crystallinity and crystal perfection. Increasing crystallization time has two effects on a semi-crystalline system. The preformed crystals will be annealed, the crystals becomes more stable by molecular reorganization process and annealing, as mentioned before. Annealing behavior was reported even in crosslinked low density polyethylene[49, 50, 51] where molecular mobility was reduced and annealing effects small. Therefore, the presence of annealing process in LLDPE is quite reasonable because of more favorable chain mobility. As thickening and reorganization takes place, intermolecular force increases and enthalpy($H_{crystal}$) of crystal decreases. Thus heat of fusion $\Delta H_f (J/g)$ $(= H_{melt} - H_{crystal})$ increases. This means that more energy is needed for the crystals to melt. Simultaneously, new amorphous molecules will be transformed to the crystalline phase. In other words, after a system depletes

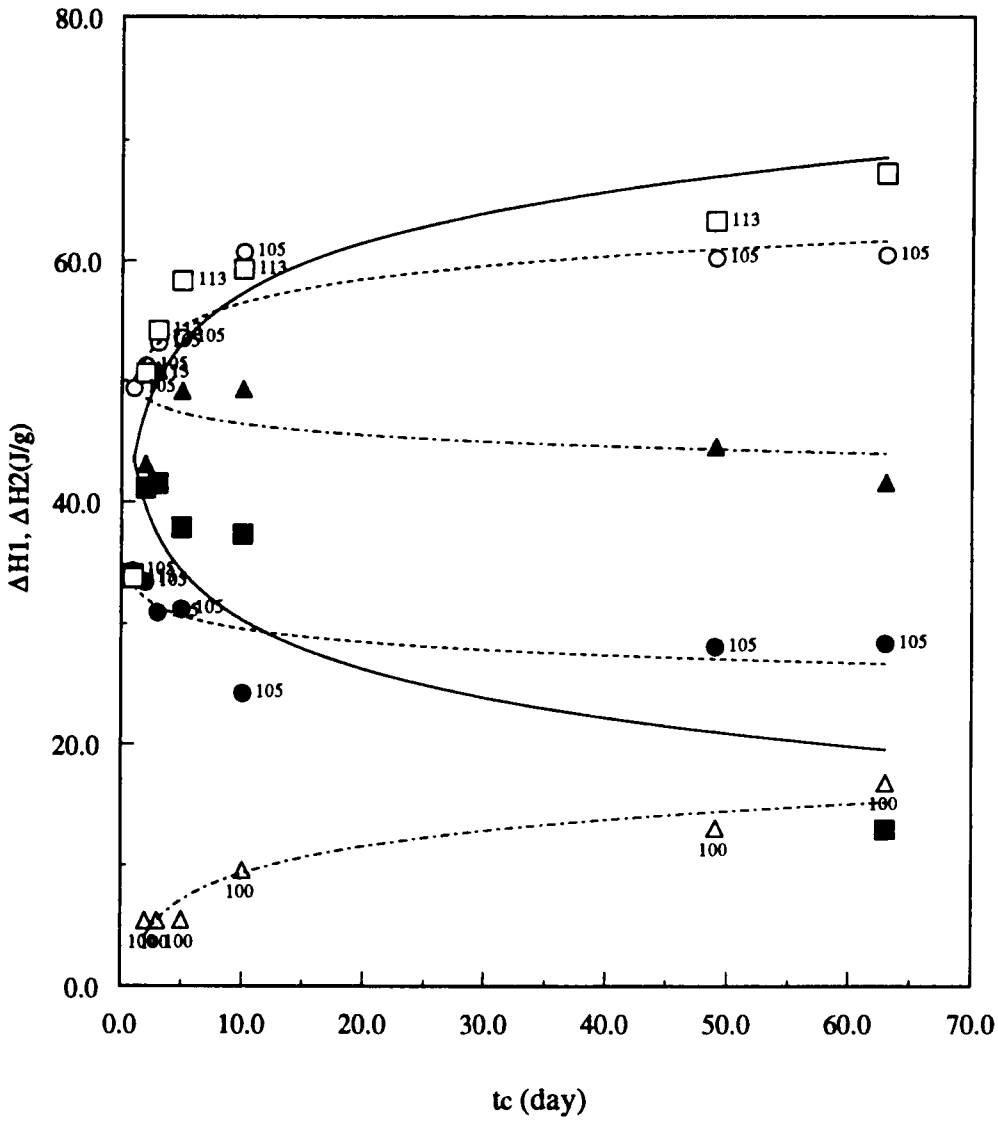


Figure 4.1.2.12. Heat of fusion, ΔH1 above T_c and ΔH2 just below T_c, of high molecular weight EO copolymers with crystallization time at labeled temperatures. Open and clossed symbols are ΔH1 and ΔH2, respectively. Square, circle, and triangle are H7-O, H10-O, and H16-O, respectively.

polymer chains consisted of long A-sequence that can form the longest lamellar thickness, next polymer chains with next long A-sequence that can form next longest lamellar thickness will register on the pervious formed crystal surface, or the nucleus when secondary nucleation is assumed. Both effects will contribute to an increase of heat of fusion and to the continuous distribution of lamellar thickness above T_c. Thus the area under the DSC curve above the T_c increases. All the polymer chains, however, cannot participate in crystallization at a particular temperature, since there are highly branched or low molecular weight polymer chains that form unstable crystal at the high T_c. Those molecules will be crystallized on cooling, making second peak, T2. The area of the second peak and the gap between the T1 and T2 peaks depends on how many polymer molecules, which are related to the second peak for short crystallization time, are incorporated in the first peak for long crystallization time. More incorporation will cause that second peak to become weak. In the case of narrow molecular weight distribution, the second peak will strongly depend on the branch concentration. Similarly, the polymer chains with high branch contents will have a short distance (i.e., sequence length) between two branching points. The crystals being obtainable from these chains are unstable at high T_c because they form thin lamellae. They are stable only at low T_c (at high supercooling).[16] Therefore, the area of the second peak of H16-O changes a little with crystallization time whereas that of H7-O decreases drastically.

The third peaks (or humps) around 40 and 50℃ are not sensitive to crystallization time, except that the peak of quenched H16-O is lower than others crystallized isothermally. As expected, since polymer chains crystallizing in this range will be in the molten state at high crystallization temperatures, there is no effect of isothermal time on this peak.

4.1.2.3. Degree of Crystallinity with Crystallization Temperature, Time and Branch Content.

The relationships among degree of crystallinity, isothermal crystallization time, and temperature are shown in **Figure 4.1.2.13** for high molecular series, **Figure 4.1.2.14** for low molecular weight series of EO copolymers and **Figure 4.1.2.15** for EB and EP copolymers. The indicated numbers are crystallization time (unit : day) and the degree of volume $V_c(\%)$ and weight crystallinity $W_c(\%)$ are obtained from the area between the crystallization temperature and the base line beyond base line return point.

The heat of fusion decreases as crystallization temperature increases (i.e., supercooling decreases). This may be due to the contribution of reduction of crystallinity rather than that of increasing of crystal perfection. The reduction of crystallinity is due to an decrease of nucleation density with increasing temperature.

The degree of crystallinity increases with increasing crystallization time due to the primary crystallization until radial growth of spherulite finishes by impingement and then due to the secondary crystallization after impingement of spherulite, or deviation point from the Avrami plot. The crystallinity increase was observed in all samples. Even highly branched LLDPE (L39-O) shows the increase of degree of crystallinity although the increase is small compared to low branched LLDPE. The degree of crystallinity decreases with branch content because of the role of the branches as defects that cause chain irregularity.

Figure 4.1.2.16 is the plot of heat of fusion and weight crystallinity of the sample crystallized at various temperatures and times against branch content. The overall trend of

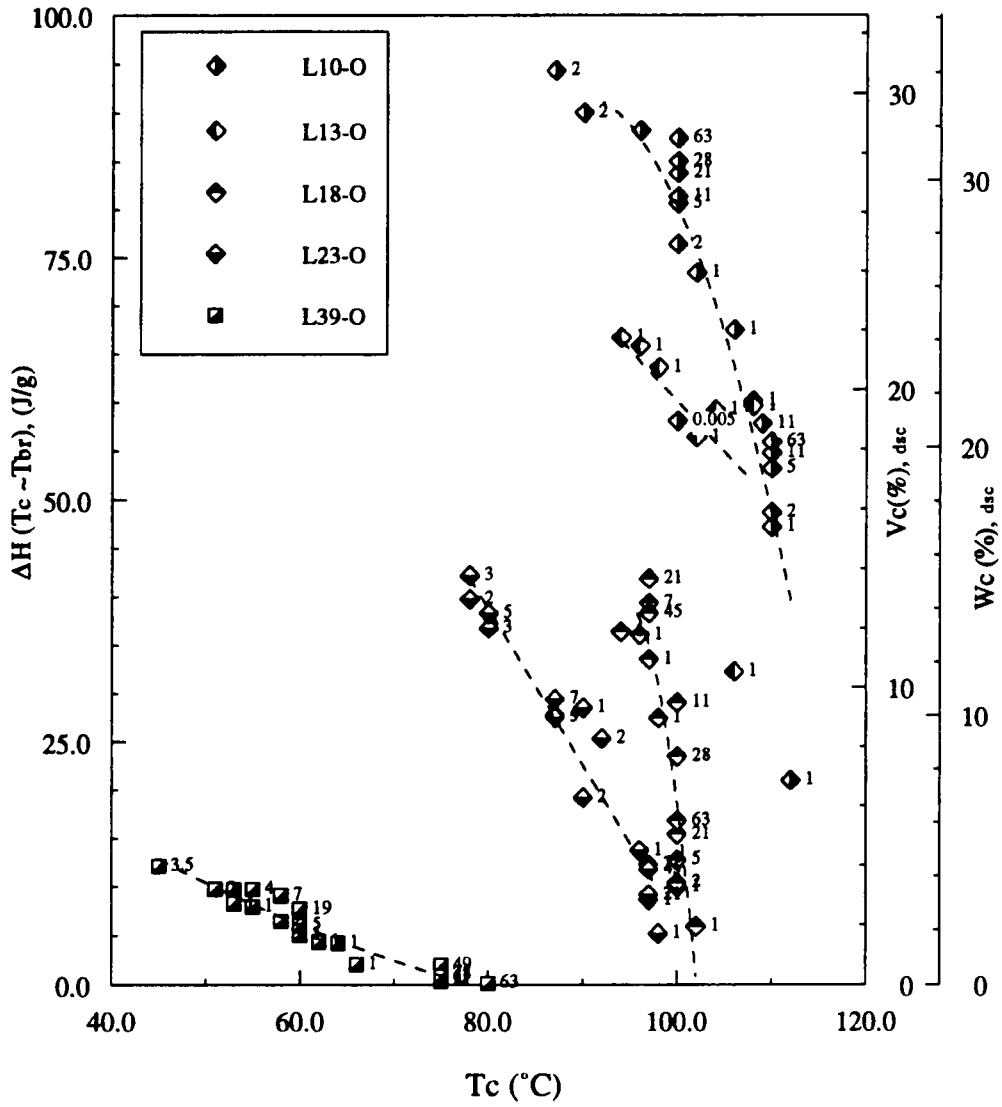


Figure 4.1.2.13. Heat of fusion (ΔH, J/g), degree of volume ($v_c(\%)$,dsc) and weight crystallinity ($w_c(\%)$,dsc) obtained between T_c and base line return temperatures (T_{br}) as a function of T_c for low molecular weight EO copolymers. Labeled numbers are isothermal crystallization time, t_c (day).

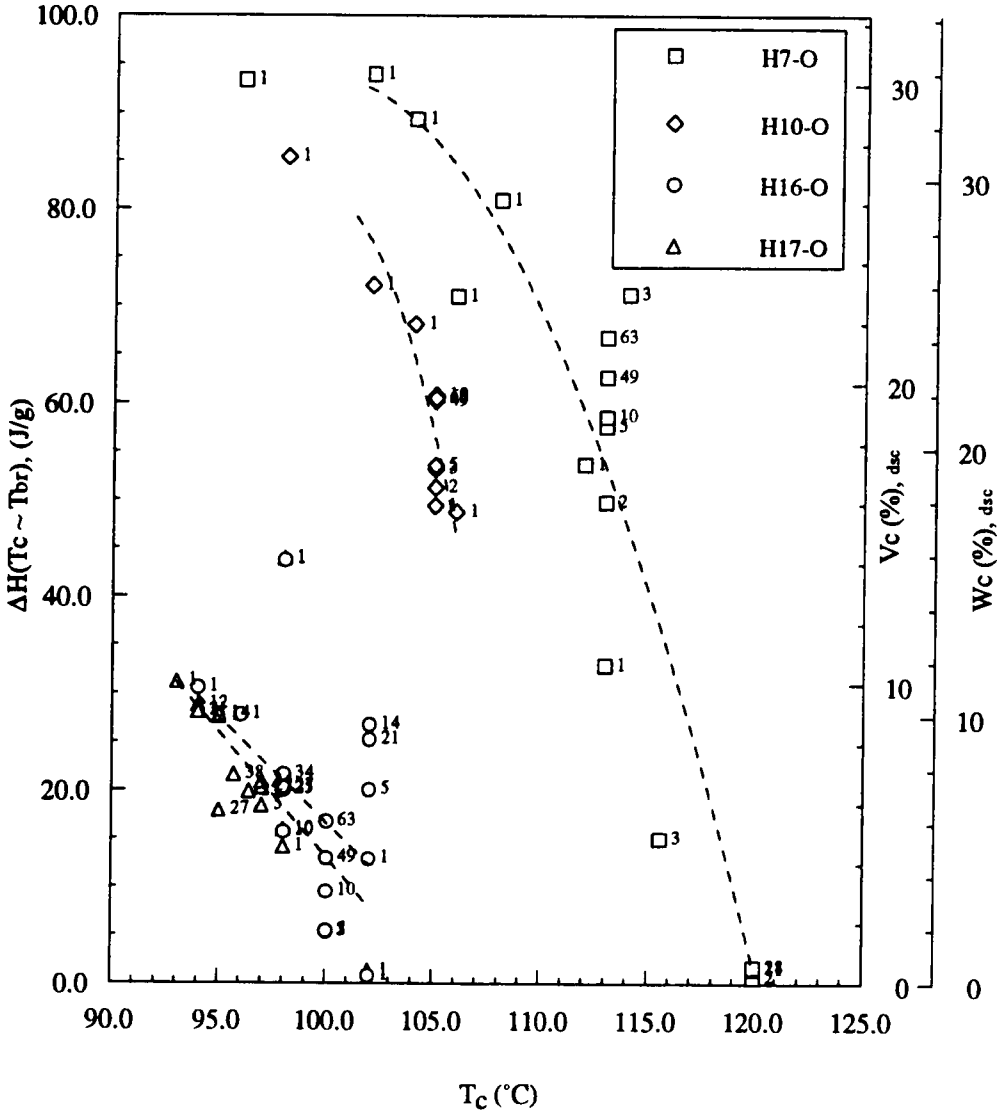


Figure 4.1.2.14. Heat of fusion (ΔH, J/g), degree of volume ($v_c(\%)$,dsc) and weight crystallinity ($w_c(\%)$,dsc) obtained between T_c and base line return temperatures (T_{br}) as a function of T_c for high molecular weight EO copolymers. Labeled numbers are isothermal crystallization time, t_c (day).

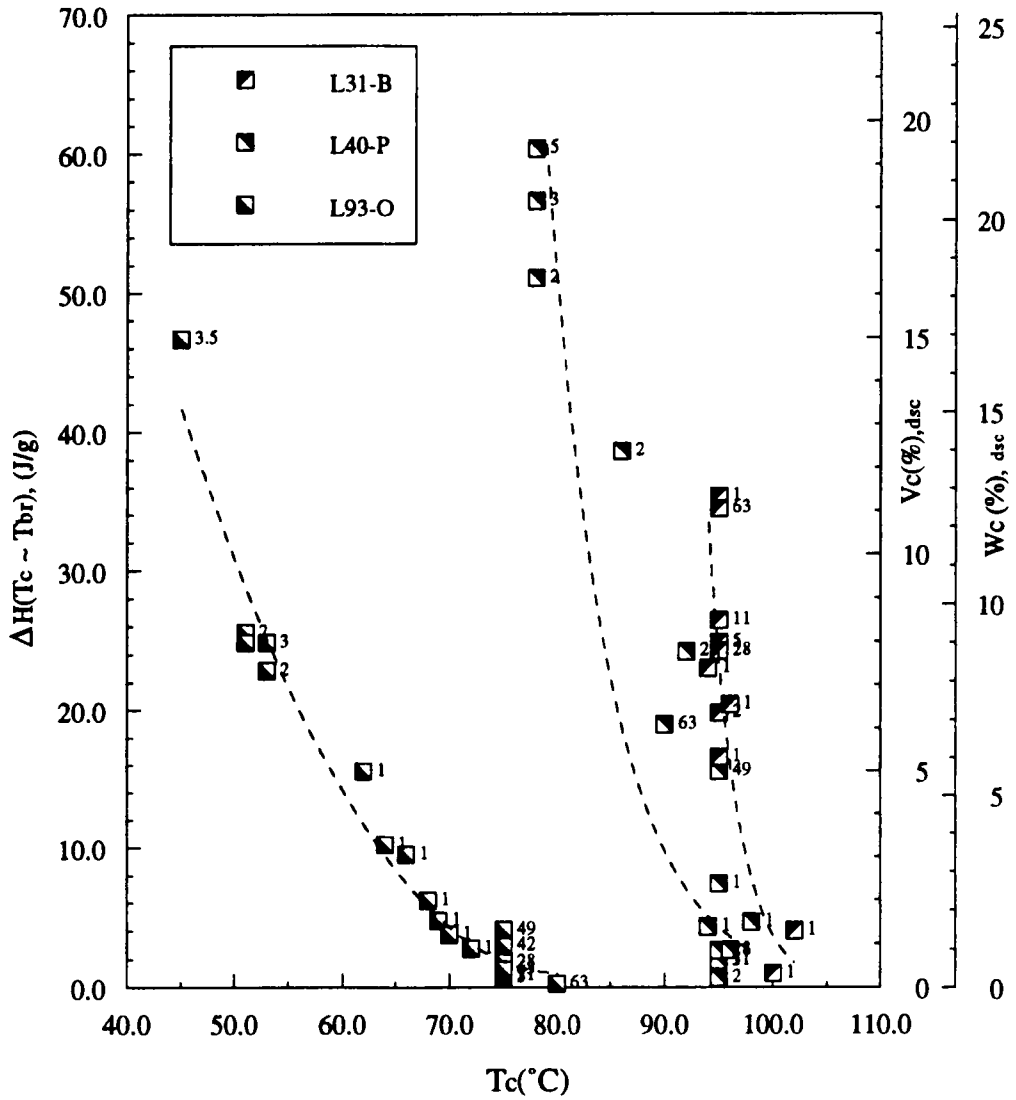


Figure 4.1.2.15. Heat of fusion (ΔH, J/g), degree of volume ($v_c(\%)$,dsc) and weight crystallinity ($w_c(\%)$,dsc) obtained between T_c and base line return temperatures (T_{br}) as a function of T_c for low molecular weight EP ans EB copolymers. Labeled numbers are isothermal crystallization time, t_c (day).

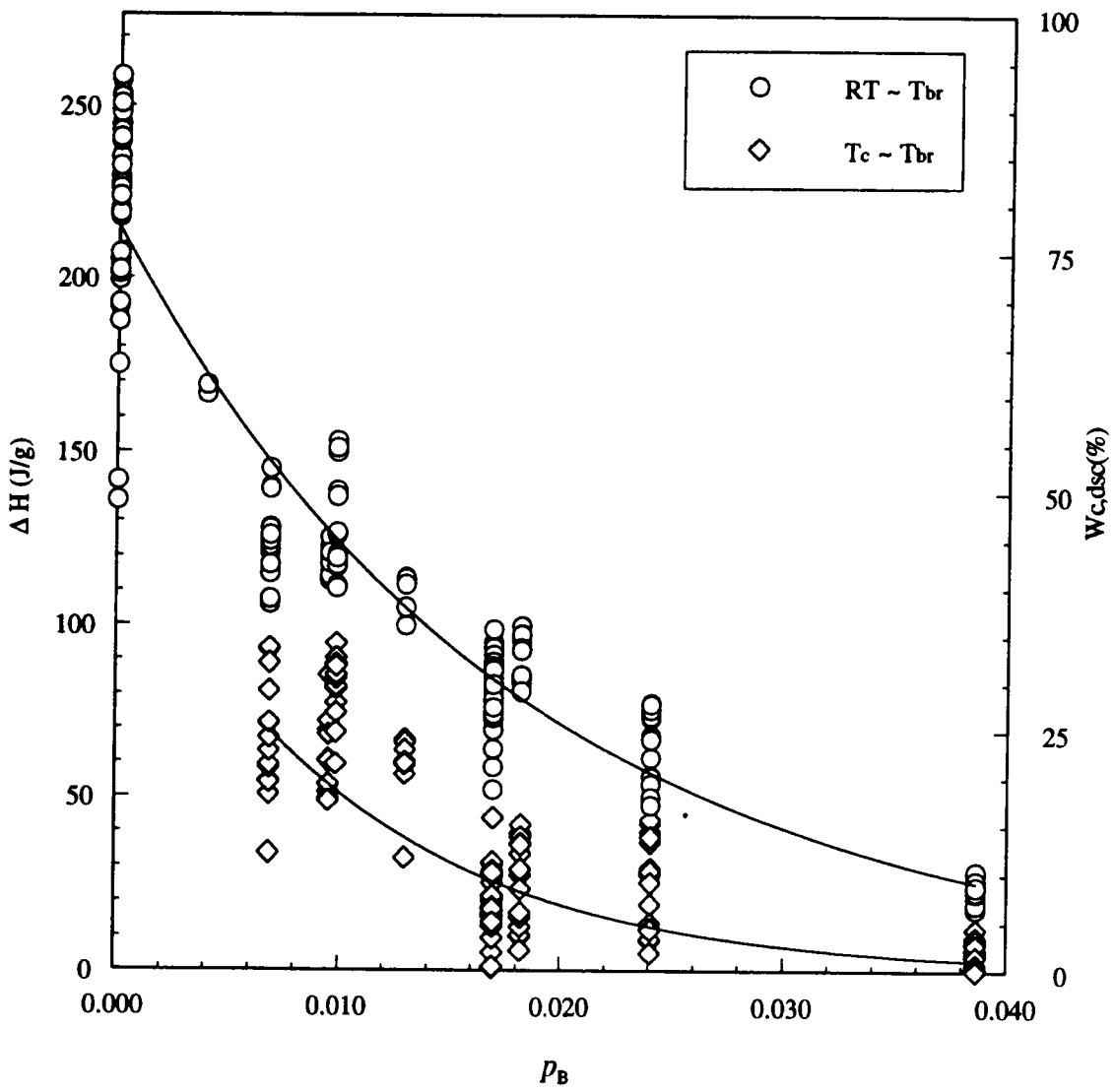


Figure 4.1.2.16. Heat of fusion (ΔH, J/g) and weight crystallinity ($w_c(\%)$,dsc) of EO copolymers crystallized at various temperature and time with branch content.

these parameters in both $\Delta H_{total}(RT \sim T_{br})$ and $\Delta H1(T_c \sim T_{br})$ decreases with branch content.

4.2. Crystallization Kinetics

4.2.1. Avrami Analysis

The reduced crystallinity and the Avrami plot are shown as **(a)** and **(b)** in **Figures 4.2.1.1 ~ 4.2.1.5** for EO copolymers. The reduced (or relative) crystallinity $(1-X_t)$ is obtained from the following equation.

$$1 - X_t = (I_t - I_o)/(I_\infty - I_o) \qquad (4.2.1)$$

where I_o, I_t, and I_∞ are the measured transmitted light intensities at initial time, time t, and the final time of crystallization. The reproducibility of the intensity profile was obtained when the remeasurements were carried out at some crystallization temperatures. The rate constant (K) and the Avrami indexes (n) are obtained from the intercept and the slope of the Avrami plot **(b)**, respectively. Avrami index n was determined including the initial point and n' from taking the section of **(b)** corresponding to the linear range of **(a)**. The analysis of the Avrami index permits one understanding of the growth dimensions and the morphology. The half time ($t_{1/2}$), rate of crystallization (or reciprocal half time $1/t_{1/2}$ (sec^{-1})) and induction time (t_i) were estimated from **(a)**. These parameters are listed in **Table 4.2.1.1.**

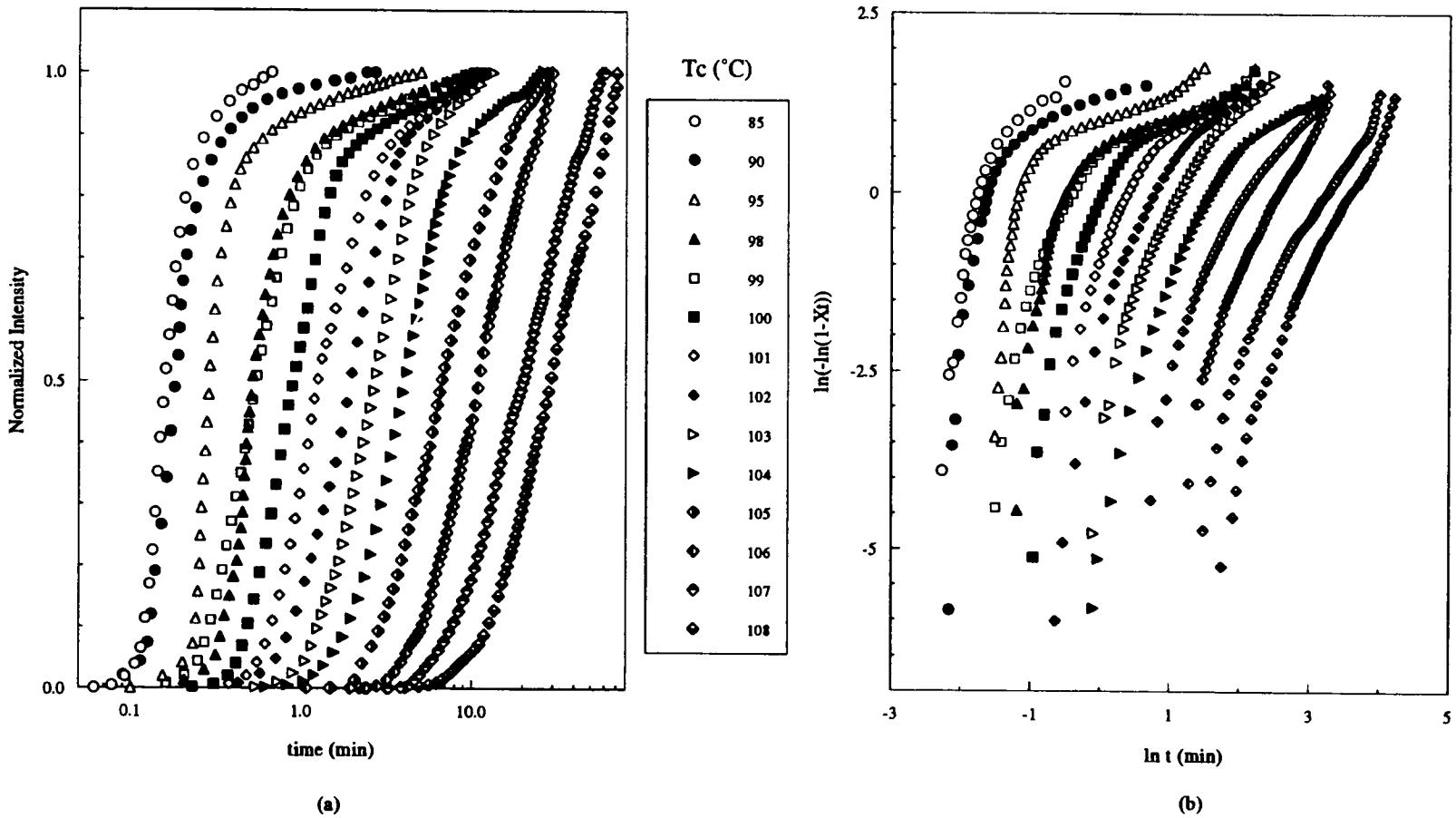


Figure 4.2.1.1. Normailzed Intensity (a) and Avrami plot (b) of L10-O at the indicated temperature.

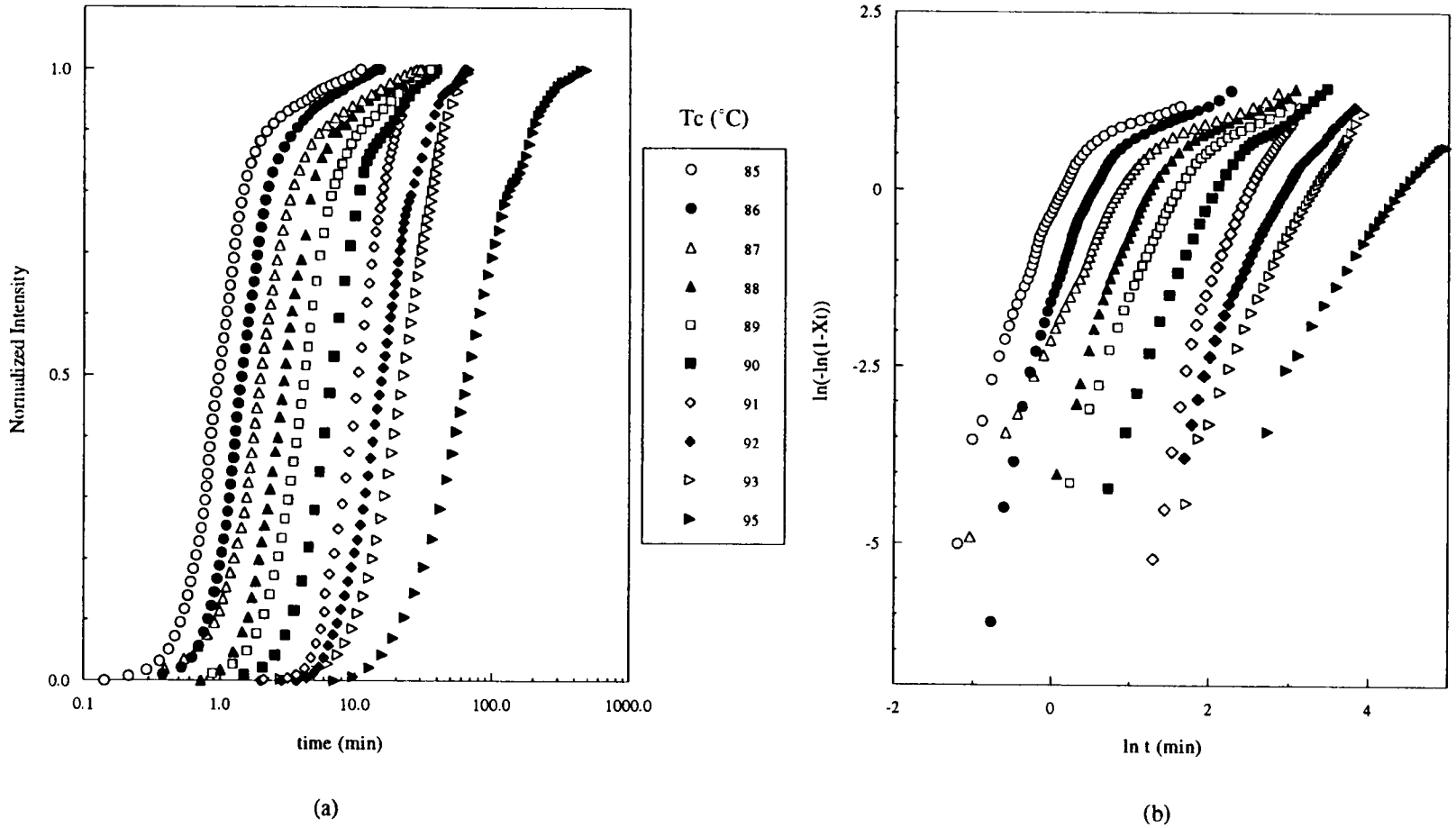


Figure 4.2.1.2. Normalized intensity (a) and Avrami plot (b) of L18-O at the indicated temperature.

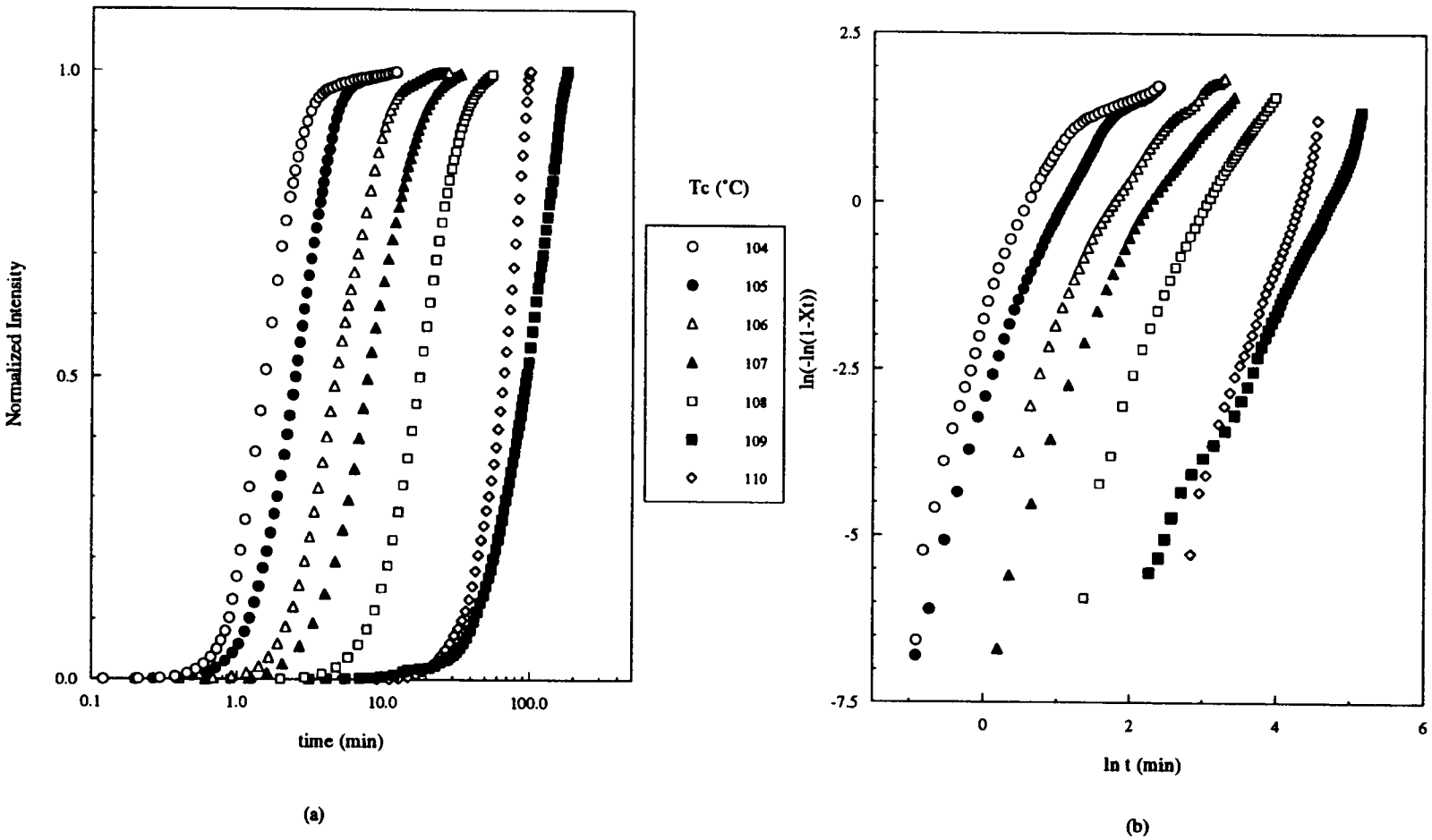


Figure 4.2.1.3. Normalized Intensity (a) and Avrami plot (b) of H7-O at the indicated temperature.

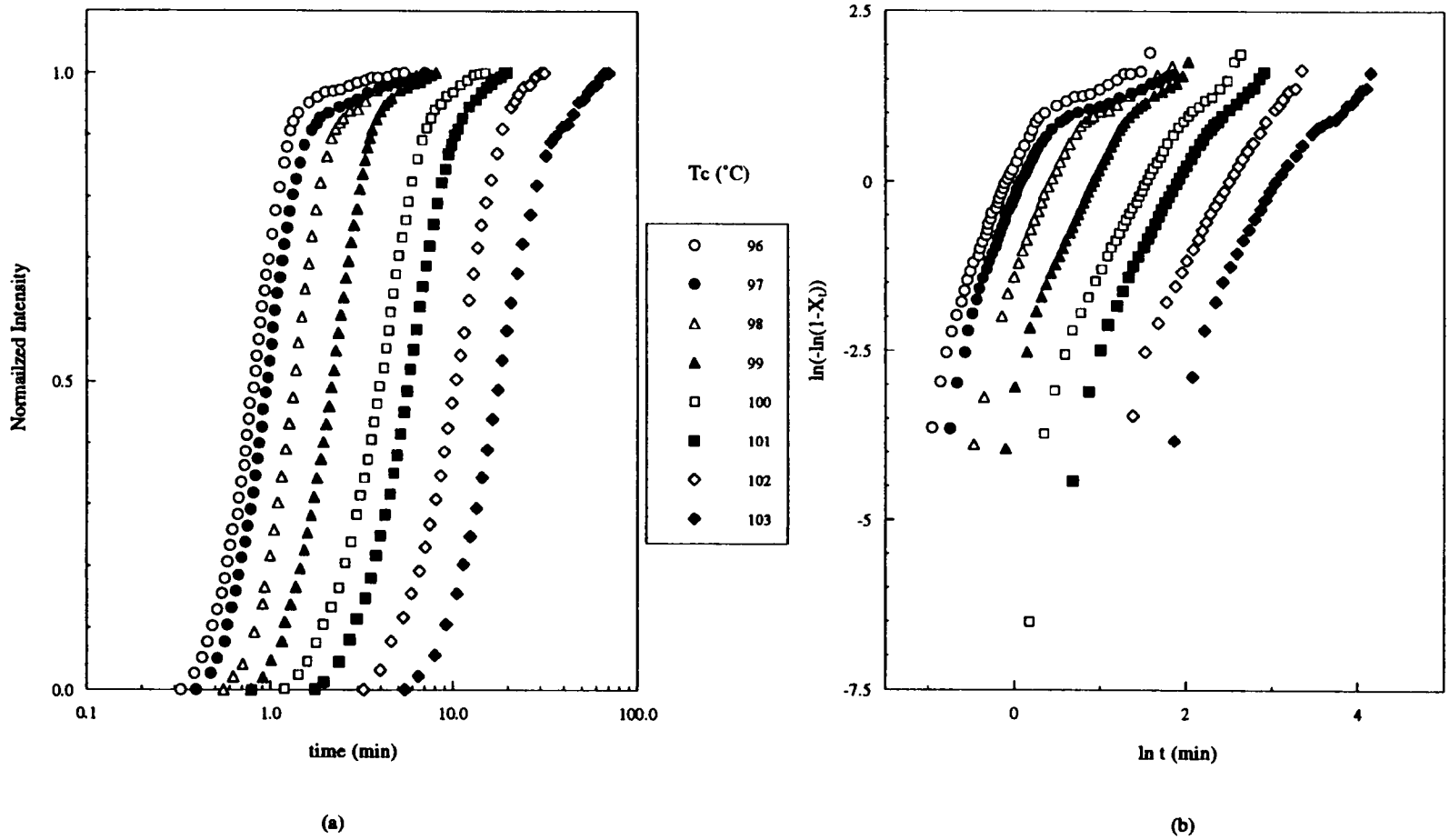


Figure 4.2.1.4. Normalized Intensity (a) and Avrami plot of H10-O at the indicated temperature.

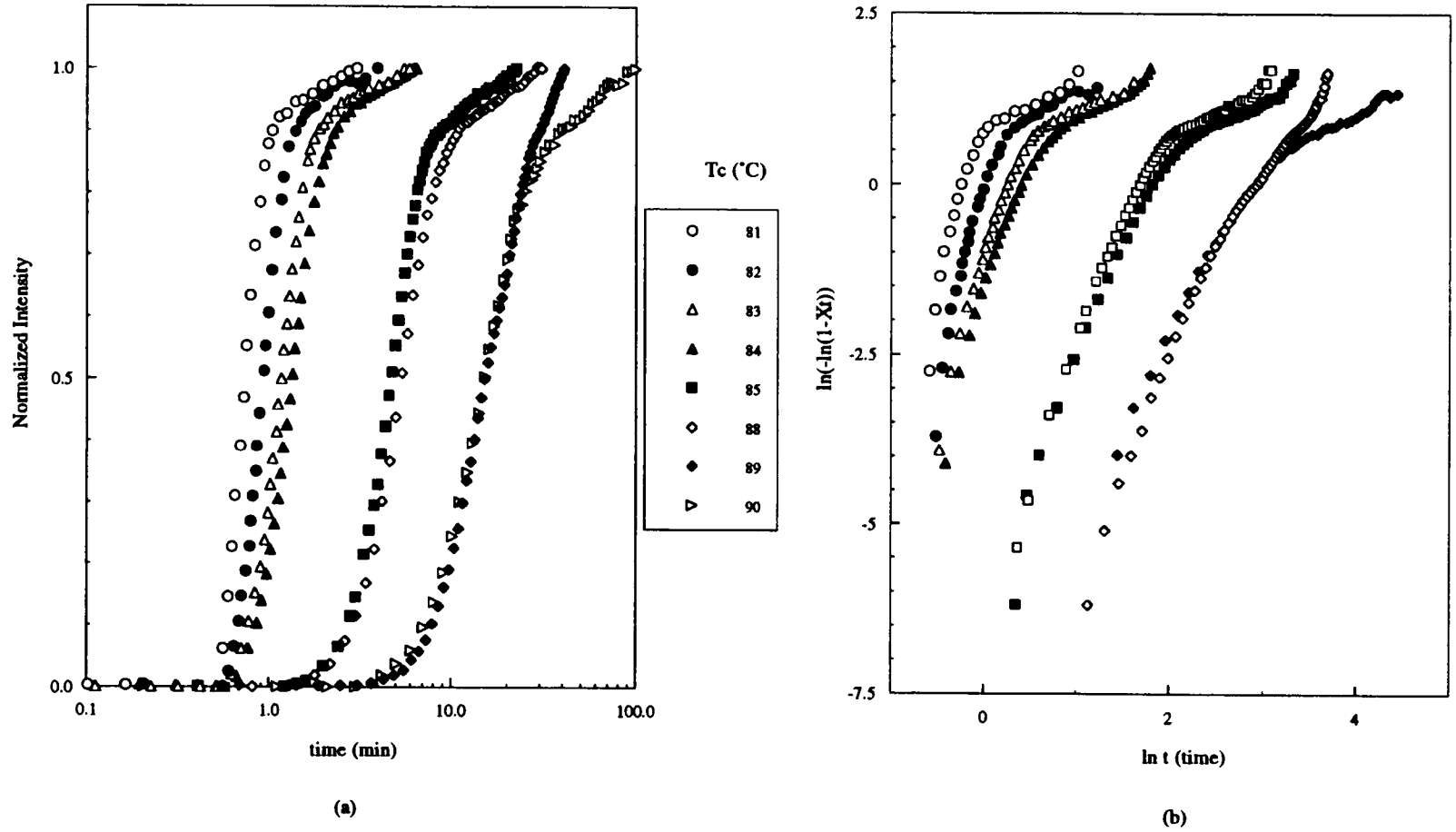


Figure 4.2.1.5 Normalized intensity (a) and Avrami plot of H16-O at the indicated temperature.

Table 4.2.1.1. Induction(t_i(sec)), half time ($t_{1/2}$(sec)) and Avrami index obtained from bulk crystallization using transmitted depolarized light intensity.

Samples	T_c(°C)	t_i(sec)	$t_{1/2}$(sec)	t_∞(min)	n	n′
L10-O	85.0	6.3	9.4	0.7	-	-
	90.0	6.9	-	2.4	-	-
	95.0	13.2	17.5	5.0	-	-
	98.0	18.1	31.0	10.0	8.6	-
	99.0	13.3	31.2	10.1	6.7	-
	100.0	23.0	52.1	11.0	6.4	2.0
	101.0	29.0	73.1	9.9	5.2	2.1
	102.0	31.5	115.9	11.0	5.4	2.0
	103.0	54.2	164.2	13.3	5.9	2.0
	104.0	54.5	244.7	26.1	5.2	2.0
	105.0	125.0	340.83	26.7	5.3	1.9
	106.0	315.9	655.54	27.6	7.6	2.1
	107.0	266.6	1203.3	26.2	5.4	2.1
	108.0	345.2	1730.5	69.7	5.3	2.0
L18-O	85.0	18.2	58.6	10.8	3.3	2.5
	86.0	27.9	86.3	14.0	3.9	2.7
	87.0	21.2	118.7	25.0	2.6	2.5
	88.0	64.4	177.0	37.4	3.2	3.4
	89.0	75.9	250.7	34.8	3.6	2.1
	90.0	124.5	401.0	38.7	3.8	2.3
	91.0	220.2	628.3	35.4	4.1	2.4
	92.0	324.7	951.4	60.0	3.8	2.1
	93.0	333.3	1357.0	66.9	3.4	2.2
	95.0	910.6	3703.1	476.6	2.8	1.6
H7-O	104.0	24.1	93.0	13.0	4.0	3.3
	105.0	24.0	146.5	12.8	4.1	2.9
	106.0	66.2	282.6	29.4	4.0	3.0
	107.0	72.6	462.1	35.5	4.0	2.9
	108.0	235.6	996.6	58.9	3.7	2.8
	109.0	418.4	5560.7	178.7	2.3	2.4
	110.0	1018.2	3890.9	97.0	3.8	3.0
H10-O	96.0	23.1	48.9	5.4	5.4	3.4
	97.0	28.4	57.5	7.0	6.1	3.5
	98.0	37.5	80.9	7.0	5.4	3.3
	99.0	54.3	131.2	8.1	5.0	3.1
	100.0	71.4	236.1	15.0	4.2	2.8
	101.0	118.5	334.9	19.8	4.7	2.6
	102.0	238.5	591.6	30.3	3.7	2.3
	103.0	386.7	1057.5	45.4	4.0	2.5
H16-O	81.0	33.3	43.9	3.0	-	5.5
	82.0	35.8	55.3	3.9	-	5.8
	83.0	37.1	70.0	5.9	6.4	5.2
	84.0	39.6	80.0	6.5	6.5	4.3
	87.0	86.1	283.0	22.4	4.8	3.6
	88.0	84.8	320.2	30.6	5.3	3.5
	89.0	185.5	905.8	40.3	4.4	3.6
	90.0	245.3	904.4	99.1	3.2	2.6

t_∞(min) ; time (sec) at the end of crystallization.

n; Avrami index including initial point.

n′ ; Avrami index obtained from the linear region except for initial point.

4.2.2. Rate of crystallization

• by reciprocal half time, $1/t_{1/2}$

The rate of crystallization was analyzed using the reciprocal half time ($1/t_{1/2}$ (sec^{-1})) as a function of temperature **(a)** and supercooling **(b)** in **Figure 4.2.2.1.** As T_c increases (i.e., supercooling decreases), the rate of crystallization decreases. As branch content increases, the rate of crystallization decreases at a fixed T_c and the crystallization rate, $1/t_{1/2}$, versus temperature curve shifts to lower temperature. There is a molecular weight dependence of the $1/t_{1/2}$ at a constant branch content. The rate of crystallization of low molecular weight L10-O is larger than that of high molecular weight H10-O. Also the highly branched low molecular weight sample, L18-O, has a higher rate of crystallization than relatively lower branched high molecular weight H16-O. Both molecular weight and branch content affect the rate of crystallization, the molecular weight effect being bigger than the branch effect.

The supercooling analysis is based on theoretical background and makes it possible to compare the rate of crystallization accurately. When the $1/t_{1/2}$s of L10-O and H7-O are compared with crystallization temperature (see **Figure 4.2.2.1 (a)**) rather than supercooling (see **Figure 4.2.2.1 (b)**), the rate of crystallization of H7-O is larger than that of L10-O. However, when $1/t_{1/2}$ is plotted against ΔT, the rate of crystallization of H7-O is smaller than that of L10-O. When the rate of crystallization is analyzed as a function of supercooling ($\Delta T = T_m^o - T_c$), the experimental result that the molecular weight effect on $1/t_{1/2}$ is larger than the effect of branch content becomes more distinct. L10-O and L18-O show higher rates of crystallization than H7-O and H16-O at a fixed ΔT.

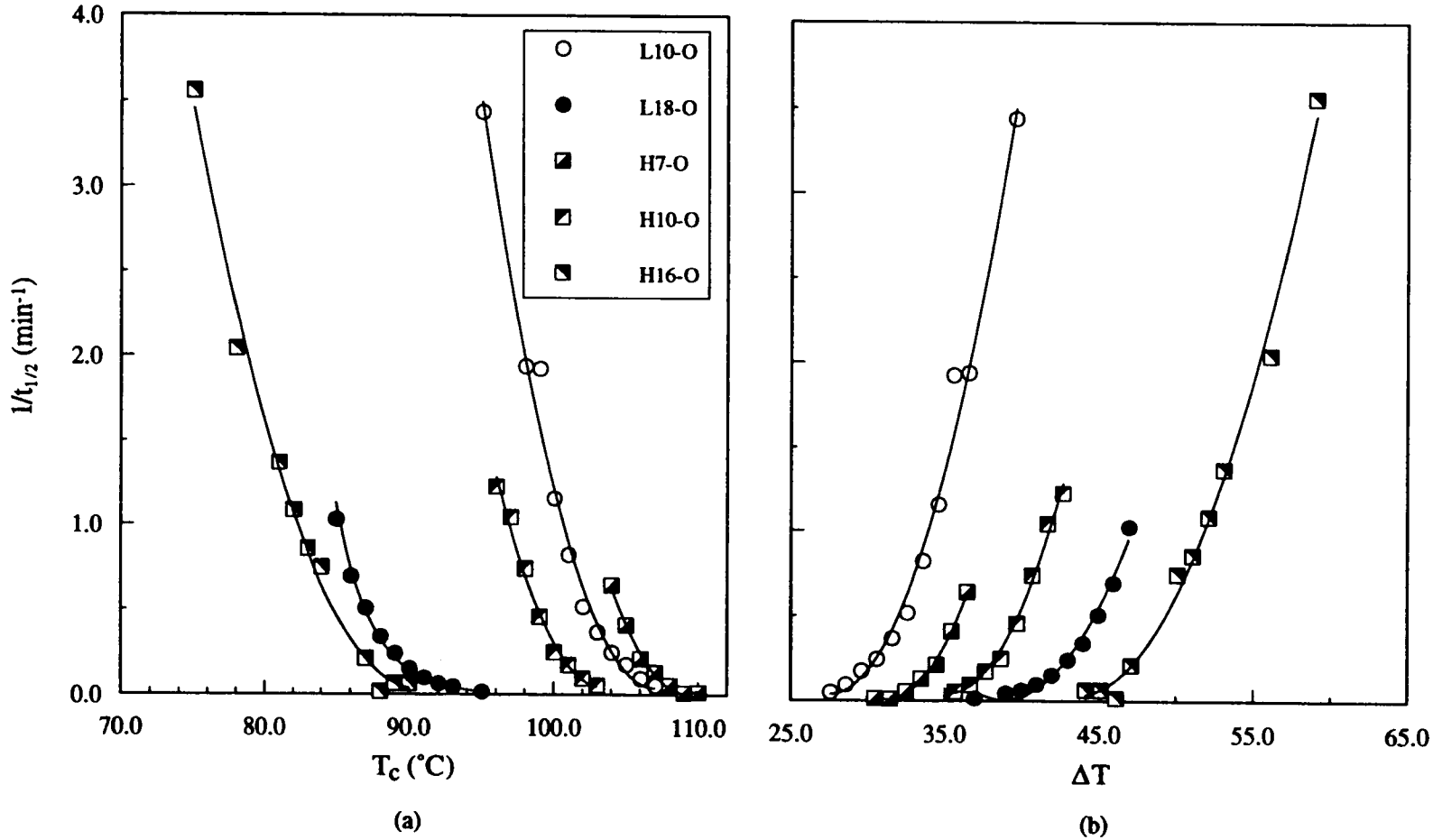


Figure 4.2.2.1. Plots of reciprocal half time (min^{-1}) as a function of crystallization temperature (a) and super cooling (b).

• by reciprocal initial time, $1/t_i$

The induction time was determined by reading a point at which the light intensity starts to increase. The reciprocal induction time can represent the rate $1/t_i$ of initial crystallization as shown in **Figure 4.2.2.2 (a)** and **(b)**. The general tendency of $1/t_i$ with T_c and ΔT and the dependence of $1/t_i$ on branch content and molecular weight are similar to that of $1/t_{1/2}$.

4.2.3. Secondary Nucleation

The crystallization regime plot of EO copolymer is obtained from **equation(2.4.5)** and **(2.4.6)**. The input values were $U^* = 1500\ cal/mole$ and $T_\infty = T_g - 30K$, where T_g of polyethylene was tested using $-40\,^{\circ}C$ [44] and $-125\,^{\circ}C$[52]. The equilibrium melting temperatures for the copolymers were obtained in this study and the method and values will be reviewed in a later chapter.

4.3. Equilibrium Melting Temperature (T_m^o)

To obtain the equilibrium melting temperatures (T_m^o) of linear polyethylenes and EO copolymers as a function of molecular weight and branch content, the extrapolation techniques such as the Hoffman-Weeks plot and the Thompson-Gibbs plot are applied in this study.

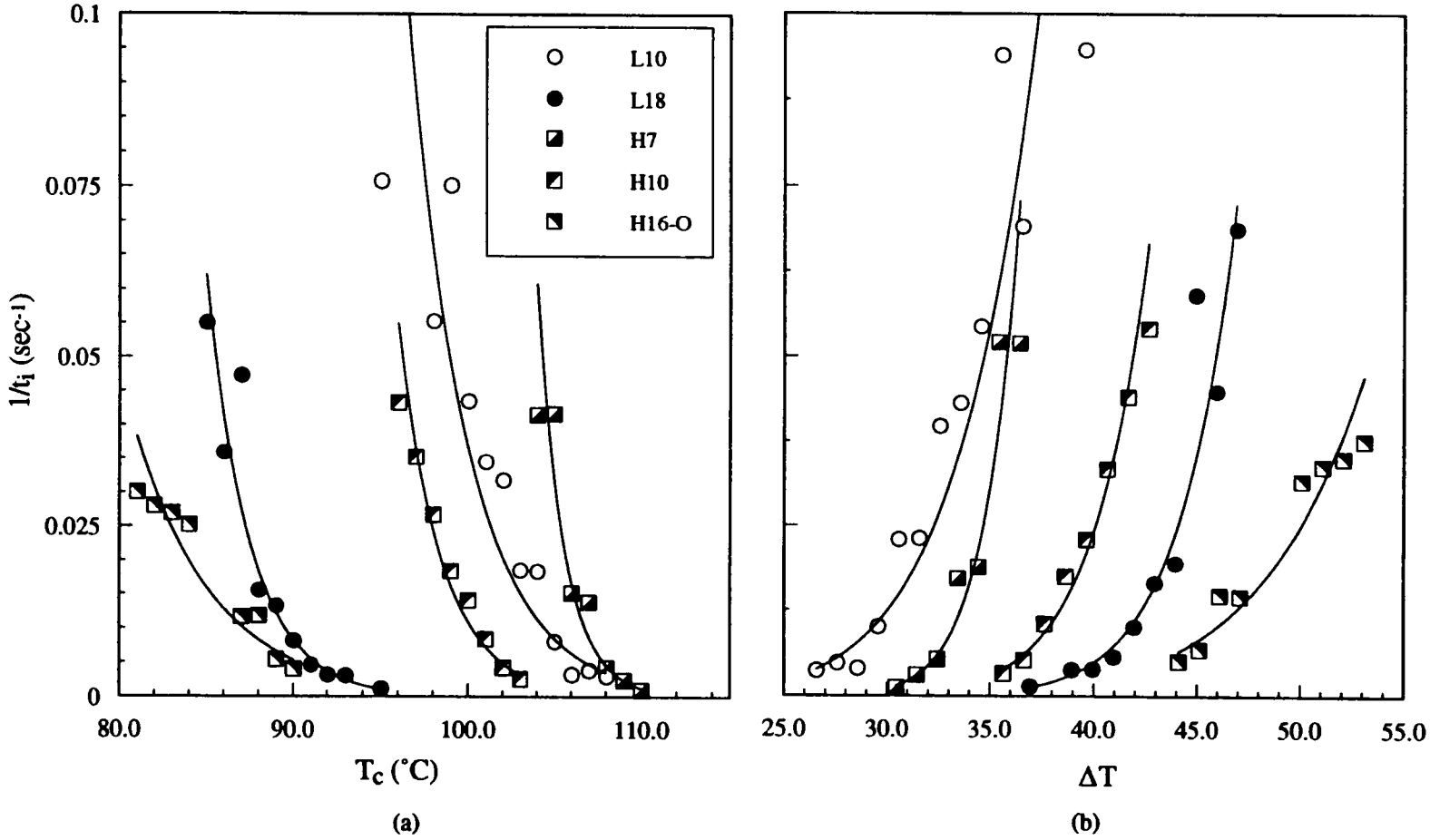


Figure 4.2.2.2. Plots of reciprocal initial time(sec^{-1}) as a function of crystallization temperature (a) and supercooling (b).

4.3.1. Hoffman-Weeks Plots

Peak melting temperatures of EO copolymers were plotted against the crystallization temperature in **Figure 4.3.1.1** for high molecular weight copolymers and **Figure 4.3.1.2** for low molecular weight copolymers. The weight average crystallinity was obtained from the heat of fusion of DSC under the same condition with the hot stage. The plots of T_m versus T_c for the EO copolymers show the clear curvature. In order to get T_m^o, the intercept was obtained by taking the low supercooling region, at which most weight crystallinity was less than 1.0%. The labeled values indicate the crystallization time and the weight crystallinity, which were obtained from DSC. The interception points for high molecular weight samples decrease with the branch content in such a following way H7(157.6 ^oC) > H10(128.8 ^oC) > H16(120.7 ^oC) while the intercept for low molecular weight L10 is 152.5 ^oC. L18-O shows the parallel relation between the melting temperature and the crystallization temperature, $T_m = T_c + const.$

4.3.2. Thompson-Gibbs Plots

The melting temperatures, T_ms, as a function of the number average lamellar thickness, l, were plotted in **Figure 4.3.2.1** for linear polyethylenes of medium (M-LPE) and high molecular weight (H-LPE) , **Figure 4.3.2.2** for EO copolymers of high molecular weight, and **Figure 4.3.2.3** for EO copolymer of low molecular weight. The numerical values for **Figures 4.3.2.1 ~4.3.2.3** are listed in **Table 4.3.2.1.** (Comment : When generating the above **Figures** using the values in **Table 4.3.2.1**, if the same T_m^os with the reported values in this study can not be obtained, it is due to the round-off error). The melting temperature was obtained from the peak temperature of DSC with a heating rate

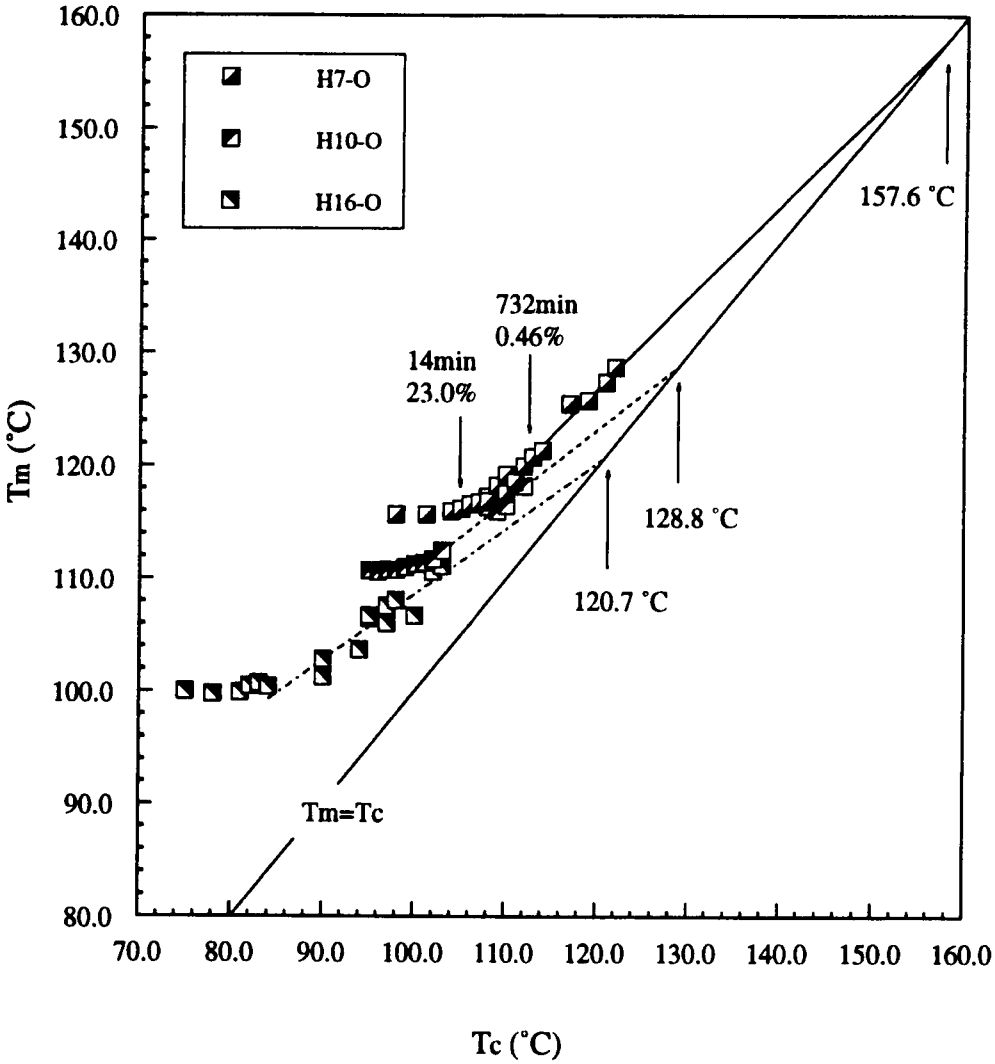


Figure 4.3.1.1. Plot of melting temperatures against crystallization temperatures for the ethylene/1-octene random copolymers of high molecular weight. Labeled numbers are the crystallization time and the weight crystallinity.

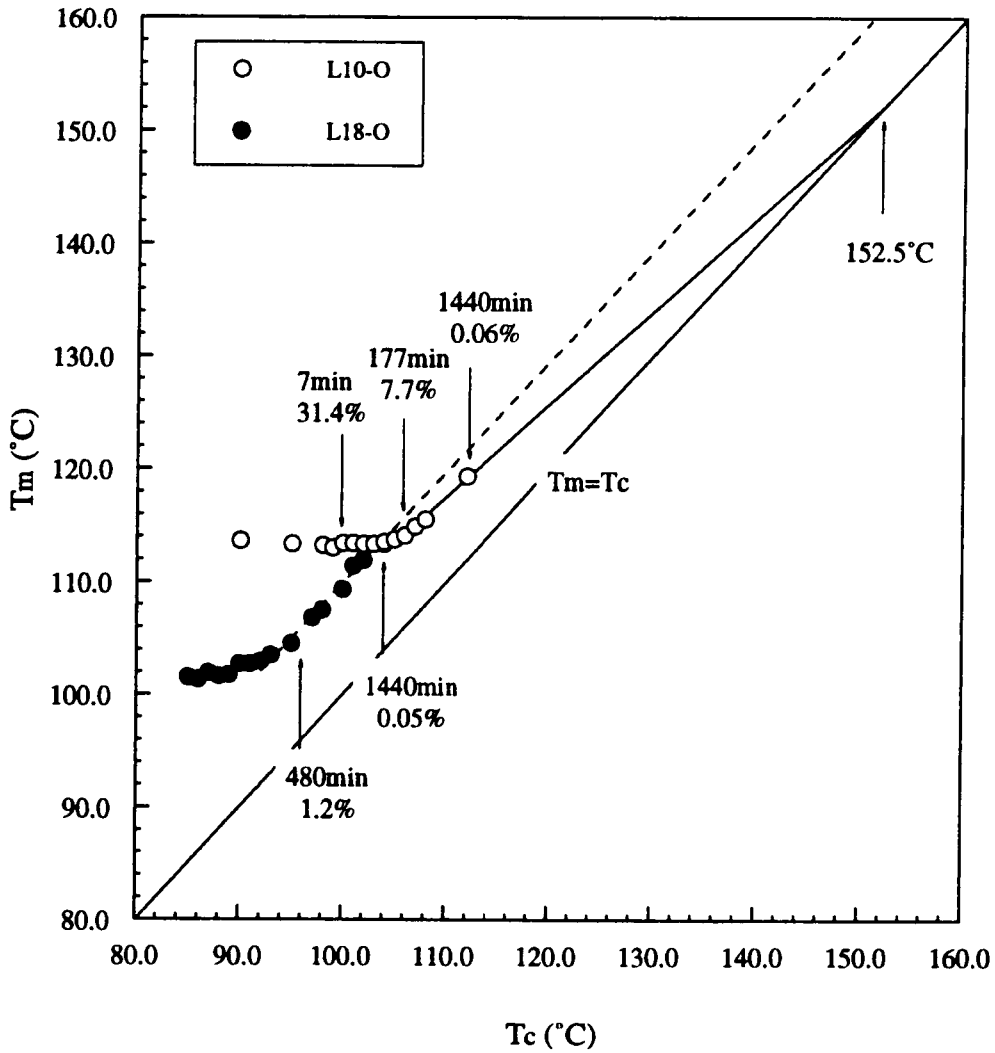


Figure 4.3.1.2. Plot of melting temperatures against crystallization temperatures for the ethylene/1-octene random copolymers of low molecular weight. Labeled numbers are the crystallization time and the weight crystallinity.

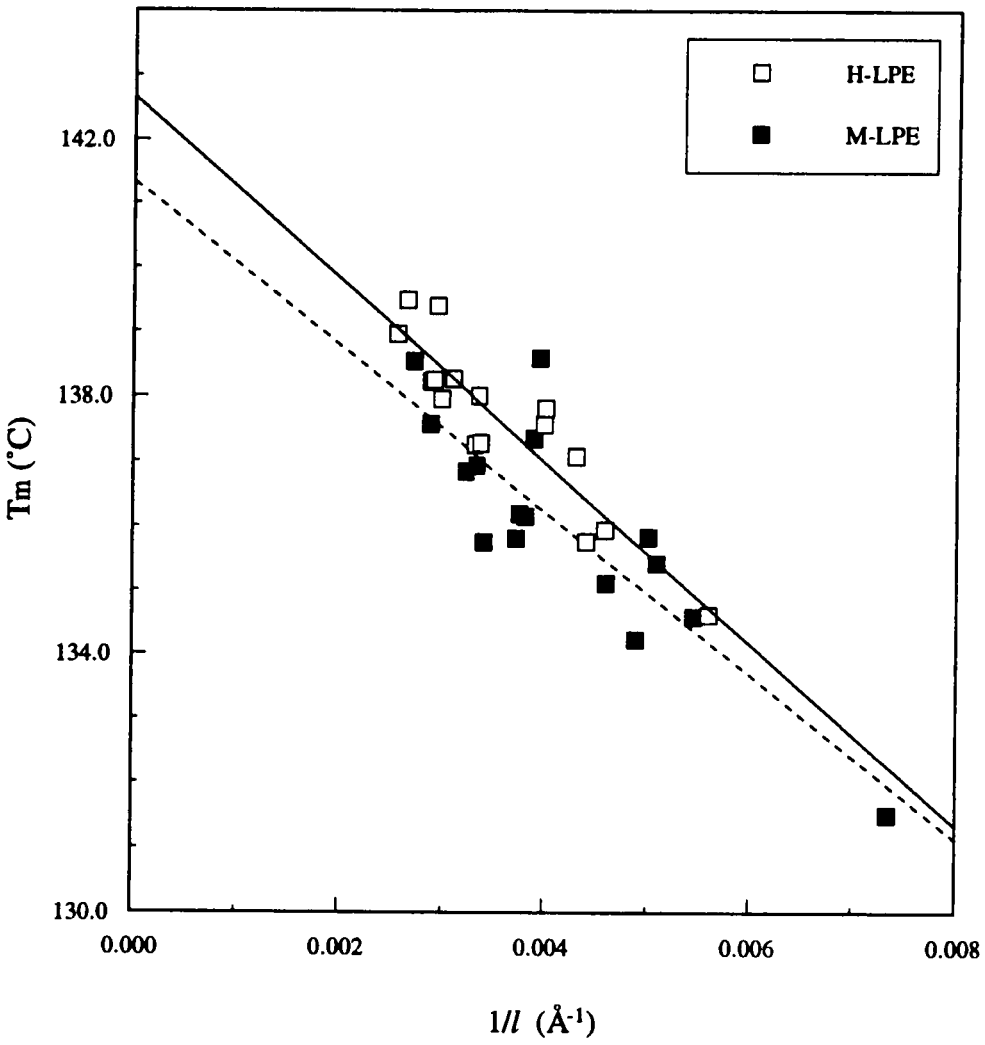


Figure 4.3.2.1. Peak melting temperature(°C) against reciprocal lamellar thickness($Å^{-1}$) for linear polyethylene of high and medium molecular weight.

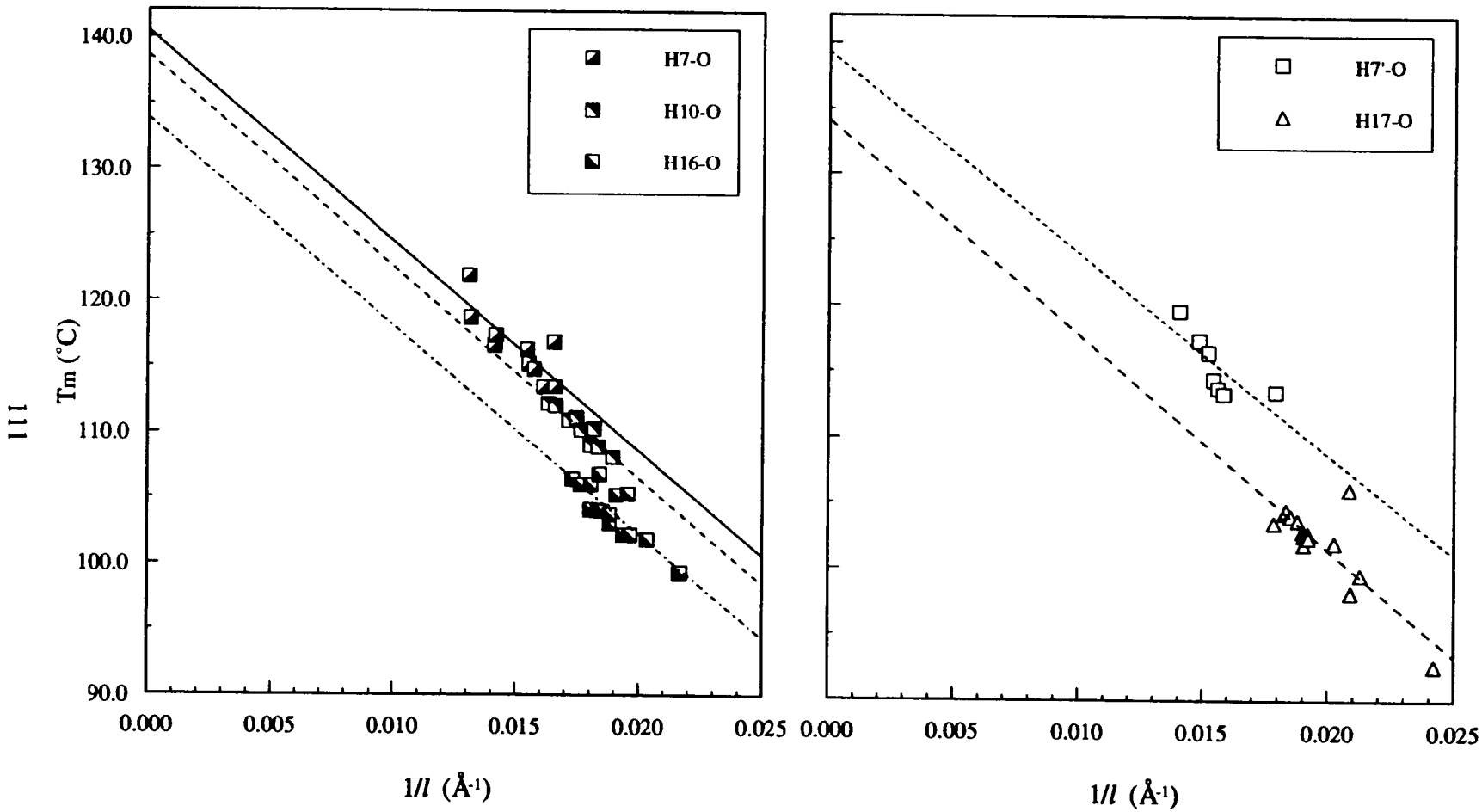


Figure 4.3.2.2. Peak melting temperature(°C) against reciprocal lamellar thickness($Å^{-1}$) of high molecular weight EO copolymers.

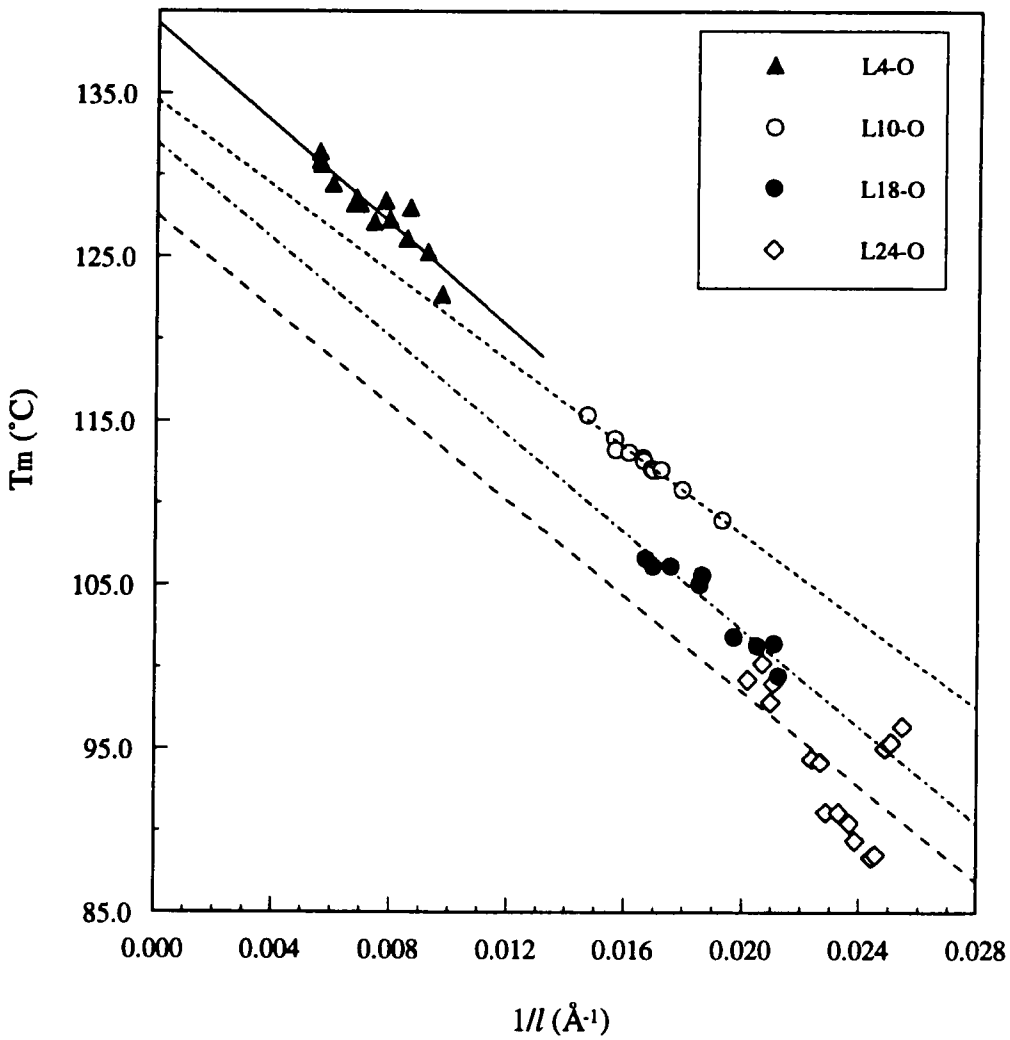


Figure 4.3.2.3. Peak melting temperature(°C) against reciprocal lamellar thickness($Å^{-1}$) for low molecular weight EO copolymers.

Table 4.3.2.1. Peak melting temperatures and lamellar thicknesses of LPE and EO copolymers.

Code	Tc (°C)	t_c (day)	T_m(°C)	v_c(%) [a]	L (Å)	l (Å)
H-LPE [b]	quenched [a]	quenched [a]	134.6	66.0	270.8	178.6
	100	1	135.9	71.1	306.4	217.9
	113	1	135.8	71.3	318.2	226.8
	115	1	137.1	71.9	322.9	232.1
	118	28	138.0	83.1	259.1	298.2
	118	38	137.8	69.6	358.4	249.6
	118	48	139.4	82.9	410.1	339.9
	120	38	138.2	84.8	355.9	343.6
	120	48	138.2	90.4	358.4	347.2
	121	28	137.3	92.1	377.1	301.7
	123	28	137.3	76.7	349.8	296.6
	125	28	137.6	71.9	348.0	250.1
	125	38	138.0	86.6	386.8	335.0
	127	4	138.3	85.9	375.7	322.8
	130	6	139.5	88.8	426.4	378.4
	130	17	139.0	92.7	423.1	392.0
M-HPE [b]	quenched [a]	quenched [a]	131.5	59.6	228.5	136.2
	100	1	134.6	66.3	276.5	183.4
	113	1	135.4	68.9	285.2	196.5
	115	1	135.8	69.6	287.0	199.7
	118	28	136.2	80.6	325.6	262.3
	118	38	135.1	70.0	310.4	217.2
	118	48	136.2	76.9	346.2	266.1
	125	48	137.3	85.2	315.1	256.8
	120	4	135.8	81.9	309.3	268.5
	130	3	135.8	88.1	340.5	293.4
	130	6	137.6	64.3	318.1	347.4
	130	17	138.5	76.4	336.0	368.7
	120	28	138.6	78.4	395.3	253.2
	120	38	136.9	89.7	327.1	300.1
	123	38	134.2	90.0	385.8	204.5
	127	10	136.9	89.3	413.1	310.0

Table 4.3.2.1. (continued)

Code	Tc (°C)	t_c (day)	T_m(°C)	v_c(%) [a]	L (Å)	l (Å)
	quenched [a]	quenched [a]	122.7	62.8	164.3	103.1
	100	1	125.3	56.4	192.5	108.7
	113	1	126.1	57.4	205.1	117.8
	115	1	128.0	57.3	203.1	116.2
	118	28	129.4	64.6	258.7	167.2
	118	38	128.6	61.8	239.0	147.6
	118	48	127.1	61.8	219.4	135.5
L4-O [b]	120	4	128.2	60.0	242.1	145.3
	120	38	130.7	62.5	287.1	179.4
	120	48	130.9	63.2	286.0	180.8
	123	28	131.4	60.4	299.1	180.7
	123	38	128.2	63.0	236.9	149.4
	123	48	127.3	60.5	208.7	126.3
	125	28	128.4	57.6	223.7	128.8

a) Quenched in room temperature
b) Intensity of SAXS was measured at room temperature and lamellar thickness was obtained from $l = L \times v_c$.

Table 4.3.2.1. (continued)

Code	Tc (°C)	t_c (day)	T_m(°C)	l (Å)
H7-O [c]	102	1	113.5	60.3
	104	1	113.5	62.0
	106	1	114.8	63.6
	108	1	115.2	64.5
	113	1	116.8	60.5
	113	2	116.6	70.8
	113	5	116.3	64.8
	113	10	117.3	70.5
	113	49	118.7	76.1
	113	63	121.9	76.4
H7'-O [c]	102	1	113.3	63.1
	104	1	113.5	55.9
	106	1	114.4	64.8
	108	1	113.8	64.1
	112	1	116.5	65.7
	114	3	117.3	67.3
	115.6	3	119.6	71.2
H10-O [c]	98	1	108.1	52.8
	102	1	108.8	-
	104	1	108.9	54.5
	105	1	109.0	55.6
	105	2	110.2	56.7
	105	3	110.9	58.3
	105	5	111.5	-
	105	10	111.1	57.4
	105	7	112.0	60.3
	105	9	112.2	61.2
	106	1	110.3	55.1

Table 4.3.2.1. (continued)

Code	Tc (°C)	t_c (day)	T_m(°C)	l (Å)
H16-O [c]	94	1	99.3	46.2
	96 (94)[a]	1	99.3	46.2
	98	10	103.7	53.2
	98	25	104.0	54.1
	98 (97)	28	104.0	54.6
	98 (96)	34	104.1	55.5
	100	2	103.1	53.2
	100	3	105.3	51.2
	100	5	105.2	52.5
	100	10	106.0	55.4
	100	49	106.4	57.9
	100	63	106.0	56.8
	102	1	106.8	54.4
	102 (96)	5	101.8	49.2
	102 (95)	14	102.2	51.6
	102 (95)	27	102.2	50.9
H17-O [c]	94 (93)	1	98.2	47.9
	96 (95)	1	99.6	47.0
	98 (?)	1	92.7	41.3
	98	10	104.0	54.0
	98(96.4)	25	103.7	53.2
	98(97)	2	104.3	54.7
	98(97)	34	104.5	54.5
	98(95.7)	38	103.5	56.0
	102	1	106.0	48.0
	102(97)	5	102.6	52.5
	102(94)	12	101.9	52.5
	102(95)	14	102.4	52.0
	102(94)	21	102.7	52.1
	102(95)	27	102.9	52.7
	104(98)	1	102.0	49.4

Table 4.3.2.1. (continued)

Code	Tc (°C)	t_c (day)	T_m(°C)	l (Å)
L10-O [c]	100	7.5 min	109.0	51.9
	100	1	110.9	55.8
	100	2	112.1	58.1
	100	5	112.0	59.1
	100	28	113.3	64.0
	100	63	113.9	64.0
	102	1	112.1	59.3
	106	1	113.1	62.1
	110	1	112.6	60.2
	110	11	112.8	60.3
	110	63	115.4	68.1
L18-O [c]	98 (97)	1	101.9	50.8
	100	1	105.1	54.0
	100	5	106.2	57.0
	100	21	106.2	59.0
	100	63	106.6	59.9
	97 (92)	7	101.5	47.5
	97 (89.2)	27	101.4	48.8
	97 (94.2)	45	99.5	47.1
	102	1	105.6	53.7
L24-O [c]	78	2	95.4	39.9
	78	3	95.1	40.2
	80	3	88.5	40.7
	80	5	88.4	41.0
	87 (84.1)	4	91.1	42.9
	87 (84.1)	5	90.5	42.3
	87 (84)	7	91.1	43.8
	90 (83.5)	1	89.4	41.9
	90	2	94.2	44.1
	92 (88.7)	2	94.4	44.7
	96 (91.6)	1	96.4	39.3
	97 (94.1)	1	97.9	47.7
	97 (92.8)	7	99.3	49.6
	97	21	100.3	48.4
	97 (95)	45	99.0	47.5

c) Intensity of SAXS was measured at T_c or peak separating point. The values in parentheses are the separating point around T_c of DSC thermogram. The inconsistency between T_c and separating point of DSC may be due to the experimental error from handling sample and oil bath temperature or the insufficient time for segregation of peaks. Lamellar thickness was determined from the self-triangle zone with corrected base line in the case of base line missing. This method will be mentioned in later section.

10 °C/min, assuming to correspond to the average lamellar thickness. The lamellar thicknesses were estimated from the 1-dimensional correlation function analysis of the SAXS intensity profile. The detail description of this method will be mentioned in the section of SAXS study. In the Thompson-Gibbs plots, T_m versus $1/l$, an intersection at which the reciprocal lamellar thickness goes to zero in the case of the infinite lamellar thickness was determined as an equilibrium melting temperature, T_m^o.

For linear polyethylenes, the intersection of high molecular weight is higher than that of medium molecular weight (see **Figure 4.3.2.1**). For EO copolymers of high and low molecular weight, the intersections shift down with increasing branch content in the system.

4.4. Morphology Study using SAXS.

4.4.1. Intensity Measured at Ambient and Crystallization Temperature.

4.4.1.1. Quenched Samples

SAXS profiles observed from 5m geometry, which measured at room temperature, of samples quenched to ambient temperature are shown in **Figure 4.4.1.1**. SAXS profiles of linear polyethylene (H-LPE) of high molecular weight show the strongest Bragg peak (the first maximum) at the lowest scattering vector, q while that of medium molecular weight linear polyethylene (M-LPE) shows the second strong peak at second low q. As branch content increases the intensity decreases and the first maximum migrates toward

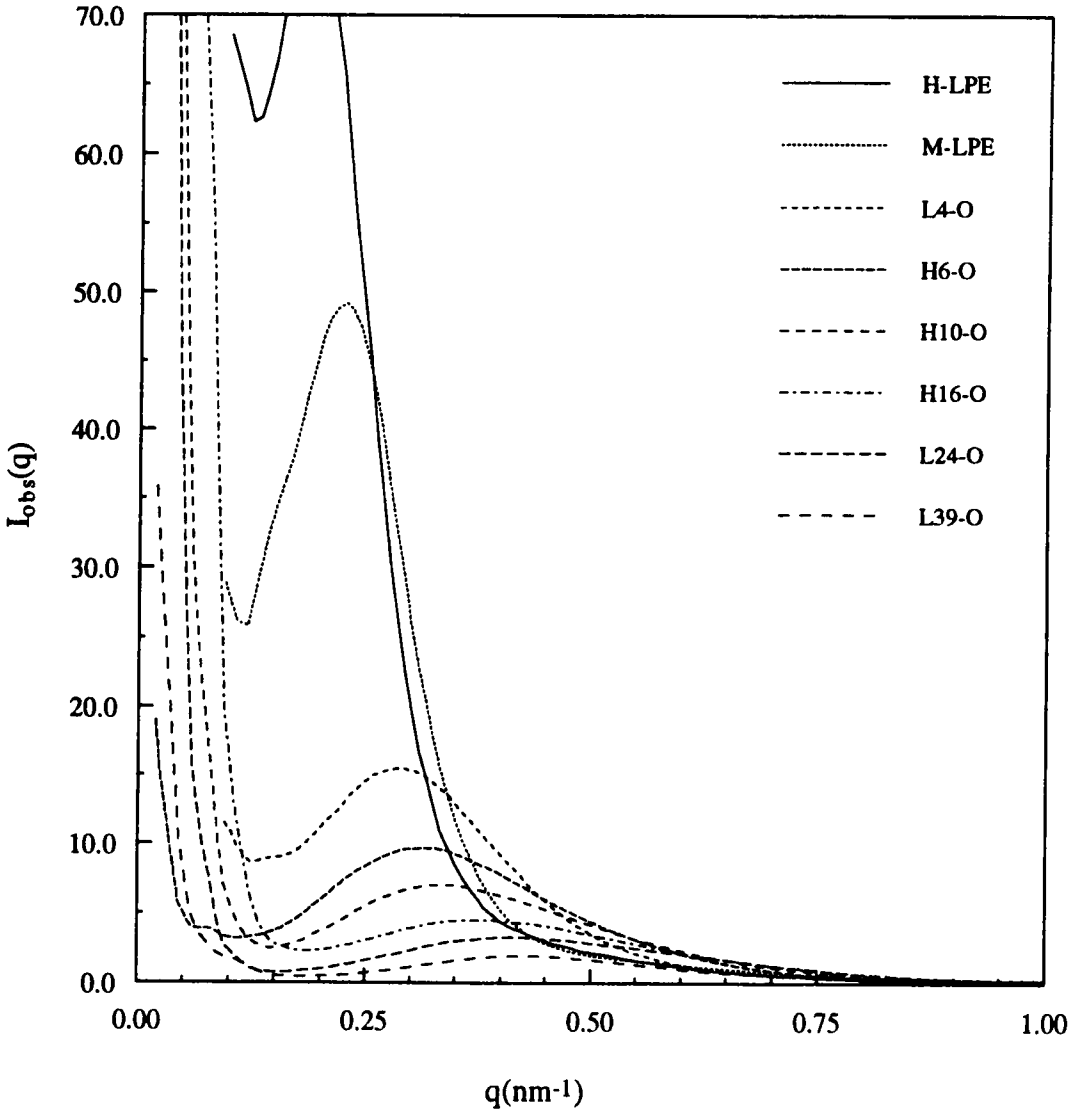


Figure 4.4.1.1. SXAS intensity profiles for the quenched LPE and EO copolymers.

high $q(nm^{-1})$. Even low branch levels (e.g., L4-O) cause the intensity to decrease to 5 times lower than that of H-LPE and about 3 times lower than that of M-LPE. As branch content increases further there is a reversal of the first maximum peak between L24-O and L39-O while the tendency of the intensity change is consistence with other samples. A comparison of SAXS behavior for L24-O and L39-O will be discussed in later. All the samples quenched to ambient temperature show the first maximum in the SAXS intensity profiles. Lorentz corrected intensity profiles for the quenched LPE and EO copolymers are shown in **Figure 4.4.1.2**.

4.4.1.2. Measured at Crystallization Temperatures

The intensity of SAXS measured at the crystallization temperatures is represented in **Figure 4.4.1.3**. The crystallization temperature corresponding to each melting temperature was given in **Table 4.3.2.1**. As melting temperature increases, the first maximum peak shifts to low scattering vector and the intensity increases. The intensity profile of H6-O($T_c = 113\ ^{\circ}C$, $t_c = 49$days) with highest melting temperature does not show a clear first maximum peak. However, when the Lorentz plot is constructed, the peak appears clearly as shown in **Figure 4.4.1.4**. A question is why the samples with same melting temperature have different peak positions. This behavior will be discussed in a later section.

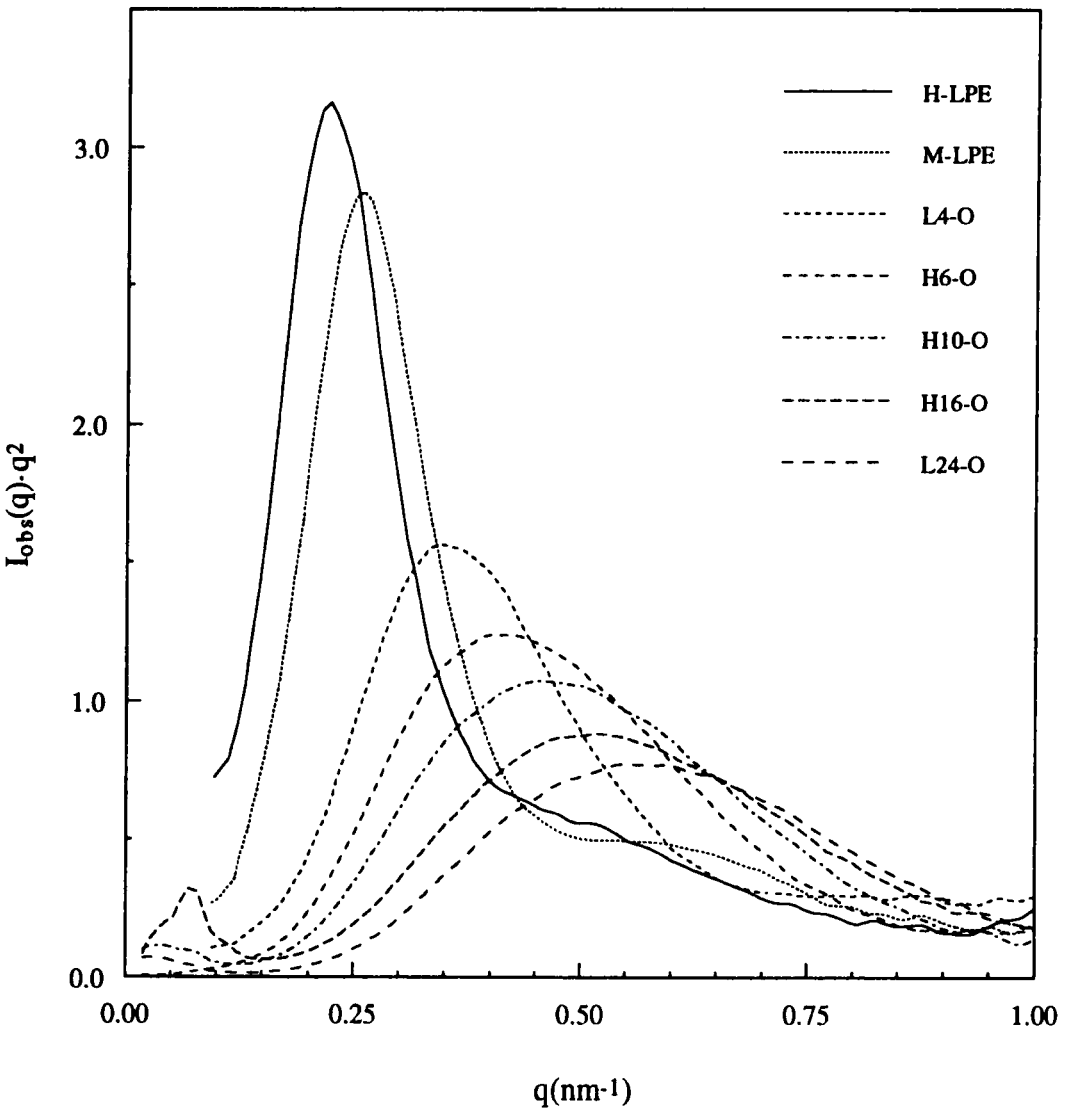


Figure 4.4.1.2. Lorentz corrected SAXS intensity profiles for quenched LPE and EO copolymers.

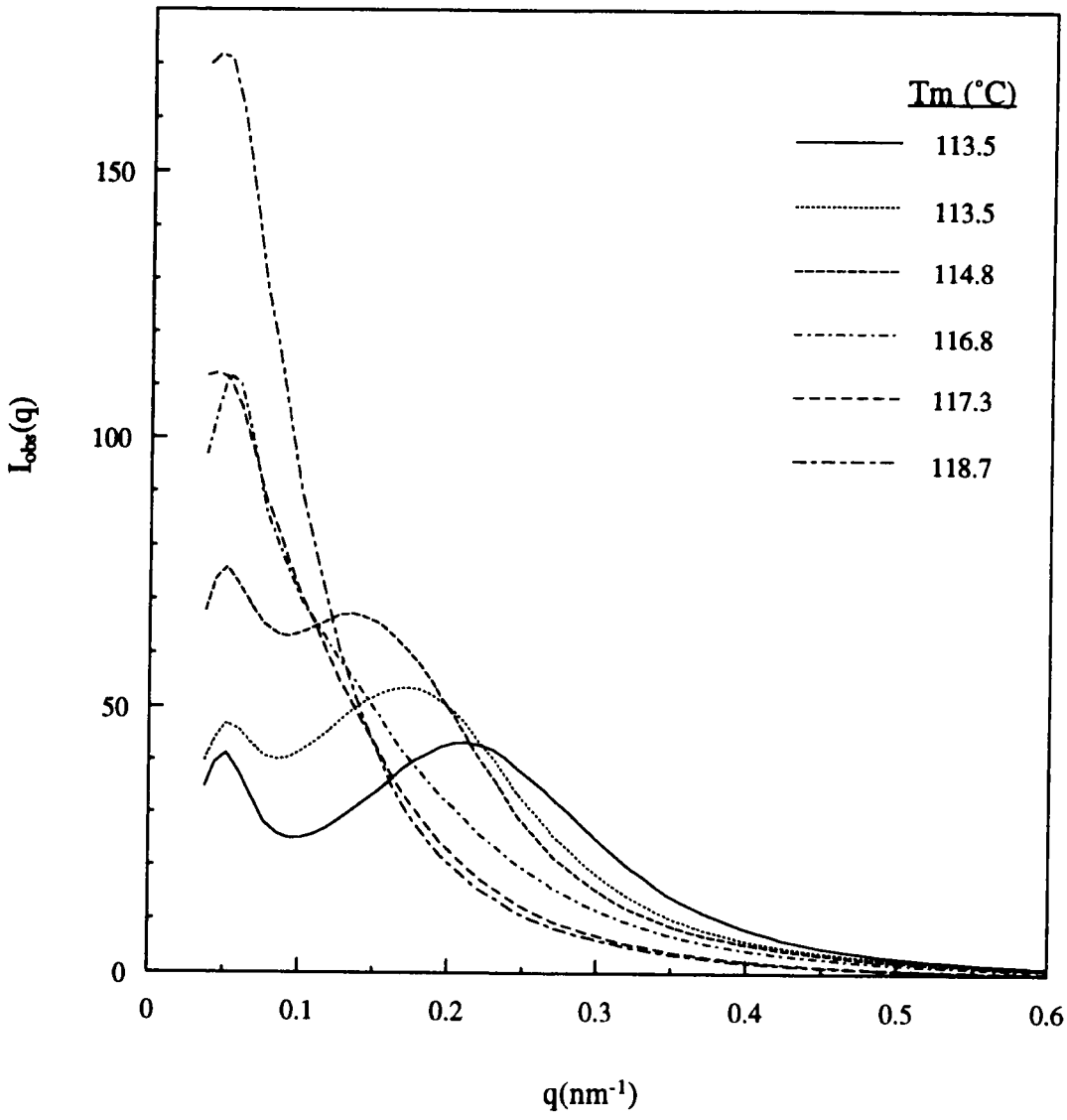


Figure 4.4.1.3. SAXS intensity profiles for H6-O with different melting temperatures.

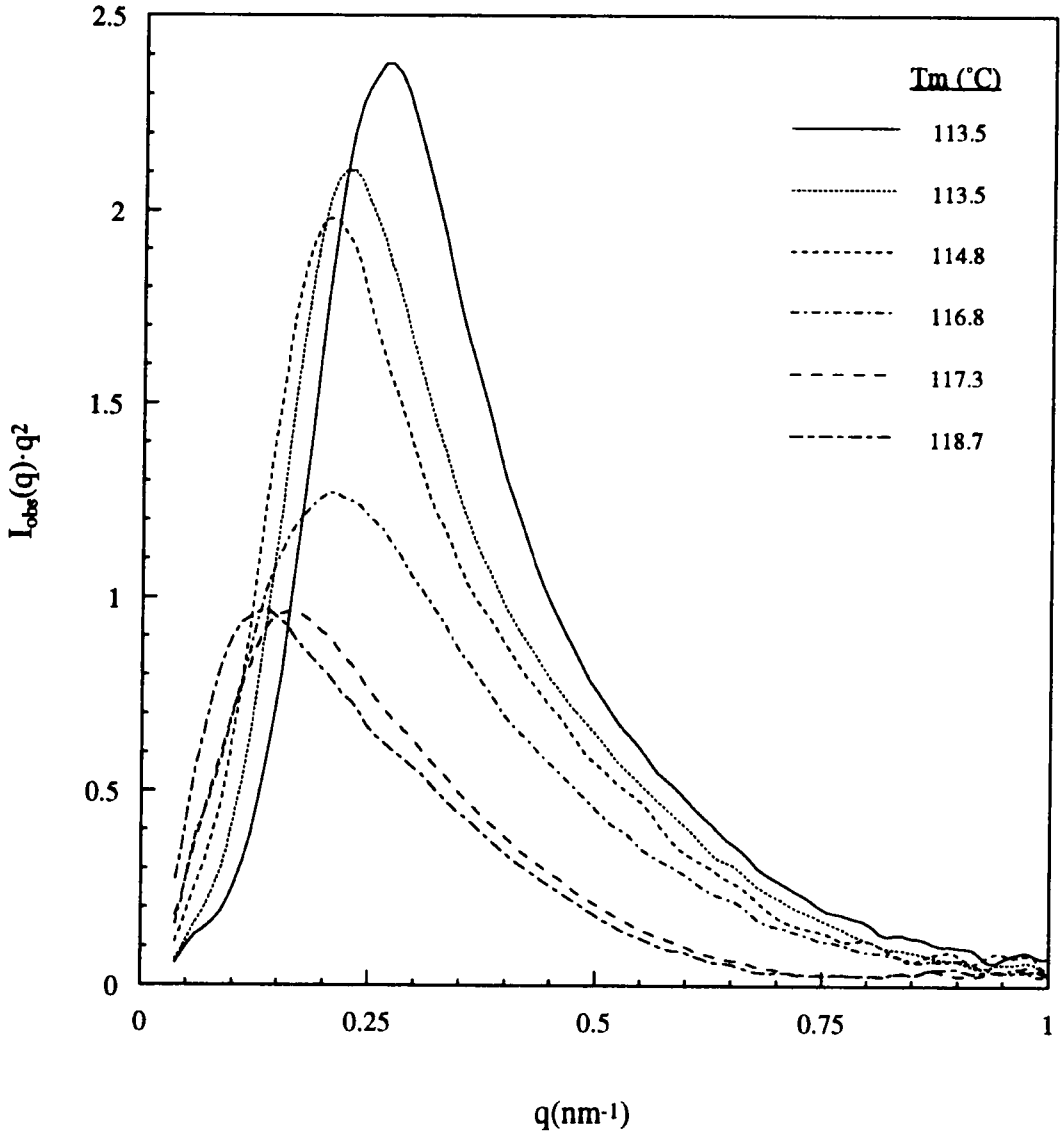


Figure 4.4.1.4. Lorentz corrected SAXS intensity profiles for H6-O with different melting temperatures.

4.4.1.3. Temperature Effect on SAXS Intensity for Linear Polyethylene.

The SAXS intensities were measured at different temperature for the sample of linear polyethylene crystallized at 130 °C for 17 days. The observed intensity and Lorentz corrected intensity profiles are shown in **Figure 4.4.1.5** and **Figure 4.4.1.6**. As measuring temperature increases, the intensity increases and first maximum ($q_{1\,max}$) is almost constant. **Figure 4.4.1.6** shows the second peak (q_2) as a shape of shoulder. The ratio of both peaks is about $q_{1\,max}/q_2 = 1.9$.

4.4.2. Tail Region Effect on SAXS analysis

The measured intensity of most samples does not reach zero intensity in the high q region when it is measured in the range of $q(nm^{-1}) \approx 0.04 \sim 1.06$ using the 5m geometry. An example is shown in **Figure 4.4.2.1**. The observed intensity (solid line) from 5m geometry is above zero intensity. Although this tail region intensity behavior is not related to the Bragg peak shown in **Figure 4.4.2.1**, it is required to obtain the intensity profile of tail region around and beyond $q(\mathrm{nm}^{-1}) = 1.0$ in order to understand the background intensity behavior. For this purpose, the tail region intensity profile was obtained from the range of $q(nm^{-1}) = 0.92 \sim 4.90$ using the 1m geometry. The combined total intensity profiles from 5m and 1m show that both intensities are exactly on the same intensity profiles around $q(nm^{-1}) \approx 0.6 \sim 1.0$ and the intensity beyond $q(\mathrm{nm}^{-1}) = 1.0$ decreases continuously. Also 5m geometry can cover the Bragg region with high resolution while 1m geometry does not cover this region for L39-O quenched in air. Since other samples used in this study have the first maximum lower than that of L39-O (see

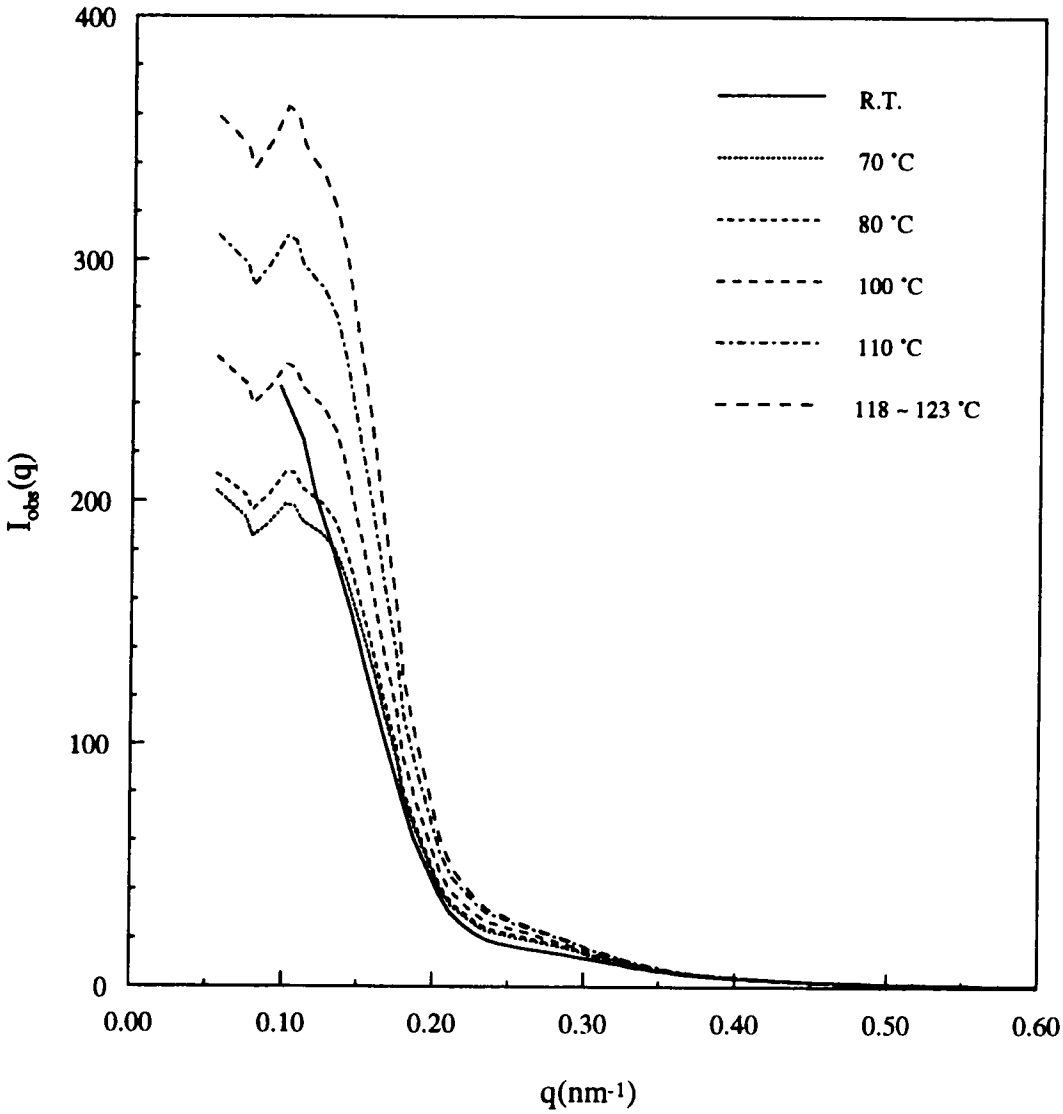


Figure 4.4.1.5. SAXS intensity profiles for H-LPE (Tc = 130 °C, t_c = 17days) measured at different temperatures.

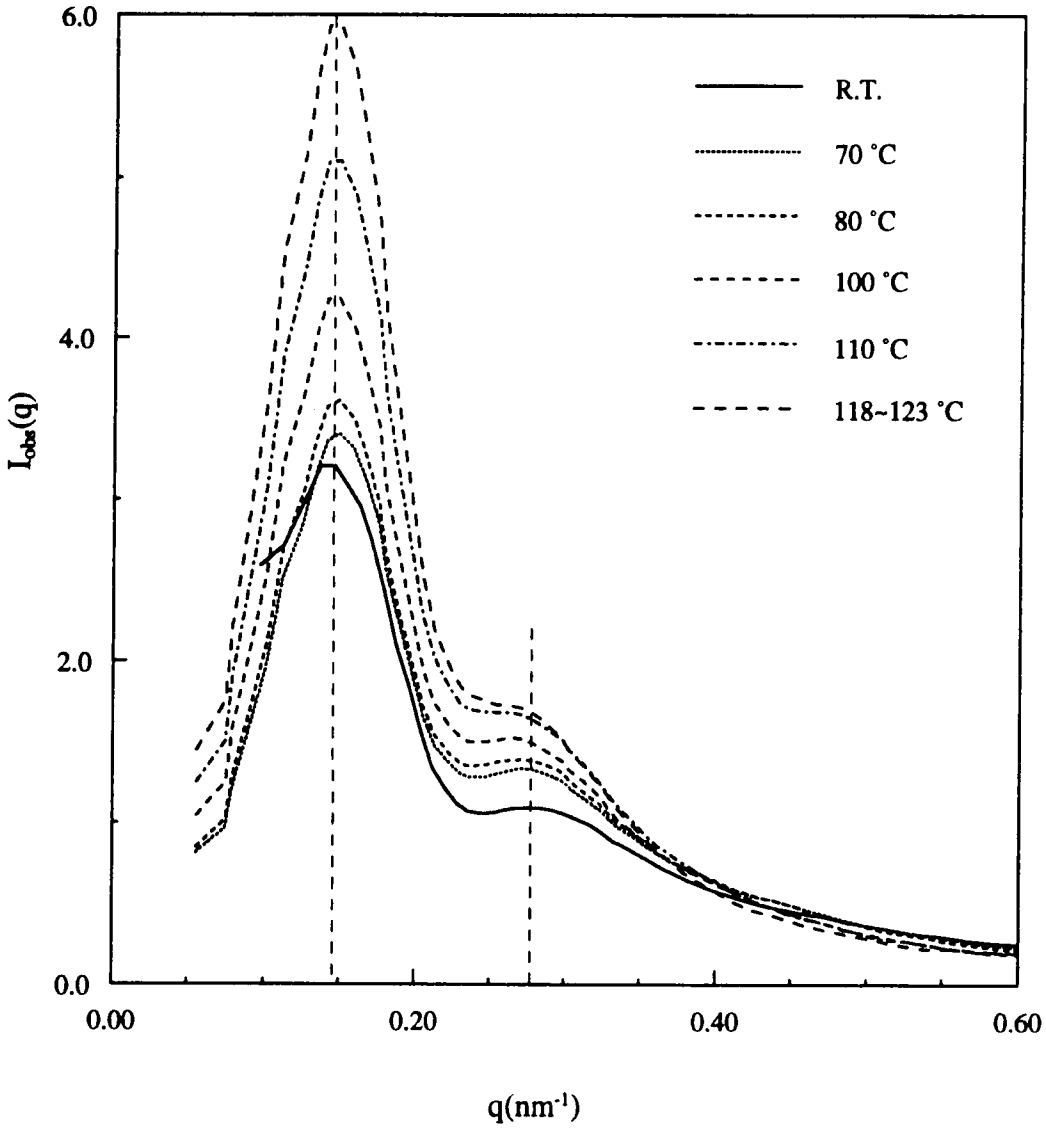


Figure 4.4.1.6. Lorentz corrected SAXS intensity profiles for H-LPE (Tc=130 °C, t_c=17days) measured at different temperatures.

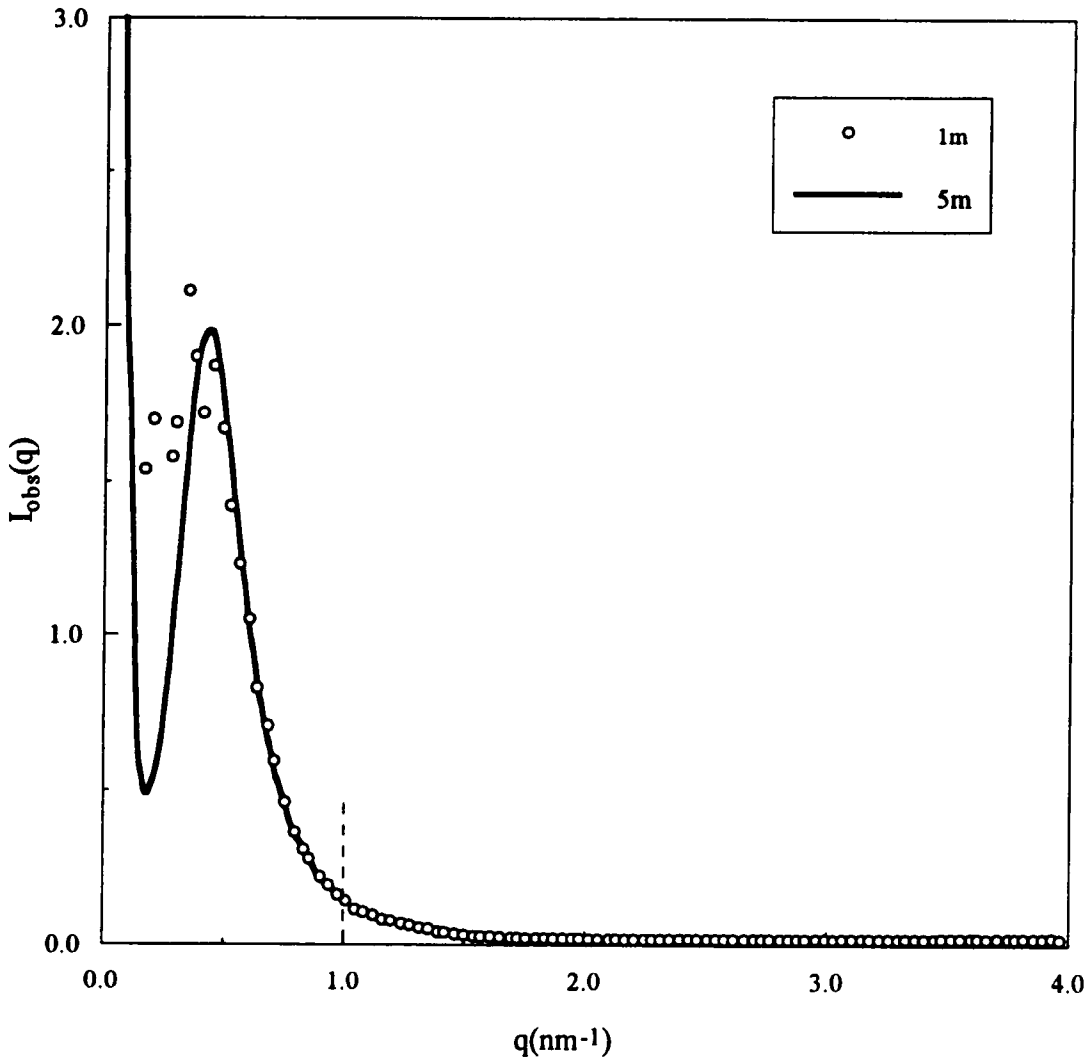


Figure 4.4.2.1. SAXS intensity profiles obtained from 5m and 1m geometry of L39-O quenched in ambient temperature.

Figure 4.4.1.1) the geometry used to measure the lamellar thickness is reasonable. The detailed analysis of this tail region will be discussed in later.

In **section 5.4.3**, the tail region intensity will be calculated and the calculated intensity be compared to that measured actually from 1m geometry.

4.4.3. Theoretical Development for Estimation of Interfacial Layer Thickness using SAXS

4.4.3.1. Theoretical Background for Transition Layer Thickness

The corrected net absolute intensity was obtained as described in the experimental section. Assuming Bragg's law is applicable, the long period ($L = 2\pi/q_{max}$) can be calculated from the maximum peak position of the Lorentz corrected SAXS pattern (i.e., plot of $I(q)\cdot q^2$ versus q).

The $q_{max}(nm^{-1})$ is the best estimated scattering vector that is obtained from the first derivatives of the second order polynomial fitting equation around the symmetry region of Lorentz corrected SAXS pattern. The long period represents that the summation of the amorphous phase length (l_a) and the crystalline phase length (l_c) for a two-phase system with sharp phase boundary. However, in the case of a three-phase model with diffuse transition boundary, the L is expressed as $L = l_a + l_c + 2l_{trz}$, where l_{trz} is the diffuse transition (or interfacial) layer thickness from the crystalline to the amorphous phase or vice versa. The transition layer thickness can be obtained from line broadening of NMR, internal mode of LAM mode of Raman spectroscopy[53, 54 55 56] and SAXS.

There are two general approaches to get l_{trz} from the SAXS. One is to use the one-dimensional correlation function[57, 58, 59] based on the linear gradient of electron density, and the other is to use a modified Porod's law suggested by Ruland[60, 61]. The displacement from the slope in the so-called self-correlation triangle section[62] can be used to calculate interfacial layer thickness for linear-gradient model. However, the modified Porod's law method is usually recommended for polymers.[58]

According to the Porod's law, the intensity ($I_{ideal}(q)$) decreases proportionally to q^{-4} at the tail region scattering vector for an ideal two-phase system with a sharp phase boundary as shown

$$\lim_{q\to\infty} I_{ideal}(q) = K_p'/q^4 \qquad (4.4.3.1)$$

where $K_p' = (2\pi)^4 K_p$ and $I_{ideal}(q)\cdot q^4$ reaches a constant, K_p, which is called Porod's constant. However, deviation from Porod's law has been observed.[58, 60, 61] In our case, the intensity in the tail region decreased with the form of fractal dimensions. These values were obtained by the multiplying exponent of q, 4, with the slope of the near zero region (i.e., large q region which assumed to follow Porod's law) in the plot of $\log I(q)$ versus $\log(1/q^4)$. So there seems to be no point in describing the intensity in tail region as decreasing with q^2, q^4, or q^6. More important thing is the direction of deviation since it involves physical meaning. Positive deviation from the Porod's law is caused by the presence of thermal density fluctuations or mixing within the phase. Negative deviation is related to the existence of a diffuse transition layer in the system. To obtain the correct transition layer thickness, the intensity, $I_{Fl}(q)$, due to the electron density fluctuations has to be subtracted from the net corrected absolute intensity. This electron density fluctuation in the system with defects is shown schematically in **Figure 4.4.3.1**. Electron

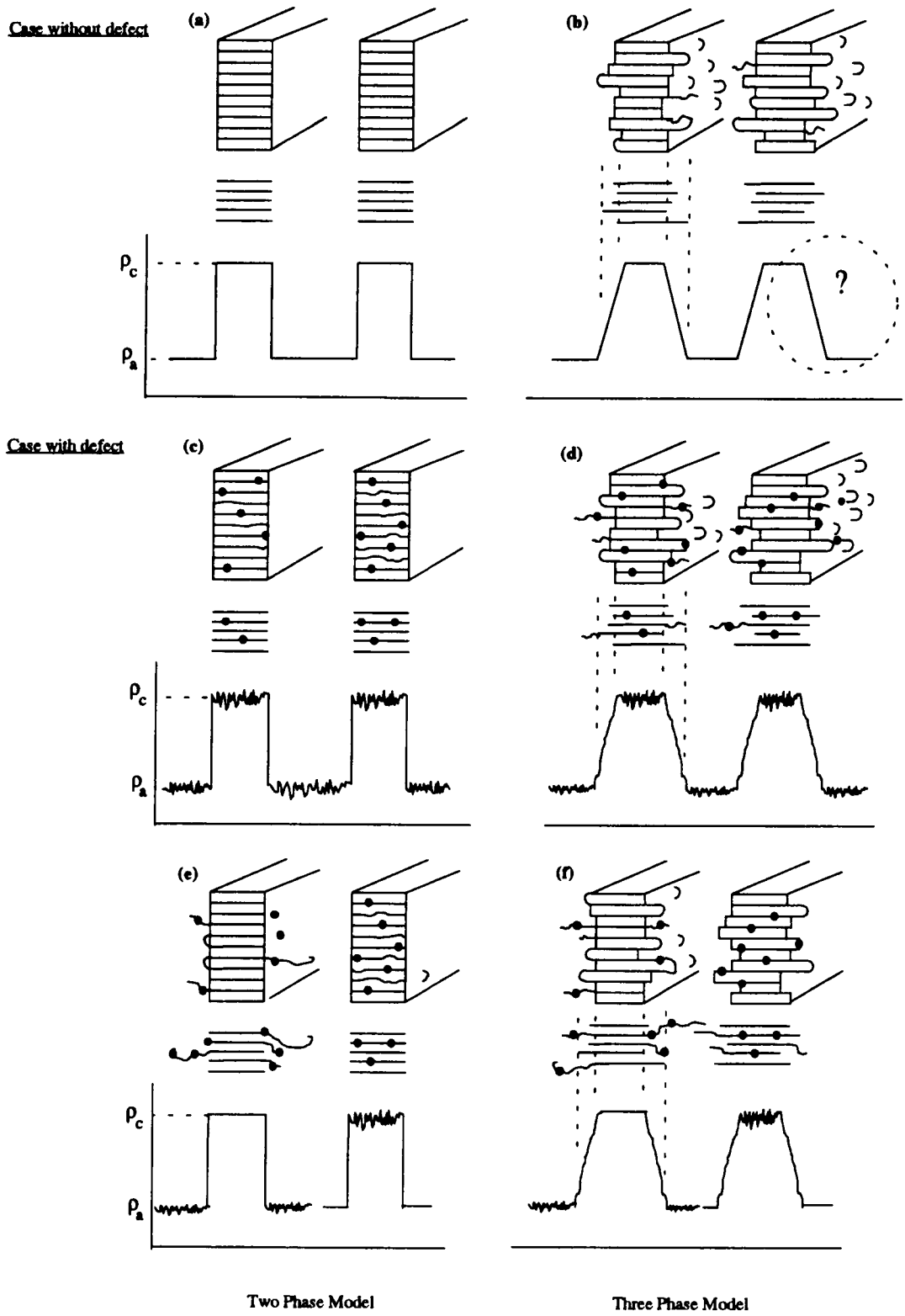


Figure 4.4.3.1. Schematic diagram showing electron density fluctuation due to defects and interfacial layer in systems

density fluctuation known to cause the positive deviation from the Porod's law, which shows the opposite effect to scattering behavior caused by the transition layer, can be calculated using the empirical equations of Vonk [58] or Ruland [35].

Vonk's expression for slit smeared intensity is

$$I_{Fl}(q) = Fl + b \cdot q^n \qquad (4.4.3.2)$$

where Fl is the thermal density fluctuation constant at $I_{Fl}(0)$, b is a constant. Exponent n has even values to fit the curve to the experimental SAXS patterns.

Ruland 's expression is

$$I_{Fl}(q) = Fl \cdot \exp(b \cdot q^2) \qquad (4.4.3.3)$$

From the intercept of log-log plot of **equation (4.4.3.2)** or **(4.4.3.3)** the I_{Fl} is obtained. Therefore the observed scattering intensity, $I_{obs}(q)$, which is the net corrected absolute scattering intensity, $I_{NCAI}(q)$, by **equation (3.6.4)** of **Chapter 3**, is given by

$$\lim_{q \to \infty}[I_{obs}(q)] = I_{ideal}(q) \cdot H^2(q) + I_{Fl}(q) \qquad (4.4.3.4)$$

The intensity correcting the background intensity due to electron density fluctuation becomes

$$\lim_{q \to \infty}[I_{FlCor}(q)] = I_{ideal}(q) \cdot H^2(q) \qquad (4.4.3.5)$$

where $I_{FlCor}(q) = I_{obs}(q) - I_{Fl}(q)$

where $I_{ideal}(q)$ is Porod's intensity from the ideal two-phase system and $H^2(q)$ represents negative deviations from Porod's law due to the transition region. The form of $H^2(q)$ depends on the chosen model for describing the electron density profile of the interfacial layer. The electron density profile, $\rho(r)$, of a system with a transition region is given by the convolution product of the electron density variation, $g(r)$, of the ideal two phase system and the smoothing function, $h(r)$.

$$\rho(r) = g(r) * h(r) = \int_{-\infty}^{\infty} g(u)h(r-u)du \qquad (4.4.3.6)$$

The observed scattering intensity (unit: el/cm^3), $I_{obs}(q)$, of the system is

$$I_{obs}(q) = \frac{I(q)}{I_e(q) \cdot V} = \frac{|F(q)|^2}{V} \qquad (4.4.3.7)$$

where $I_e(q)$ is the Thomson scattering intensity from a single electron, V is irradiated volume, and the $F(q)$ is the amplitude of the system which is given by the Fourier transform of the function $\rho(r)$.

$$F(q) = \mathcal{F}\{\rho(r)\} = \mathcal{F}\{g(r)\}\mathcal{F}\{h(r)\} \qquad (4.4.3.8)$$

where

$$\mathcal{F}\{\rho(r)\} = \int_{-\infty}^{\infty} \rho(r)\exp(iqr)dr \qquad (4.4.3.9)$$

From **equations (4.4.3.7)** and **(4.4.3.8)**

$$I_{obs}(q) = \mathcal{F}\{g(r)*g(r)\} \cdot \mathcal{F}\{h(r)*h(r)\} \qquad (4.4.3.10)$$

where

$$\mathcal{F}\{g(r)*g(r)\} = I_{ideal}(q) = \frac{K_p}{q^4} \qquad (4.4.3.11)$$

$$\mathcal{F}\{h(r)*h(r)\} = H^2(q) \qquad (4.4.3.12)$$

Using the relations of **equations (4.4.3.10)**, **(4.4.3.11)**, and **(4.4.3.12)**, we can obtain **equations (4.4.3.4)** and **(4.4.3.5)** for the case without electron density fluctuation and with correction of electron density fluctuation, respectively.

If the linear electron density gradient across the interface boundary is considering, $H^2(q)$ takes the autocorrelation Fourier transform of a top hat function, $h(r)$, of width E and height $1/E$.[58]

$$h(r) = \begin{cases} 1/E & (r \le |E/2|) \\ 0 & (r > |E/2|) \end{cases} \qquad (4.4.3.13)$$

$$H^2(q) = \frac{\sin^2(Eq/2)}{(Eq/2)^2} \qquad (4.4.3.14)$$

By expanding the sine-function into the power series and truncating the higher order after the second term, **equation (4.4.3.14)** become a more tractable form for graphical analysis.

$$H^2(q) = (1 - E^2q^2/12) \qquad (4.4.3.15)$$

From **equations (4.4.3.1)**, **(4.4.3.5)**, and **(4.4.3.15)**, the observed scattering intensity corrected thermal density fluctuation can be expressed as

$$\lim_{q\to\infty}[I_{Flcor}(q)\cdot q^4] = \lim_{q\to\infty}[K_p'(1-E^2q^2/12)] \qquad (4.4.3.16)$$

where E, the transition layer thickness, is obtained from the plot $I_{FlCor}(q)\cdot q^4$ versus. q^2 of **equation (4.4.3.16)** derived from the model assuming a the linear gradient of electron density within the phase boundary.

If the electron density decreases sigmoidally within the phase boundary between the crystalline and the amorphous region, $H^2(q)$ is a Fourier transform of the autocorrelation of a Gaussian function, $h(r)$.[61]

$$h(r) = \exp(-r^2/2\Delta^2)/\Delta\sqrt{2\pi} \qquad (4.4.3.17)$$

$$H^2(q) = \exp(-\Delta^2\cdot q^2) \qquad (4.4.3.18)$$

where Δ means the transition layer thickness as a standard deviation of Gaussian function.

From **equations (4.4.3.1)**, **(4.4.3.5)**, and **(4.4.3.18)**

$$\lim_{q\to\infty}[I_{Flcor}(q)\cdot q^4] = \lim_{q\to\infty}[K_p'\exp(-\Delta^2\cdot q^2)] \qquad (4.4.3.19)$$

By expanding the exponential function, **equation (4.4.3.19)** become approximately

$$\ln(I_{FlCor}(q)\cdot q^4) = \lim_{q\to\infty}[K'_p(1-\Delta^2 q^2)] \qquad (4.4.3.20)$$

The determination of a diffuse transition layer thickness (Δ) using pin-hole collimation can be calculated from the negative slope of the plot $\ln(I_{FlCor}(q)\cdot q^4)$ versus q^2.of **equation (4.4.3.19)** (or plot $I_{FlCor}(q)\cdot q^4$ versus q^2 of **equation (4.4.3.20)**) under the assumption of a sigmoidal-electron density gradient across the boundary. To avoid the truncation effect, **equation (4.4.3.19)** was used in this study.

According to Koberstein, et al.[60] the range of applicability for each modified Porod's law model is given as all $\Delta\cdot q$ for sigmoidal-electron density gradient model (**equation (4.4.3.19)**), $\Delta\cdot q < 0.051$ for expanded sigmoidal model (**equation (4.4.3.20)**), and $E\cdot q < 0.19$ for expanded linear gradient mode (**equation (4.4.3.16)**) by allowing for 5% error in the estimation of Δ and E. Thus, the sigmoidal gradient model is advantageous in view of the fact that the exact form for graphical analysis can be plotted in the full $\Delta\cdot q$ range for pin-hole collimation.

4.4.3.2. Development of Mathematical Model and Analytical Approach

Even though the sigmoidal model obtained from the Gaussian function gives a reasonable result, sometimes, it gives an unreasonable thin transition thickness (for example, H7-O crystallized at 113'C for 9 weeks has $\Delta \approx 3$ Å at room temperature). Also, the linear gradient model shows too thick a transition layer thickness (for example, H7-O crystallized at the same condition has $E \approx 44$ Å at in-situ). Therefore, an intermediate model has been developed in this study. Moreover, to find a new smoothing (ghost) function and to solve its convolution product has its own interest regardless its

usefulness. The electron density profile of the ideal two phase system was assumed to follow the uniform distribution function as before. The triangular angular smoothing function is used.

$$h(r)=\begin{cases}=-\dfrac{A}{T}|r|+A & ,|r|\le T,\quad (T=2T_0)\\ =0 & ,|r|\le T\end{cases} \qquad (4.4.3.21)$$

where A is $1/T$, and the autocorrelation Fourier transform of the **equation (4.4.3.21)** becomes

$$H^2(q)=\frac{16\sin^4(Tq/2)}{(Tq)^4} \qquad (4.4.3.22)$$

Therefore, a modified Porod's intensity is given by

$$\lim_{q\to\infty}(I_{FlCor}(q)\cdot q^4)=K_p'\cdot\frac{16\sin^4(Tq/2)}{(Tq)^4} \qquad (4.4.3.23)$$

equation (4.4.3.23) can be a tractable form for the graphical analysis by taking the first two terms of the expanded series for the case of $Tq/2 << 1.0$.

$$\lim_{q\to\infty}(I_{FlCor}(q)\cdot q^4)=K_p'\cdot(1-\frac{1}{6}T^2q^2) \qquad (4.4.3.24)$$

where the transition layer thickness, T, can be obtained from the negative slope and the intercept of the plot $I_{FlCor}(q)\cdot q^4$ versus q^2 as follows:

$$T=\sqrt{\frac{-6\cdot\text{slope}}{\text{intercept}}} \qquad (4.4.3.25)$$

Electron density profiles calculated using various models are given in **Figure 4.4.3.2** and a summary of the models for estimating the transition layer thickness from the pin-hole collimation is shown in the **Figure 4.4.3.3**.

The relations among the transition layer thickness, of sigmoidal-electron density gradient model, that, E, of linear-electron density gradient model, and the T in this study can be obtained from the ratio of each scattering intensity, **equations.(4.4.3.20)**, **(4.4.3.16)**, and **(4.4.3.24)**.

$$E(=\sqrt{12}\Delta) > T(=\sqrt{6}\Delta) > \Delta \qquad (4.4.3.26)$$

The transition layer thickness, T, of this study has thickness intermediate between that of the linear gradient model and of the sigmoidal model.

4.4.3.2.1. Slit collimation

Although pin-hole collimation is an ideal collimation and all the equations for estimating the transition layer thickness can use pin-hole collimation scattering intensity directly, slit collimation is used widely since it provides a higher intensity and resolving power and lower parasitic scattering due to the collimator edge. The intensity obtained from slit collimation is the smeared one. Therefore, the desmearing procedure of the experimentally observed SAXS intensity is required. However, many methods for the desmearing have been known to cause a statistical error at the large scattering angle that is related to the transition layer.[63] The theoretical treatment of the smeared intensity has

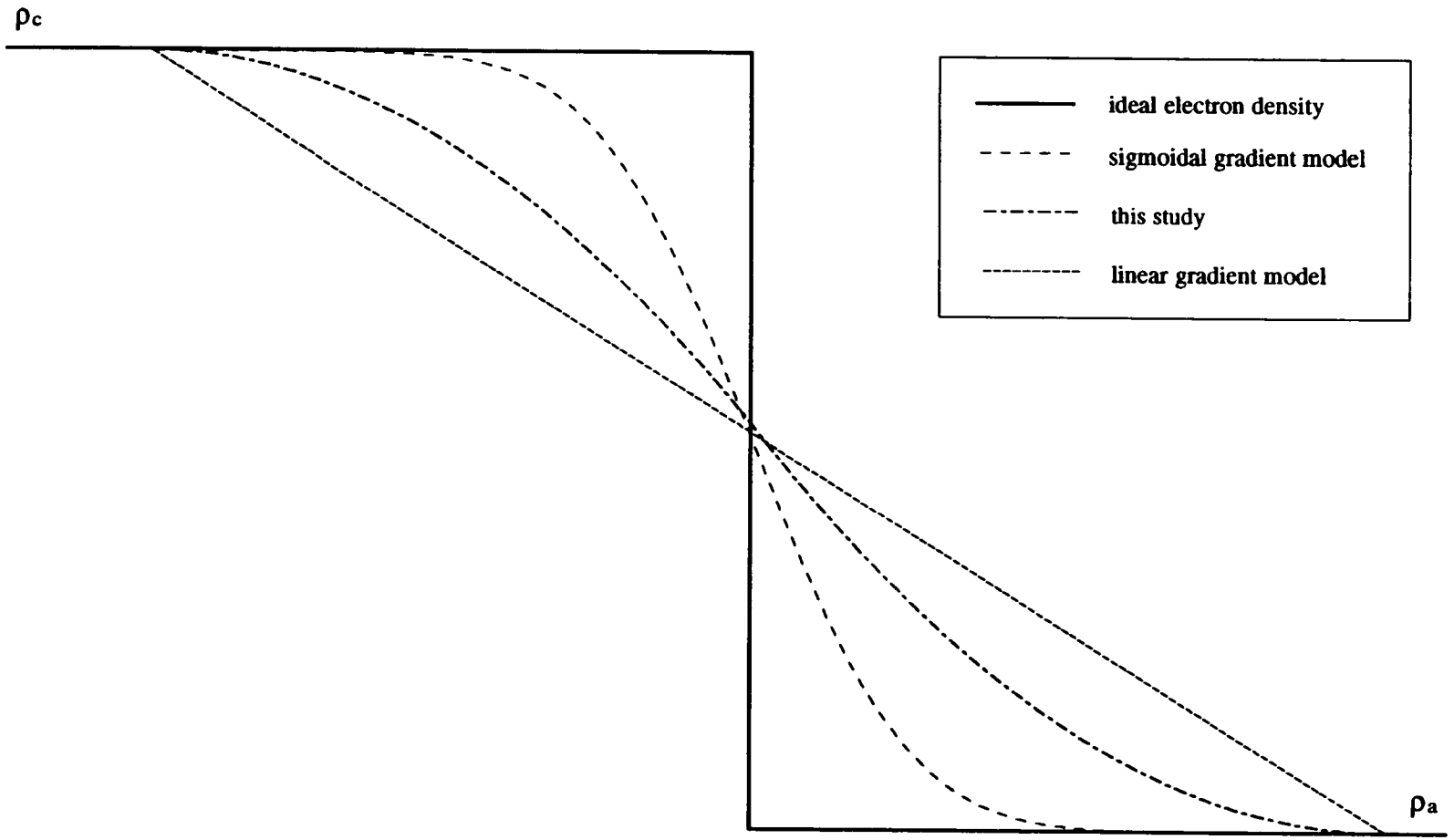
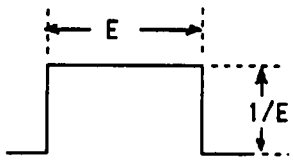
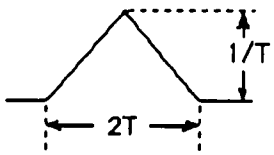


Figure 4.4.3.2. Electron density profiles obtained from the convolution product of an ideal electron density, g(r) for two phase system and the various ghost functions, h(r), where the x-axis was normalized. (see text for the detail condition of h(r) functions).

Ideal electron density profile g(r)			
Smoothing (ghost) function h(r)			
Expected (or observed) electron density profile $\rho_{expected}(r) = g(r)*h(r)$			
Modified Porod's law form	$I_{FICor}q^4 = K'_p \frac{\sin^2(E\cdot q/2)}{(E\cdot q/2)^2}$	$I_{FICor}q^4 = K'_p \frac{16\sin^4(T\cdot q/2)}{(T\cdot q)^4}$	$I_{FICor}q^4 = K'_p \exp(-\Delta^2 q^2)$
Expanded form	$I_{FICor}q^4 = K'_p(1-\frac{E^2q^2}{12})$ (for $E\cdot q/2 << 1.0$)	$I_{FICor}q^4 = K'_p(1-\frac{T^2q^2}{6})$ (for $T\cdot q/2 << 1.0$)	$I_{FICor}q^4 = K'_p(1-\Delta^2q^2)$ (for $\Delta\cdot q << 1.0$)
Plot for graphical analysis	for expanded form $I_{FICor}q^4$ vs. q^2	for expanded form $I_{FICor}\cdot q^4$ vs. q^2	• for exponential form $\ln(I_{FICor}q^4)$ *vs.* q^2 • for expanded form $I_{FICor}q^4$ *vs.* q^2
Determination of transition layer thickness	$E = \sqrt{\frac{-12\cdot slope}{intercept}}$	$T = \sqrt{\frac{-6\cdot slope}{intercept}}$	• for exaction solution $\Delta = \sqrt{-slope}$ • for expanded form $\Delta = \sqrt{\frac{-slope}{intercept}}$
reference	Ruland, Vonk	this study	Ruland

where, $K'_p = (2\pi)^4 \cdot K_p$

Figure 4.4.3.3. Various modified Porod's law for the pin-hole collimation with a scattering vector, $q = 4\pi\cdot\sin\theta/\lambda$.

been preferred to the desmearing methods. The smeared intensity , $\tilde{I}(q)$, can be expressed by

$$\tilde{I}(q) = \int_{-\infty}^{\infty}\int_{-\infty}^{\infty} W_l(u)W_w(t)I_{FICor}[((q^2 - t^2) + u^2)^{1/2}]dtdu \qquad (4.4.3.27)$$

where $W_l(u)$ and $W_w(t)$ are the weighting function of the slit length and the slit width, respectively. And t and u, are arbitrary variables for integration and have no physical meaning.

If we assume that the slit width contribution can be neglected **equation (4.4.3.27)** become

$$\tilde{I}(q) = 2\int_{0}^{\infty} W_l(u)I_{FICor}(q^2 + u^2)^{1/2}du \qquad (4.4.3.28)$$

From **equation (4.4.3.5)** that describes the negative deviation from the Porod's law, **equation (4.4.3.28)** can be represented by

$$\tilde{I}(q) = 2\int_{0}^{\infty} W_l(u)I_{FICor}(q^2 + u^2)^{1/2}H^2(q^2 + u^2)^{1/2}du \qquad (4.4.3.29)$$

By assuming infinite slit-length the slit smeared intensity can be approximated by

$$\tilde{I}(q)\cdot q^3 = K'(1 - T^2q^2/3) \qquad \text{for } Tq/2 << 1.0 \qquad (4.4.3.30)$$

where $K' = W_l(0)K'_p\pi/2$, $K'_p = (2\pi)^4 \cdot K_p$, and $W_l(0)$ is constant. In this case, the transition layer thickness from the plot of $\tilde{I}(q)\cdot q^3$ versus q^2 is given by $T = \sqrt{3(-\text{slope})/\text{intercept}}$

An alternative method to obtain slit smeared intensity for the case of infinite slit length was suggested by Bonart *at. el.*[64]

$$\tilde{I}(q) = 2H^2(q)\int_0^{\infty} W_l(u) I_{ideal}(q^2 + u^2)^{1/2} du \qquad (4.4.3.31)$$

where $H^2(q) = 1 - T^2q^2/6$ for the triangular smoothing function. The slit smeared intensity becomes

$$\tilde{I}(q)\cdot q^3 = K'(1 - T^2q^2/6) \qquad \text{for } Tq/2 << 1.0 \qquad (4.4.3.32)$$

The transition layer thickness in this case can be obtained from the plot of $\tilde{I}(q)\cdot q^3$ against q^2.

The successful application of all the equations to estimate the transition (interfacial or phase difuse boundary) layer thickness depends on how having reliable tail region intensity. Of course, the tail region intensity can be extrapolated to large scattering vector using the Porod's law or modified Porod's law to generate the best fit to the curve. Although this extrapolation method has been used for one-dimensional correlation function (1-DCF) approach to obtain the lamellar thickness, however, when there is highly scattered intensity in tail region, the extrapolation method can result in a the reliability problem. Furthermore, the problem becomes worse when we extrapolate from low angle region which has not reached the background to high angle region which shows two different deviation behaviors from Porod's law. Roe[65] mentioned similar problems and Roe tried to deal with these difficulties using a model.

In the 5 m geometry ($0.040 \leq q(nm^{-1}) \leq 1.060$) that was used to determine the lamellar thickness, the tail region seems to be the starting line for entering the background. Whereas, the 1 m geometry ($0.9160 \leq q(nm^{-1}) \leq 4.8620$) has the following advantages: it covers more background than that of 5 m. Thus, it provides information such as electron density fluctuation related to the high q region. In this study, 1 m geometry was used to study background intensity and electron fluctuation density component of EO copolymer system with defects as well as LPE. The procedures and the models to obtain the transition layer thickness were described earlier.

4.4.4. Interfacial Layer Thickness of LPE and EO Copolymers

The intensity reflecting interfacial layer thickness is observed between the scattering vectors of the Bragg peak and the background. The scatering vector range, ($0.040 \leq q(nm^{-1}) \leq 1.060$), of 5m geometry is enough to measure interfacial layer thickness as well as lamellar thickness.

The plots **(a)** of the sigmoidal model and the plot **(b)** of the linear-, semi-sigmoidal model are shown in **Figure 4.4.4.1** for H7-O and **Figure 4.4.4.2** for L39-O in the case with background correction and without background correction, respectively. The lightly branched H7-O has a steep negative slope change while that of highly branched L39-O is not clear. This means that H7-O has a thicker phase boundary than L39-O. The negative slope obtained from subtracting the positive deviation of background produces the steeper slope change. The importance of correcting background intensity can be demonstrated in the case of L39-O. The slope of L39-O without correction of background intensity is almost flat or a little positive, suggesting that there is no interfacial layer

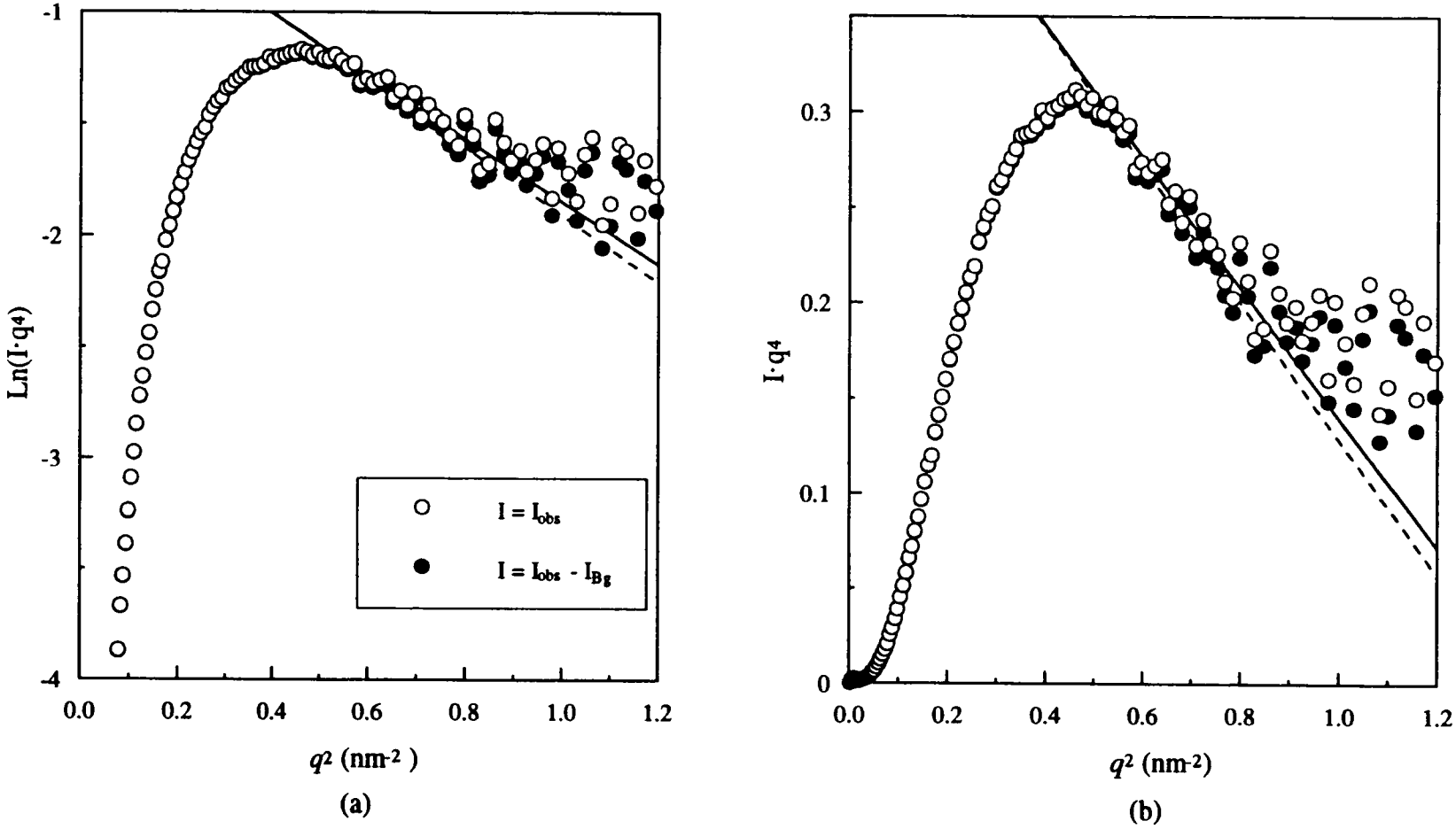


Figure 4.4.4.1. Graphical demonstration ((a) for sigmoidal-gradient model, (b) for linear- and semi-sigmoidal-gradient models)showing the effect of background intensity correction on estimating interfacial layer thickness. (sample; H16-O quenched at ambient temperature).

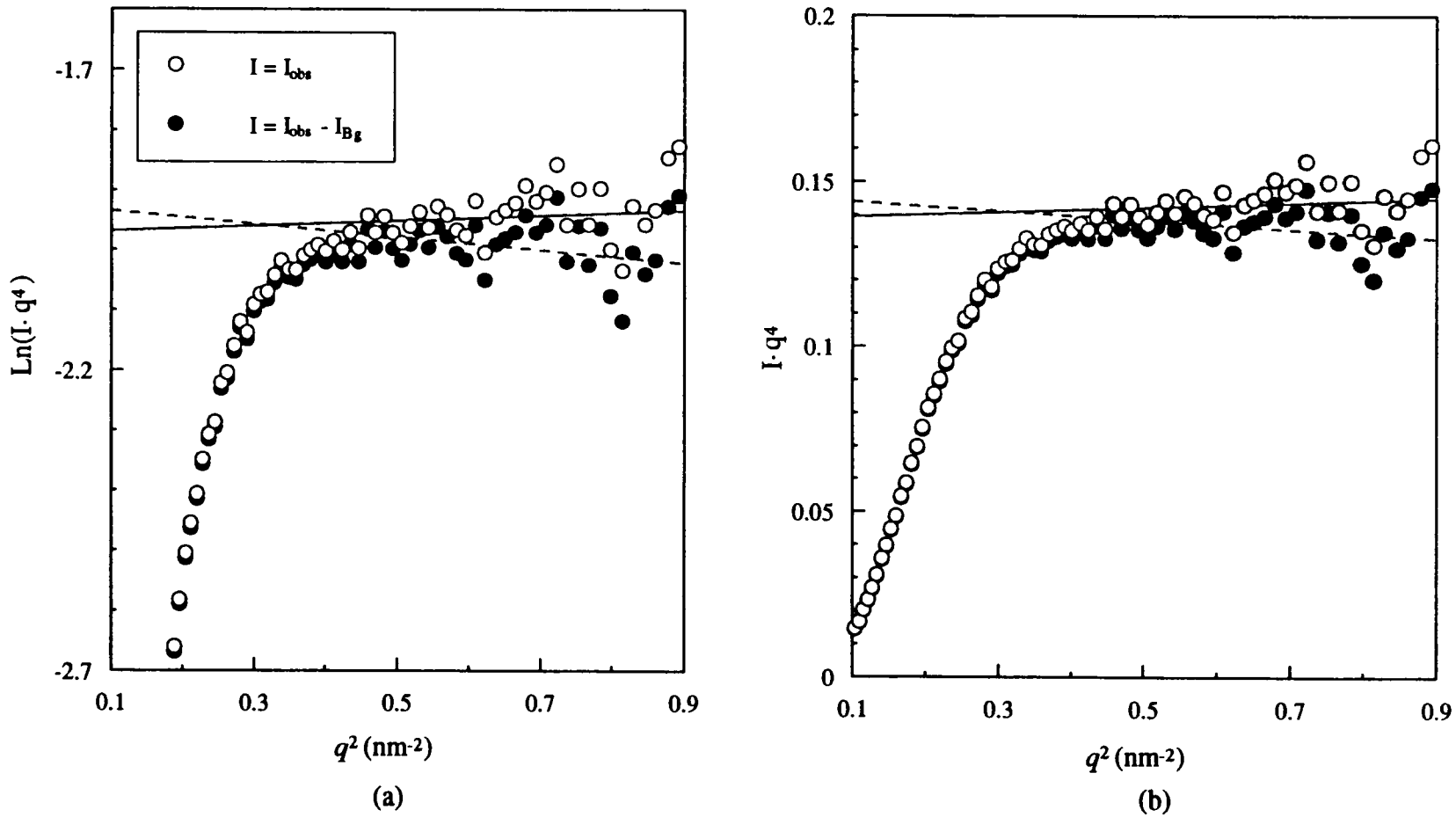


Figure 4.4.4.2. Graphical demonstration ((a) for sigmoidal-gradient model, (b) for linear- and semi-sigmoidal-gradient models) showing the effect of background intensity correction on estimating interfacial layer thickness. (sample; L39-O quenched at ambient temperature).

thickness in the system. However, when the positive background is corrected, the slope direction becomes negative, showing that a transition boundary exists in L39-O system. This background correction is more sensitive around the scattering vector region relating to the interfacial layer (i.e., transition region) and as q decreases the correction effect is not visible.

The plot to estimate the interfacial layer thickness for LPE and a series of EO copolymers quenched in ambient temperature is shown in **Figure 4.4.4.3** assuming linear and semi-sigmoidal model and **Figure 4.4.4.4** assuming sigmoidal model. The background subtracted intensity was used to obtain accurate interfacial layer thickness. As branch contents increase from L4-O to L24-O, the slope becomes moderate and apparently levels-off at L39-O. There are two negative slopes for LPE. In this case, the negative slope was chosen comparing the slope of modified Porod plots to the curvature at near zero region of 1-DCF of **Figure 4.4.4.5**, although both methods reflect the intensity behavior of the high q region.

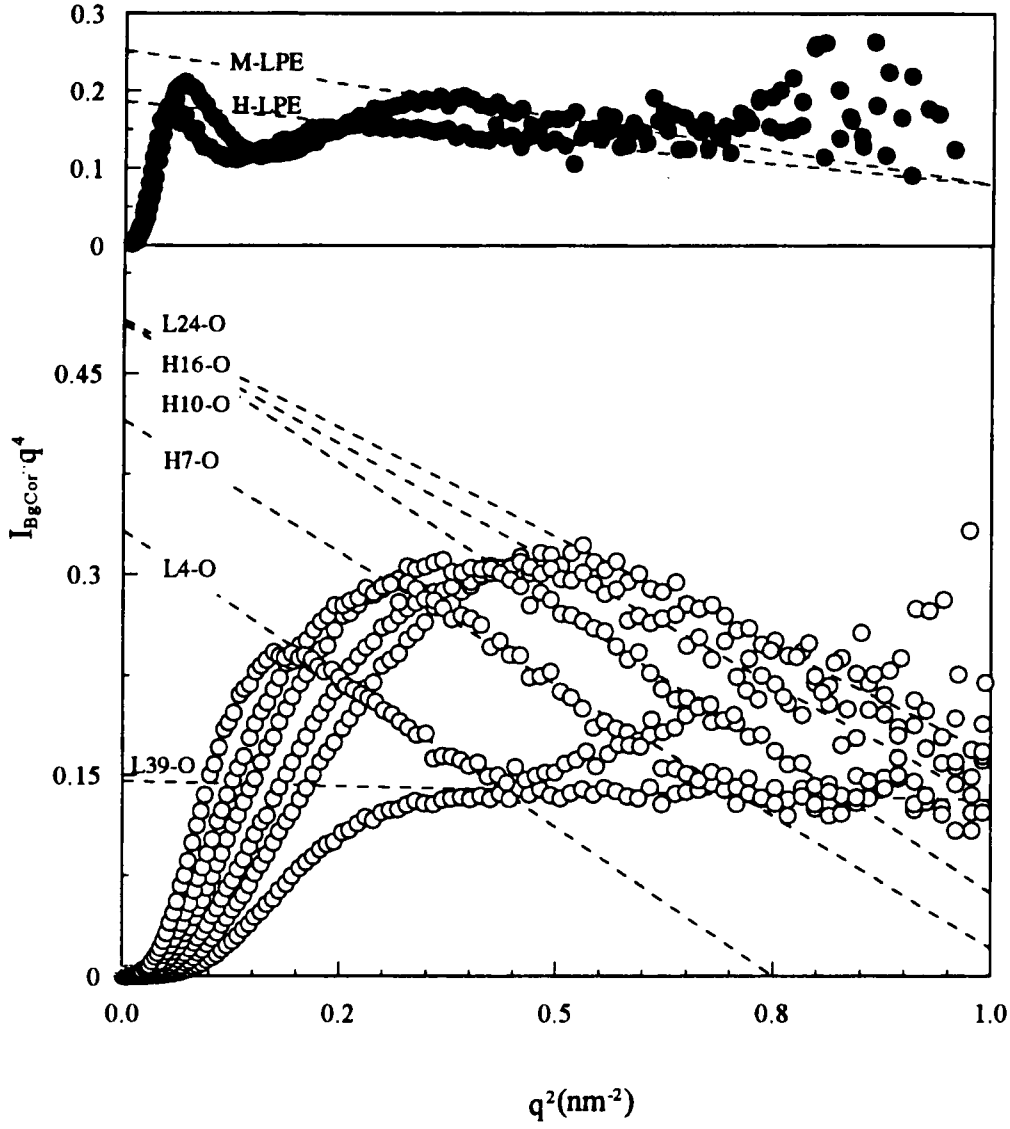


Figure 4.4.4.3. Plot to estimate interfacial layer thickness of the quenched LPEs and EO copolymers, using linear and semi-sigmoidal electron density gradient model.

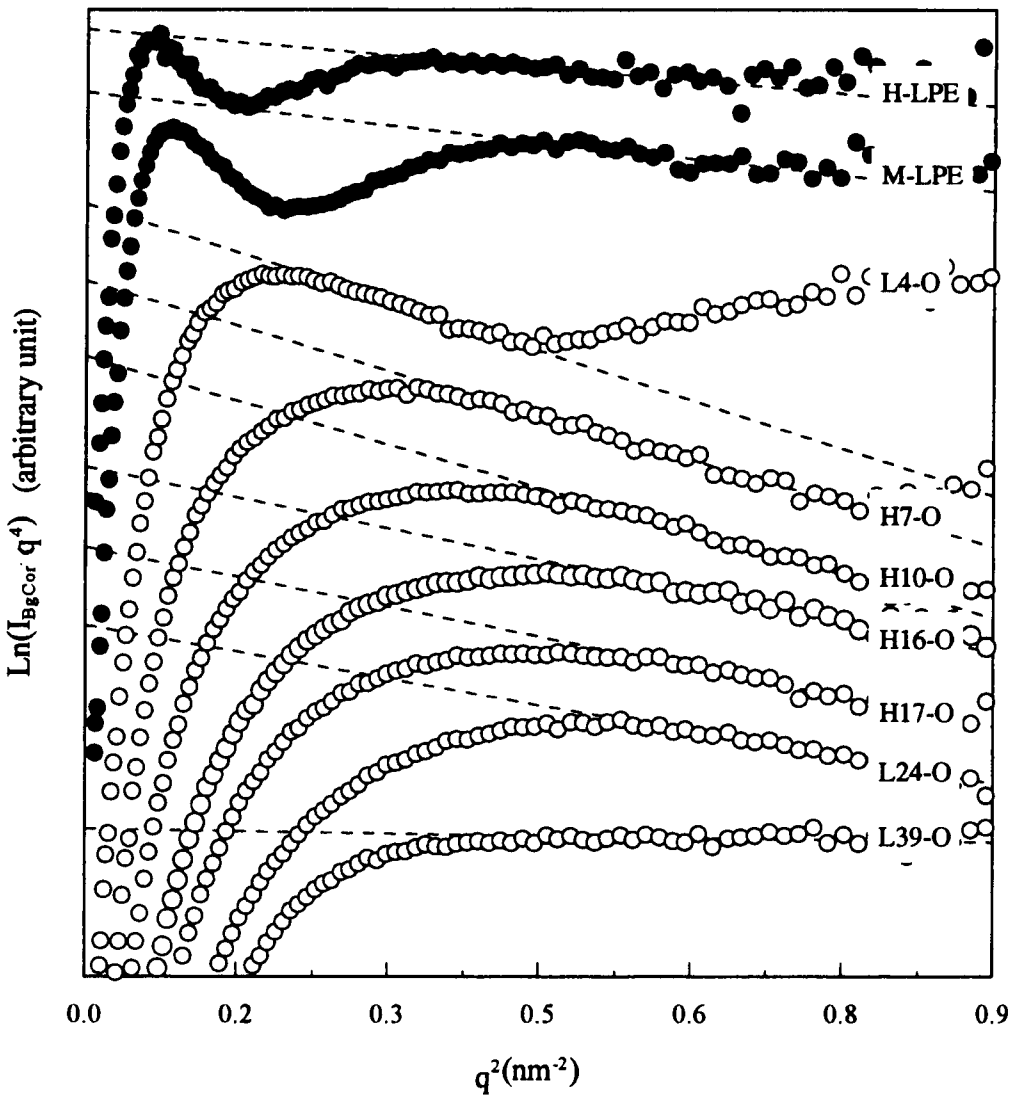


Figure 4.4.4.4. Plot to estimate interfacial layer thickness of the quenched LPEs and EO copolymers, using sigmoidal electron density gradient model.

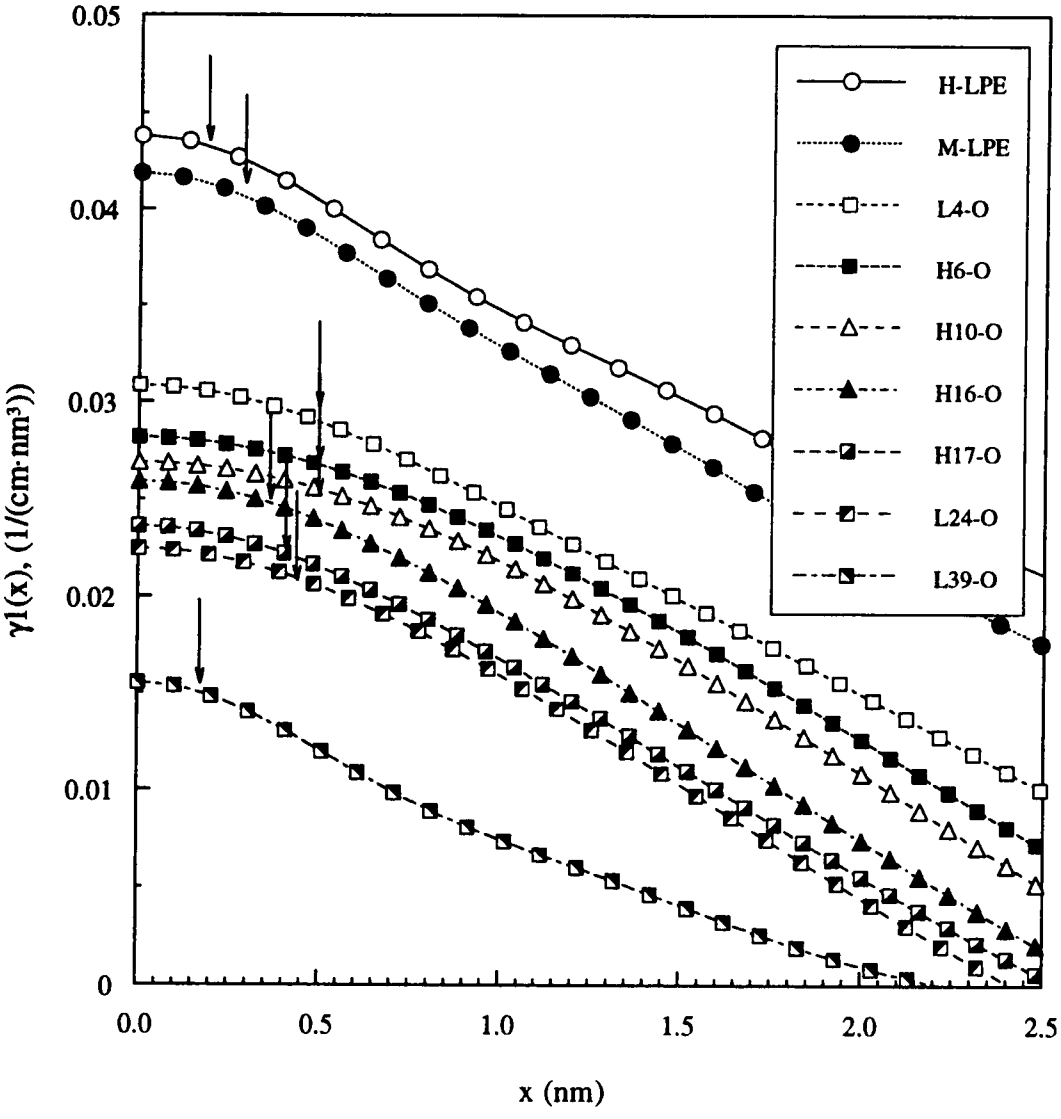


Figure 4.4.4.5. One-dimensional correlation function showing invariant and transition layer variation as a function of defects.

5. DISCUSSION

5.1. Thermal Analysis

5.1.1. EO, EB and EP Copolymers

The fact that melting, crystallization temperature, and heat of fusion (or crystallinity) are reduced means that the branches are defects in a crystallizable polymer. In branched polymers, the multiple melting thermogram of LLDPE may be due to the segregation of polymer molecules during crystallization. This segregation is dominated by the branch amount for a highly branched polymer and by molecular weight for a low branched polymer according to this study. The branch, branch point and branch end play roles as defects in crystallization because their different molecular size will not have the same crystallography as the polyethylene main chain. If we can assume that the chain growth stops whenever they meet a defect, the available chain lengths for crystallization become reduced. This assumption is reasonable because the crystal system has more free energy when it accommodates defects in the crystalline phase. This excess free energy causes an unfavorable condition for crystal growth due to the increased energy barrier. As long as the system cannot overcome this increased energy barrier or reject the defect to the amorphous phase, the stem growth stops at the defect location. After all, sections of chain with a long distance between two branch points will crystallize at high crystallization temperature and parts consisting of short distances between branch points will crystallize at lower crystallization temperature. However in a LLDPE of low branch content since many stems can deposit before encountering a defect, the defect effect will

be reduced. In this case the segregation by molecular weight will dominate as is well known.

It is an important fact that different branch lengths affect melting and crystallization temperature as well as morphology. The melting temperatures of some EO copolymers are lower than EB and EP copolymers that are highly branched. This means the branch is not a point defect but a size defect. There are two ways to describe the effect of branch on the crystallization process. One is based on crystallization progress and the other is based on the location of the branch after crystallization. In crystallization progress, the branch will hinder the attachment of the chains to crystal surface or nucleus, due to increased entropy as long as they are not included in the crystalline phase. Therefore, long branches will have wider hindering radii than short branches. And the crystal size and lamellar thickness of EO copolymer will be reduced resulting in larger melting and crystallization temperature depressions compared to those of EB and EP. Also, the crystallization depression will cause lowering of melting temperature due to the formation of thin lamellae. The location of the branch after crystallization can affect the T_m and T_c. A branch group can be inside or outside the crystalline phase. In the inclusion case, it is possible for these branches to change the conformation of neighboring chains in order to produce the space for inclusion of the branch defect. The crystallography will be distorted from ideal. As the size of the defect increases, the distortion will be increased. This study did not concentrate on what parts of the branch are in the crystalline phase and how a long branch enters the crystal. If branches are long enough to crystallize, the defects are the branch end and the branch point. On the other hand, if the branches are not long enough to crystallize, they can be expelled from crystalline phase. Although we do not know this critical branch length, both the inclusion of the defect and the exclusion of

the defect from the crystalline phase cause the depression of T_m,, T_c, and ΔH_f. The inclusion and exclusion possibilities will be discussed in separate chapter.

5.1.2. Melting Temperatures of Homogeneous and Heterogeneous EO Copolymers.

So far thermal analysis of homogeneous EO copolymers has been discussed based on the analysis of DSC. The homogeneous EO copolymers showed that there is a linear relationship between T_m and p_B without molecular weight effect in **Figure 4.1.2.4.** In other words, T_m decreases linearly with defect content for the homogeneous EO copolymers. The values extrapolated to zero defect content coincide with T_m of the linear polyethylenes produced using homogeneous (uniform site) catalyst.

It is essentially required to compare T_m of the heterogeneous EO (HTEO) copolymer with that of homogeneous EO (HMEO) copolymer in order to know whether both LLDPEs produced using different catalyst system have identical thermal properties. For this purpose, the HTEO copolymes with $\overline{M}_n/\overline{M}_w < 2.0$, which fractionated using TREF method, were used. This comparison is represented in **Figure 5.1.2.1**. The HTEO copolymers do not show the clear linear relationship between T_m versus p_B found in the case of HMEO copolymers. Despite that fact, a surprising point is the experimental result that T_m of HTEO copolymer is depressed in much less degree than that of HMEO copolymers. The difference of T_m between HMEO and HTEO copolymers increases with increasing defect content. For instance, the difference of T_m between both systems is about $25^{\circ}C$ at around 2.0% of defect content. A spontaneously arising question is why T_m of HTEO copolymer is always higher than that of HMEO. The T_m of HTEO copolymer with about 2.0% defect content is even higher than that of H7-O with defect

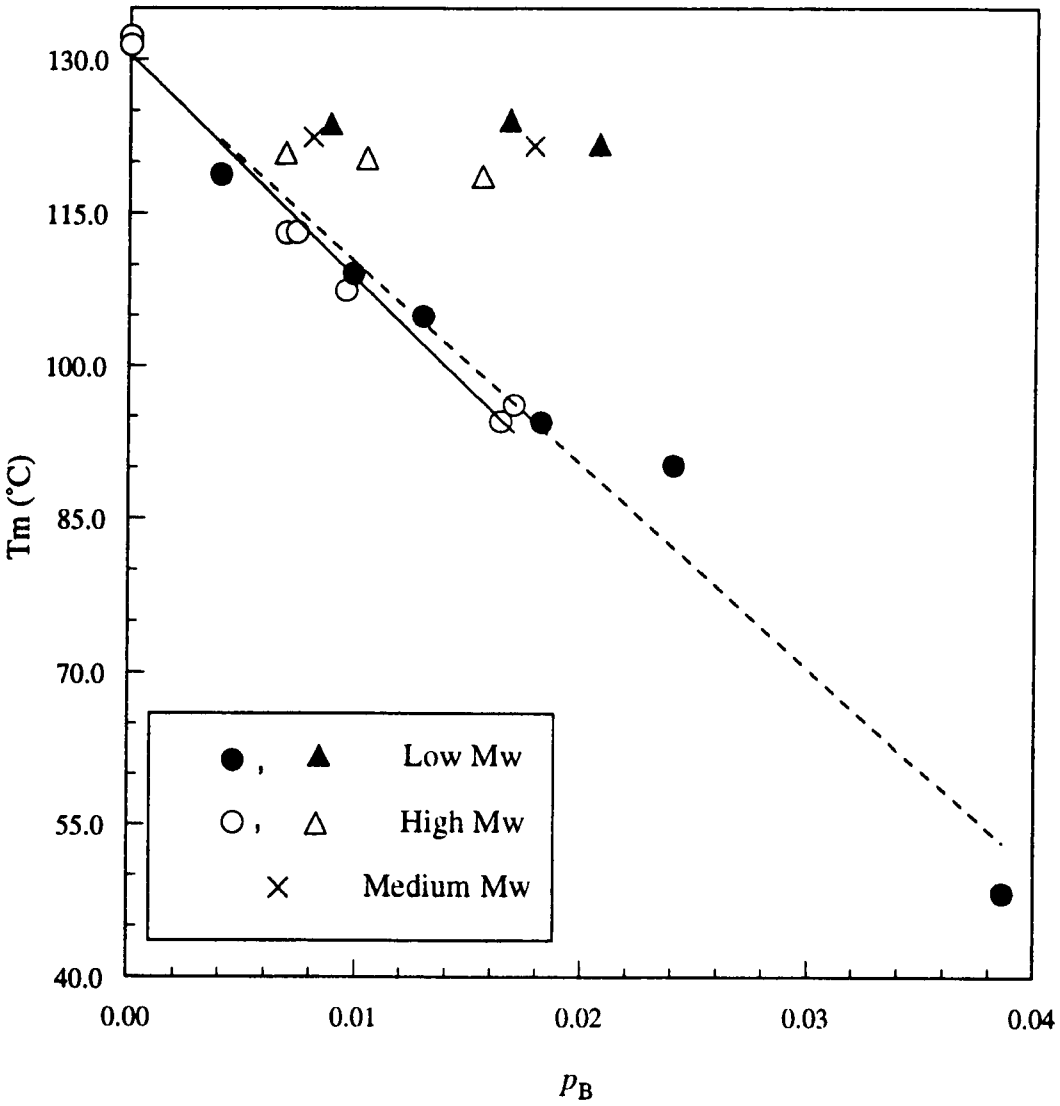


Figure 5.1.2.1. Peak melting temperatures as a function of branch content for the fast cooled homogeneous (circle) and heterogeneous (triangle and cross) EO random copolymers.

content of 0.7%. (This question is also directly related to the question why regime transition temperature of HTEO is higher than that of HMEO copolymers, which will be shown in the crystallization kinetics study). This question can be explained by considering the defect distribution in the polymer chain.

The HTEO copolymers obtained from the heterogeneous catalyst (i.e., classical Ziegler-Natta catalyst) are consisted of the inter- and the intra-heterogeneous distribution of branches while the HMEO copolymers from the homogeneous catalyst have the better uniform distribution of branches along the main chain. A schematic diagram for heterogeneous and homogeneous copolymers is shown in **Figure 5.1.2.2**. In the heterogeneous copolymer, the branches (i.e., B-counits) locally distribute. This local distribution of branches separates the polymer chain with two parts. One is long A-sequence length without branch and the other is short A-sequence. An extreme case is the polymer chain consisting of long A-block and short B-block. After all, in the case of the heterogeneous copolymer, the long A-sequence length will be crystallized at high crystallization temperature, excluding the branch concentrated part and causing high melting temperature. The exclusion of highly branched chain region is more probable since inclusion requires a large excess energy to be provided experimentally. This long A-sequence part will behave similar to the chain of linear polymer allowing chain folding and thickening. In other words, the branch content of HTEO copolymer contributes little to the melting temperature as long as the A-sequence length long enough. In fact, **Figure 5.1.2.1** shows that the T_m of HTEO copolymers are close to those of linear polyethylenes. On the other hand, the homogeneous copolymers have a more uniform distribution (i.e., delocalization) of defects on the chain, which reduce the A-sequence chain length. Melting temperature of HMEO copolymer is depressed by both inclusion and exclusion of defect. Inclusion reduces the heat of fusion while exclusion reduces the

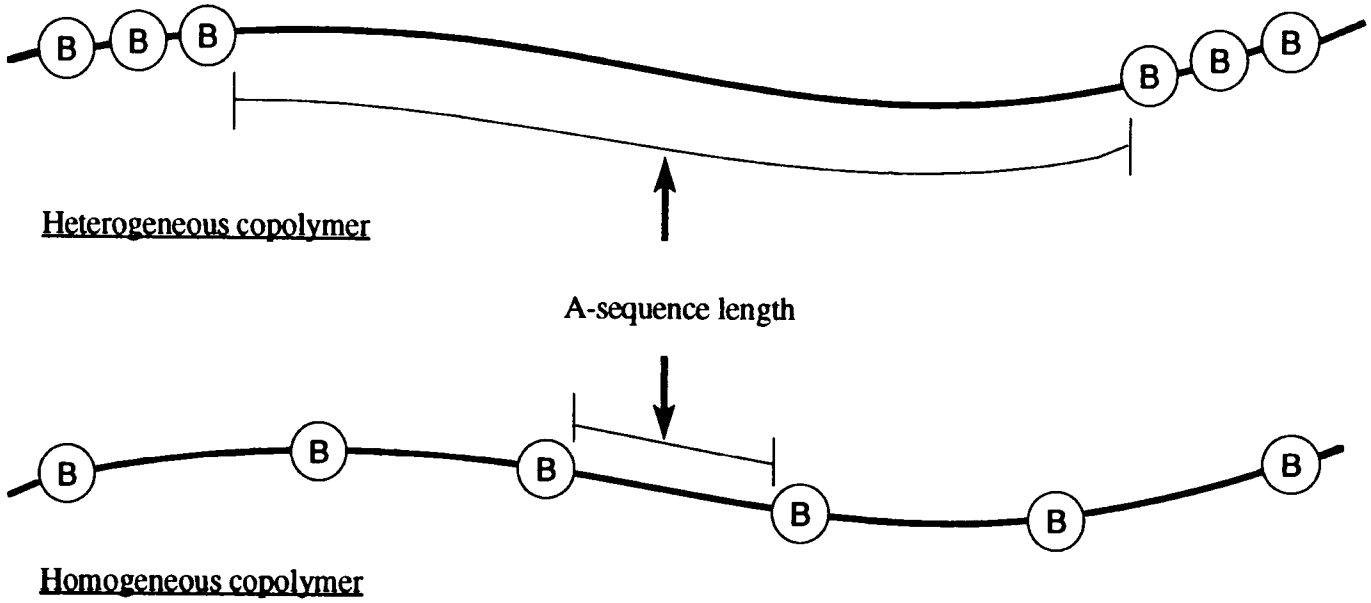


Figure 5.1.2.2. Schematic diagram for heterogeneous and homogeneous copolymers of extreme case.

lamellar thickness. (Inclusion and exclusion of defect will be discussed in **Section 5.3**). Therefore the heterogeneous copolymer has higher T_m than that of the homogeneous copolymers although two copolymers have the same branch content numerically. Similarly, crystallization temperature of heterogeneous copolymers becomes higher than that of the homogeneous copolymers. The less clear relationship between T_m and defect content may also be due to the heterogeneous distribution of defects.

In conclusion, one of the most important factors governing T_m of olefin type copolymers is the branch distribution in copolymer system rather than branch content. The regime transition study for HTEO and HMEO copolymers is another evidence to support the importance of defect distribution on melting behavior as well as crystallization process.

5.2. Bulk Crystallization

5.2.1. Avrami Analysis

Crystal growth mechanism and nucleation type can be obtained with Avrami exponent (or index). A question is which part of slope must be chosen for estimating Avrami index. Both the initial part including the initial point, and the linear region around half time without including the initial point in the plot of reduced crystallinity versus time (**(a)** of **Figure 4.2.1.1 ~ 4.2.1.5**) give different Avrami values, n and n', respectively (**Table 4.2.1.1**). Avrami index was plotted as a function of crystallization temperature (**Figure 5.2.1.1**) and branch content (**Figure 5.2.1.2**).

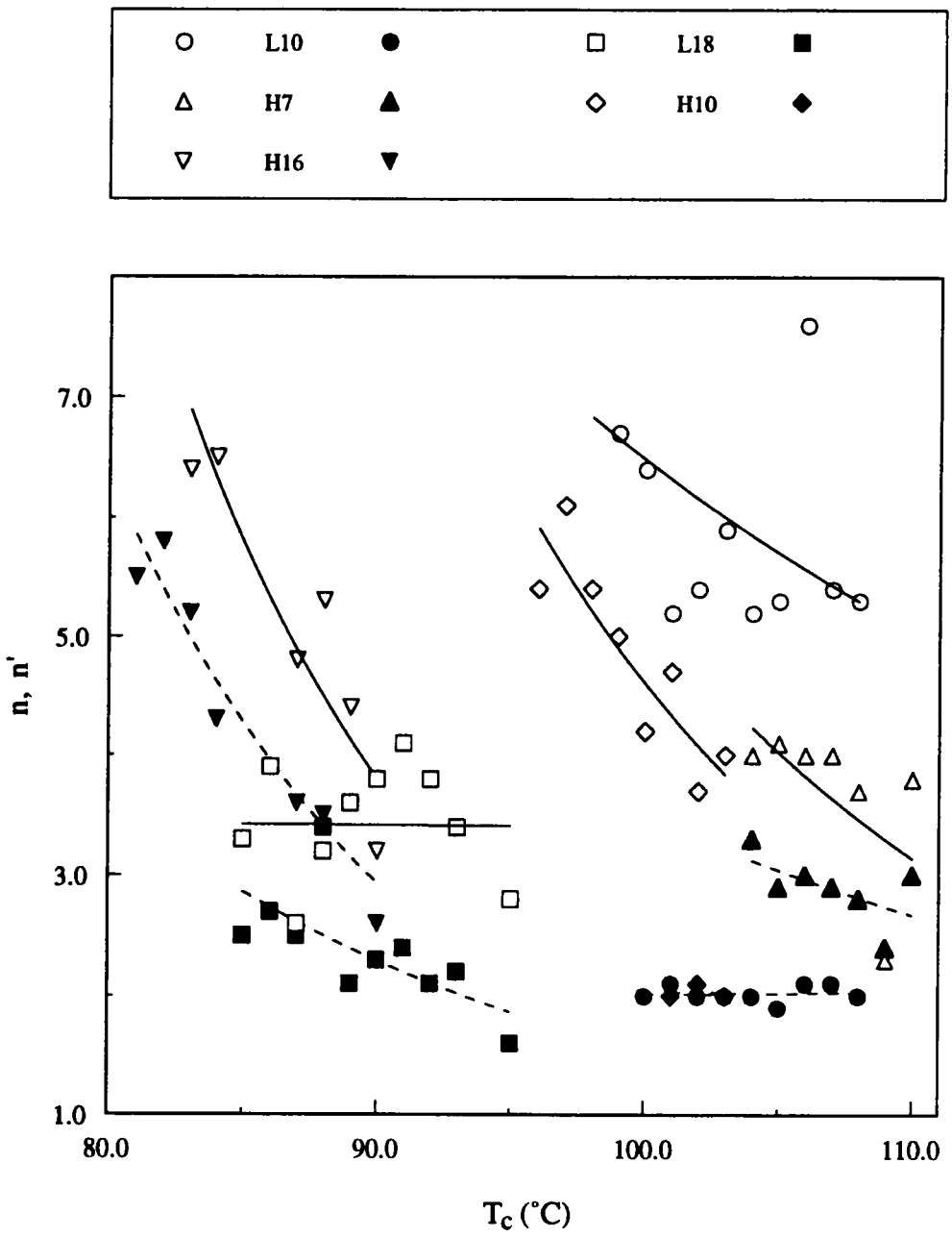


Figure 5.2.1.1. Avrami index with crystallization temperature. (open and closed symbol : obtained including initial point and except initial part, respectively).

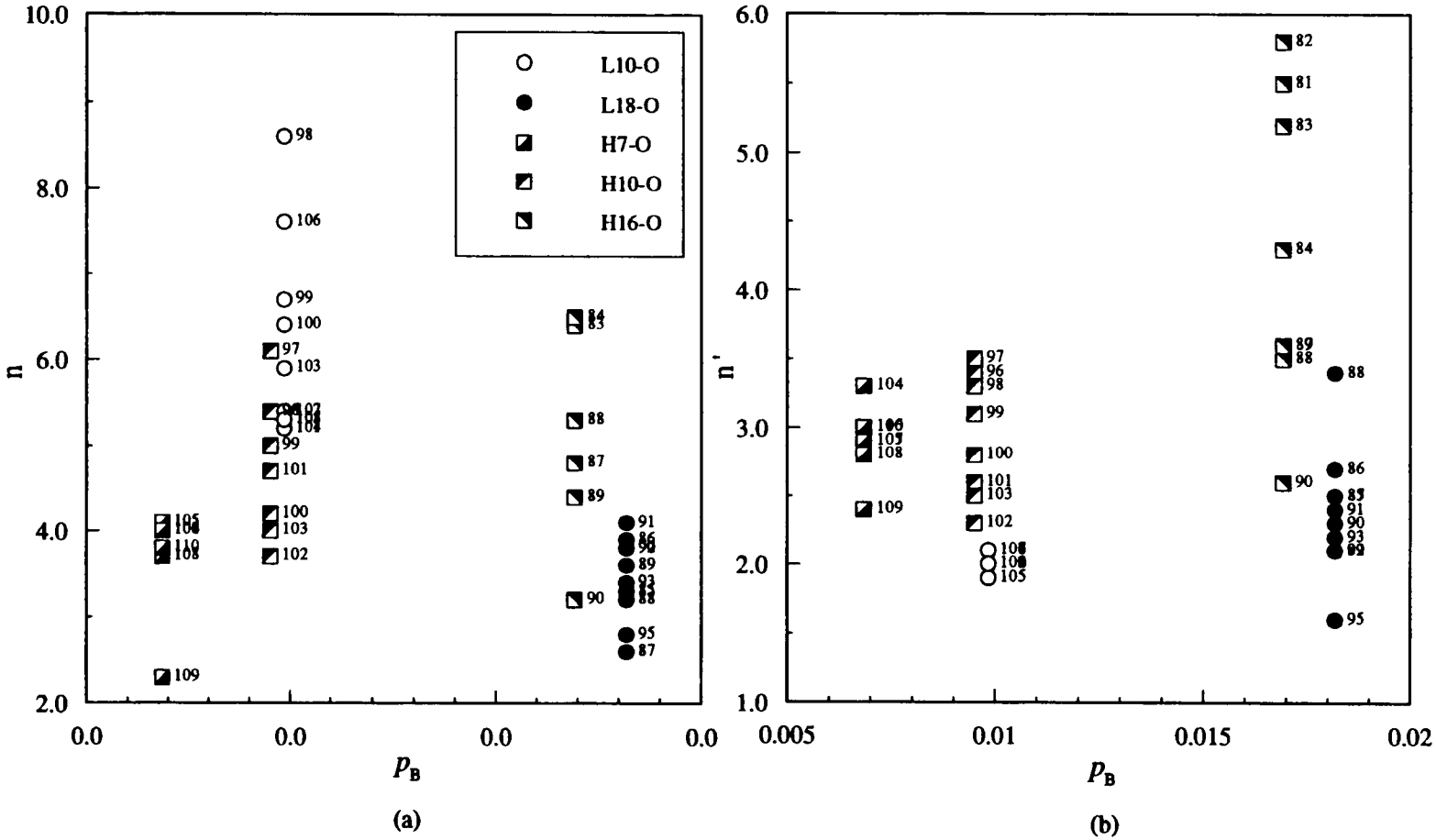


Figure 5.2.1.2. Avrami index n (a) and n' (b) as a function of branch content, obtained including initial point and except initial part, respectively.

The non-integer values of Avrami index, unlike integer value n expected theoretically, were observed in all systems. The fraction may be due to the co-existence of two different nucleation types as well as different growth mechanism. In the following discussion, the fraction of Avrami index will be rounded off for simplicity.

5.2.1.1. At Early Stage of Crystallization Process.

The Avrami analysis of the early crystallization stage is important because the crystal embryo or nuclei are sufficiently isolated to satisfy the assumption behind the Avrami equation. The growth analysis of crystal embryo or nuclei was obtained from the region within the reduced crystallinity of less than 3%.

• Crystallization Temperature Effect

As crystallization temperature increases, the values of n for most samples decrease, except for the case of H7-O. This indicates that crystal growth at early stage depends on crystallization temperature. High value of Avrami index indicates the complicated geometry (e.g., sheaf shape) while a low value the simple geometry (e.g., rod shape). L10-O has the values between $n \approx 8$ and $n \approx 5$ in the form of non-integers. The values of non-integer may be due to the co-existence of different nucleation process or the nonuniform shape of the crystals(i.e. deformed from the ideal geometry). Unlike L10-O, the n values of H7-O show almost constant integer values, $n \approx 4.0$, indicating uniform nucleation in system.

• Branch Content and Molecular Weight Effect

The branch and molecular weight influence is shown in **Figure 5.2.1.2.** There is an inconsistency between high and low molecular weight. In the high molecular weight samples , both the values of n increase with branch content. On the other hand, in the samples of low molecular weight, the n values of low branched samples are lower than those of highly branched samples.

For the high molecular weight series, branched H10-O and H16-O have a severe deviation from integer n unlike that of low branched H7-O. Understanding of this behavior is not possible at present. A possible explanation is to consider the distribution of branches along the main chain. As far as the copolymers have uniform inter- and intra-distribution, the nucleation mechanism should be consistent in the whole temperature range. Lowest branch content can satisfy this uniform distribution since the sequence length is sufficiently long to crystallize without facing the branch. As branch content increases the uniform distribution can not be satisfied as mentioned in thermal analysis **section 4.1** and **5.1**. At high temperature only high A-sequence length will be participated and the morphology should match with lowest branch content. In fact, the values n of H10-O at high T_c are close to $n \approx 4.0$ of H7-O, which represents the sporadically formed (heterogeneous) spherical crystal embryo (i.e., initial spherulite).

For the branched samples of low molecular weight, the branch effect becomes more complicated. The low branched L10-O starts initial crystal growth in the form of a sheaf by the heterogeneous (sporadic) process ($n \geq 6$) at low T_c or by the homogeneous (simultaneous) nucleation ($n \geq 5$) at high T_c whereas high branched L18-O ($n = 3 \sim 4$) forms a spherulite by homogeneous and heterogeneous nucleation. A fact that cannot be

understood is why highly branched L18-O must form spherulite type growth and low branched L10-O sheaf-like growth. One possible explanation can be done by comparing Avrami index of the crosslinked low density polyethylene. According to the data by Phillips and Kao [44], the highly crosslinked polyethylene and gel (low chain mobility and high viscosity) tend to have the low Avrami index around $n \approx 2.5 \sim 4.0$ while lightly crosslinked polyethylene and gel (high chain mobility and low viscosity) to have $n \approx 5.0 \sim 6.0$. The comparison of the Avrami exponents between EO copolymers and crosslinked polyethylenes imply that the viscosity of medium (or chain mobility) can be a factor to determine the crystallization mechanism. The Avrami exponents decrease as the branch content and the viscosity of medium increase.

The molecular weight influence on the initial crystal growth can be shown by comparison of L10-O and H10-O with the same branch content. When the values of n are compared at the same temperature (for example $T_c = 103°C$), the values n of L10-O (melt index : 26.70), $n = 5.9$, are higher than that, $n = 4.0$, of H10-O (melt index : 0.50). To understand the relationship between the branch content and the viscosity is required.

5.2.1.2. Crystallization Process at Middle Stage.

The analysis of linear region around the reduced crystallinity 50% can give information about the mechanism of growing crystal. The Avrami index n' of the middle stage of crystallization is smaller than n of the initial stage. The complicated geometries of initial crystals converge to more simple geometries with time. Most crystal aggregates are disks or spherulites, except for the H16-O at low crystallization temperature.

• Crystallization Temperature Effect

The change of Avrami index n' at the middle stage crystallization is less severe compared to that of n at the initial stage except for H16-O. This means the morphology change is small with temperature. In fact, the rate of crystallization increases linearly with crystallization time.

• Branch Content and Molecular Weight Effect

As branch content in system increases, the Avrami exponent shows non-integer values. The theoretically derived Avrami exponents were for the case of the simple geometries such as sheaf, rod, disk and sphere whose dimension is uniform. The deviation from integer value may mean that the geometry and dimension of the growing crystal is not uniform. In fact, even a single spherulite in the system tends to show a different growth rate in different directions. However, if there is the expulsion of the low molecular weight molecules (LMWM) and defects such as branching points, branch ends, branches, and main chain ends from the crystalline phase as a crystal grows, the growth front will confront the different thermodynamic environments which cause the chemical potential to change unlike before. Also the expelled defect fraction or low molecular weight molecules may not be distributed equally on all growth front directions due to the viscosity of the medium and the crystal growth cannot be uniform under the localization of LMWM and defects. The less LMWM and defects on growth front, the faster crystal growth. This uneven growth makes its geometry nonuniform, which may cause the non-integer Avrami index. Therefore the high branched sample H16-O has a more deviated Avrami index. The non-integer value indicates the actual system is not ideal.

The molecular weight effect on the Avrami analysis of the branched polymer can be analyzed by comparison of L10-O and H10-O. The geometry of low molecular weight L10-O is not sensitive to crystallization temperature and may be the uniform disk shape geometry due to the integer value of Avrami exponent. On the other hand, the high molecular weight H10-O has the non-uniform spherical shape at low crystallization temperature and the non-uniform disk-like shape at high crystallization temperature. The reason is not easy to understand.

The comparison of n and n' for L10-O, H10-O and H16-O show the crystal change from sheaf-like form to disk or spherical geometry as it grows.

5.2.2. Rate of Crystallization

- Molecular Weight Effect

The effect of molecular weight on the crystallization rate can be analyzed when a branch content is fixed. When L10-O and H10-O are compared, the crystallization rate of high molecular weight H10-O is lower than that of low molecular weight L10-O and the crystallization temperature of H10-O shifts toward lower temperature. The difference between the crystallization temperatures of low and high molecular weight polymer at constant crystallization rate is about $20^{\circ}C$. The reason may be due to the chain mobility since the chain must have a conformational change to transform from the amorphous state to the crystalline phase. If we disregard the branch effect or assume the contribution of the branch effect is equal due to the same amount of branch content, we can consider both branched polymers like linear polymers. In this case, we can apply the reptation theory.

According to de Gennes[66], the entangled polymers can rearrange their conformation through reptation process. The self-diffusion coefficient D of a single free chain P in a gel is dependent on the chain length (or molecular weight) as follows:

$$D \sim 1/M^2 \qquad (5.2.2.1)$$

and the relaxation time required for complete renewal of the chain conformation

$$\tau \sim M^3 \qquad (5.2.2.2)$$

Also the long chain will have high friction coefficient $\zeta_r = n\zeta_o$ on reptation causing the rate of crystallization to slow. Here ζ_o, are the friction coefficients of the repeating unit, n. High molecular weight H10-O needs more time for conformational change and its long chain will cause higher friction coefficient. Therefore the crystallization rate is reduced with molecular weight as shown in **Figure 4.2.2.1.** and **4.2.2.2**. .

• Branch Effect

At constant crystallization temperature or supercooling, the highly branched polymer chains have lower rates of crystallization. The branch effect on the reptation rate ($\bar{r}_{rept}$) is not well known theoretically. Relying on experience, branching may cause an extra friction force during a polymer chain movement due to the junction point and bulky side group. Side chains also possess their own frictional force. If we assume that they contribute as a linearly independent manner, the total friction force $f(n,n_i,n_j,n_k,T)$ for $T >> T_g$ can be expressed as follows:

$$\zeta_t(n,n_i,n_j,n_k,T) = n \cdot \zeta_o(T) + \sum_i n_i\zeta_i(T) + \sum_j n_j\zeta_j(T) + \sum_k n_k\zeta_k(T) \quad (5.2.2.3)$$

where n, n_i, n_j and n_k are the number of repeating unit of the main chain, the number of the branch chain with length *i*., the branching point and the branch end. And ζ_o, ζ_i, ζ_j and ζ_k are the corresponding friction coefficients. When we consider that the reeling-in rate contributes to crystal growth, the rate of crystallization should decrease with increasing branch content as following manner[67]

$$\bar{r}_{repl}(\sim 1/t_{1/2}) \sim \bar{f}_c/\zeta_t(n,T) \qquad (5.2.2.4)$$

$$\bar{f}_c = (1/l_g^*)a_o b_o(\delta l)(\frac{\Delta H_f \Delta T}{T_m^o}) \qquad (5.2.2.5)$$

where $\bar{f}_c$ is the mean force drawing the polymer chain onto the substrate that is proportional to ΔG. (see **Figure 4.2.2.1.** and **4.2.2.2**). Also as branch length increases, the rate of crystallization will decrease. As branch length increases further the reptation process becomes impossible causing no crystallization. Despite this quite empirical explanation, we can reach the same expectation that there is no reptation process in the case of the polymer chain with long enough branch using reptation theory developed for explaining viscoelastic behavior of star shaped polymers.[68,69]

Crystallization temperature for a given crystallization rate shifts to lower temperature with the branch content. This behavior can be rationalized using the **relationship (5.2.2.4)** and **equation (5.2.2.5)**. For the highly branched polymer chain to be crystallized, the mean force, $\bar{f}_c$, associated with crystallization should overcome the total friction coefficient. Therefore, the low crystallization temperature (i.e., high supercooling) is necessary for highly branched chain to be crystallized as long as the crystallization temperature is above the glass transition temperature.

5.2.3. Secondary Nucleation Kinetics

Another method to analyze the crystallization kinetics was developed by considering the relative values of the rate of nucleus deposition, $i(nuclei/cm/\text{sec})$, and the lateral spreading rate, $g(cm/\text{sec})$, of the growing crystal face. Depending on i and g, three Regimes may develop. In Regime I, g is much greater than i as a single surface nucleus leads to completion of the substrate face and the overall growth (or crystallization) rate is $G_I = i \cdot g$. In Regime II, both i and g rates are comparable, more surface nuclei are involved in substrate completion and $G_{II} = b_0(2ig)^{1/2}$. In Regime III, i is greater than g and the crystal growth rate G_{III} is governed by the rate of deposition of nuclei. In this case, G_{III} becomes again proportional to i.

There was extensive research conducted on bulk kinetics study of polyethylene. It has been shown that there is a Regime I-II transition for linear polyethylene[70], and linear low density polyethylenes (ethylene/1-octene random copolymers) obtained using heterogeneous catalyst[71] and Regime III for crosslinked linear polyethylenes due to elimination of reptation by Phillips *et. al.*[15]. The main objective of this study is to use copolymers with branches distributed randomly. The bulk kinetics of EO copolymers produced using uniform site catalyst (a kind of metallocene catalyst) will be studied as a function of molecular weight and branch content. The results will be compared to those of copolymer fractions from heterogeneous catalystis by Lambert *et.al.*[71]

The reciprocal half time $1/t_{1/2}\,(\text{sec}^{-1})$ was used for the regime analysis instead of the linear growth rate $G(cm/sec)$ by Lauritzen-Hoffman[72, 73]. This was verified by Magill[74] and then by many authors.[44, 71, 75] Magill reported that there is a correspondence between reciprocal half time and linear growth rate. Phillips *et. al.*,[15] showed that values of

$\sigma\sigma_e$ from reciprocal half time analysis can be compatible with those from linear growth rate in the kinetics study of crosslinked polyethylenes, while Lambert *et.al.*,[71] showed the bulk kinetic data may not be used to estimate fold surface free energy (σ_e) but may be used to determine regime transition temperatures. In this study the σ_e was obtained from the Thompson-Gibbs plot.

5.2.3.1. By Reciprocal Half-time ($1/t_{1/2}$)

The regime analysis to understand the crystallization process is performed with the rate of crystallization by reciprocal half-time ($1/t_{1/2}$) in **Figure 5.2.3.1**, assuming the heterogeneous **(a)** and the homogeneous **(b)** secondary nucleation. Of interest is the experimental result that the plot of the homogeneous secondary nucleation shows the same regime transition behavior as that of the heterogeneous nucleation. To know which nucleation type is a reasonable process, the results of regime analysis such as the slope of each regime and the surface energy were compared for both cases. When the ratio of regime slopes is compared, L10-O is close to the theoretical value, $K_g(I)/K_g(II) = 2.0$ for heterogeneous nucleation while H10-O is close to the theoretical one for homogeneous nucleation. Superficially, this comparison can indicate the prevailing nucleation mechanism. However when the values of $\sigma\sigma_e$ are considered, the values obtained from the case of the homogeneous nucleation are non-sensibly large. Therefore, the assumption of the homogeneous nucleation can not be applied in linear low density polyethylene even allowing a large enough error range. According to Lambert and Phillips [71], the kinetic parameter such as σ_e may not be obtained from the bulk kinetics data, In fact, the values of lateral surface energy σ are much higher than the literature values (especially, in the case of homogeneous nucleation, σ values are unreasonably high) when the values of

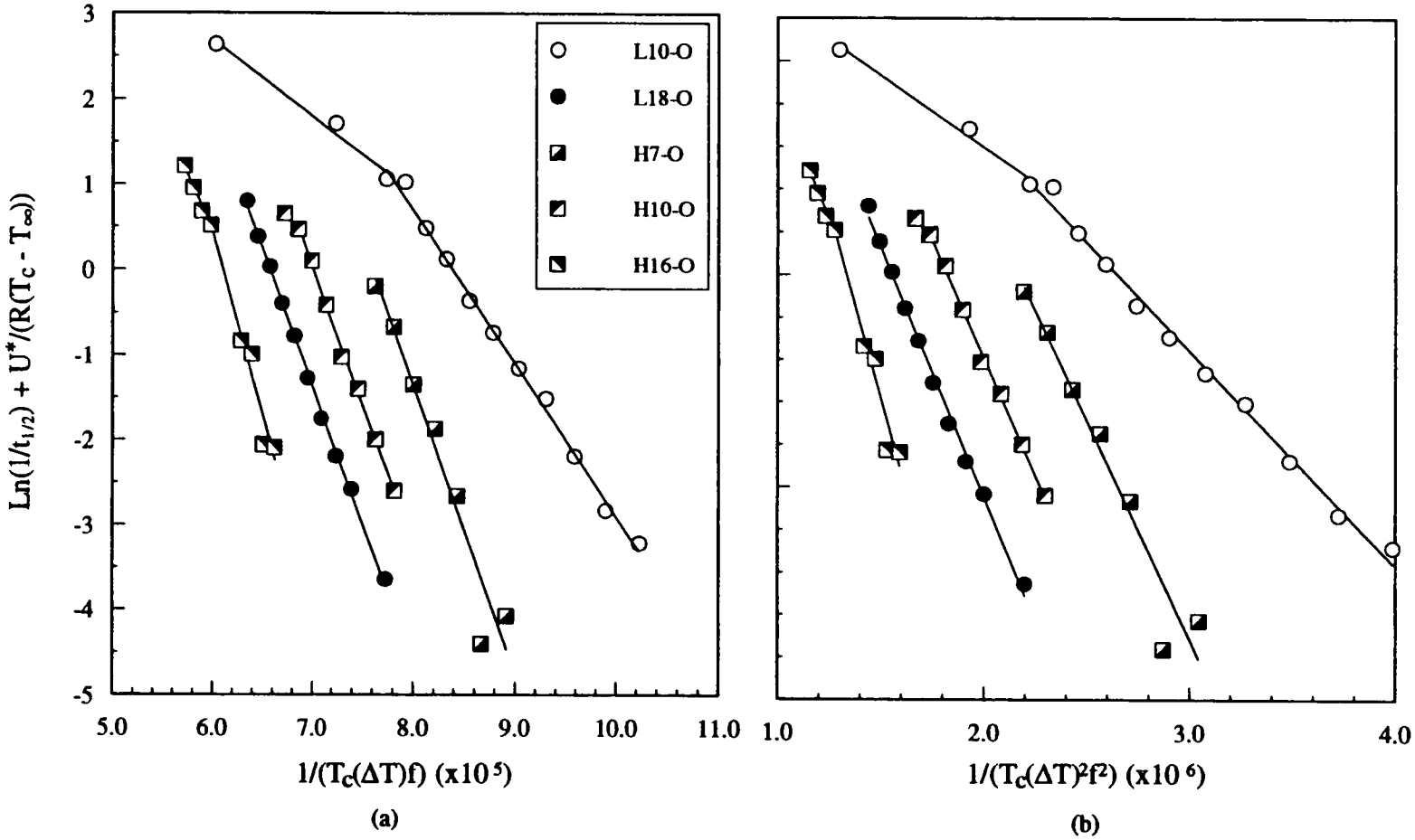


Figure 5.2.3.1. Regime plots of the bulk crystallization kinetics analyzed with half time ($t_{1/2}$) assuming a heterogeneous (a) andhomogeneous (b) secondary nucleation (T_∞ = -70 °C, U* = 1500 cal/mole).

σ_e are obtained independently from the Thompson-Gibbs plot. The value of σ_e is somewhat wide range from 30 to 140 erg/cm^2 [76,77,78] Ultimately the system of homogeneous olefin copolymer should be controlled by heterogeneous nucleation. The ratio, $K_g(I)/K_g(II)$, deviates from the theoretical value. This deviation from theoretical values may be due to the possibility that the system is not crystallized strictly by the relative rate of i and g in each regime (see **Table 5.2.3.1** and **5.2.3.2**).

• Input Parameter Effect

Two different glass transition temperatures, $T_g = -40\ ^\circ C$[44, 71] and $T_g = -125\ ^\circ C$[52], obtained from the literature were used to check the importance of this parameter. As expected from the secondary nucleation equation, the glass transition temperature does not affect the regime transition behavior since the term of T_g will contribute only to the shift of the y-axis. The calculated results are shown in **Figure 5.2.3.1 ~ 4** and **Table 5.2.3.1** and **5.2.3.2**) In a like manner, the value of the activation energy U* will not affect the regime transition behavior but only the shift of the y-axis.

• Molecular Weight Effect

The observed regime I – II transition (T_{I-II}) of L10-O and H10-O was observed at 96.5 and 97.5 $^\circ C$, respectively. T_{I-II} of low molecular weight sample L10-O is close to T_{I-II} of high molecular weight H10-O. However when the transition point was determined from supercooling, the regime I-II transition supercooling, $(\Delta T)_{I-II} = 38.1\ ^\circ C$, of low molecular weight (L10-O) was observed as much as $3^\circ C$ lower than that,

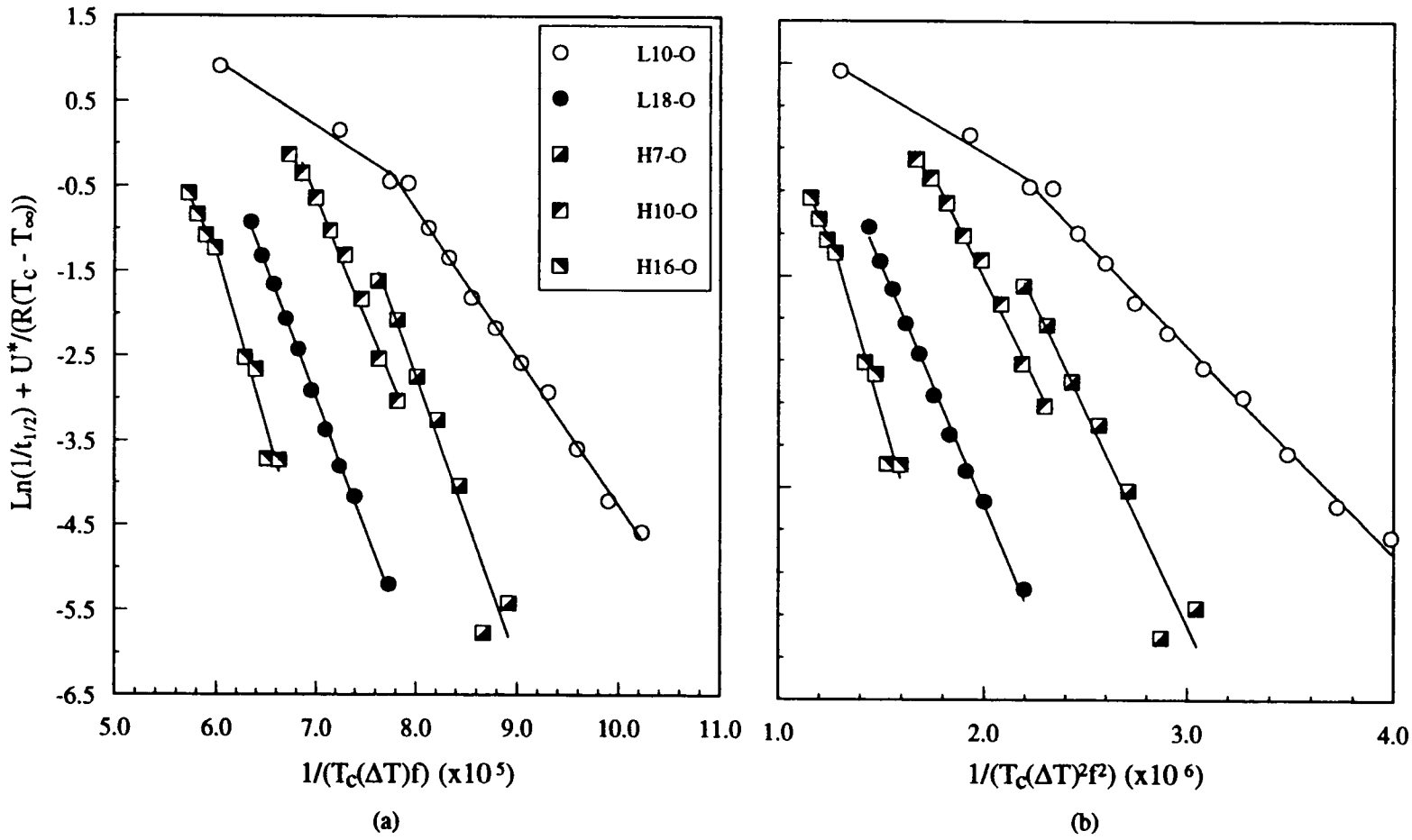


Figure 5.2.3.2. Regime plots of the bulk crystallization kinetics analyzed with half time ($t_{1/2}$) assuming a heterogeneous (a) and homogeneous (b) secondary nucleation (T_∞ = -155 °C, U* = 1500 cal/mole).

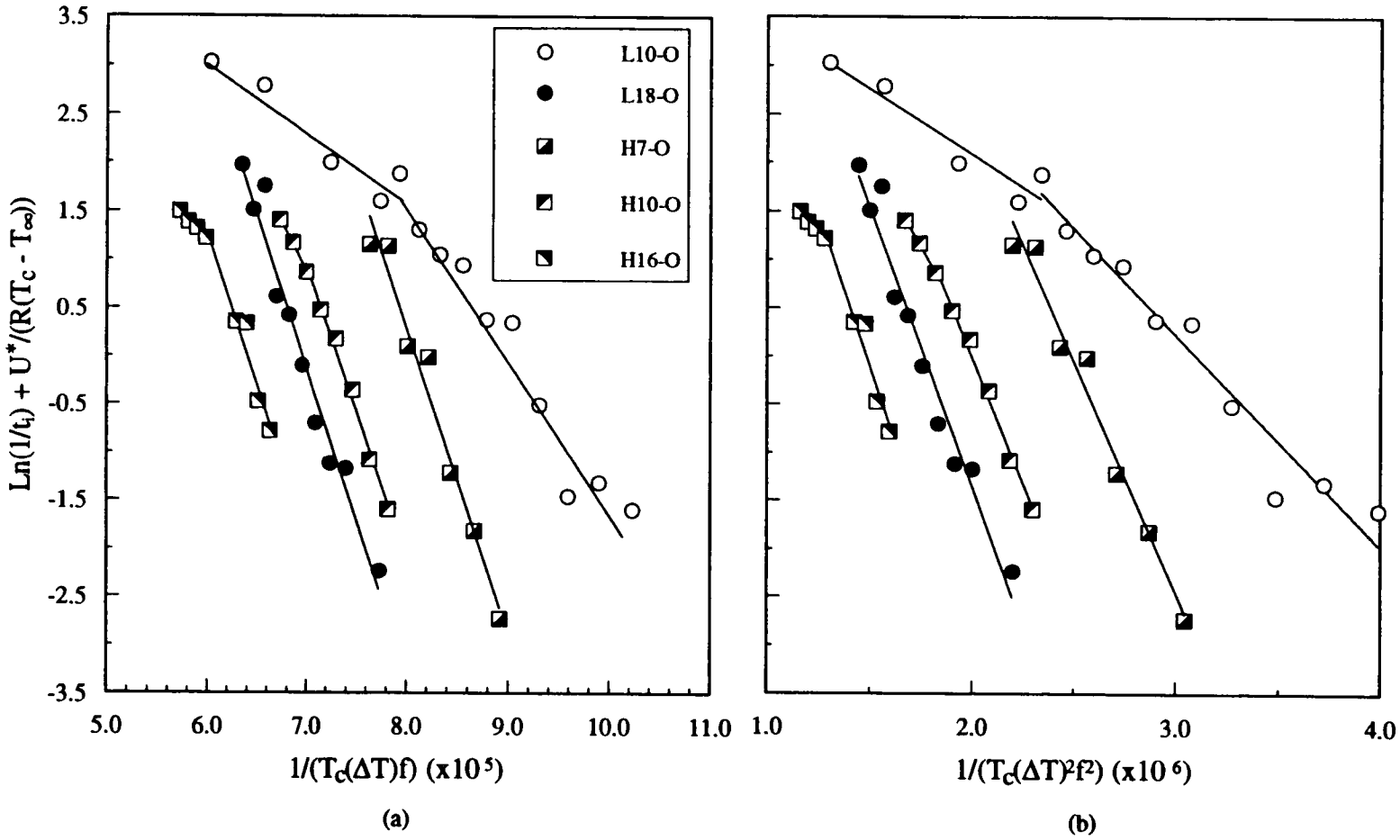


Figure 5.2.3.3. Regime plots of the bulk crystallization kinetics analyzed with initial time (t_i) assuming a heterogeneous (a) and homogeneous (b) secondary nucleation (T_∞ = -70 °C, U* = 1500 cal/mole).

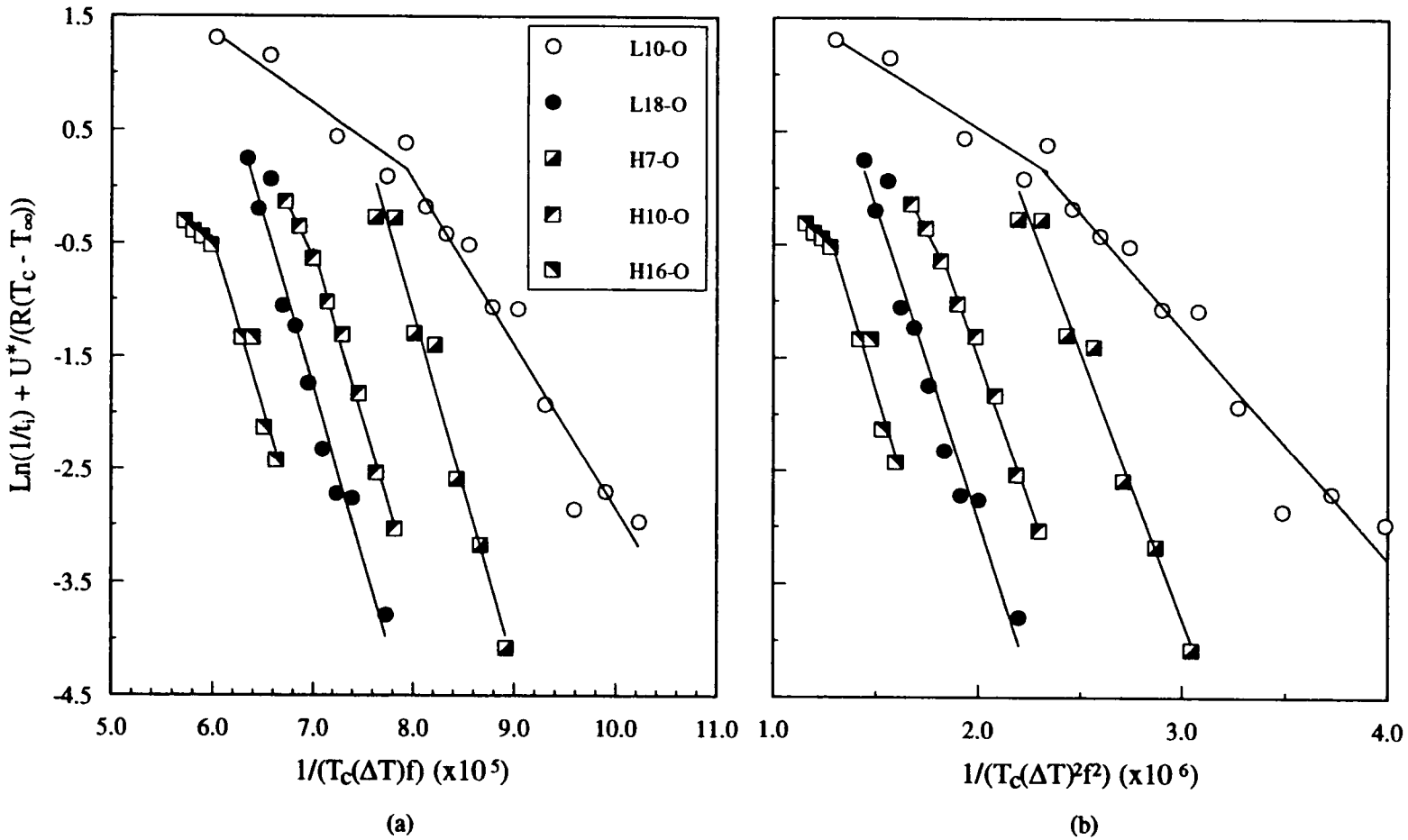


Figure 5.2.3.4. Regime plots of the bulk crystallization kinetics analyzed with initial time (t_i) assuming a heterogeneous (a) and homogeneous (b) secondary nucleation (T_∞ = -155 °C, U* = 1500 cal/mole).

Table 5.2.3.1. Analysis of regime slopes.(T_∞ = -70 °C, U*=1500 *cal/mole*)

sample	reciprocal time (sec^{-1})	for heterogeneous nucleation						for homogeneous nucleation					σ_e[a] (erg/cm^2) from Thompson-Gibbs Eq.
		$\ln(1/t)_o$ (sec^{-1})	$K_g(I)$ / $K_g(II)$ ×10^5	$\frac{K_g(I)}{K_g(II)}$ (dev. %)	$\sigma\sigma_e$ (erg^2/cm^4)	σ (erg/cm^2)	$T_{I\text{-}II}$ ($\Delta T_{I\text{-}II}$) (°C)	$\ln(1/t)_o$ (sec^{-1})	$K_g(I)$ / $K_g(II)$ ×10^4	$\frac{K_g(I)}{K_g(II)}$ (dev. %)	$\sigma\sigma_e$ (erg^2/cm^4)	σ (erg/cm^2)	
L10-O	$1/t_{1/2}$	15.08(I) 8.02(II)	1.80 0.89	2.02 (+1.1)	1058.8 1045.8	22.8 22.5	96.5 (38.1)	6.72 4.83	2.540 1.667	1.52 (-23.8)	14957 19633	322 422	46.5
L18-O		21.08(I)	3.21		1901.4	36.2		9.13	5.879		34846	664	52.5
H7-O		25.86(I)	3.40		1974.9	35.8		11.15	5.147		29869	541	55.2
H10-O		22.59(I) 10.22(II)	3.21 1.42	2.26 (+12.8)	1872.5 1659.1	33.4 29.6	97.5 (41.1)	10.08 5.08	5.534 2.654	2.09 (+4.3)	32261 30943	576 553	56.0
H16-O		26.09(I) 16.47(II)	4.28 2.67	1.60 (-19.9)	2521.5 3151.7	45.2 56.6	84.0 (49.9)	11.63 7.98	8.717 5.871	1.48 (-25.8)	51390 69224	923 1243	55.7
L10-O	$1/t_i$	14.28(I) 7.51(II)	1.58 0.74	2.13 (+6.8)	931.0 871.6	20.0 18.7	96.5 (38.1)	6.84 4.78	2.206 1.347	1.64 (-18.1)	7932 25982	171 559	
L18-O		21.90(I)	3.15		1866.5	35.6		10.16	5.76		34153	651	
H7-O		25.59(I)	3.17		1836.7	33.3		11.93	4.80		27833	504	
H10-O		22.39(I) 14.70(II)	3.06 1.98	1.54 (-22.7)	1786.2 2303.9	31.9 41.1	97.5 (41.1)	10.43 7.50	5.23 3.65	1.43 (-28.4)	30483 42510	544 759	
H16-O		20.02(I) 7.19(II)	3.13 1.00	3.13 (+56.5)	1844.7 1176.7	33.1 21.1	84.0 (49.9)	9.46 4.02	6.39 2.19	2.91 (+45.9)	37690 25858	677 464	

dev.% = $[(K_g(I) / K_g(II) - 2)/2] \times 100$

a) σ_e was estimated from Kelvin temperature scale. Lamellar thickness was determined from the small angle X-ray scattering spectroscopy.

Table 5.2.3.2. Analysis of regime plots.(T_∞ = -155 °C, U*=1500 *cal/mole*)

sample	reciprocal time (sec^{-1})	for heterogeneous nucleation						for homogeneous nucleation					σ_e[a] (erg/cm^2) from Thompson-Gibbs Eq.
		$\ln(1/t)_o$ (sec^{-1})	$K_g(I)/K_g(II)$, $\times 10^5$	$K_g(I)/K_g(II)$ (dev. %)	$\sigma\sigma_e$ (erg^2/cm^4)	σ (erg/cm^2)	T_{I-II} (ΔT_{I-II}) (°C)	$\ln(1/t)_o$ (sec^{-1})	$K_g(I)/K_g(II)$, $\times 10^6$	$K_g(I)/K_g(II)$ (dev. %)	$\sigma\sigma_e$ (erg^2/cm^4)	σ (erg/cm^2)	
L10-O	$1/t_{1/2}$	13.15(I) 5.52(II)	1.74 0.76	2.28 (+14.5)	1025.9 895.1	22.1 19.2	96.5 (38.1)	5.05 2.78	2.46 1.43	1.72 (+14.0)	8403 28997	181 624	46.5
L18-O		18.58(I)	3.09		1828.5	34.8		5.65	7.10		33512	638	52.5
H7-O		29.98(I)	3.34		1939.5	35.1		5.05	9.52		29335	531	55.2
H10-O		19.22(I) 10.91(II)	2.84 1.64	1.73 (-13.4)	1654.5 1915.6	29.5 34.2	97.5 (41.1)	8.26 4.98	4.89 3.06	1.59 (+20.1)	28530 35724	509 638	56.0
H16-O		23.35(I) 13.44(II)	4.11 2.46	1.67 (-16.5)	2423.0 2897.0	43.5 52.0	84.0 (49.9)	9.46 5.63	8.38 5.40	2.98 (+49.0)	49392 63612	887 1142	55.7
L10-O	$1/t_i$	11.64(I) 5.08(II)	1.45 0.62	2.34 (+16.9)	853.9 731.4	18.4 15.7	96.5 (38.1)	4.91 2.78	2.05 1.13	1.81 (-9.3)	12078 13297	260 286	
L18-O		19.40(I)	3.03		1793.6	34.2		8.12	5.54		32818	625	
H7-O		23.70(I)	3.10		1801.3	32.6		10.31	4.70		27298	495	
H10-O		20.64(I) 12.41(II)	2.98 1.87	1.59 (-20.3)	1735.5 2174.5	31.0 38.8	97.5 (41.1)	8.65 5.62	5.08 3.44	1.47 (-26.2)	29615 40120	529 716	
H16-O		17.28(I) 4.15(II)	2.96 0.78	3.79 (+89.7)	1746.2 922.1	31.2 16.6	84.0 (49.9)	7.29 1.67	6.05 1.72	3.52 (+75.9)	35691 20245	959 363	

$dev.\% = [(K_g(I)/K_g(II) - 2)/2] \times 100$

a) σ_e was estimated from Kelvin temperature scale. Lamellar thickness was determined from the small angle X-ray scattering spectroscopy.

$(\Delta T)_{I-II} = 41.1\ ^{\circ}C$, of high molecular weight (H10-O). Physically, the analysis by supercooling is more reasonable based on the secondary nucleation theory. To understand the molecular weight effect on the crystallization kinetics at fixed branch content, let's think of classical reptation behavior of a polymer chain. The rate of reptation of a single chain, so-called reeling-in rate, $r(cm/\text{sec})$, from the molten state to the substrate decreases with chain length as well as the rate of surface spreading $g(cm/\text{sec})$. The comparison of g with r is more easy to understand the reptation behavior of a single chain than with the net nucleation rate, $i(nuclei/\text{sec}\cdot cm)$, because of the consistency of the dimension. Both rate r and g have a known molecular weight dependence. The reeling-in rate r is faster as much as about c times than surface spreading rate g.[79] (Comment : Here the constant c was 36 in Hoffman and Miller's condition for linear polyethylene. These values may be different in our sample and supercooling condition). The fact of $r > g$ seems to be reasonable due to the niche on the substrate which will reduce the thermodynamic barrier. This may make the multiple nucleation possible leading to the physical phenomena of regime II. However, this imagines depends on the substrate length (L). We can consider two extreme cases, depending on the relative quantity of the distance, $l_{reptation}$, from an arbitrary place at which a single chain starts to move to the substrate and the substrate length, L : case (i) $l_{reptation} \geq cL$ and case (ii) $l_{reptation} << cL$. The case (i) can cause the surface spreading domination, since the faster r can not interrupt a polymer chain to spread on the substrate due to the long traveling distance to substrate and the system will have the same result with the regime I of the secondary nucleation theory. The case (ii) may lead to multiple nucleation on the substrate with the same manner probably leading regime III. Faster r will allow a single polymer chain to deposite on the thermodynamically favorable location of substrate and shorter $l_{reptation}$, than L will make a reeling-in polymer chain interrupt the surface spreading of the already-deposted polymer chain. As $l_{reptation}/L$ is reduced at constant L, the more polymer chains to be on the

substrate, which creates more nitches. As more thermodynamically favorable nitches are created the rate of deposition and growth rate will be accelerated. In fact, this bebavior can explain the fact that the initial stage of the S-shape light intensity profile shows sharp upturn at low temperature compared to that at high temperature. The regime II may be between these two extreme conditions.

The unknown fact is the effect of molecular weight on the $l_{reptation}$ and L. If we can calculate L experimentally, we can estimate $l_{reptation}$. Explanation is possible using the linear growth rate. In this study the rate of crystallization ($1/t_{1/2}$) was used for the same purpose. As shown in **Figure 4.2.2.2**, the rate of crystallization of H10-O is slow compared to that of L10-O due to the increasing of frictional force with the chain length. Phenomenologically, this slow rate of crystallization can be related to the slow reeling-in rate r while g is still favored thermodynamically. The large supercooling that is the necessary condition for high molecular weight to overcome the total friction coefficient (see **equation (5.2.2.5)**) and the slow reeling-in rate r for high molecular weight (see **equation (5.2.2.4)**) will cause the transition temperature T_{I-II} to occur at a high supercooling compared to low molecular weight.

• Branch Effect

Low branched H10-O has a higher regime I-II transition temperature $T_{I-II} = 97.5\ ^{\circ}C$ and lower transition supercooling $\Delta T_{I-II} = 41.1\ ^{\circ}C$ than high branched H16-O has $T_{I-II} = 84.0\ ^{\circ}C$ and $\Delta T_{I-II} = 49.9\ ^{\circ}C$, respectively.

This regime transition behavior of the branched polymer chain as a function of supercooling can be understood as the same way with the molecular weight effect using **equation (5.2.2.3) ~ (5.2.2.5)**. Based on **equation (5.2.2.3)** and **(5.2.2.4)** the reeling-in rate $\bar{r}_{repl}$ for high branched chain must be slow or zero due to the large total friction coefficient, $\zeta_t(n,n_i,n_j,n_k,T)$. For a single polymer chain to reptate to the substrate, it is required for $\bar{f}_c$ to be larger than friction coefficient. Remember $\bar{f}_c$ is the mean force drawing the polymer chain onto the substrate and proportional to the supercooling. Therefore, the high supercooling is necessary condition for high branched polymer chain to overcome the total friction coefficient (based on **equation (5.2.2.5)**). Chose an arbitrary temperature as regime transition temperature, the regime I-II transition temperature T_{I-II} for branched polymer takes place at low crystallization temperature and high supercooling than linear polymer. Therefore, the highly branched H16-O has lower crystallization temperature, $T_{I-II} = 84.0\ ^{\circ}C$, and higher supercooling, $\Delta T_{I-II} = 49.9\ ^{\circ}C$, than those, $T_{I-II} = 97.5\ ^{\circ}C$ and $\Delta T_{I-II} = 41.1\ ^{\circ}C$, of the low branched H10-O.

Of course, as temperature decreases, the friction force may be increased. Therefore thr eeling-in rate depends on the relative contribution of $\zeta_t(n,n_i,n_j,n_k,T)$ and $\bar{f}_c$. Below a certain temperature but above a glass transition temperature, if the contribution of $\zeta_t(n,n_i,n_j,n_k,T)$ become much larger than $\bar{f}_c$, there is no reeling-in process.

A surprising fact is that the regime transition temperatures of this study are very much lower than the literature values by Lambert and Phillips[71]. Their regime I-II transition temperatures are almost the same with $T_{I-II} = 125.0^{\circ}C$ of linear polyethylene. Even if LLDPE with 22 hexyl branches/1000 carbons shows the regime I-II transition temperature just $2.0^{\circ}C$ lower than that of liner polyethylene. The answer for this behavior can be extracted from the discussion on the melting temperature of homogeneous

and heterogeneous EO copolymers in **Section 5.1.2**. As described in earlier section, the difference of both systems is the defect distribution. The former has heterogeneous and the latter have rather uniform distribution of branches in chain (see **Figure 5.1.2.2**).

In the case of heterogeneous copolymer, the long A-sequence length will be crystallized at high crystallization temperature, excluding the branch concentrated part. This A-sequence part will behave similar to the linear polymer as long as A-sequence is long enough. Therefore, the branch content of heterogeneous copolymer contributes little to the regime transition temperature. On the other hand, the homogeneous copolymers have the better even distribution (i.e., delocalization) of branch on the chain, which reduce the A sequence chain length and lower the crystallization temperature. Therefore, although the polymers have the same branch content numerically, the heterogeneous copolymer is crystallized at high crystallization and the homogeneous copolymer crystallized at much lower crystallization. The previous melting study for heterogeneous and homogeneous EO copolymers also supports the importance of defect distribution on crystallization process.

5.2.3.2. By Reciprocal Initial-time ($1/t_i$)

One problem of kinetics study by measuring the transmitted light intensity is to reach the constant light intensity at the final stage. Unfortunately, this requirement cannot be achieved within experimental time scale since this region is related to the secondary crystallization process, which is very slow process. An example of this kind problem is shown above $T_c = 106.0\ ^{\circ}C$ in **Figure 4.2.1.1**. Normalized light intensity does not level off due to relatively short crystallization time, about 1 hr. To avoid this problem the

initial time was tested and compared to the result from $1/t_{1/2}$. The regime transition temperature obtained from $1/t_i$ coincides with that from $1/t_{1/2}$. But the ratios of slopes for regime I and II deviate more than those from $1/t_{1/2}$ analysis. However the values of σ obtained from the analysis of $1/t_i$ are similar to those from $1/t_{1/2}$ except for highly branched H16-O. Therefore, the reciprocal initial time may be selectively used to confirm the analysis of $1/t_{1/2}$ and may predict the regime transition temperature, thus avoiding long crystallization times.

5.3. Equilibrium Melting Temperature, T_m^o

The equilibrium melting temperature (T_m^o) of linear polyethylene is one of the controversies in polymer physics, many studies having been reported. However, there is inconsistency among literature values as listed in **Table 5.3.1**, although only the values obtained from the plots of T_m^o versus $1/l$ are listed. In the case of random copolymers the equilibrium melting point is depressed. Flory suggested that equilibrium melting point depression equation in the case of complete exclusion of defects from the lattice forming two phase(exclusion model). On the other hand, Sanchez-Eby derived the depression equation in the case of uniform inclusion of defects in the crystal forming solid solution (uniform inclusion model). Neither of these theories has been tested experimentally for olefin type random copolymer due to the difficulty of obtaining T_m^o. In the following section, a systematics discussion on the study of T_m^o carried out in this study is described.

Table 5.3.1. Equilibrium melting temperatures determined from the plot of T_m versus $1/l$ for linear polyethylenes.[a]

T_m° (°C)	Samples[b]	Molecular weight	References
145.8	-	-	H. E. Bair, T. W. Huseby and R. Salovey, Amer. Chem. Soc. Polym. Preprints, **9**, 795 (1968). J. D. Hoffman, G. T. Davis, J. I. Lauritzen, Treatise on Solid State Chemistry (Ed. N. B. Hannay), **3**, Chap 7, Plenum, NY (1976).
143.5±0.5	-	-	R. G. Brown and R. K. Eby, J. Appl. Phys., **35**, 1156 (1964).
142.0±0.3[c]	various	various	D. C. Bassett, A. M. Hodge and R. H. Olley, Proc. Roy. Soc. London, **A377**, 39 (1981).
141±0.5	various	various	K. H. Illers and H. Hendus, Makromol. Chem., **113**, 1 (1968).
139.0[d]	Marlex 6009	-	E. Martuscelli and M. Pracella, Polymer, **5**, 306 (1974).
138.15	Marlex 6001 [e]	-	J. Runt, I. R. Harrison, and S. Dobson, J. Macromol. Sci. Phys., **B17**, 99 (1980).

a) L. Mandelkern, G. M. Stack and P. J. M. Mathieu, Anal. Cal., 5, 223.
b) bulk crystallized.
c) Our analysis showed 140.84 °C instead of 142.0 °C when the data in reference was reanalyzed.
d) obtained from the plot of T_m versus reciprocal long period (not lamellar thickness). Thus, this value is not recommended for comparison, since the analysis is not correct based on Thompson equation.
e) suspension crystallization.

5.3.1. Hoffman-Weeks Plots

There are two distinctive phenomena in the plot of T_m versus T_c for the EO copolymers, which don't obey the theoretical expectation. One is the case of the anomalously high values of T_m^o for H7-O and L10-O or the case that T_m runs in the identical slope with T_c like the case of L18-O, causing no intersection point. Another is the deviation from linearity giving rise to the curvature.

Overestimation and $T_m = T_c + c$

Let us think about the first case. The crystallization temperature region for extrapolation is the high crystallization temperature that is closer to the equilibrium melting temperature (or equilibrium condition) than the low crystallization temperature. As mentioned in **Section 2.5.2**, when we consider that the Hoffman-Weeks plots were derived for the case of low supercooling to satisfy the linear relationship between the observed melting temperature and the crystallization temperature, the extrapolation region chosen here is reasonable. The overestimation tendency for H7-O and L10-O may be due to the inappropriate heating rate. As is well known, heating rate causes superheating or lamellar thickening during heating process. A question is whether a heating rate 10 °C/min used in this study is fast enough to prevent the thickening of thin lamellae or slow enough to prevent the superheating of thick lamellae for all the samples. The thickening occurs when the thermodynamically unstable thin lamella goes to the stable thick lamella. In this case, if a heating rate is slow and a system stays long enough at a particular temperature, the chance for a lamella to be thick will be increased and the melting temperature measured actually becomes the melting temperature of the thickened crystal. Therefore the

measured melting temperature of a sample becomes higher giving rise to diverge from $T_m = T_c$.

Superheating may occur for a thick crystal due to the thermal lag. If a heating rate 10 °C/min is so fast, the inside of a crystallite is not the same thermal environment with the outside of the crystal that is contact with the heating chamber and with the instrument itself by reason of heat transfer. Correspondingly, the inside of a crystal will be melted later, the measured temperature will be overestimated and the slopes in Hoffman-Weeks plot become more stiffer causing the intersection shifts to higher or infinitely high temperature.

The phenomenon of $T_m = T_c + c$, where $c \approx 10\ ^\circ C$, for L18-O in **Figure 4.3.1.2** have been also reported for the EO copolymers and the hydrogenated butadiene,[80] but the reason has not been understood. Although the constant c may be related to the molecular reorganization, it is not easy to give the exact physical meaning on c and to comprehend why highly branched low molecular weight L18-O show this kind of tendency.

Curvature

An attempt to explain the deviation from linearity in the plot of T_m versus T_c was done by Dalal *et.al.*, for *cis*-polyisoprene.[81], based on **equation (2.5.18)**. They claimed δl contributes as much as 10% to the lamellar thickness of cis-isoprene and suggested that $\delta l(\Delta H)(\Delta T)/2\sigma_e T_m^\circ$ cannot be neglected. In our case, a high supercooling effect can contribute to this term rather than lamellar thickness. In both cases **equation (2.5.18)** can be expanded in a binomial series as shown in

$$T_m = T_m^\circ - \frac{\Delta T}{\gamma}\left\{1 - \left(\frac{\delta l \Delta H_f}{2\sigma_e T_m^\circ}\right)\Delta T + \left(\frac{\delta l \Delta H_f}{2\sigma_e T_m^\circ}\right)^2 (\Delta T)^2 - \cdots\right\} \qquad (5.3.1.1)$$

For the case of $l = l_s^*$ (i.e. γ=1) **equation (5.3.1.1)** reduces to the expanded form of **equation (2.5.16.)** as shown by Alamo *et. al.*[79]. Taking only to second term in the parentheses and using the necessary parameters, ΔH_f, σ_e and T_m° listed in the **Table 5.3.1.1**, the melting temperatures calculated as a function of crystallization temperature are shown in **Figure 5.3.1.1** and **Figure 5.3.1.2** for high and low molecular weight, respectively. The ΔH_f for each copolymer were calculated using the equation

$$\Delta H_f(p_B) = 55.9 + 0.1942 T_m^\circ(p_B) - 7.2 \times 10^{-4} T_m^\circ(p_B)^2 \qquad (5.3.1.2)$$

suggested by Dole and used by E. Martuscelli et. al.[82]. T_m° and σ_e were obtained from the plot of the reciprocal lamellar thickness vs. the observed melting temperature (**Figure 4.3.2.2** and **Figure 4.3.2.3**). Here δl was assumed as $10\,\text{Å}$. The ratio of the lamellar thickness to initial lamellar thickness, so called thickening coefficient γ, was adjusted to have the best fitting curve with the observed melting temperature and the values were listed in **Table 5.3.1.1**. As B-counit increases the γ decreases. This means that the accumulated B-counits outside the crystalline phase, which were expelled from the lattice during the crystallization process, play roles as obstacles for the copolymer crystallization.

An arising general question is about the assumption(?) behind **equation (2.5.18)**, which γ is temperature independent constant. This kind of question is always raised

Table 5.3.1.1. Thermodynamics parameters and thickening coefficients of EO copolymers.[a]

Code	$T_m^o(p_B)$ [b] (°C)	$T_m^o(p_{B,c}=p_B)$ [c] (°C)	$T_m^o(p_{B,c}=p_{eq})$ [d] (°C)	ΔH_f (J/g) [e]	σ_e (erg/cm^2)	γ_l [c]	γ_h [d]	γ [f]
L10-O	134.55	114.94	152.5	288.67	142.04	7.31	1.22	1.17
L18-O	-	106.00	∞	288.67	-	4.52	1.00	1.00
H7-O	140.44	117.93	157.3	288.58	163.72	8.17	1.22	1.22
H7'-O	139.30	-	-	288.62	-	-	-	-
H10-O	138.64	112.91	128.6	288.63	167.42	7.57	1.59	1.12
H16-O	133.86	102.53	120.7	288.67	170.47	7.88	1.71	1.05
H17-O	134.10	-	-	288.67	-	-	-	-

a) Detail meanings of notations in head columns will be described in **Section 5.3.4** and **5.4**.
b) Obtained from the plot of T_m vs. $1/l$.
c) Determined from lower slope region of Hoffman-Weeks plot.
d) Determined from higher slope region of Hoffman-Weeks plot.
e) From **equation (5.3.1.2)**.
f) Estimated from best fitting in the plot of actual T_m vs. T_c using column 2 and **equation (5.3.1.1)**.

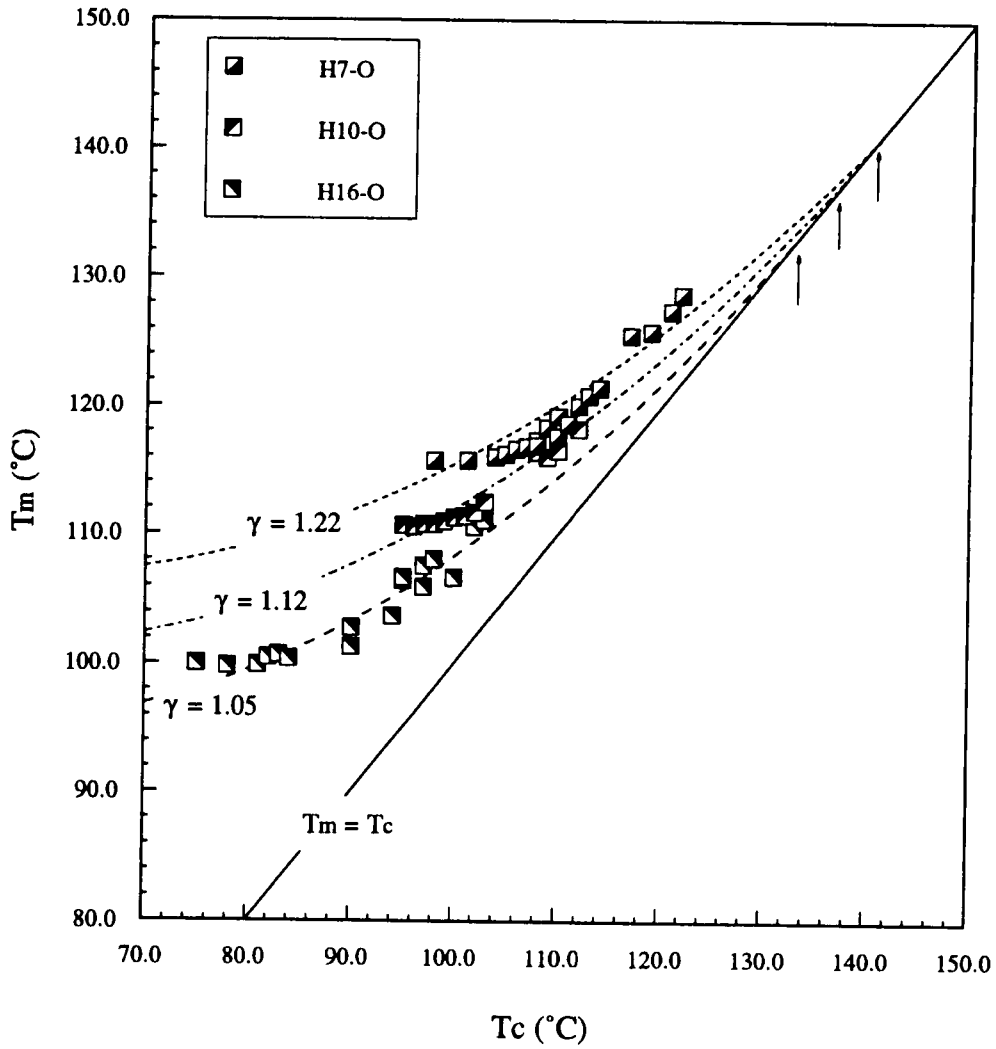


Figure 5.3.1.1. Observed and calculated melting temperatures (°C) against crystallization temperatures (°C) for high molecular weight EO copolymers.

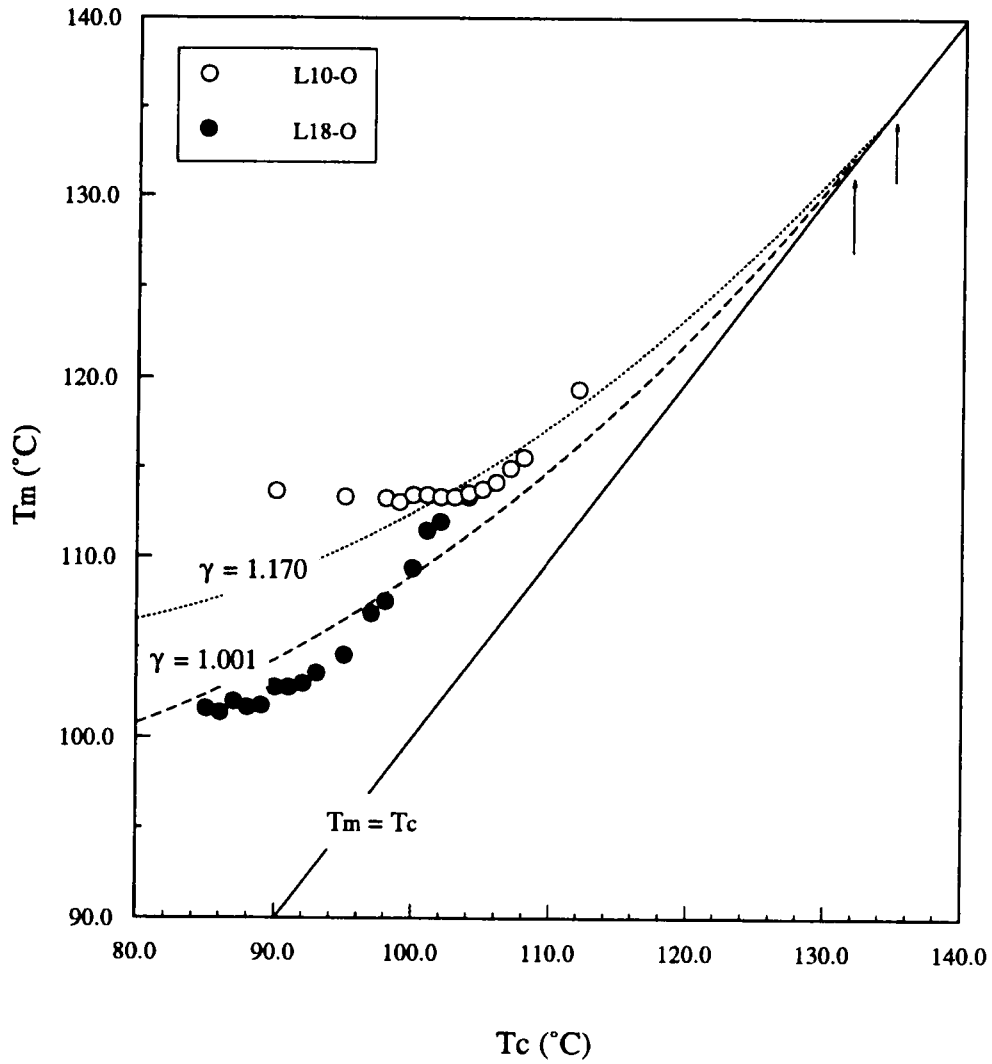


Figure 5.3.1.2. Observed and calculated melting temperatures (°C) against crystallization temperatures(°C) for low molecular weight EO copolymers.

when a numerical value is obtained from the slope in an arbitrary plot. (For instance, average fold surface energy from the slope of Thompson-Gibbs plot). When the fact that annealing and defect behavior are dependent on the temperature is considered, γ should be a function of temperature.

Another factor causing deviation is the possibility of the change of the intra- and the inter-sequence length distribution with crystallization time and crystallization temperature as far as the copolymer does not have the same sequence length. This phenomenon was studied in **Section 4.1 and 5.1**. For examples, the chains with large sequence length between two branches will be crystallized first at high crystallization temperature, at which the chains with small sequence length will be molten state. The chains with small sequence length will be crystallized at lower crystallization temperature. The change of sequence lengths on the way of crystallization will cause the change of the thermodynamic properties of system. Even if the imaginary polymer system consisted of uniform sequence length, the change of the chemical potentials(i.e. partial molar quantity of Gibbs free energy), $\mu_i = (\partial G/\partial n_i)_{T,P,n_j}$ during crystallization (or on melting) cannot be avoided, because of the change of B-counit content outside the crystalline phase by inclusion and exclusion process of defects, as far as they are not homopolymer. The different gradients in chemical potentials will cause the different rearrangements of molecules. Finally, all these variables will cause deviation from the linearity of the plot of T_m versus T_c. The γ should be a function of these all variables. Therefore, the application of the plot of T_m versus T_c to the copolymer system seems to be not reasonable. On the other hands, for the case of homopolymer that does not have the sequence length distribution, the equilibrium melting temperature may be obtained from the Hoffman-Weeks plot in spite of the arbitrariness of the melting temperature.

In later section, this curvature will be used to study the defect location in system.

5.3.2. Thompson-Gibbs Plots

Because of the problems of Hoffman-Weeks plots described in the previous section, reliable T_m° for the EO copolymers could not be obtained. An more reliable and reasonable method is to rely on the classical fact that melting temperature is a linear function of the thickness of a single folded lamella, Thompson-Gibbs equation (**equation (2.5.14)**).

The most important step of this work is to determine the lamellar thickness precisely as well as the melting temperature. The ORNL 10m-SAXS with high resolution power was used and the SAXS intensity was measured at isothermal crystallization temperature (Detail experimental methods were described in **Chapter 3**). When we consider that SAXS intensity profile results from the average of the whole crystal thickness, to include the thin lamellar thickness due to the quenching process will cause a reduction of the number average lamellar thickness compared to when the thin lamellae are removed. In other words, the reason we measured the SAXS intensity at T_c is to avoid the discontinuous lamellar thickness distribution effect(see **Section 4.1** and **5.1**) crystallized below T_c during quenching process. In other words we want as narrow a lamellar thickness distribution as possible. Sometimes, the separating point in DSC melting thermogram does not coincide the crystallization temperature T_c of oil bath. In this case, the temperature at which the DSC melting thermogram separates was chosen for the measurement of SAXS intensity. **Figure 5.3.2.1** shows an example of the DSC thermograms where the peaks are separated at the center of crystallization temperature.

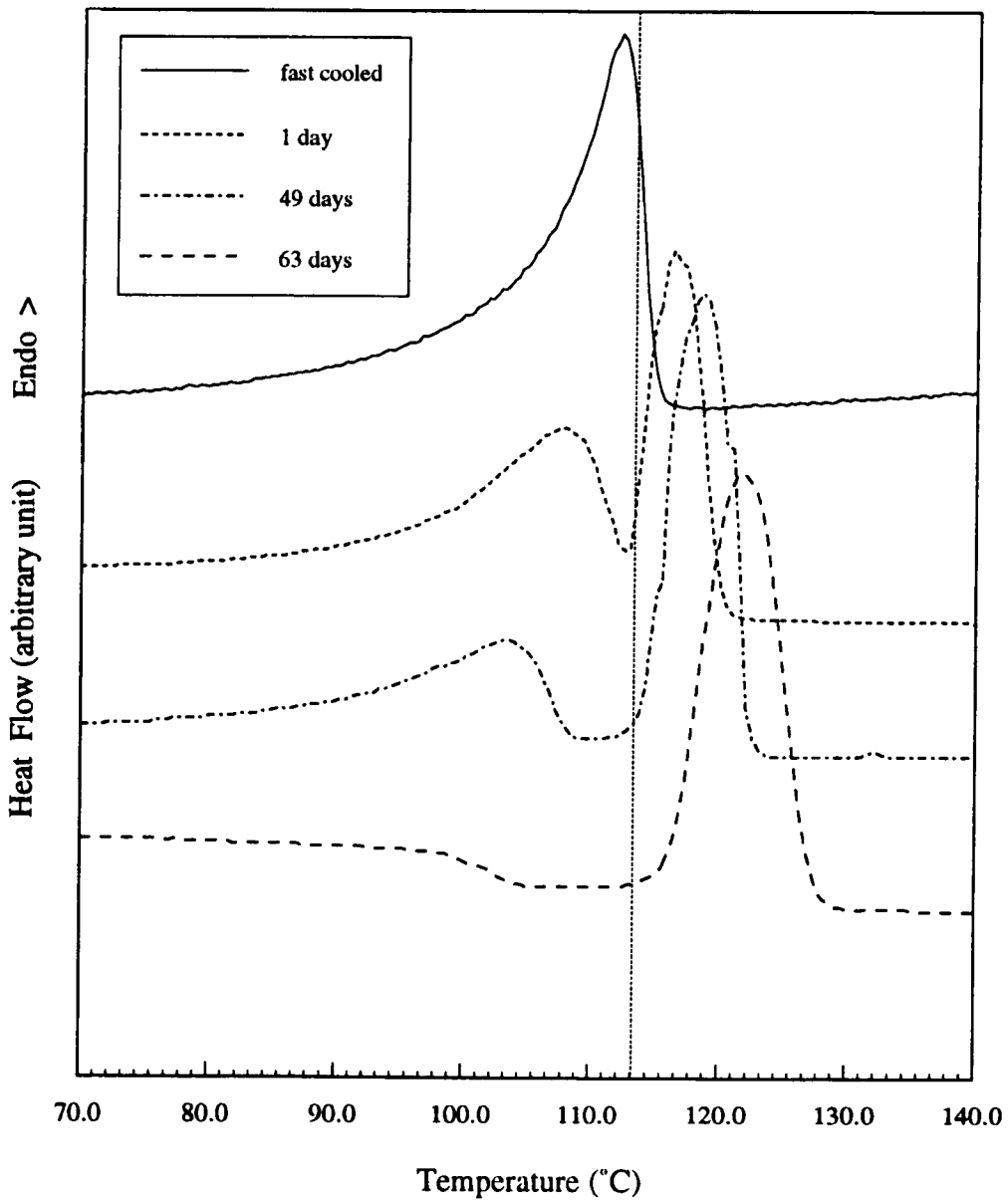


Figure 5.3.2.1. Melting thermograms of H7-O fast cooled and crystallized at 113 °C for indicated times.

SAXS intensity was measured at this separating point. The lamellar thickness was obtained by analyzing the SAXS intensity profile using the 1-dimensional correlation function.

The T_m°s obtained from Thompson-Gibbs plots (**Figure 4.3.2.1 ~ 4.3.2.3**) are listed in the last column of **Table 5.3.2.1**. The T_m° of linear polyethylene depends on the molecular weight. High molecular weight H-LPE has high $T_m^\circ = 142.6\ ^\circ C$ while medium molecular weight M-LPE does low $T_m^\circ = 141.3\ ^\circ C$. The molecular weight dependence is also shown between the branched polyethylene H10-O ($T_m^\circ = 138.6\ ^\circ C$) of high molecular weight and L10-O ($T_m^\circ = 134.5\ ^\circ C$) of low molecular weight. This molecular weight dependence will be discussed in the later **Section 5.3.3** independently.

The observed melting temperatures of EO copolymers decrease linearly as number average lamellar thickness decreases as shown in the plot of observed melting temperature against reciprocal number average lamellar thickness. Mentioned in **Section 5.3.1**, the thickening coefficient decreases with branch content in the system, which demonstrates that branches prevent lamellae from becoming thick. Thompson-Gibbs plot, however, shows the lamellar thickness is not the only factor controlling the melting temperature. At fixed lamellar thickness the melting temperatures of low branched samples (for example, H10 and H16 of **Figure 4.3.2.2** or L10-O and L18-O of **Figure 4.3.2.3**) are always higher than those of highly branched samples. This may be due to defects in the crystalline phase. Incorporation of some defects in the crystalline phase causes the distortion of chain regularity which make the secondary force between chains weak and leads to a lowering of melting temperature even at the same lamellar thickness.

Table 5.3.2.1. Equilibrium melting temperatures, $T_m^\circ(n, p_B)$, of LPE and EO copolymers.

Code [a]	$\overline{M}_w$ $(g/mole)$	$\overline{M}_n$ $(g/mole)$	$\overline{M}_w/\overline{M}_n$	Density (g/cm^3)	mole % of branching point $(p_B)\times 10$	T_m (°C)	$T_m^\circ(n, p_B)$, °C[f]
H-LPE	101,300	53,900	1.88	0.9540	0.00 [b]	132.25	142.7 ± 0.7
M-LPE	77,600	38,200	2.03	0.9510	0.00 [c]	131.43	141.3 ± 1.0
H7-O	-	43,600	-	0.9180	6.84	113.19 [e]	140.4
H7'-O	98,400	44,800	2.2	0.9180	7.32	113.25	139.3
H10-O	-	48,800	-	0.9126	9.50	107.54 [e]	138.6
H16-O	-	45,200	-	0.9003	16.34	94.54 [e]	133.9
H17-O	102,700	48,700	2.11	0.9003	16.92	96.19	134.1
L4-O	59,900	27,300	2.19	0.9365	3.98	118.81	139.3
L10-O	-	23,700	-	0.9195	9.83	109.21 [e]	134.6
L13-O	51,800	25,000	2.07	0.9110	12.93 [d]	105.00	
L18-O	-	24,900	-	0.9027	18.17	94.46 [e]	131.9
L24-O	46,900	21,800	2.15	0.8975	24.04	90.24	127.5
L39-O	48,000	22,800	2.11	0.8700	38.62	48.23 [e]	

a) H, M, L ; high, medium, and low molecular weight
LPE ; linear polyethylene
Numbers ; branch content
O ; octene comonomer
b) Trans/1000C = 0.003, vinyls/1000C = 0.135, vinylidenes/1000C = 0.013
c) Trans/1000C = 0.027, vinyls/1000C = 0.128, vinylidenes/1000C = 0.023
d) Trans/1000C = 0.298, vinyls/1000C = 0.045
e) measured at a DSC heating rate 10°C/min in this work
f) determined from the plot of melting temperature versus lamellar thickness in this study

Of interest is the case of linear polyethylenes. Despite a branch-free system, T_m of high molecular H-LPE is higher than that of M-LPE at constant lamellar thickness (see **Figure 4.3.2.1** and **5.3.3.2**). Only defect in linear polyethylene is the chain ends if H-LPE and M-LPE are truly branch-free state). This leads us to realize the importance of chain ends on morphology, crystallization behavior and melting behavior.

The possibility of defect incorporation into the crystalline phase will be described in the **Section 5.3.5**.

5.3.3. Molecular Weight Effect

5.3.3.1. Equilibrium Melting Temperatures of Linear Polyethylenes from Literature

The equilibrium melting temperatures of linear polyethylenes, which were determined from the Thompson-Gibbs equation, have been reported as shown in **Table 5.3.1**. If the values obtained from other methods were added, much more equilibrium melting temperatures can be shown[83].

Despite the fact that only the equilibrium melting temperatures obtained from Thompson-Gibbs equation were collected, all the values are different from each other. Except for the value by Bassett *et. al.*, the values in **Table 5.3.1** originated from the analysis of small angle X-ray scattering (SAXS) intensity. The lamellar thicknesses by these authors were obtained from Bragg's peak of SAXS intensity (or Bragg's peak with Lorenz correction). Among these values, T_m^o by Martuscelli & Pracella is not

recommended for comparison since Thompson-Gibbs plot were constructed using long period (L) instead of lamellar thickness (l).

Of interest is T_m^o of Basset *et. al.* They used the gel permeation chromatography (GPC) to get the stem length, which is the synonym with lamellar thickness, of the etched samples.

The purpose of this **Section 5.3.3** is to check whether there is a molecular weight (MW) effect on T_m^o or not. Unfortunately, most literature do not mention molecular weights of their samples clearly. Maybe they seem to disregard the MW effect, or to think their material have high molecular weight enough to satisfy the level-off region (see **Figure 5.3.3.4**) of Broadhurst or Flory and Vrij analysis whose region is not very sensitive to MW. Even Bassett *et. al.* who knew well the molecular weight effect on T_m^o constructed Thompson-Gibbs plot including the melting temperatures of all the samples that were fractionated with MW (**Figure 2-a in reference 84**). They reported $T_m^o = 142.0 \pm 0.3\ ^oC$ for linear polyethylenes. Regenerated plot using their data is shown in **Figure 5.3.3.1** and the value of T_m^o is $T_m^o = 140.8\ ^oC$. There is an inconsistency of about $1.0\ ^oC$. A similar approach was used by Illers & Hendus[85]. $T_m^o = 141.0 \pm 0.5\ ^oC$ was suggested from the plot of T_m vs. $1/l$ including melting points of linear polyethylenes that were measured by several authors. Wunderlich *et. al.*, obtained $T_m^o = 141.0\ ^oC$ using a very slow heating technique in the dilatometer to reach the equilibrium condition.[86] These values are lower than Flory-Vrij 's value, $T_m^o = 145.5\ ^oC$. To understand the inconsistency of values, we need to check MW effect on equilibrium melting temperature. If MW affects equilibrium melting temperature, the melting temperatures obtained from different molecular weight ranges cannot be used to construct Thompson-Gibbs plots since they will cause decreasing or increasing true equilibrium

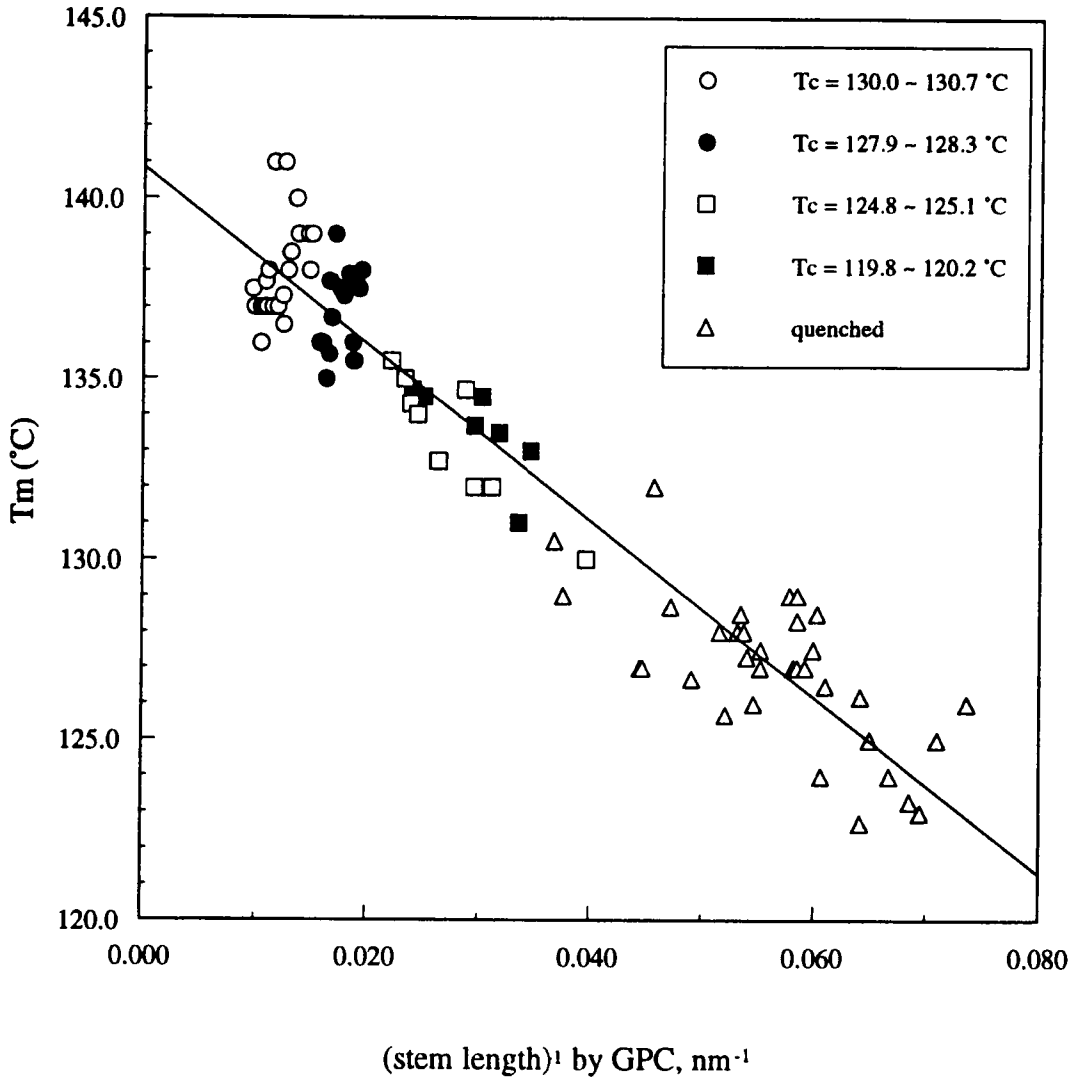


Figure 5.3.3.1. Plot of peak melting points against reciprocal stem length using the data by D. C. Bassett *et. al.*, (Proc. R. Soc. Lond. A377, 39 (1981)).

melting temperatures, where true equilibrium melting point means the one obtained from narrow MW distribution and same MW range.

Considering MW effect on T_m^o, the data (**Table** in **Appendix reference 84**) by Basset *et. al.*, are reanalyzed in the following **Section 5.3.3.2** and compared to the results of this study.

5.3.3.2. Determination of T_m^o of Linear Polyethylenes as a Function of Molecular Weight

5.3.3.2.1. Using the Data of D. C. Bassett *et. al.*

The only literature that shows the molecular weight of samples was that by Bassett *et. al.*(**Table in appendix of reference 84**). They fractionated the two linear polyethylenes, Rigidex 140-60 and Rigidex 50, and bulk-crystallized each fraction at different crystallization times and temperatures. Using the crystallized samples after nitration. mass average chain lengths of etched samples were determined using GPC. [83,87] As mentioned earlier, since they did not analyze the data as a function of MW, their data were re-analyzed to obtain T_m^o as a function of molecular weight. To obtain enough data points, similar molecular weights were grouped and the average MW of each group was taken as shown in **Table 5.3.3.1**. The corresponding plots of T_m against reciprocal stem length are shown in **Figure 5.3.3.2**. Intercept points which reflect T_m^o's are clearly raised as MW increases. This can be explained by the possibility that the higher molecular weight of the sample the longer is the extended chain that can be obtained. The highest value ($T_m^o = 144.1\ ^oC$) is close to Flory-Vrij's value ($T_m^o = 145.35\ ^oC$). Of course, the fact

Table 5.3.3.1. Molecular weights* and corresponding equilibrium melting temperatures.

Fractions*	$\overline{M}_w$	$\overline{M}_n$	$\overline{M}_w/\overline{M}_n$	Averaged $(\overline{M}_w)_{Avg}$	Averaged $(\overline{M}_n)_{Avg}$	Tm° (°C)**
L12	20,900	12,600	1.66			
LM5	26,000	19,800	1.31	23,500	16,200	139.0
LM10	29,600	20,000	1.48			
M12	30,700	22,800	1.35			
H12	37,300	29,300	1.27			
MM10	36,500	29,200	1.25	33,500	25,300	139.1
HM10	43,600	35,400	1.23			
LM6	47,500	32,600	1.45			
LM11	51,800	29,800	1.74	47,600	32,600	139.6
MC7	60,200	47,500	1.27			
MC6	61,300	46,000	1.33	60,800	46,800	-
MC8	71,500	58,800	1.22	-		-
Hi5	111,000	51,400	2.16			
MM11	126,000	72,400	1.74			
Hi10	156,000	55,100	2.83			
Hi6	156,000	77,100	2.03	137,300	64,000	142.1
HM11	442,000	222,000	1.99	-		144.1
Whole polymer						
Rigidex 140-60	53,900	16,800	3.21	-		-
Rigidex 50	67,800	11,600	5.85	-		140.4
Marlex 5	91,800	12,200	7.55	-		-
Manolene 6003	134,000	20,800	6.44	-		-
Rigidex9	170,000	11,300	15.1	-		141.4
HO20-54P	231,000	28,200	8.21	-		-
Hifax 1900	> 2,000,000	-	-	-		142.9
Hostalen G.U.R.	~ 4,000,000	-	-	-		-
Birmingham 2 HDPE	< 6,000,000	-	-	-		-
This study						**Tm° (°C)*** **
M-LPE	77,600	38,200	2.03	-		141.3 ± 1.0
H-LPE	101,300	53,900	1.88	-		142.7 ± 0.7

*) fraction 5, 10, 11, 12 extracted from Rigidex 50.
fraction 6, 7, 8 extracted from Rigidex 140-60 (D. C. Bassett et. al. Proc. R. Soc. Lond. A377, 25 (1981)).
**) analyzed in UT using the data in the appendix by D. C. Bassett et. al., Proc. R. Soc. Lond. A377, 39 (1981).
***) measured in this study from the plot of melting temperature vs. reciprocal lamellar thickness.

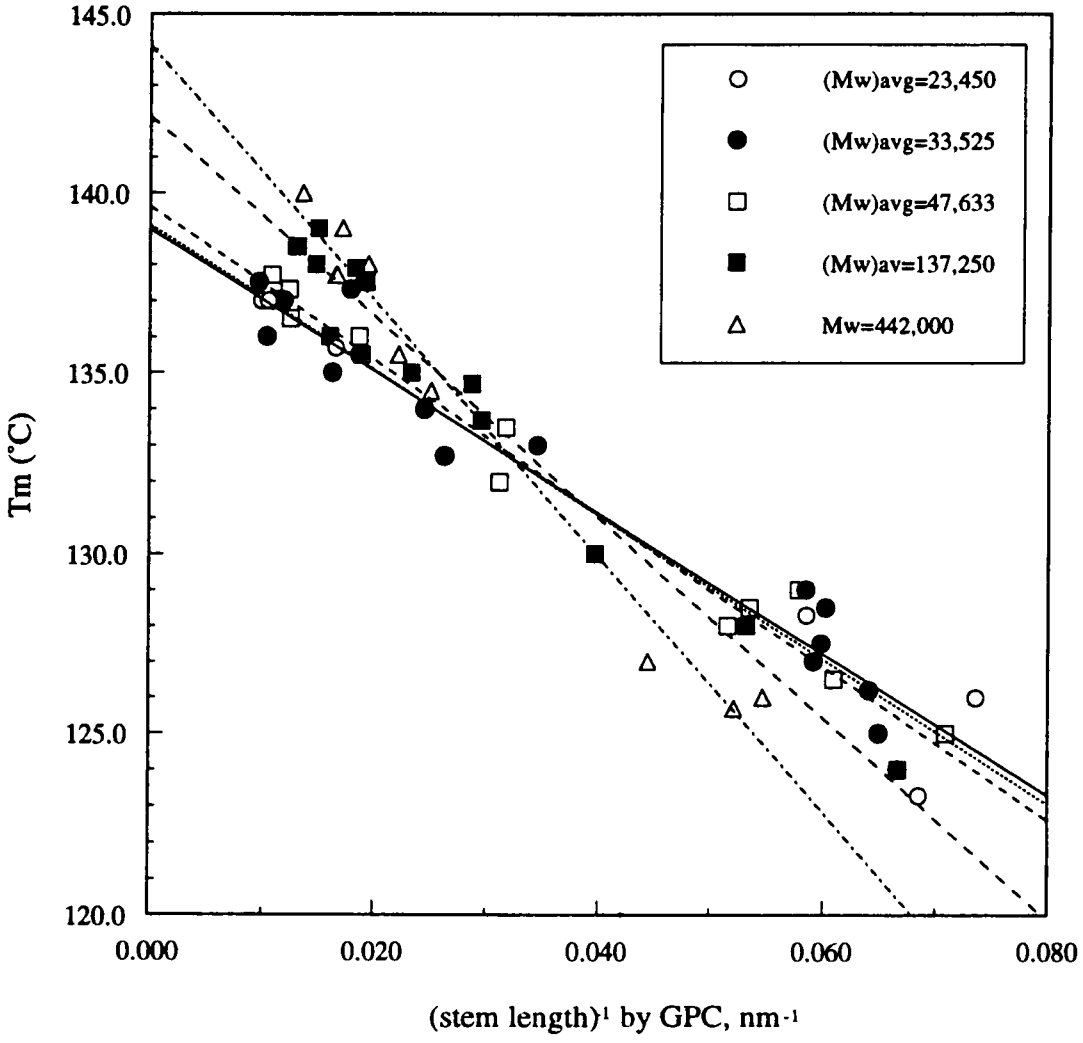


Figure 5.3.3.2. Plot of melting temperatures against reciprocal stem length at indicated molecular weights, reanalyzing the data by D.C. Bassett *et.al.*

that we used Flory-Vrij value for comparison does not mean Flory-Vrij's value is absolutely right. This will be discussed in **Section 5.3.3.4**.

5.3.3.2.2. From This Study

Two T_m^os of linear polyethylenes with two different molecular weights and narrow molecular weight distribution (≈2.0) were obtained in this work from the relationship of T_m and lamellar thickness l (see **Figure 4.3.2.1**). Lamellar thickness was measured from SAXS intensity analysis by 1-dimensional correlation function. The T_m^o of linear polyethylene with Mw = 77,600 is 141.3 °C and that with Mw = 101,300 is 142.7 °C (see **Table 5.3.2.1** or **5.3.3.1**).

The prediction that there is MW effect on T_m^o of linear polyethylenes, which has guessed only from melting temperatures of n-alkanes, has been experimentally proved through the this section. Using the systematic study of T_m^o on linear polyethylenes, an empirical equation to predict T_m^o of linear polyethylenes is suggested in the following section.

5.3.3.3. Empirical Estimation of T_m^o for Linear Polyethylenes

Equilibrium melting temperatures (T_m^o) discussed in previous **Section 5.3.3.2** showed a strong MW dependence. Since T_m^o is the temperature at which infinitely large crystal melts and infinitely large crystal will be obtained from the infinite MW, if we know T_m^o's of linear polyethylenes with MW, we can get the equilibrium melting

temperatures for infinite MW by constructing the plot of T_m° versus reciprocal MW and taking an intercept. Here an arising question is what kind of MW is appropriate for this analysis. Most reliable MW is absolute MW from scattering experiment. Unfortunately, our MW was obtained using GPC. The molecular weight from GPC is not absolute but relative one to that of standard sample. Simple test for chosing appropriate MW can be carried out considering low molecular weight chains as impurities, since polymers always have some amount of low molecular weight chains.

Table 5.3.3.2 demonstrates well the effect of impurities of low MW. Last two columns are the index[88] to show degree of deviation from MW of pure polymer. The lower the MW of impurities becomes the less the average MW becomes. For example, in the case of the polymer of $M = 100{,}000\, g/mole$, even 1% of impurities with $M = 500\, g/mole$ causes $\overline{M}_n \approx 33{,}400$ while $\overline{M}_w \approx 99{,}000$. The degree of deviation from the MW of pure polymer, which is $M/\overline{M}_n = 2.99$ for number average MW and $M/\overline{M}_w = 1.01$ for weight average MW. Number average MW is much more sensitive to the content of low MW in system even though that the amount is less than 1%, while weight average MW dose not much deviate from MW of pure polymer. Therefore the actual polymer MW may be distorted even if small amount of impurities exists in polymer system. **Table 5.3.3.2** shows as increasing low molecular weight in system the index, M/Mn, for number average MW ($\overline{M}_n$) is increased sharply while that, M/Mw, of weight average MW ($\overline{M}_w$)is still around 1.0. Therefore $\overline{M}_w$ is thought more reliable than $\overline{M}_n$. Weight average molecular weight from GPC was used for constructing the plot of T_m° versus reciprocal molecular weight.

Table 5.3.3.2. Impurity (low molecular weight) influence on number and weight average molecular weight.

M of impurity	w_i of impurity n_iM_i	M of pure polymer	$\overline{M}_n$ of impure polymer	$\overline{M}_w$ of impure polymer	$\overline{M}_w/\overline{M}_n$	$M/\overline{M}_n$ [a]	$M/\overline{M}_w$ [a]
500	0.001	100,000	83,400	99,900	1.20	1.20	1.00
	0.01	100,000	33,400	99,000	2.96	2.99	1.01
	0.02	100,000	20,100	98,000	4.88	4.98	1.02
1,000	0.001	100,000	91,000	99,900	1.10	1.10	1.00
	0.01	100,000	50,300	99,000	1.97	1.99	1.01
	0.02	100,000	33,600	98,000	2.92	2.98	1.02
10,000	0.001	100,000	99,100	99,900	1.01	1.01	1.00
	0.01	100,000	91,700	99,000	1.08	1.09	1.01
	0.1	100,000	52,600	90,000	1.71	1.90	1.11
	0.2	100,000	35,700	80,000	2.24	2.80	1.25
10,000	0.001	50,000	49,800	50,000	1.00	1.00	1.00
	0.01	50,000	48,100	49,500	1.03	1.04	1.01
	0.1	50,000	35,700	45,000	1.26	1.40	1.11
	0.2	50,000	27,800	40,000	1.44	1.80	1.25

a) degree of deviation from molecular weight of pure polymer.

T_m^o as a function of MW is shown in **Figure 5.3.3.3**, using the data listed in **Table 5.3.3.1**. The empirical equation to estimate T_m^o as a function of $\overline{M}_w$ is as follows:

$$T_m^o(^oC) = 144.42 - 2.302 \times 10^5 \cdot \frac{1}{M_w} \qquad (5.3.3.1)$$

The equilibrium melting temperatures of two low MW groups were not considered in this plot because of severe deviation. **Equation (5.3.3.1)** make it possible to predict T_m^o as a function of MW. The T_m^o obtained from the intercept is 144.42 ^oC within the error range of Flory-Vrij value, $T_m^o = 145.35 \pm 1.0\ ^oC$, obtained from the analysis of n-alkanes.

At this time it is necessary to review Flory and Vrij analysis and to compare it with **equation (5.3.3.1)** for finite MW region, although T_m^o for infinite MW between Flory-Vrij equation and **equation (5.3.3.1)** is similar within 1 ^oC error limit.

5.3.3.4. Modification of Flory-Vrij Equation

As introduced in **Section 2.5.3**, Broadhurst and Flory and Vrij developed independently the semi-theoretical equations to estimate the T_m^o's of linear polyethylenes as a function of chain length based on melting thermodynamics and melting temperatures of n-alkanes. But the values obtained from their analysis never have been compared to the values of T_m^o determined experimentally for real polymer system.

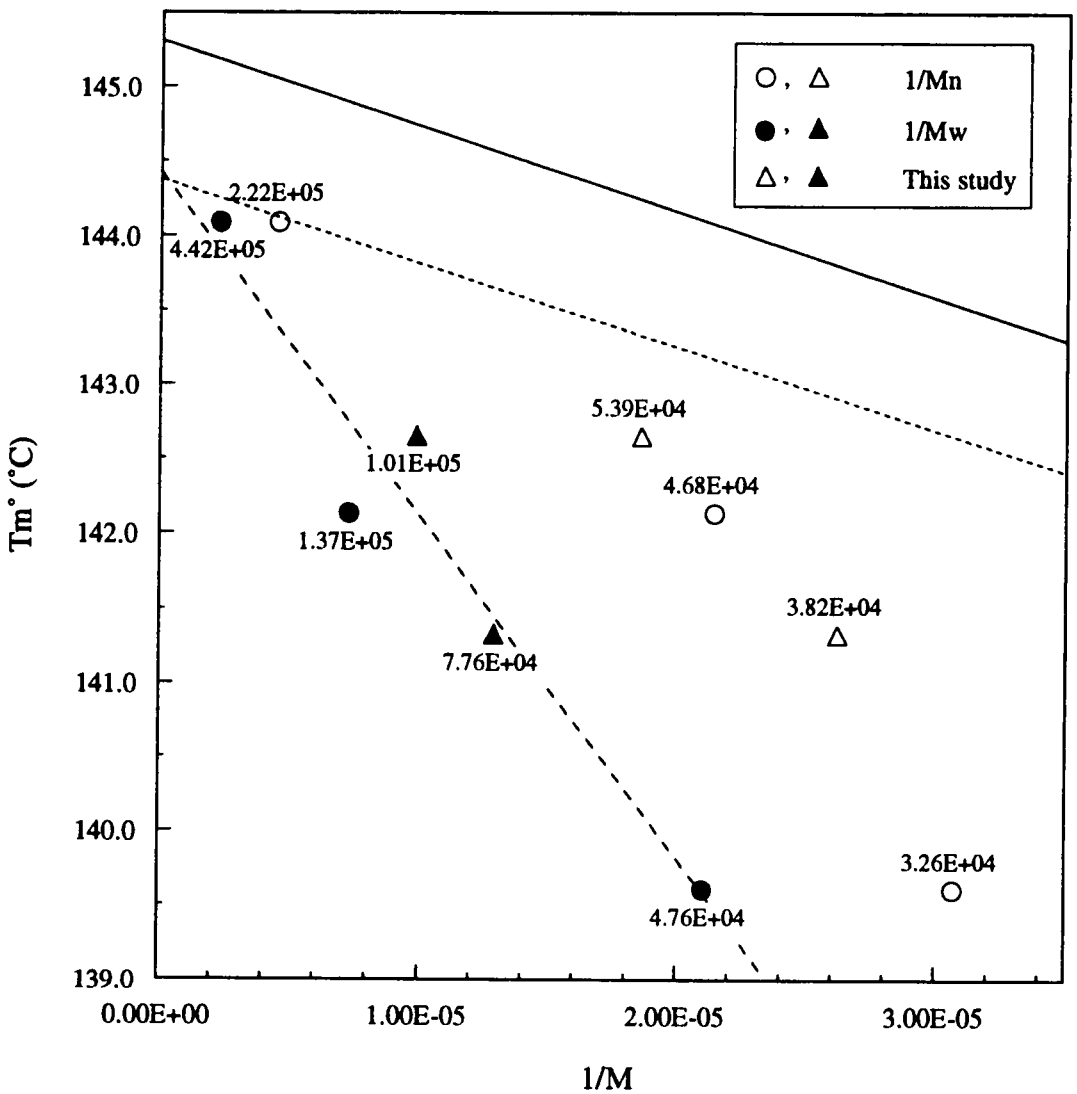


Figure 5.3.3.3. Equilibrium melting temperatures against reciprocal molecular weights.Solid and dotted lines are the values calculated with Flory-Vrij equation and modified equation (5.3.3.7), respectively.

Usually, the melting temperature, $T_m(n)$, of n-alkanes has been expressed in the following well-known form under the assumption that the heat of fusion and the entropy of fusion are a linear functions of chain length [89].

$$T_m(n) = T_m^\circ \frac{n+a}{n+b} \tag{5.3.3.2}$$

where a and b are fitting constants and the melting temperature of **equation (5.3.3.2)** converges to the given equilibrium melting temperature as chain length n approaches infinity. **Equation (2.5.24)** that includes the nonlinear entropy contribution term $R\ln(cn)$ of the chain ends can be rearranged in the form of **equation (5.3.3.2)** with the constants a and b

$$a = \frac{\Delta H_e - (\Delta C_{p,e}/2)T_m^\circ}{\Delta H_u - (\Delta C_p/2)T_m^\circ} \tag{5.3.3.3}$$

$$b = \frac{T_m^\circ}{\Delta H_u - (\Delta C_p/2)T_m^\circ} \times \left\{(\Delta S_e - \Delta C_{p,e}) + R\ln(n) - \left(\frac{n\Delta C_p}{2} - \frac{n\Delta C_{p,e}}{2}\right)\left(1 - \frac{T_m(n)}{T_m^\circ}\right)\right\} \tag{5.3.3.4}$$

Ignoring the second order term on the right hand side of **equation (2.5.24)**, the simplified form results follows:

$$T_m(=T_m(n)) = T_m^\circ \frac{n + \dfrac{\Delta H_e}{\Delta H_u - (\Delta C_p/2)T_m^\circ}}{n + \dfrac{T_m^\circ}{\Delta H_u - (\Delta C_p/2)T_m^\circ}\left\{R\ln(n) + \Delta S_e - \dfrac{n\Delta C_p}{2}\left(1 - \dfrac{T_m(n)}{T_m^\circ}\right)\right\}} \tag{5.3.3.5}$$

where $\Delta H_e = -2150 cal/mole$, $\Delta S_e = 2.45 cal/mole/K$, $\Delta C_p = 1.0 cal/mole/K$, and $\Delta H_u = 950 cal/mole$ were estimated by Flory and Vrij (ref) for the case of $T_m^\circ = 418.5K(145.35\ ^\circ C)$, and **equation (5.3.3.5)** has the same form as shown by Hoffman and Miller [90]

$$T_m(n) = 418.5 \cdot \left[\frac{n - 2.903}{n + 0.565\{1.987 \ln(n) + 2.45 - 0.5n(1 - T_m(n)/418.5)\}} \right] \quad (5.3.3.6)$$

where chain length, n, of *n*-alkane is a degree of polymerization for linear macromolecules, and $n = M/14.03$ for linear polyethylene. (Comment : There is a mistyped number, 2.093, of **equation (32)** in **reference 90** (Hoffman and Miller, Macomolecules, 21,3038, 1988). The constant 2.903 on the numerator of **equation (5.3.3.6)** is correct value).

The rearranged Flory-Vrij equation has been constructed by assuming that the enthalpy is a linear function of chain length and that the entropy term due to the destruction of paired end group on melting is not a linear function of chain length but $R\ln(cn)$, unlike that by Broadhurst.[91] Later Hay modified the Flory-Vrij equation, changing the entropy term $R\ln(cn)$ due to the uncoupling of terminal units in the molecular crystal with $R\ln[n(n-1)/2]$.[92] This new entropy term was obtained assuming the end groups are excluded from the crystalline phase and, on melting, these end groups penetrate into the region that was crystalline before melting. This penetration causes the increasing of entropy. However, Mandelkern and Stack[93] critically reviewed the equation modified by Hay. They claimed the entropy changes during the melting process were oversimplified and the basic model to be imagined by Hay, which assumed the terminal units are excluded from the crystalline region, cannot describe the n-alkane crystal properly, because the n-alkanes form molecular crystals within which the terminal units

are paired. There is also an analytical difference. Flory and Vrij expanded the free energy ΔG_u whereas Hay expanded ΔH_u and ΔS_u in Taylor series, respectively. It has been known that these separate expansions do not give the correct temperature dependence of free energy of fusion. Even if the analytical error on expansion in the Taylor series was corrected, the value of T_m° was still too high (151.0°C given by Mandelkern and Stack, 1985).

Therefore, in order to evaluate melting temperatures of *n*-alkanes for the case of $T_m^\circ = \lim_{n\to\infty} T_m(n) = 144.42\ ^\circ C$ determined in this study, the Flory and Vrij's original assumption have been used. The parameters for the Flory-Vrij equation were modified to obtain a best fit to the melting temperatures of the *n*-alkanes with $T_m^\circ = \lim_{n\to\infty} T_m(n) = 144.42\ ^\circ C$. Using the following input parameters, $\Delta H_u = 960 cal/mole$ rather than $\Delta H_u = 950 cal/mole$, $\Delta H_e = -2090 cal/mole$, $\Delta S_e = 2.45 cal/mole/K$, and $\Delta C_p = 1.3 cal/mole/K$, the modified Flory-Vrij equation is given:

$$T_m^\circ(n) = 417.57 \cdot \left[\frac{n - 3.0352}{n + 0.6064\left\{1.987\ln(n) + 2.45 - 0.65n(1 - T_m^\circ(n)/417.57)\right\}} \right] \quad (5.3.3.7)$$

The calculated melting temperatures were obtained with Flory-Vrij **equation (5.3.3.6)** and the modified **equation (5.3.3.7)**. Equilibrium melting temperature of linear polyethylene is still a controversy and its accurate determination is important for the evaluation of many physical and thermodynamic properties. Two equilibrium melting temperatures, $T_m^\circ(n \to \infty) = 145.35\ ^\circ$ by Flory and $T_m^\circ(n \to \infty) = 144.42\ ^\circ C$ in this study, were compared by extrapolation method to the measured melting temperatures $C_{11}H_{24} \sim C_{100}H_{202}$ compiled by Broadhurst[94], ref. Flory and Vrij), $C_{120}H_{242}$ (T_m=119.05°C) and $C_{140}H_{282}$ (T_m=121.05°C)[95], and $C_{192}H_{386}$ (T_m=127.50°C)[96,97] of the

n-alkanes (with an orthorhombic crystal structure). (Here, Celsius temperature scale was obtained from Kelvin temperature scales by relationship of $T(°C) = T(K) + 273.15$. Some values may be different with the literature values due to the temperature conversion). **Equation (5.3.3.7)** gives an average deviation $-0.06\ °C$ and a standard deviation $0.49\ °C$ whereas **equation (5.3.3.6)** gives $-0.35\ °C$ and $0.50\ °C$ in the range of $n = 11 \sim 192$. When we restrict our analysis to the n-alkane melting data, $n = 11 \sim 100$, used by Flory and Vrij, **equation (5.3.3.6)** gives less standard deviation $0.37\ °C$ compared to that $0.44\ °C$ of **equation (5.3.3.7)** while the average deviation of **equation (5.3.3.6)** and **(5.3.3.7)** is $-0.26\ °C$ and $0.03\ °C$. When only the high n-alkane region, $n = 50 \sim 192$, was considered, the average and the standard deviation were $-0.27\ °C$ and $0.68\ °C$ for Flory-Vrij equation and $0.20\ °C$ and $0.58\ °C$ for modified Flory-Vrij equation.

Of interest is the condition when $T_m(K) = 414.3(n-1.5)/(n+5.0)$ by Broadhurst[91], which was obtained with the T_m's between $C_{44}H_{90}$ and $C_{100}H_{202}$ and the assumption that the heat of fusion and the entropy of fusion are linear function of chain length, the melting temperature converges to the $141.5\ °C$ with good fitting result in spite of its poor theoretical backgrounds. This was interpreted as due to an accidental cancellation of error by Wunderlich *et. al.*[95]

Equation (5.3.3.7) was checked using the observed T_m of only n-alkanes that form the molecular crystal. **Figure 5.3.3.4** shows the observed and the calculated T_m of n-alkanes. In fact, the T_m of n-alkane molecular crystals are equal to the corresponding T_m^o based on the fact that they form fully extended zigzag conformations. There are no molecular weight and crystal chain length distributions in the molecular crystal. On the other hand, Wunderlich *et. al.* added the etched single crystals and the crystals prepared under the condition of slow cooling at high pressure to the high MW region and concluded

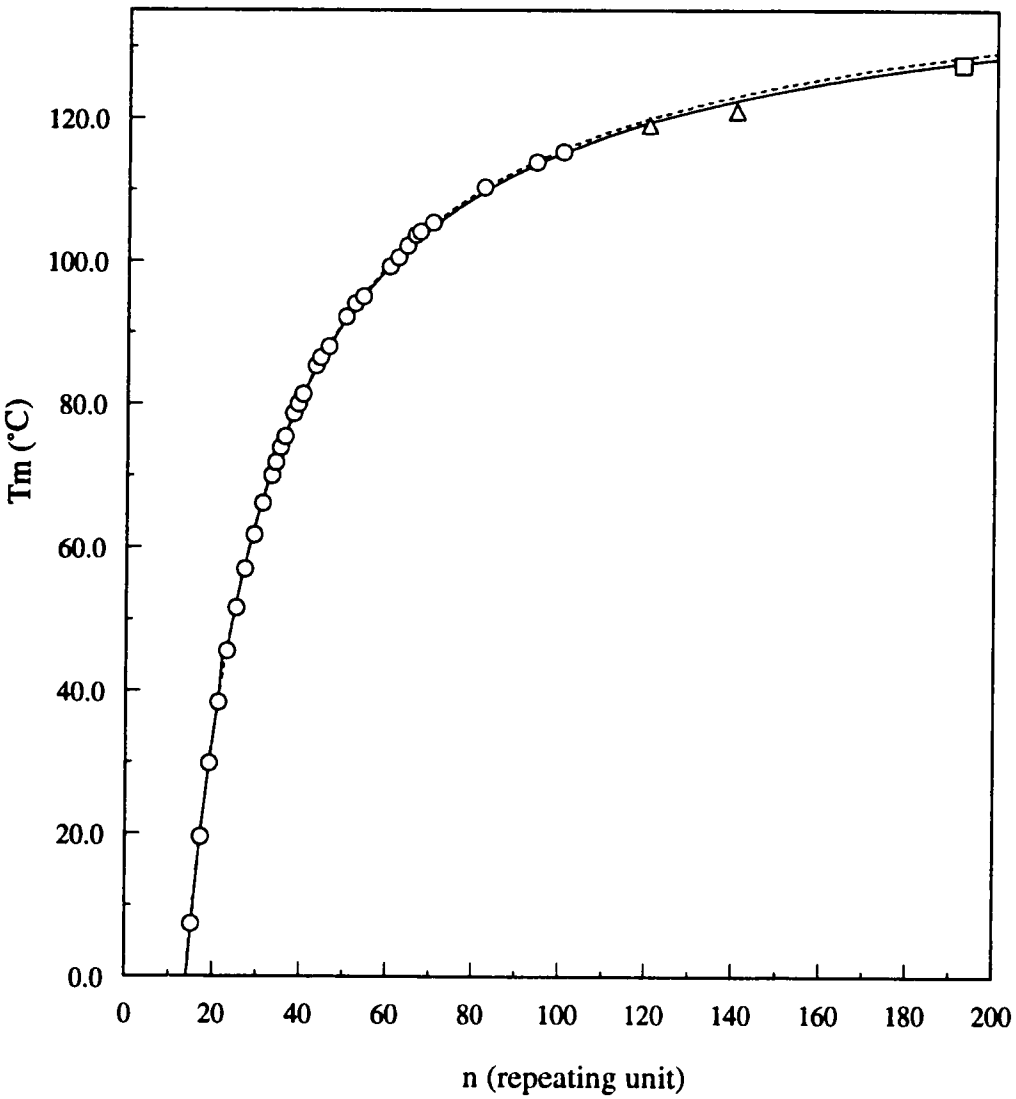


Figure 5.3.3.4. The observed and the calculated melting temperatures of *n*-alkanes. (dotted line; with 145.35°C by Flory & Vrij, solid line; with 144.42°C in this study)

141.45 °C as T_m^o of linear polyethylene.[95] Even though the T_m's of higher molecular weight crystals will give us more reasonable extrapolation to infinite crystal and their experimental conditions were controlled to reach equilibrium condition, if they still have different crystal thicknesses along the c-axis due to the molecular weight distribution of original polymers, the Flory and Vrij's or Broadhurst's methods cannot be applied correctly in that case because those extrapolation methods have been developed on the strict basis of orthorhombic n-alkanes that have uniform chain length. Recently, the n-alkane with longest chain length, dononacontahectane $C_{192}H_{386}$, was synthesized by Lee and Wegner [97] by the oxidative oligomerization of an α,ω-diethynylalkane with 24 carbon atoms and its melting temperature was reported as 127.5 °C [98]. The observed melting temperature of this *n*-alkane and fitting curve using $T_m^o(n \to \infty) = 145.35$ ° is shown in **Figure 5.3.3.4**. The experimental data of n-alkanes by the $C_{100}H_{202}$ are close to the extrapolation curves obtained from **equation (5.3.3.6)** and **equation (5.3.3.7)** which were constructed with $T_m^o(n \to \infty) = 145.35$ ° and $T_m^o(n \to \infty) = 144.42$ °C, respectively. However, as repeating units go behind $C_{100}H_{202}$ equilibrium melting temperatures calculated from Flory-Vrij equation deviate from the melting points of n-alkanes. **Figure 5.3.3.4 and 5.3.3.5** clearly show that the melting temperatures calculated from **equation (5.3.3.6)** deviate more than those of **equation (5.3.3.7)** in the range of longer chain length.

Stack *et al.*(1989) reexamined the Flory-Vrij analysis adding the melting point of $C_{192}H_{386}$ and found the value 144.5 °C is in apparent good agreement with experiment. However, they also suggested that the partial melting of n-alkanes, being a disruption of chain end ($-CH_3$)of n-alkanes as a prelude to final melting, can cause deviation from the model of the molecular crystal. However this study supports the value of $T_m^o(n \to \infty) = 144.42$ °C that is in the low limit of the Flory-Vrij value,

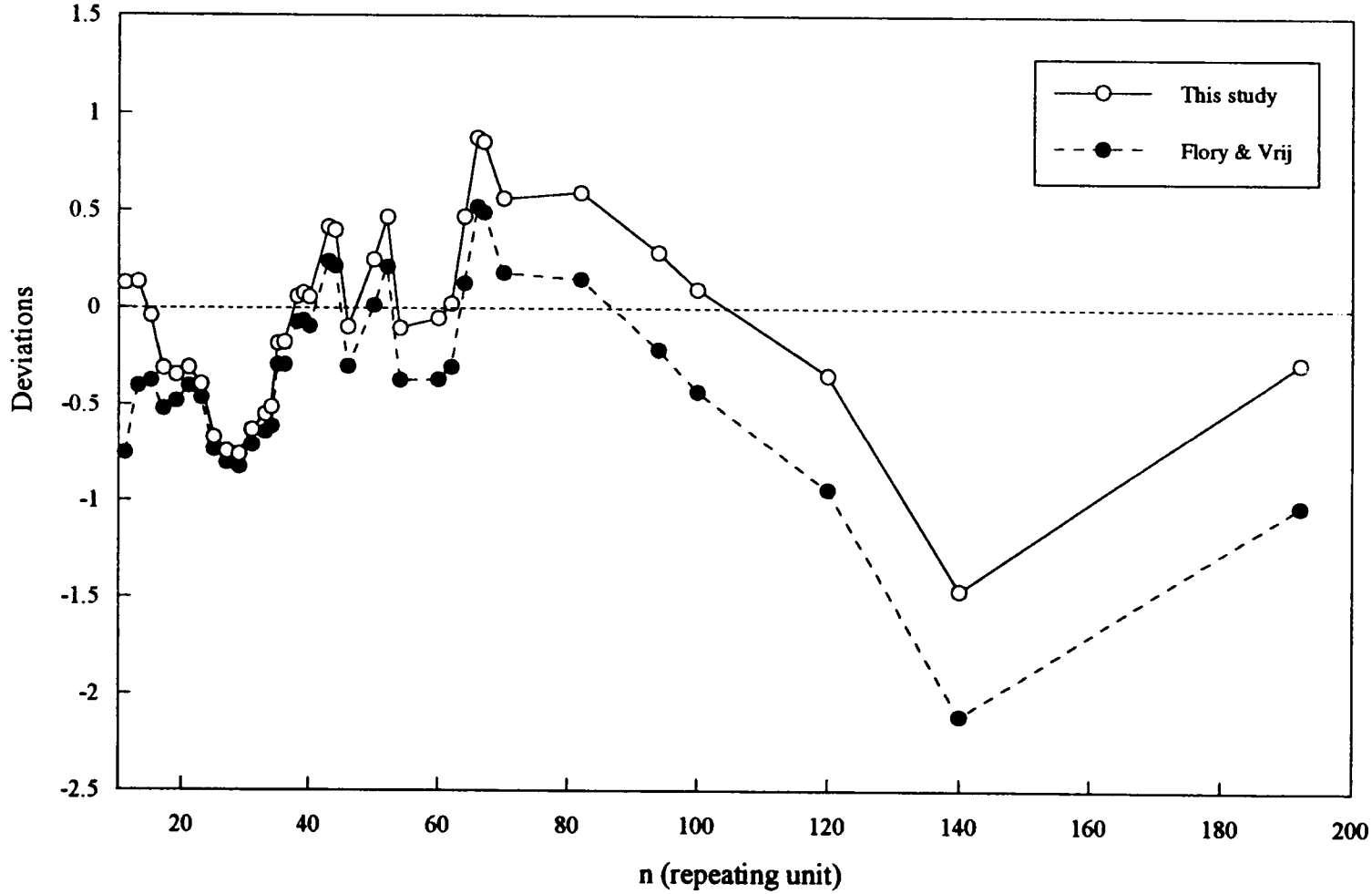


Figure 5.3.3.5. Deviations between the calculated and the measured melting temperatures of n-alkanes.

$T_m^o(n \rightarrow \infty) = 145.35 \pm 1.0\ ^oC$. Finally the results of this study and Stack *et al.*, lead us to reach the fact that Flory-Vrij value may be overestimated as much as about 1.0 ^oC even though we don't know the exact melting process.

Looking back on **Figure 5.3.3.3,** let's compare the values between the theoretical and the empirical equations. The values of the T_m^o determined experimentally and calculated using Flory-Vrij and modified equation are summarized in **Table 5.3.3.3**. The values from Flory and Vrij are not sensitive to MW whereas those from **equation (5.3.3.1)** are quite dependence to MW as shown in **Figure 5.3.3.3**. In addition the values from the Flory-Vrij analysis are higher than the experimental values even if the modified Flory-Vrij equation is used. The $T_m^o(n)$ of linear polyethylene that was obtained from the intercept in **equation (5.3.3.1)** was 144.42℃ being lower by as much as 0.93℃ than the,145.35 ℃, of Flory and Vrij who reported 418.5±1K for equilibrium melting temperature of linear polyethylene. The conversion factor 273.15 was used to convert Kelvin scale to Celsius scale. **Equation (5.3.3.1)** of this study is more sensitive to the MW effect on $T_m^o(n)$ than Flory-Vrij equation.

5.3.4. Defect (or Branch) Content Effect

So far we have considered the MW effect on $T_m^o(n)$ of linear polyethylene. Now let's go to the defect effect on T_m^o. The equilibrium melting point depression equation was developed independently without regarding MW effect. However as shown in **Figure 5.3.4.1**, T_m^o of EO copolymer depends on molecular weight for low defect content. T_m^o of high molecular weight samples are higher than those of low molecular weight samples in the region of less than 1% defect fraction. This means the molecular weight effect needs

Table 5.3.3.3. T_m^* (°C) calculated from the various conditions.

Code	$p_e \times 10^3$	Mw (g/mole)	Mn (g/mole)	determined in this study Tm°(°C)	Fitting equation (5.3.3.1) Tm°(Mw)	Tm°(Mn)	Mw corrected Flory's eq. with Tm°(Mw) =142.13	with Tm°(Mn) =140.11	Flory' s eq. with Tm°(Mw) =142.13	Tm°(Mn) =140.11
H-LPE	0	101300	53900	142.65	142.14	141.23	142.14	141.23	142.13	140.11
M-LPE	0	77600	38200	141.33	141.45	140.02	141.45	140.02	142.13	140.11
L4	3.98	59900	27300	139.33	140.57	138.37	139.16	136.97	140.71	138.70
L10	9.83		23700	134.55		137.48		134.07	138.63	136.64
L11	10.86								138.27	136.28
L13	12.93	51800	25000		139.97	137.83	135.43	133.33	137.53	135.56
L18	18.17		24900	131.92		137.81		131.50	135.68	133.72
L24	24.04	46900	21800	127.51	139.51	136.90	131.11	128.60	133.62	131.68
L39	38.62	48000	22800		139.62	137.22	126.18	123.94	128.53	126.64
H7	6.84	(94000) [a]	43600	140.44		140.54		138.12	139.69	137.69
H7'	7.32	98400	44800	139.30	142.08	140.64	139.47	138.05	139.52	137.52
H10	9.5	(105000) [a]	48800	138.64		140.93		137.57	138.75	136.76
H16	16.34	(97000) [a]	45200	133.86		140.67		134.91	136.33	134.36
H17	16.92	102700	48700	134.10	142.17	140.92	136.17	134.95	136.12	134.16

Code	Tm°=144.42 (Mw=100550) of Flory &Vrij	(Mn=45000) of Flory &Vrij	with Tm°=144.35 [b] (Mw=100550) of Flory &Vrij	(Mn=45000) of Flory &Vrij	Mw corrected Flory's eq. with Tm°(Mw) of Flory & Vrij Tm°=144.42	Tm°=144.35 [b]	Tm° (°C) by Flory's eq original Flory-Vrij values Tm°=145.35	fitting eq. (5.3.3.1) Tm°=144.42	from Tm° vs. p_e [b] Tm°=144.35
	143.78	143.09	143.72	143.02					
H-LPE	143.79	143.29	143.72	143.22	143.79	143.72	145.35	144.42	144.35
M-LPE	143.61	142.87	142.81	142.81	143.61	142.81	145.35	144.42	144.35
L4	143.39	142.32	143.33	142.26	141.97	141.90	143.91	142.98	142.92
L10		142.03		141.97			141.80	140.88	140.87
L11							141.43	140.51	140.45
L13	143.25	142.15	143.18	142.08	138.63	138.57	140.69	139.77	139.71
L18		142.14		142.07			138.81	137.90	137.84
L24	143.14	141.85	143.07	141.78	134.59	134.53	136.71	135.82	135.75
L39	143.16	141.95	143.10	141.88	129.50	129.44	131.54	130.67	130.61
H7		143.05		142.98			142.88	141.95	141.89
H7'	143.77	143.08	143.70	143.02	141.14	141.08	142.70	141.78	141.72
H10		143.18		143.12			141.92	141.00	140.93
H16		143.09		143.03			139.46	138.55	138.49
H17	143.79	143.18	143.73	143.12	137.74	137.68	139.25	138.35	138.28

a) obtained by assuming $\overline{M}_w/\overline{M}_n = 2.15$

b) determined from intercept(Tm°=144.35) of Tm° vs. p_e of H- series assuming molecular weight independence.

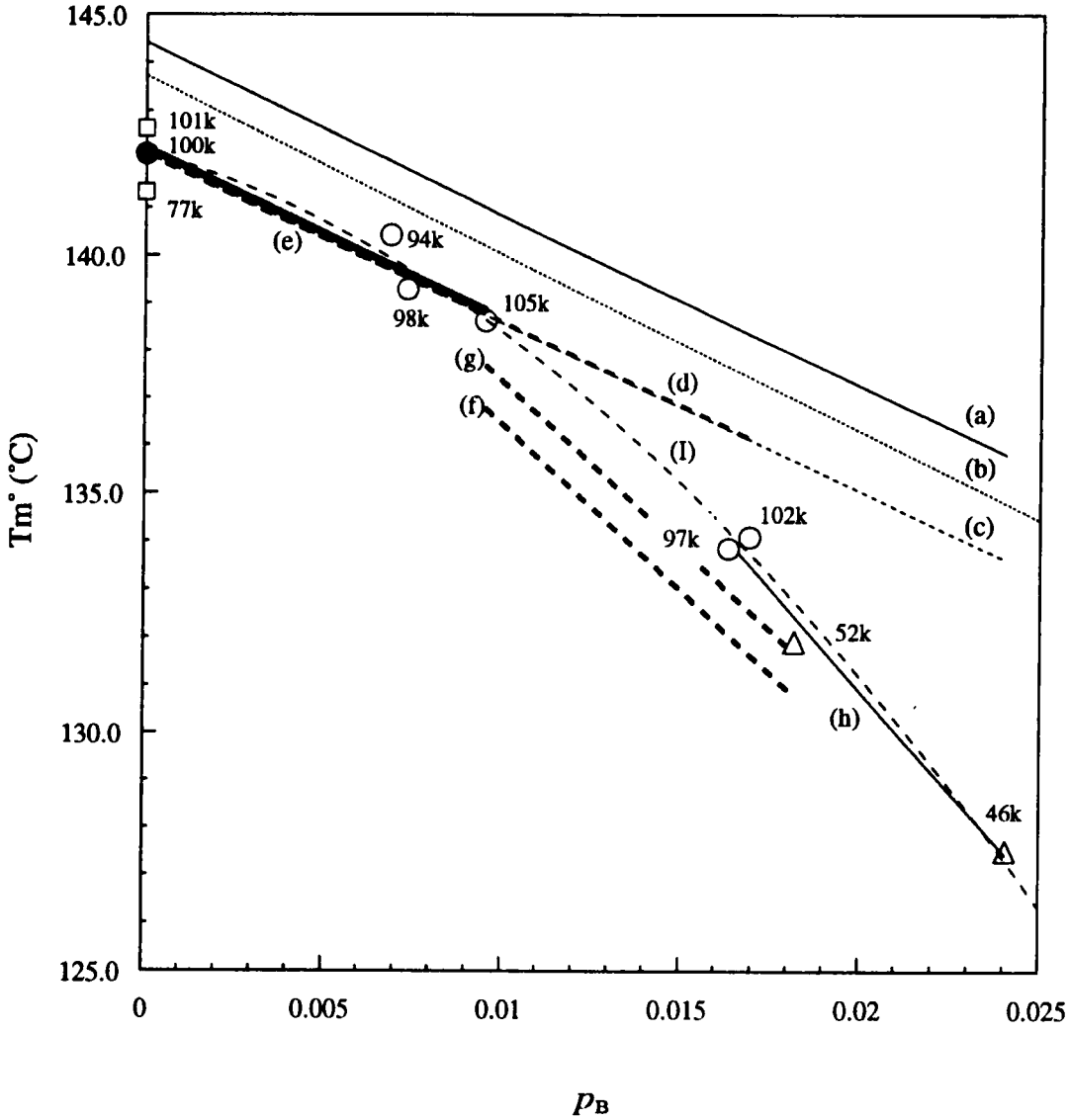


Figure 5.3.4.1. Equilibrium melting temperatures of LPE (square) and EO copolymers (circle; high Mw, triangle; low Mw) as a function of branch point mole fraction at the indicated weight average molecular weight (k=1000 g/mole; closed circle stand for Tm° calculated with **equation (5.3.3.1)**).

to be considered in addition to Flory's equation for copolymers. Flory did not consider molecular weight effect on equilibrium melting point depression of random copolymer. The best way to avoid the molecular weight effect is to use samples with same molecular weight. Since this requirement cannot be satisfied easily in experimental condition, we need to correct molecular weight effect with **equation (5.3.3.1)**. When we look through the samples with high molecular weight, the molecular weights of copolymers are in an acceptable range, $M_w = 98,400 \sim 102,700$ and $M_n = 43,600 \sim 48,800$. On the other hand, $\overline{M}_w$ of linear polyethylene is in the acceptable range but $\overline{M}_n$ shows higher than the range. In spite of the fact that $\overline{M}_w$ of linear polyethylene are in the range, we used averaged molecular weight due to the difference of $\overline{M}_n$. The averaged $(\overline{M}_w)_{Avg}$ for high molecular weight is 100,550 and similarly $(\overline{M}_n)_{Avg}$ for low molecular weight is 53,400.

Shown in **Figure 5.3.4.1** are the T_m^os of the EO copolymers as a function of the MW and branch content, together with those of the linear polyethylenes. the T_m^o's determined experimentally and calculated using **equation (5.3.3.1)** at zero defect amount (i.e., at the origin) are shown in open symbol and solid symbol, respectively and other closed circles and triangles are experimental values determined in this study. The alphabets in parentheses are explained in **Table 5.3.4.1**. The T_m^o of EO copolymers decreases slowly with branch content up to 1.0% and sharply beyond 1.0%. It also shows a strong MW dependence as well as a branch content dependence at low branch content. As branch content increases further, the T_m^o for high and low MW falls on the same extrapolated fitting line (broken line). This suggests that the MW effect becomes weak and the defect effect dominates T_m^o of the copolymers. In summary, the following relationship can be expressed

Table 5.3.4.1. Analysis method for **Figure 5.3.4.1, 5.3.4.2** and $T_m^\circ(^\circ C)$s of linear polyethylene used to calculate theoretical values.

Code in Figure	Equation type	function type	with $T_m^\circ(^\circ C)$	obtained from equation	Application range (p_B)	Comments for column 4
(a)	Flory	$f(p_B)$	144.42	$T_m^\circ(M) = 144.416 - 2.302\times10^5/\overline{M}_w$	-	this work
(b)		$f(p_B, M)$	$T_m^\circ(n)$	Flory and Vrij Analysis	-	Flory & Vrij
(c)			142.13	$T_m^\circ(M) = 144.416 - 2.302\times10^5/\overline{M}_w$	0.0~0.01	$\overline{M}_w$ = 53,400
			140.11			
(d)			$T_m^\circ(\overline{M}_w)$			$\overline{M}_w$ = 53,400
(e)	Interpolation	-	-	-		this work
(f)	Sanchez-Eby	$f(p_B)$	144.42	$T_m^\circ(M) = 144.416 - 2.302\times10^5/\overline{M}_w$	0.016~0.025	
(g)			145.35	Flory and Vrij Analysis		Flory and Vrij
(h)	Interpolation	-	-	-		this work
(I)	Extrapolation	-	-	$T_m^\circ(^\circ C) = 142.16 - 207.62p_B - 1.7057\times10^4 p_B^2$	i) 0 ~ 0.024 ii) 0.018 ~ 0.024	this work i) for high MW ii) for low MW
(J)	Extrapolation	-	-	$T_m^\circ(^\circ C) = 140.36 - 455.99p_B - 2.780\times10^3 p_B^2$	0 ~ 0.018	this work for low MW

for low defect content in copolymer

$$\lim_{p_B=1.0\to 0} T_m^o = f(n, p_B)$$

for high defect content

$$\lim_{p_B=1.0\to \infty} T_m^o = f(p_B)$$

The equation to predict T_m^o of EO copolymers as a function of defect content for high molecular weight ($\overline{M}_w = 105{,}000 \sim 94{,}000$, $\overline{M}_w/\overline{M}_n \approx 2.15$) in the range of $p_B = 0 \sim 0.024$ is given as follows:

$$T_m^o(^oC) = 142.16 - 207.62\,p_B - 1.7057\times 10^4\,p_B^2 \qquad (5.3.4.1)$$

and for low molecular weight ($\overline{M}_w = 46{,}000 \sim 60{,}000$, $\overline{M}_w/\overline{M}_n \approx 2.15$) in $p_B = 0 \sim 0.018$

$$T_m^o(^oC) = 140.36 - 455.99\,p_B - 2.780\times 10^3\,p_B^2 \qquad (5.3.4.2)$$

In $p_B = 0.018 \sim 0.024$, **equation (5.3.4.1)** is recommended. **Equations (5.3.4.1)** and **(5.3.4.2)** correspond to **(I)** and **(J)** in **Figure 5.3.4.2**.

An interesting point is whether Flory's equilibrium melting point depression equation is right or not. As we know, there have been no experimental values to evaluate Flory's equation. Often the plots of melting temperature against defect content were done, included theoretical values obtained from Flory's equation. If T_m is not measured in the

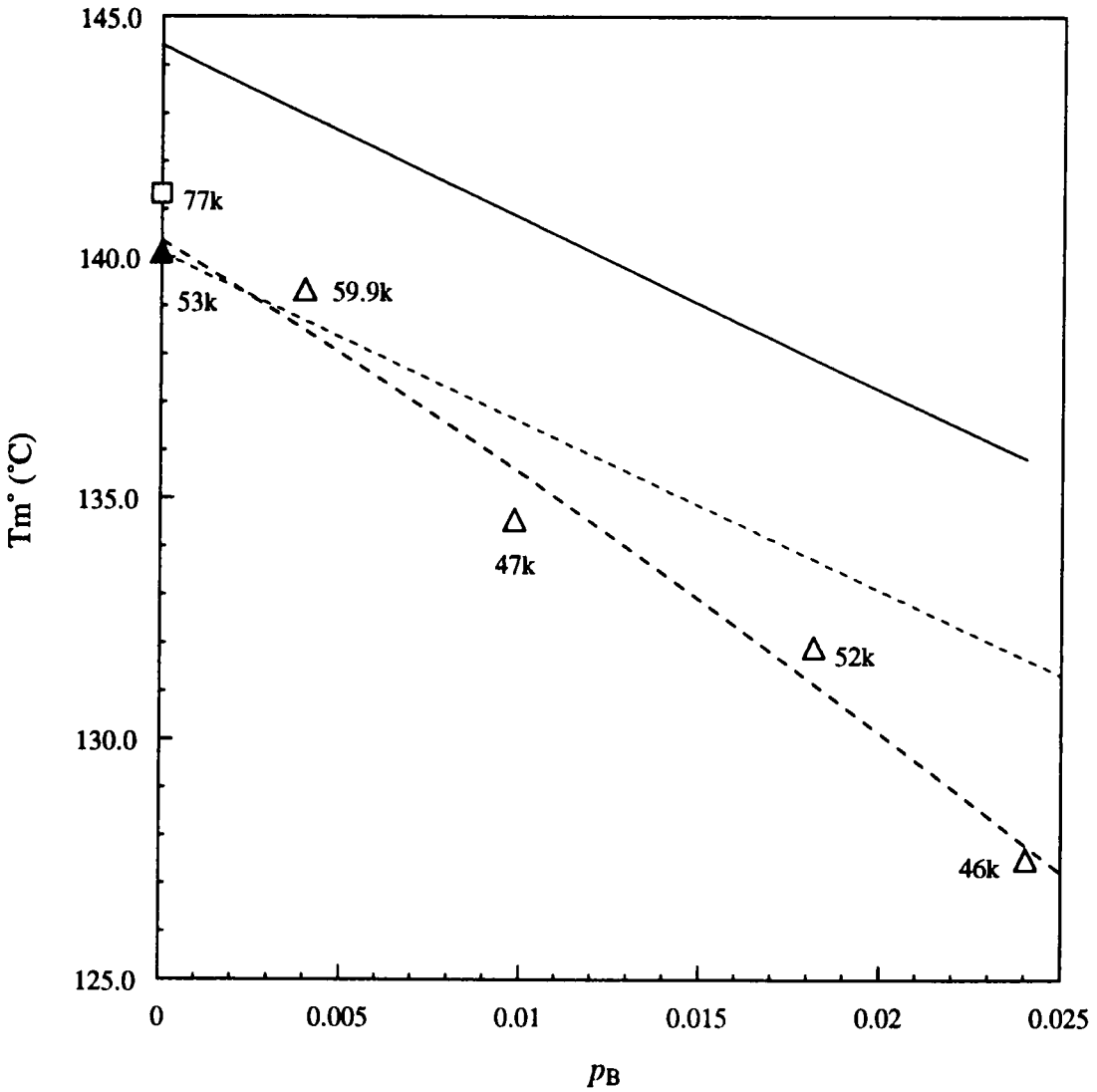


Figure 5.3.4.2. Equilibrium melting temperatures of LPE (square) and EO copolymers of low Mw as a function of branch point mole fraction at the indicated weight average molecular weight (k=1000 g/mole; closed circle stands for Tm° calculated with **equation (5.3.3.1)**).

condition of equilibrium, their approach can not evaluate Flory's equation. In the following Flory's plot, T_m^o versus p_B, for random copolymer is analyzed and discussed.

Figure 5.3.4.1 that is Flory's plot constructed in this study makes it possible to evaluate Flory's equilibrium melting point depression equation. The uppermost solid line (a) was obtained by classical analysis (Mandelkern *et. al.*, used Flory-Vrij's value and it will cause 1.0 ℃ more deviation from experimental values) with $T_m^o(n \to \infty) = 144.42\ ^oC$ of **equation (5.3.3.1)** which is T_m^o of infinite molecular weight and is 2.0 ℃ higher than the experimental values. We can understand this problem easily based on MW effect. Since the samples in this study have not infinite MW, it is necessary to correct MW contribution. No theoretical methods have been developed to correct MW and defect effects simultaneously within the limit of our knowledge. Empirically, Flory's **equation (2.5.1)** can be expressed to correct the MW effect as follows:

$$\frac{1}{T_m^o(n, p_B)} - \frac{1}{T_m^o(n)} = -(\frac{R}{\Delta H_u}) \cdot \ln(1 - p_B) \qquad (5.3.4.3)$$

where p_B is a sequence probability of non-crystallizable structure unit B in the copolymer system which represents the branch point mole fraction. When the equilibrium melting temperature $T_m^o(n \to \infty) = 144.42^oC$ of infinite MW was used, the theoretical values give the highest deviation **(a)** from the experimental values **(e)**. When the Flory-Vrij equation to correct MW was used, the calculated values **(b)** are still higher than the experimental results **(e)**. However, when the values from **equation (5.3.3.1)** are used instead of those from the Flory-Vrij equation, with $T_m^o(n) = 142.12^oC$ for the averaged $(\overline{M}_w)_{avg} = 100{,}500$ of a series of high molecular EO copolymers, or the $T_m^o(n)$s obtained as a function of each MW, the calculated $T_m^o(n, p_B)$s, **(d)** and **(c)**, coincide with the experimental values **(e)** up to 0.01 branch sequence probability p_B (i.e., less than 1.0%

branch point mole%). As branch content increases further, the values calculated from **equation (5.3.4.3)** deviate from the experimental values. The reason can be understood as follows: Flory's equation was derived under the assumption of the complete exclusion of defects from the crystalline phase. Since the hexyl branch is flexible and it is possible to rotate around single bonds, branch chains may obtain partial crystallographic register.[99, 100] In the following section, our results will show that a small number of defects can be dissolved in the crystalline phase and the amount of inclusion increases as the branch content increases, similar to results of Hosoda *et al.*[100] On the basis of the assumption that the extrapolation of the high supercooling region can predict the T_m^o for complete inclusion at the intersection of the T_m versus T_c plot[101], the possible maximum number of defects with **equation (5.3.3.7)** was estimated for $\beta = 1$ as follows: H10-O has 1.1 defects per 1000 carbons and H16-O has as much as 3.02 defects per 1000 carbons in the crystalline phase. Inclusion lower than that of H10-O is small enough to maintain a well-ordered crystalline phase and to satisfy the exclusion model. Therefore, for less than 1.0% branch content, the Flory equation can be used. As the branch content of the copolymer increases, more defects enter the crystalline phase violating the approximate exclusion condition. This may be one of the possible reasons why Flory's equation works well at low defect content and does not work at high defect content. Exclusion and inclusion transition point seems to be defect content of 1.0 % according to **Figure 5.3.4.1**.

The T_m^o behavior above high defect content (i.e., >1.0%) can be explained by considering the location of the defect. For high defect polymers inclusion of the same defect is not negligible. For example, H16-O has defects as much as 0.1% (1 defects per 1000 carbons or 7.9 defects for $\overline{M}_w = 100,500$) in the crystalline phase. (This values will be shown in **Table 5.3.5.1** of **section 5.3.5**). As enough defects are placed in crystalline phase (inclusion model), it will make the secondary force weak and lower the equilibrium

melting temperatures. The T_m^o behavior at the higher branch content permits the Sanchez-Eby equation to be tested. The reexpressed Sanchez-Eby equation incorporating molecular weight effect is as follows:

$$\frac{1}{T_m^o(n,p_B)} - \frac{1}{T_m^o(n)} = \frac{R \cdot p_B}{\Delta H_u}\left\{\frac{\varepsilon \cdot \beta}{RT_m^o(n,p_B)} + (1-\beta) + \beta \ln \beta\right\} \qquad (5.3.4.4)$$

where ε and β stand for the excess free energy due to the defect inclusion and the degree of the defect incorporation. The values of ε were calculated from the Hoffman-Weeks plot and the method used by Morra *et al.*[101] Theoretical values depend on the equilibrium melting temperatures of linear polyethylenes. The calculated values using the $T_m^o(n \to \infty) = 144.42°C$ from **equation (5.3.3.1)** and the $T_m^o(n \to \infty) = 145.35°C$ o f Flory-Vrij equation are shown as **(f)** and **(g)**, respectively. If we use the equilibrium melting temperature of a finite chain length n, the calculated values will be lowered from **(f)** or **(g)** by as much as the difference between $T_m^o(n)$ and $T_m^o(n \to \infty)$, causing deviation from experimental values. Here 10-O was calculated for both models and an extrapolation was taken between 0.016 and 0.024. The slope has roughly a similar tendency to that of the experimental values. However, there is still a difference between experimental and calculated values. Also it is not understood why the value **(g)** calculated using the Flory -Vrij value is closer to the experimental values **(e)** than that **(f)** using $T_m^o(n \to \infty) = 144.42°C$ from T_m^o versus $1/\overline{M}_w$, which was concluded in **Section (5.3.3.4)** to be the more reliable value. In fact, the Sanchez-Eby equation needs 5 parameters for correct analysis. If one of these parameters includes large error values, evaluating the Sanchez-Eby equation correctly is impossible. As B-counit increases in copolymer system, the inclusion possibility of B-counit into the crystalline phase will increase and the possibility that B-counits are not isolated in the crystalline phase will increase.

Finally, it will violate the condition that the B-counits in the crystalline phase are isolated, which is assumed by Helfand and Lauritzen for deriving the melting point depression expression of copolymer with B-counit. Therefore, within the error range 0.93℃ Sanchez & Eby's uniform inclusion model can roughly predict the equilibrium melting temperatures at high defect content ($1.6\% < p_B < 2.0\%$).

The behavior of low molecular weight materials is not as clear as that of the high molecular weight materials because of the lack of experimental data in the range less than 1.0 % defect content. If we can shift the $T_m^\circ(n, p_B)$ of copolymers as much as $T_m^\circ(n)$ of linear polyethylene from high to low molecular weight, the Flory plot of low molecular weight will show the same behavior as that of high molecular weight.

Before leaving this section, It is worth mentioning that Flory and Sanchez-Eby theories did not include the existence of the interfacial layer between the crystalline and amorphous phases. The deviation from Flory and Sanchez-Eby theories may be due to the contribution of interfacial layer on the melting. Of course, including the contribution of interfacial layer thickness for theoretical development of T_m° may be mathematically intractable. The study of interfacial layers will be given in the SAXS section.

5.3.5. Analysis of Defect Location and Content

It is helpful to know the location of the defects to understand the melting behavior of a system as well as the morphology. In order to calculate the excess free energy due to defect incorporation in the crystalline phase, **equation (2.5.6)** assuming complete inclusion of defects into the crystalline phase, or **equation (2.5.12)** assuming equilibrium

condition, can be used since we already know the composition p_B of B-counit in a copolymer and the observed enthalpy of fusion $\Delta H(p_B)$. Critical is the determination of the equilibrium melting temperatures for each case, $T_m^o(p_{B,c} = p_B)$ or $T_m^o(p_{B,c} = p_B)$. The starting point is the curvature of Hoffman-Weeks plots.

Morra and Stein[101] used the Hoffman-Weeks plot to obtain the $T_m^o(p_{B,c} = p_B)$ and $T_m^o(p_{B,c} = p_{eq})$ of the head-to-tail structure PVF_2 with the head-to-head units considered as defects in melting study of $PVF_2/PMMA$ blend system. The Hoffman-Weeks plot of PVF_2 α-crystal form shows two different slopes depending on the crystallization temperature (Hoffman-Weeks plot were studied in previous **Section 4.3.1** and **5.3.1**). From the intersections of the T_m of the copolymer crystallized from low T_c and high T_c, the corresponding $T_m^o(p_{B,c} = p_B)$ and $T_m^o(p_{B,c} = p_{eq})$ were obtained. (Here, the low T_c and the high T_c region means slope region below and above the curvature).

Such slope changes between the low and high T_c regions of the Hoffman-Weeks plots were also observed for the EO copolymers when a broad crystallization temperature range was studied (**Figure 4.3.1.1** and **Figure 4.3.1.2**). Even though $T_m^o(p_{B,c} = p_B)$ from the low T_c region can be obtained, the $T_m^o(p_{B,c} = p_{eq})$ from the high T_c region cannot be obtained. As shown in the **Figure 4.3.1.1** and **Figure 4.3.1.2**, at the high T_c region that is close to the equilibrium condition, the intercept temperatures of some copolymers show higher temperatures than even that ($144.42\ ^oC$ obtained in **Section 5.3.3**) of linear polyethylene and also the **Figure 4.3.1.2** show the parallel relation between the observed melting temperature and the crystallization temperature, $T_m = T_c + const$, where $const. \approx 10^oC$. Alternatively, The intercept, $T_m^o(p_{B,c} = p_B)$, from high supercooling region rather than low supercooling was obtained, since the intercept temperatures of some copolymers H7-O and L10-O at the high T_c region that is close to

the equilibrium condition show higher temperatures than even that of linear polyethylene as shown in the **Figure 4.3.1.1** and **4.3.1.2**. Assuming complete inclusion ($\beta = 1$), **equation (5.3.4.4)** becomes

$$\frac{1}{T_m^{\circ}(n, p_{B,c} = p_B)} - \frac{1}{T_m^{\circ}(n)} = \frac{\varepsilon \cdot p_B}{\Delta H_u \cdot T_m^{\circ}(n, p_B)} \qquad (5.3.4.5)$$

The values of ε and β can be determined from **equation (5.3.4.4)** and **(5.3.4.5)** depending on T_m° of linear polyethylene for both infinite and finite molecular weight. The parameters related to inclusion of B-counit in crystalline phase are given in **Table 5.3.5.1**. An interesting fact is that the values obtained experimentally are within the theoretical ones, 35.59~56.52 KJ/mole, calculated by Scherr *et al*[102] for isolated defects such as a kink or a Renecker defect and 23.0~54.0 KJ/mole for branched molecules.[103] This means a part of hexyl branch includes into the crystalline region in spite of its large molecular volume. Hay et al. suggested that some hexyl branches include into the crystalline lattice because flexible n-alkane unit can be the planar zigzag form in the crystalline lattice by a rotation of the C-C bonds.[99, 100]

A point required in scrutinizing **Table 5.3.5.1** is that the number of defects increases outside the crystal as well as inside the crystal as branch content increases in copolymers. Both defects located inside and outside of the crystal phase control the melting temperature. A possible physical explanation, without relying on the theoretically suggested equation, is as follows. For the defect to be in crystal some extra energy is required. When highly branched propagating chain adds comonomer (1-octene) favorably over monomer (ethene), due to the difference of monomer reactivity, defects can be localized. The chains in a defect localization region cannot overcome the energy barrier and must be expelled from the crystalline phase while isolated defect have more

Table 5.3.5.1. Parameters relating to inclusion of defects for EO copolymers.

Code	$T_m^o(p_{B,c} = p_B)$ [a] (^oC)	$T_m^o(n \to \infty) = 144.4\ ^oC$ [b], $T_m^o(n, p_B)$ [c]				$T_m^o(n) = 142.1\ ^oC$ [b], $T_m^o(n, p_B)$ [c]			
		ε [d] (KJ/mole)	β	$p_{B,c}$ [e]	$p_{B,a}$ [f]	ε [d] (KJ/mole)	β	$p_{B,c}$ [e]	$p_{B,a}$ [f]
L10-O	114.9	28.9	0.30	2.9	6.9	24.6	0.13	1.3	8.6
L18-O	106.0	20.4	0.27	4.9	13.3	18.2	0.12	2.3	15.9
H7-O	117.9	37.3	0.09	0.6	6.3	33.9	-	-	-
H10-O	112.9	31.9	0.12	1.1	8.4	29.8	0.01	0.1	9.4
H16-O	102.5	24.7	0.19	3.0	13.3	23.4	0.11	1.9	14.5

a) Obtained from the extrapolation of high supercooling region (before the upturn of curvature) in Hoffman-Weeks plot. b) obtained from equation (5.3.3.1). c) Equilibrium melting temperatures of ethylene/1-octene random (EO) copolymers determined from Thompson-Gibbs plot. d) Calculated from **equation (5.3.4.5)** assuming complete inclusion of defects. e) Defect number per 1000 carbons in crystalline phase. f) Defect number per 1000 carbons in phase boundary and amorphous phase.

possibility of incorporating into the crystalline phase. DSC thermogram analysis (**Section 4.1** and **5.1**) supported the possibility of some defect localization even in homogeneous EO copolymers. The defects accumulated outside the crystal prevent the lamellae from thickening and the crystal becomes thin, which leads to melting point depression whereas the defects in the crystalline phase make a distorted crystallography and the secondary force weakens, also contributing to melting temperature depression.

It is important to consider further whether $T_m^o(p_{B,c} = p_B)$ obtained from high supercooling region of a Hoffman-Weeks plot is really the equilibrium melting temperature for equilibrium inclusion of defects in the crystalline phase. In other words, a question is if the slope of large supercooling region in the plot of the T_m versus T_c can represent the T_m^o of the state at which the content of B-counit incorporated in lattice is equal to the total content of B-counit in copolymer. To solve this question, return to **equation(5.3.4.5)**, and focus on the degree of incorporation of B-counits in the lattice, β. As mentioned earlier, β should be unity for complete inclusion and β be zero for complete exclusion. The equilibrium melting point depression plot as a function of defect content is shown in **Figure 5.3.5.1 (a)** and **(b)** using T_m^o for $\overline{M}_w \to \infty$ and $\overline{M}_w = 100{,}000\,\text{g/mole}$, respectively. No matter where B-counits are located in system, the equilibrium melting point depression should pass through an origin in **Figure 5.3.5.1** on extrapolating, since there must be no equilibrium melting temperature depression, $1/T_m^o(n, p_B) - 1/T_m^o(n \to \infty)$ and $1/T_m^o(n, p_B) - 1/T_m^o(n)$, when there is no B-counit. The equilibrium melting temperature depression data, $1/T_m^o(n, p_{B,c}) - 1/T_m^o(n \to \infty)$, indicated as closed symbols for $\beta = 1$ do not pass through the origin as shown in linear fitting result (upper heavy solid line). The equilibrium melting point depression calculated with the excess free energy $\varepsilon = 37.3 \sim 18.2$ does not show the proper correlation of each data point although it goes through origin. Of course, the experimental error on measuring T_m^o

or extrapolating the melting temperature to intersection point in Hoffman-Weeks plot can be considered, but the errors of more than $10°C$ are required in order to satisfy the above condition. As a consequence, when T_m in the large supercooling region are extrapolated to T_c, the intercept cannot represent $T_m^o(p_{B,c} = p_B)$ properly, suggesting that each case corresponds to less than $\beta = 1$.

When T_m^o of copolymers determined from Thompson-Gibbs equation were used, the linear fitting results of equilibrium melting point depression data pass through an origin within an error limit and all these experimental data are between two extreme conditions, except for H7-O and H10-O of **Figure 5.3.5.1 (b)**, that one is Flory's exclusion model, $\beta = 0$, and another is perfect inclusion model, $\beta = 1$. The degree of inclusion, β, of the isothermally crystallized EO copolymer is 0.00 ~ 0.30 (the average degree of inclusion is $\beta = 0.19$ and $\beta = 0.09$) when ε is 37.3 ~ 28.90KJ/mole, depending on T_m^o of linear polyethylene (see **Table 5.3.5.1**). The equilibrium melting point depression plot is another version of Flory's plot (**Figure 5.3.4.1** and **5.3.4.2**) showing inclusion and exclusion behavior. When $T_m^o = 142.1\ °C$ for $\overline{M}_w = 100k$ is used, equilibrium melting point depression values of H7-O and H10-O are on the theoretical values of Flory's complete exclusion model demonstrating H7-O and H10-O follows complete exclusion model. As defect content increases further, the values of $1/T_m^o(n, p_B) - 1/T_m^o(n)$ deviate from $\beta = 0$, the case of Flory's exclusion model. This means the EO copolymers with high defect content, $0.18 \geq p_B\%.1.0$, do not obey both the perfect exclusion and the perfect inclusion models, but the uniform inclusion model between two extreme models. If whole branch length cannot be accommodated in crystalline phase, it is still possible for branch points and branch ends (methyl groups) to enter the lattice causing lattice distortion.

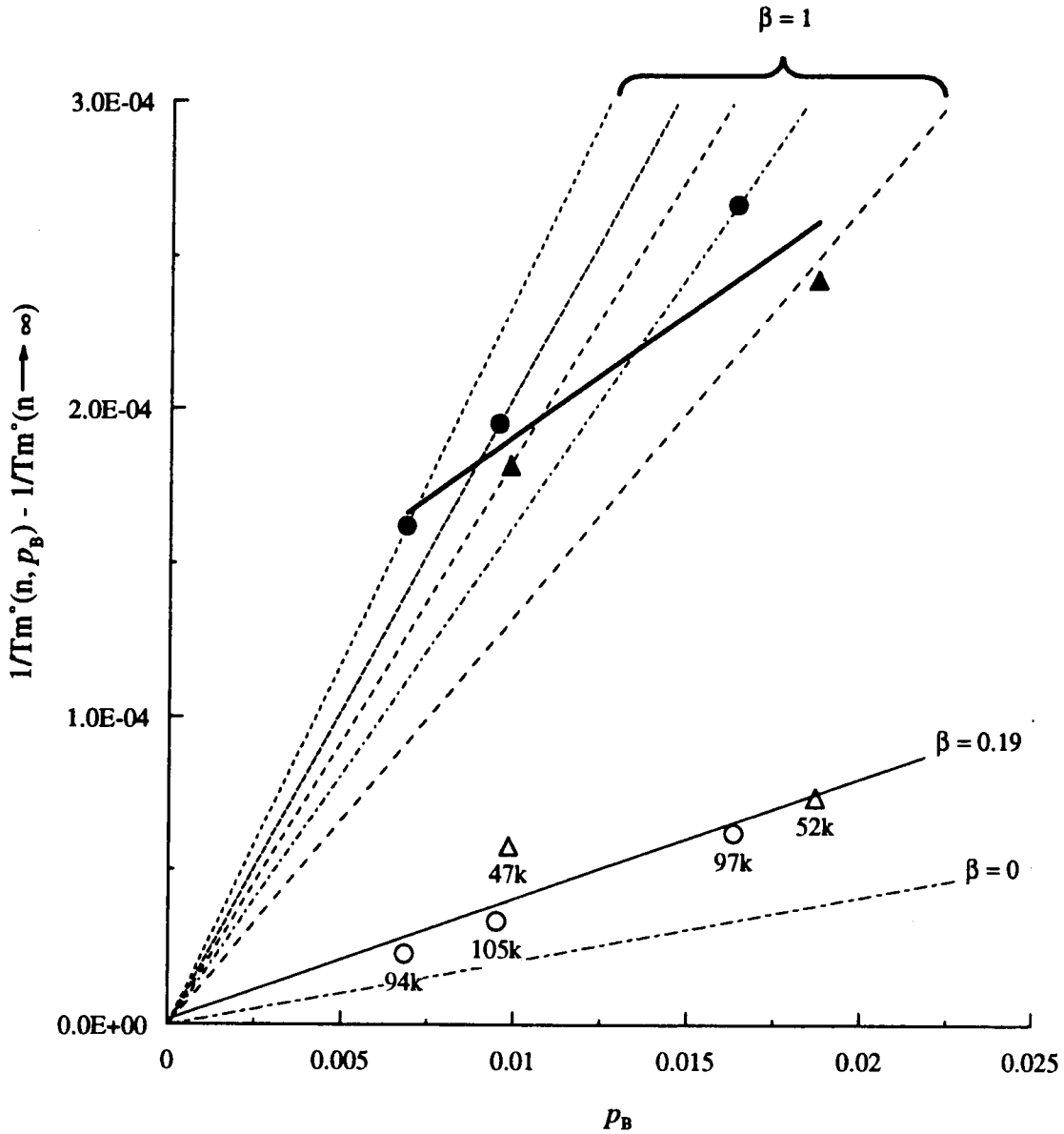


Figure 5.3.5.1. (a) Equilibrium melting temperature depression with defect content of EO copolymers. ($Tm^\circ(n \longrightarrow \infty)$ = 144.4°C for infinite molecular weight). ($Tm^\circ(n,p_B)$ from SAXS (open symbol) and Hoffman-Weeks (closed symbol)).

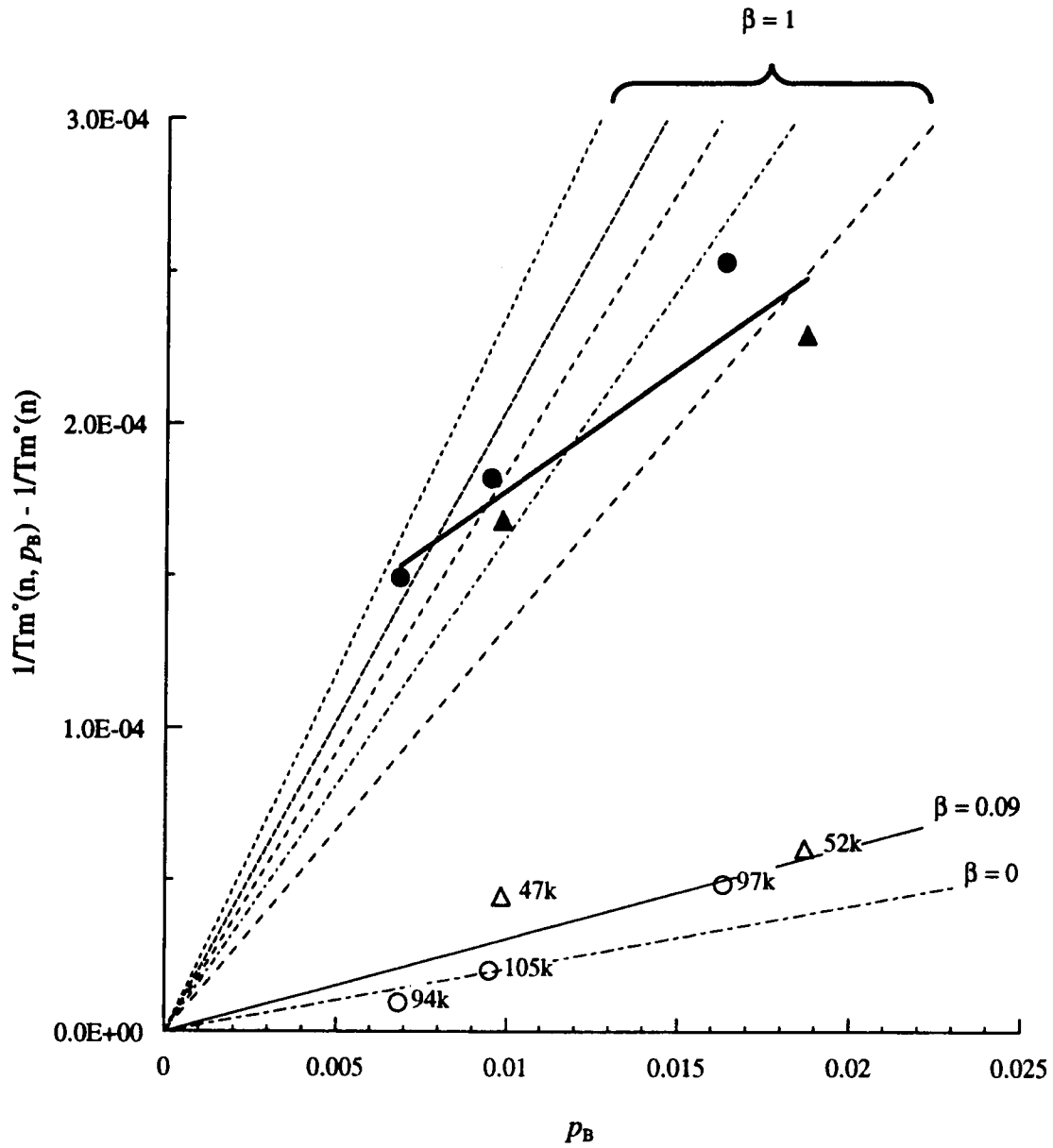


Figure 5.3.5.1. (continued) (b) Equilibrium melting temperature depression with defect content of EO copolymers. ($Tm^\circ(n)$ = 142.1°C for Mw = 100k) ($Tm^\circ(n,p_B)$ from SAXS (open symbol) and Hoffman-Weeks (closed symbol)).

The experimental fact that $\beta = 0.00 \sim 0.30$ obtained from isothermal crystallization is less than the $\beta = 0.42$ evaluated from the quenched LLDPE with hexyl branches using $\varepsilon = 83.6\,KJ/mole$ after fuming nitric etching of the quenched LLDPE with hexyl branches [99] supports the earlier theoretical idea that inclusion-favorable mechanism at high supercooling and exclusion-favorable mechanism at low supercooling occurs in the system with defect if Hay *et. al.*,[99] results are correct.

5.4. Morphology Study Using Small Angle X-Ray Scattering

5.4.1. Room and high temperature behavior

In this section the effect of temperature effect on SAXS behavior will be discussed. As shown in **Figure 4.4.1.3** and **Figure 4.4.1.4**, the reason why the first maximum peak position and intensity of samples with the same melting temperature 113.5 $^{\circ}C$ are different can be understood by considering the measurement temperature of SAXS. One sample was crystallized at 102.0 $^{\circ}C$ and another at 104.0 $^{\circ}C$ for 24 hours. Unfortunately, the melting peaks of both these samples do not separate at crystallization temperature unlike those of the other samples. The melting thermograms of both samples show a single melting peak with a shoulder above 89.7 $^{\circ}C$ and 92.8 $^{\circ}C$, respectively. The SAXS was measured at $90.0 \pm 1^{\circ}C$ for the former and at 93.0 $\pm 1^{\circ}C$ for the latter. Therefore a small crystal portion relating to the gap of 3.0 $^{\circ}C$ can contribute to the lowering of average lamellar thickness for the former while the small crystals have melted in the case of the latter causing the number average lamellar thickness increase. In fact, as listed in **Table 4.3.2.1** the lamellar thickness ($l = 62.0$ Å) of the sample crystallized at 104.0 $^{\circ}C$ is higher as much as 1.7 Å than when crystallized at 102.0 $^{\circ}C$ even though they

have the same melting temperature. However this degree of difference did not affect to the value of T_m^o estimated from the statistically stable Thompson-Gibbs plot.

5.4.2. Lamellar thickness from 1-dimensional correlation function.

The thickness of the crystalline phase can be obtained in the physical domain (i.e., real space) by using Fourier transform of reciprocal space. Here we encounter a dimension problem. One of the purposes of this study is to estimate the length of the long range order rather than the volume. In this case, only chain direction $f(x,0,0,)$ is more important than other directions $f(x,y,z,)$. Both the Fourier transforms are shown in **Figure 5.4.2.1**. One-dimensional correlation function (1-DCF) shows a distinctive first maximum that is the long period (L). On the other hand, the first maximum from the three-dimensional correlation function (3-DCF) is obscure. Also the slope of 1-DCF is two times steeper than that of 3-DCF as expected in **equation (2.6.29)**. Physically, these behaviors of both functions can be easily understood using the schematic diagram of **Figure 5.4.2.2**. In the case of a simple lamellar stack, the electron density difference $\eta(x) = \rho(x) - \bar{\rho}$ along the chain direction, i.e. perpendicular to the lamellar surface, is more obvious than $\eta(\mathbf{r}) = \rho(\mathbf{r}) - \bar{\rho}$ of all the directions in symmetrical space. In other words, the periodicity along the chain direction (i.e., length direction) is more distinguishing than that of sum of all other direction. Logically, in order to measure the length of a system, 1-DCF must be used.

The behavior of the normalized 1-DCF for the quenched LPE and EO copolymers is shown in **Figure 5.4.2.3**. The first maximum (Long period) and lamellar core thickness

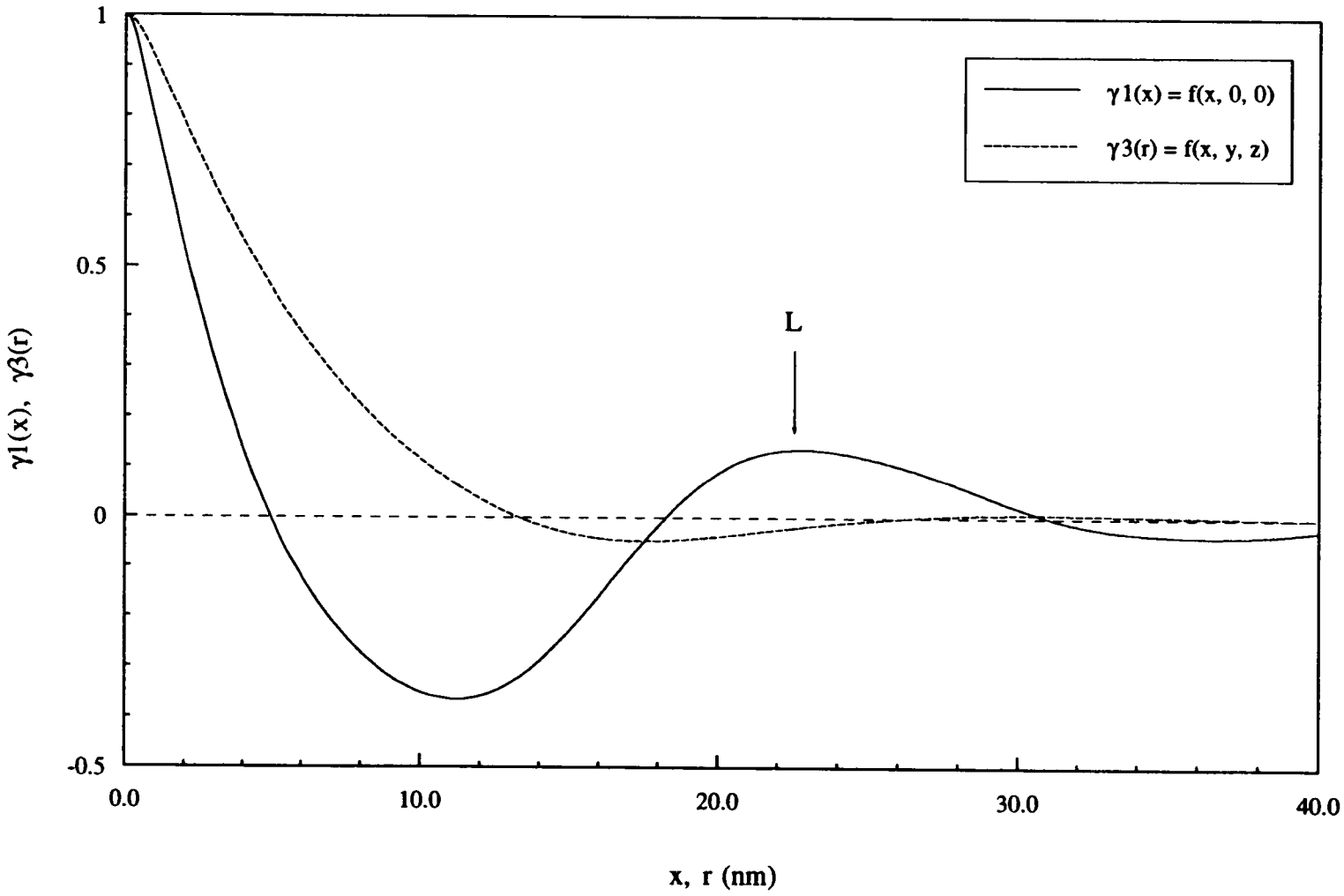


Figure 5.4.2.1. Comparison of one-, γ1(x), and three-dimensional correlation function,γ3(r), for H6-O quenched in ambient air.

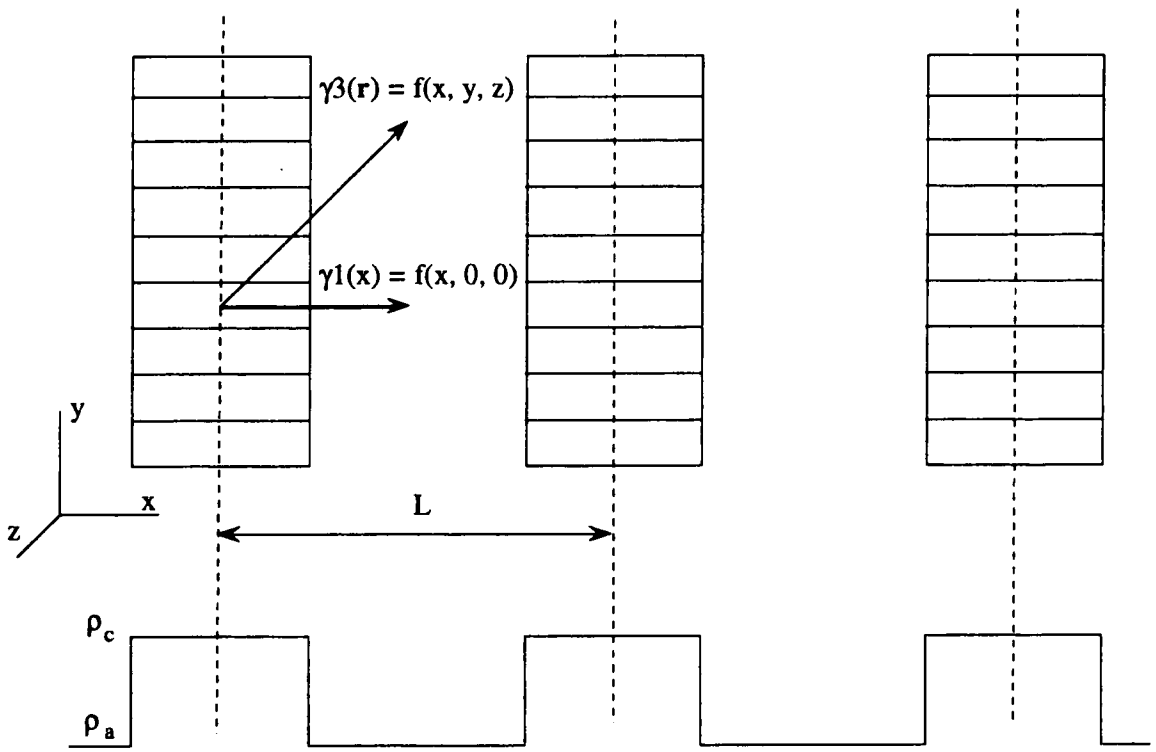


Figure 5.4.2.2. Schematic diagram showing the dimension concepts for correlation function using ideal two phase system.

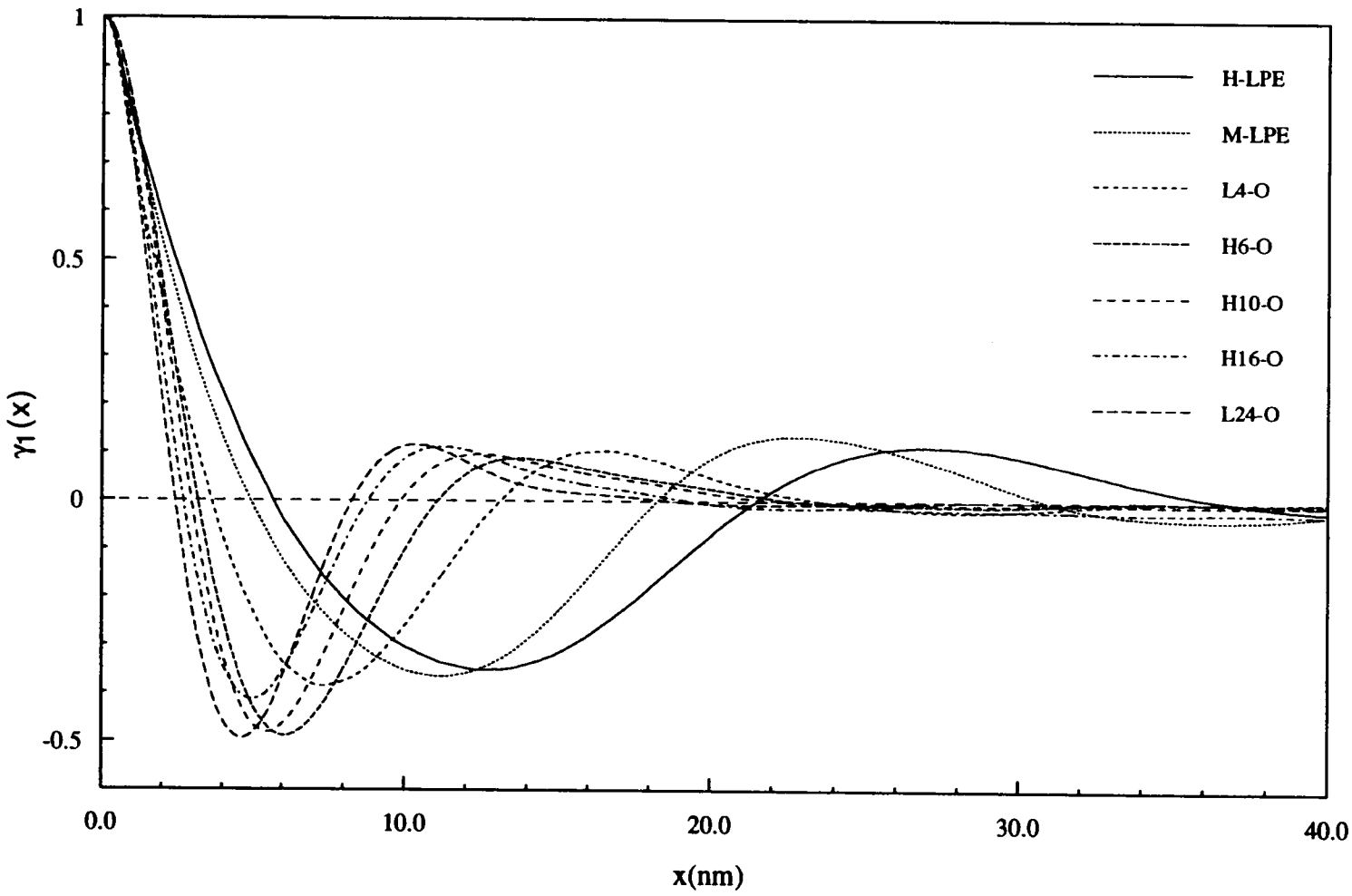


Figure 5.4.2.3. Normalized one-dimensional correlation function behavior for the quenched LPE and EO coplymers.

(d_0) decrease with increasing defect content. This behavior is due to the role of the defects in preventing lamellar growth. **Figure 5.4.2.4** is the 1-DCF of H-LPE crystallized with different time and temperature, obtained from room temperature SAXS intensity measurement. **Figure 5.4.2.5** is the 1-DCF of H-7-O from in-situ experimentation. Constructing of the Thompson-Gibbs plot to obtain T_m° requires that melting temperature be obtained as a function of lamellar thickness. Both **Figure 5.4.2.4** and **5.4.2.5** demonstrate the fact that the thick crystals melt at high temperatures. Even a small melting temperature change is reflected in the 1-DCF. However, not all the samples show a good relationship between melting and reciprocal lamellar thickness. Highly branched samples such as H16-O, H17-O and L24-O deviate from this relationship (see Thompson-Gibbs plot of **Figure 4.3.2.2** and **4.3.2.3**). The reasons of deviation may be due to that melting temperature is related to heat of fusion as well as lamellar thickness, as defects are included in crystals. The defects placed in the crystals make the secondary force weak between molecules and the melting points decrease.

5.4.3. Tail (Porod's) Region Intensity

The intensity of high scattering vector region is related to the background intensity and is called Porod's region. This background region contains information about the electron density fluctuation of a system due to the non-uniform phase and is required to be corrected in order to obtain accurate interfacial layer thickness because of their opposite scattering behavior. The following describes the methods to treat this background intensity.

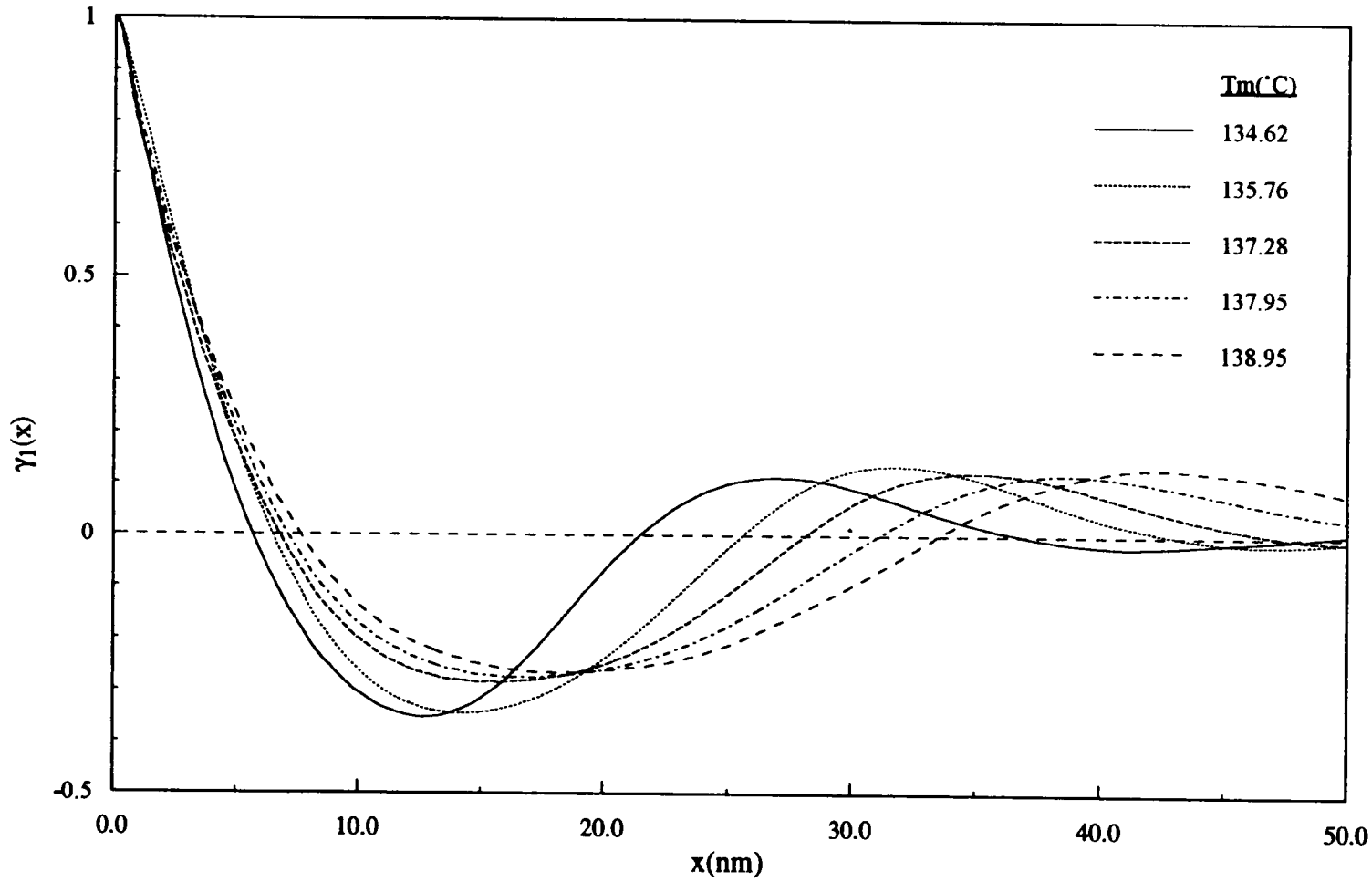


Figure 5.4.2.4. Normalized o ne-dimensional correlation function behavior of H-LPE with different melting temperatures.

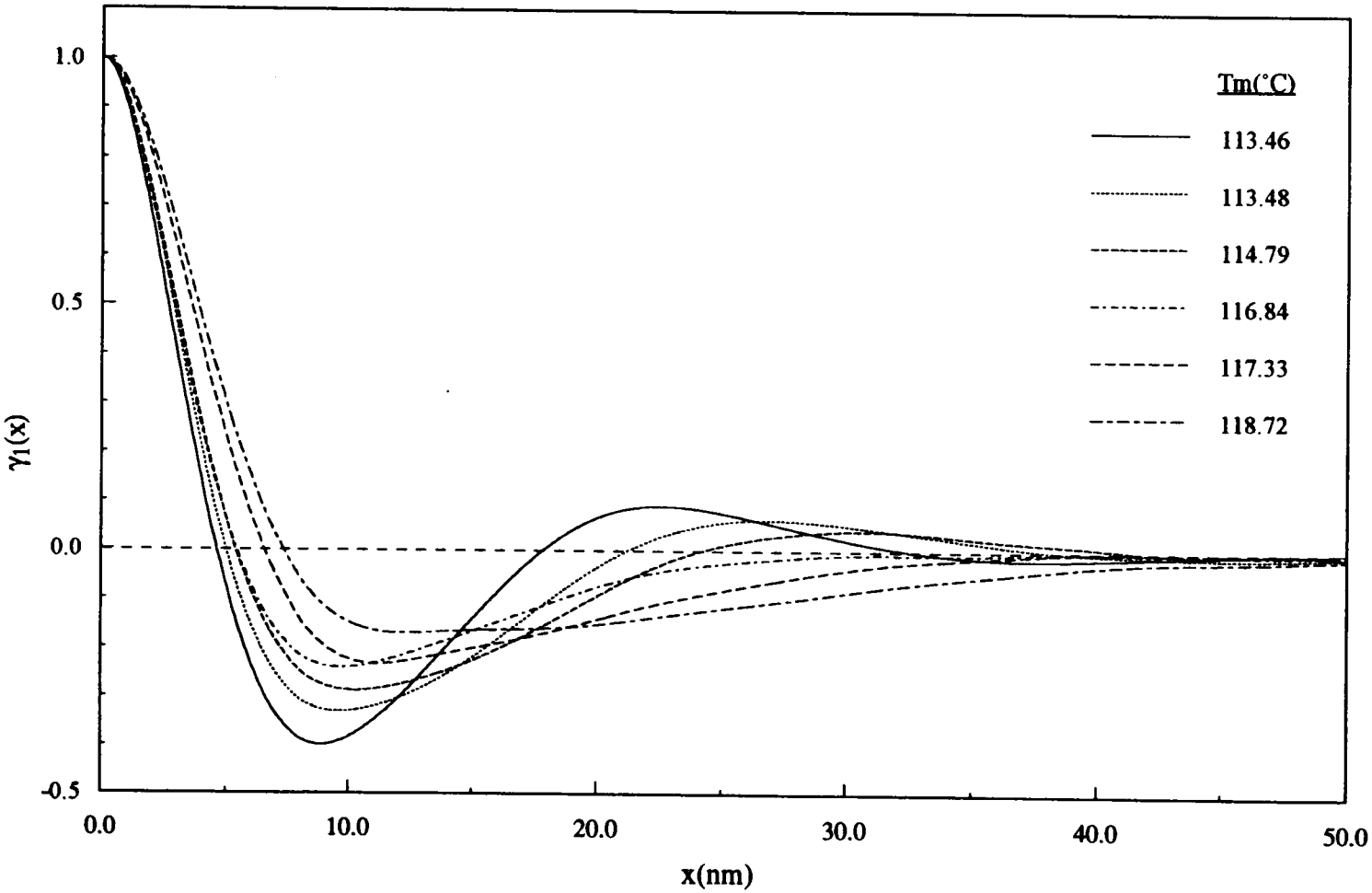


Figure 5.4.2.5. Normalized o ne-dimensional correlation function behavior of H7-O with different melting temperatures.

Extrapolated and Observed Intensity

The intensity of high scattering vector q region is necessary to obtain the intensity of $q = \infty$ region for 1-DCF as well as quantitative analysis using the invariant. **Figure 4.4.3.1** shows an example of the intensity measured at 5m and 1m, respectively, for L39-O quenched to ambient temperature. SAXS profile from 5m shows a distinctive Bragg maximum while that from 1m shows a scatter from the beam stop around the corresponding region.

To know whether the actually measured background intensity reaches to zero intensity or follows Porod's law, the Porod region of **Figure 4.4.3.1** was magnified as shown in **Figure 5.4.3.1**. The intensity (a) obtained from 5m shows severe intensity fluctuation around $q = 1.0\ nm^{-1}$ and (b) from 1m geometry relatively statistically stable intensity. At higher scattering vectors, $q \geq 1.7\ nm^{-1}$, the observed intensity does not reach zero intensity, violating Porod's law. More highly magnified SAXS background intensity profile is shown in **Figure 5.4.3.2** and does not decrease with Porod's law but upturns. This kind of positive deviation of background intensity is known to be due to heterogeneity of electron density in a system. [104]

To measure the intensity of tail region requires that the SAXS geometry be changed to 1m, requiring the recalibration of SAXS equipment and twice measurement for one sample. To avoid time and labor, we can apply a simple extrapolation technique. If the system is ideal, the intensity in the tail region decreases with Porod's law. However, most polymer systems deviate from Porod's law. This deviation occurs because the polymer system consists partly of electron density fluctuation and transition layer

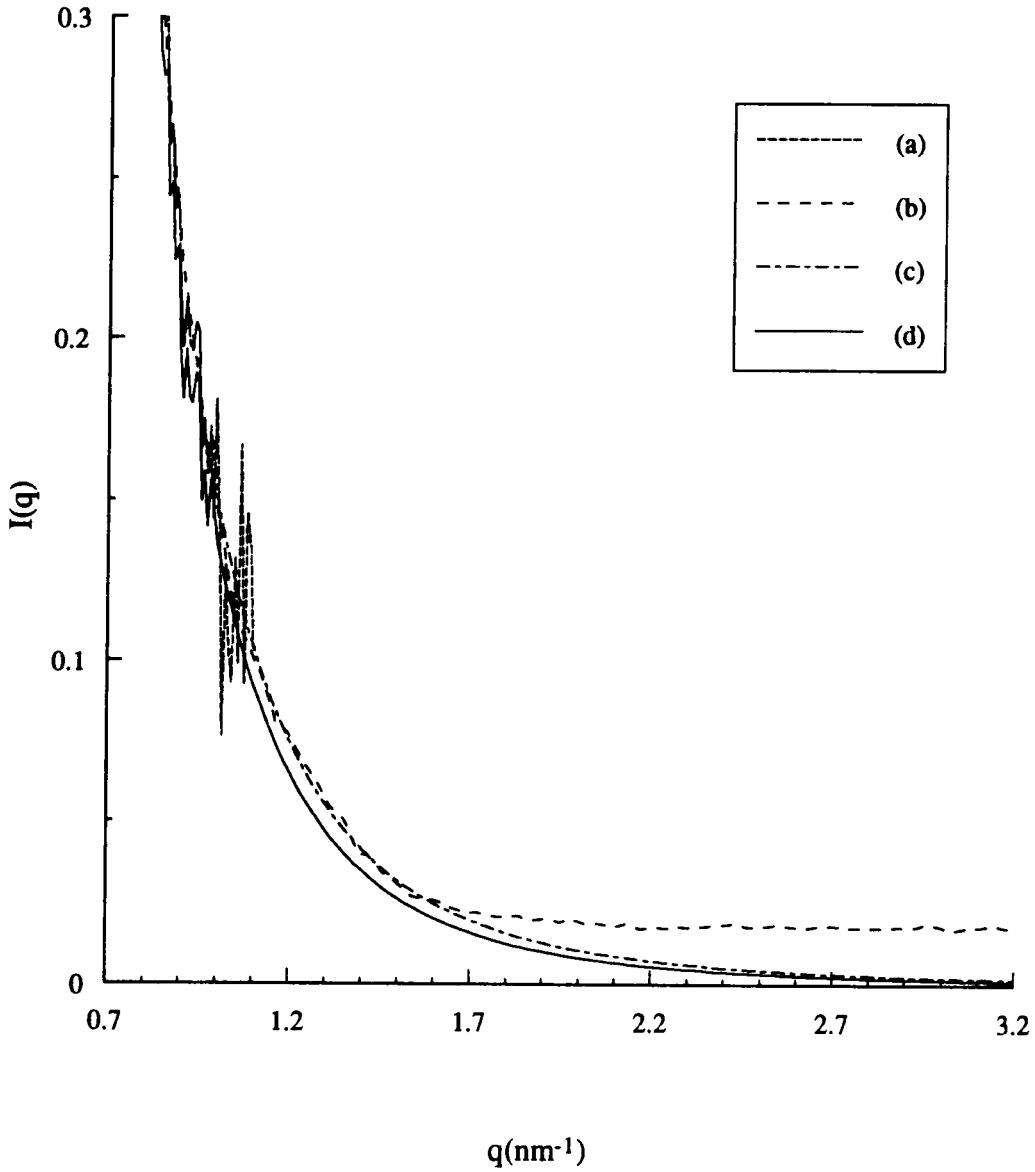


Figure 5.4.3.1. An example (sample; L39 quenched in ambient air) of the observed and the extrapolated background intensity. (see Table 5.4.3.1 for symbols)

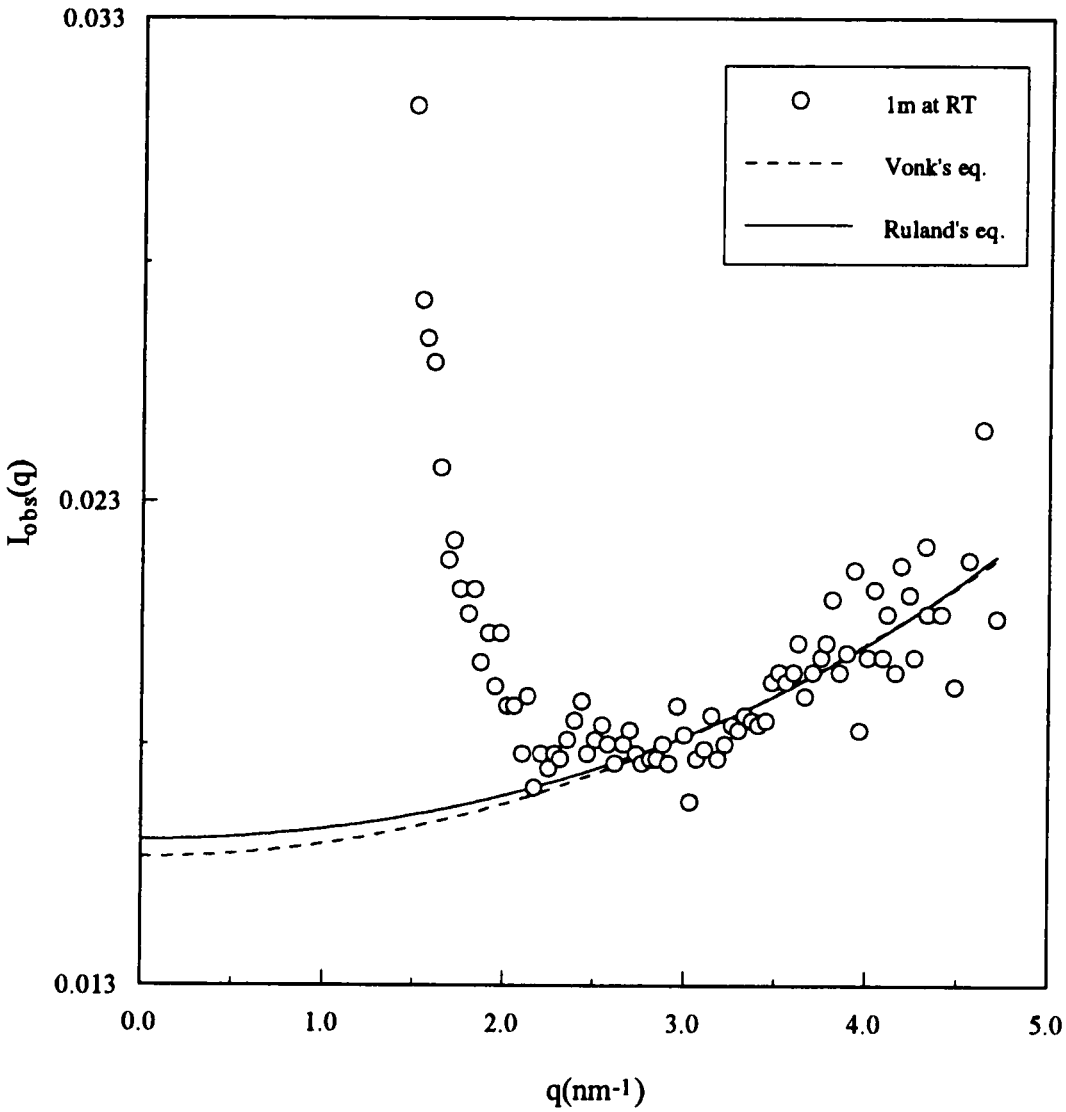


Figure 5.4.3.2. SAXS intensity profiles measured at room temperature and calculated background intensity of L39-O quenched in ambient temperature.

thickness. In fact, most our samples deviate from Porod's law. Therefore we can simply apply Porod's law to the non-ideal case as

$$\lim_{q\to\infty} I_{non-ideal}(q) = K_p' / q^n \qquad (5.4.3.1)$$

where n is an adjustable parameter to produce the best fitting results around the tail region and becomes $n = 4$ for ideal system. Using tail region intensity from 5m geometry and **equation (5.4.3.1)**, the extrapolated intensity is shown as (c) of **Figure 5.4.3.1** and it coincides with the scattering profiles from 1m geometry up to $q = 1.7\ nm^{-1}$. Beyond this scattering vector, the observed intensity increases rather than decreases while the extrapolated intensity (c) decreases with q^{-n}.

The positive deviation of SAXS intensity (see **Figure 5.4.3.2**) at high q can cause underestimation of the interfacial layer thickness and overestimation of the invariant. The correction of the background intensity due to electron density fluctuation can be performed using Vonk or Ruland's empirical equation (**equation 4.4.3.2** and **4.4.3.3**). Vonk method requires to construct a plot of $I_{obs}(q)$ versus q^2 as shown in **Figure 5.4.3.3** and Ruland method to plot $\ln I_{obs}(q)$ versus q^2 as shown in **Figure 5.4.3.4**. The calculated positive intensity for both methods matches the observed intensity, as shown in **Figure 5.4.3.2**. The intensity $I(0)$ at zero scattering vector by Ruland method gives a little higher $I(0)$ than that by Vonk method. The intensity extrapolated using background corrected intensity and **equation (5.4.3.1)** is given as (d) in **Figure 5.4.3.1**.

Table 5.4.3.1 is a summary of the analysis conditions and results of **Figure 4.4.3.1** and **Figure 5.4.3.1 ~ 5.4.3.4.**

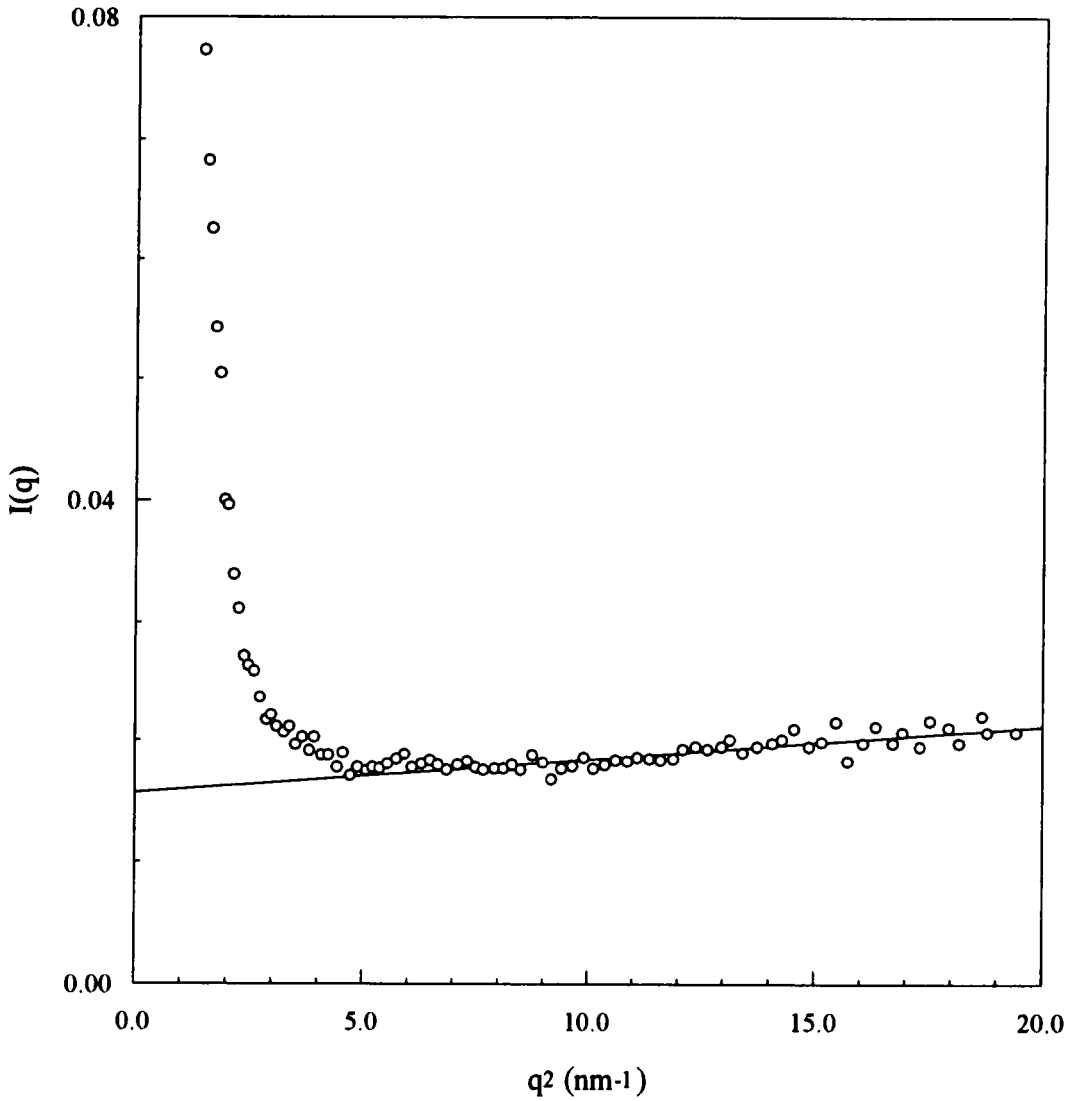


Figure 5.4.3.3. Plot to correct electron density fluctuation with Vonk's empirical equation (sample L39-O quenched in ambient temperature).

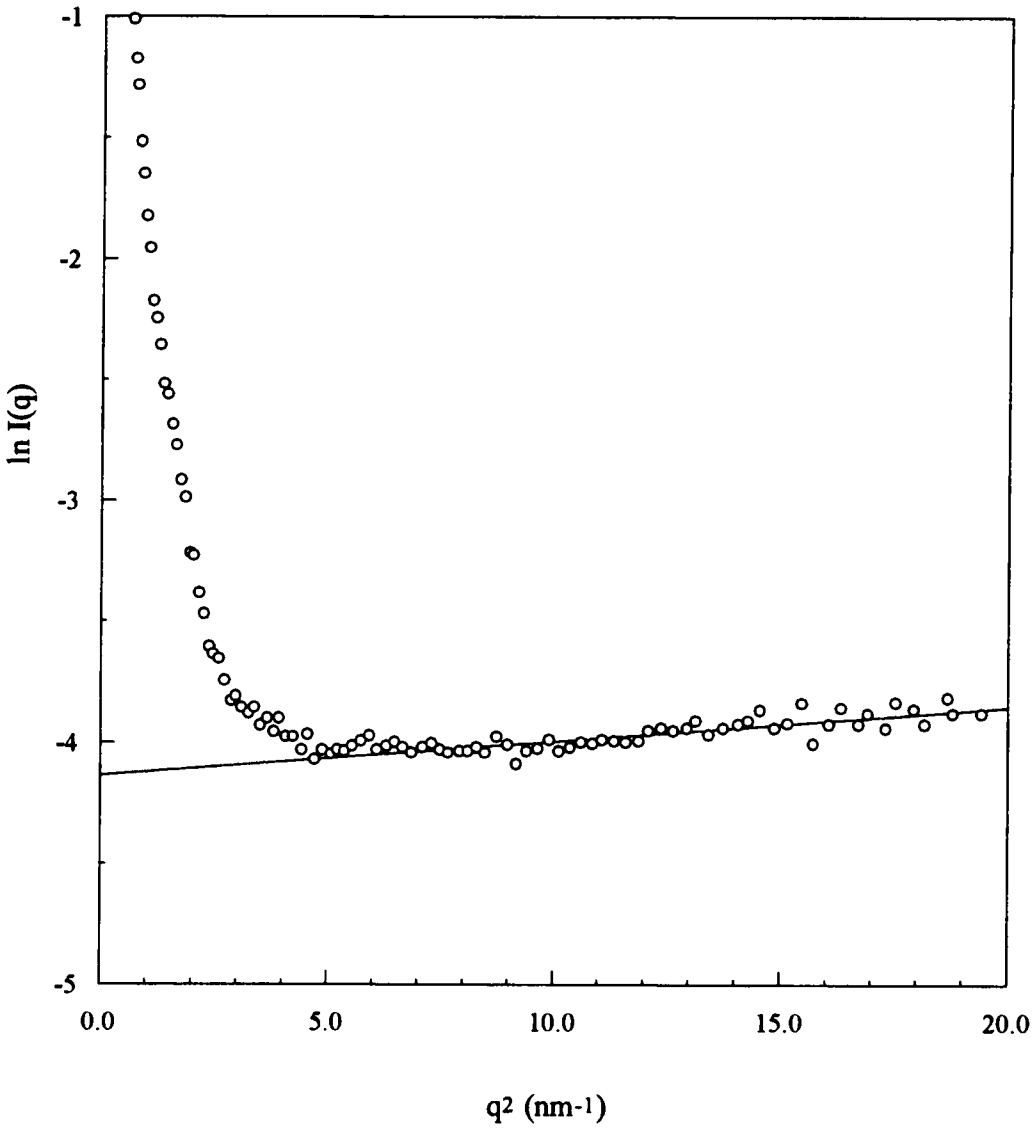


Figure 5.4.3.4. Plot to correct electron density fluctuation with Ruland's empirical equation (sample L39-O quenched in ambient temperature).

It is important to know the effect of background correction on the quantitative results. For this purpose, the invariant was calculated with four different conditions listed in **Table 5.4.3.1**. The invariant Q obtained from condition (d), having electron density fluctuation corrected, was chosen as a standard value for comparison. The background correction from both Vonk and Ruland methods contributes to invariant values, 1.55 and 1.54 $1/cm \cdot nm^3$, with the degree less than 1.0%. This quite small difference between both methods does not influence the comparison with other values. When only the scattering profiles from 5m geometry are used (i.e., condition (a)), as expected, the invariant is underestimated as much as 29% compared to the value of condition (d) due to the lack of high scattering vector region. When condition (b) is used to compensate the missing intensity of high q region, which is actually measured intensity from 1m geometry, the invariant is overestimated as much as 190 % due to the positive deviation of background. Condition (c) that is a practical applicability causes the invariant to be overestimated about 12 %, although the numerical values are very close to each other (1.55 from (d) and 1.73 from (c)). Case (d) is the best condition for quantitative analysis such as calculation of invariant or interfacial layer thickness if the background intensity can be obtained with statistic stability. Also because the intensity of this study was absolute intensity, it is possible to obtain isothermal compressibility.

Figure 5.4.3.5 shows the behavior of unnormalized 1-DCF for various cases given in **Table 5.4.3.1**. The intercept of the slope $d\gamma 1/dx$ of the "self-correlation triangle" that represents an invariant depends on the intensity at high scattering vector.[62] Case (a) shows a shoulder around $x = 10\ nm$ that is at the same location as the long period, which makes the determination of long period difficult. Case (b) creates many damping peaks losing physical meaning although the whole profile follows the other correlation function behavior. This effect is due to a Fourier ripple caused by the intensity fluctuation at high

Table 5.4.3.1. The treatment of background intensity and its effect on SAXS analysis (see **Figure 5.4.3.1** and **5.4.3.5**).

Symbol	SAXS geometry ($q(nm^{-1})$ range)	zero $q(nm^{-1})$ region	background correction due to electron density fluctuation	background $I_b(q)$	$q(nm^{-1})$ range for correlation function was obtained from	radius of gyration R_g (Å) [a]	invariant, Q $(1/cm \cdot nm^3)$ $(\times 10^2)$ [a]
(a)	5m (0.040 ~ 1.060)	No	No	No	5m	191.8	1.09 (29%)[b]
(b)	5m + 1m (0.9160 ~ 4.8620)	No	No	No	5m and 1m	195.0	4.49 (190%)[b]
(c)	5m	$I(q) = a - b \cdot q^n$	No	$I(q) = a \cdot q^{-n}$ a = porod constant for $n = 4$	5m and extrapolation ; $q \to \infty$ and $I_b(q) \to 0$	220.1	1.73 (12%)[b]
(d)	5m	n = even integer	$I_{Fl}(q) = Fl + b \cdot q^n$ n = even integer or $I_{Fl}(q) = Fl \cdot \exp(b \cdot q^2)$	n = arbitrary integer or non-integer	5m and extrapolation ; $q \to \infty$ and $I_b(q) \to 0$	220.2 220.2	1.55 or 1.54

a) sample; L39-O fast cooled in room temperature.
b) overestimation(%) based on 1.55 or 1.54 obtained from condition (d).

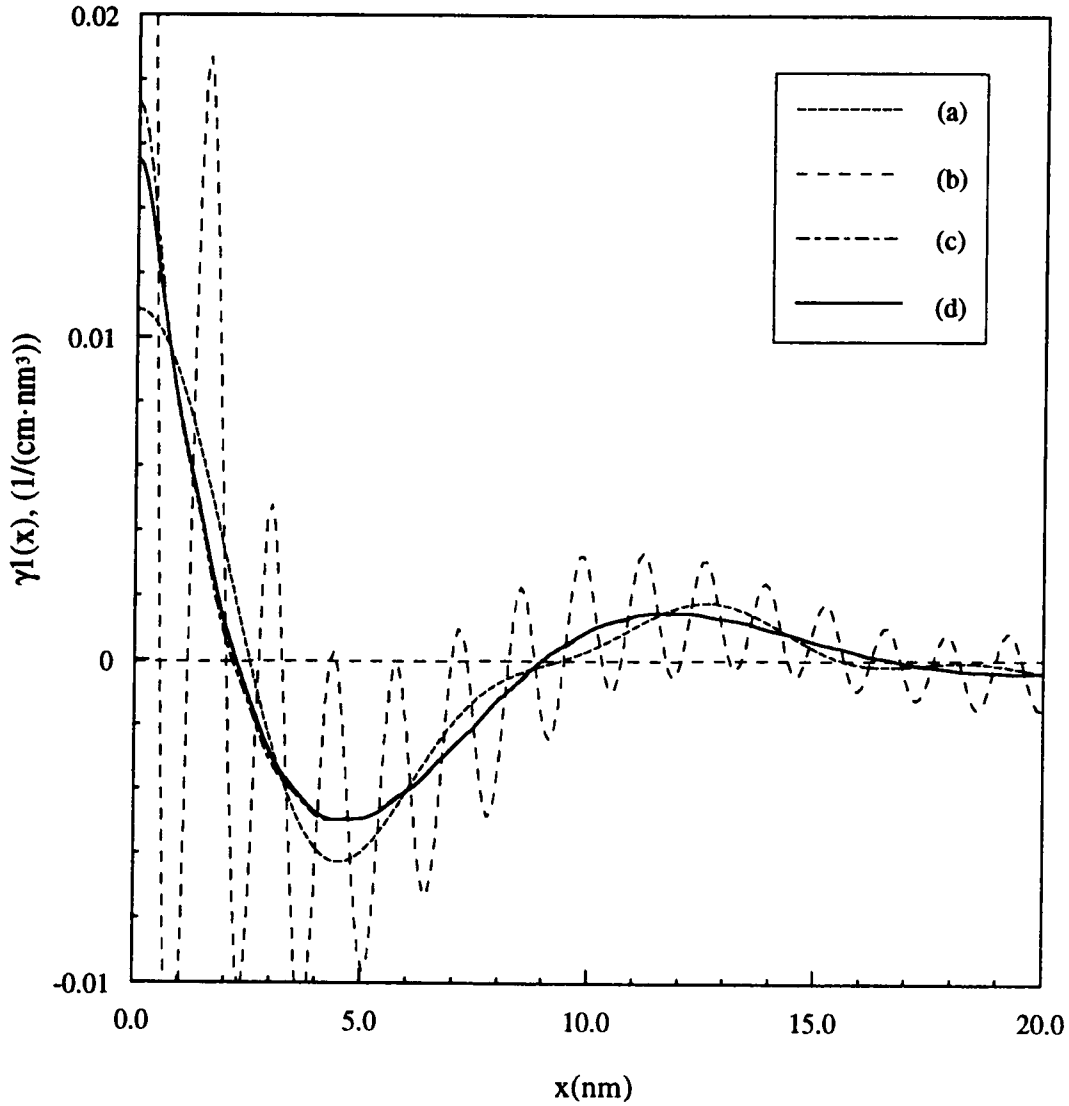


Figure 5.4.3.5. The effect of background intensity (sample; L39 quenched in ambient air) on an 1-dimensional correlation function. (see Table 5.4.3.1 for symbols).

q. This Fourier ripple effect can be removed effectively as shown in Case (c) and (d) when the high intensity region is extrapolated with **equation (5.4.3.1)** using proper fitting parameter. This is due to the smoothing effect to the correlation function by extrapolated intensity. To obtain the long period or lamellar thickness, the condition of (c) and (d) is recommended. Case (d) is the best condition to obtain the invariant. However to have the best resolution in the Bragg and Porod regions, the high scattering vector region requires independent experiment at 5m and 1m SAXS geometry. In practice Case (c) is more pragmatic than Case (d) since only the scattering vector from 5m geometry is necessary. In fact, the slopes around the self-correlation triangle region and the first maximum of Case (c) and (d) appear identical in **Figure 5.4.3.5**.

5.4.4. Electron Density Fluctuation and Invariant

The fundamental theory of scattering due to density fluctuations is well established.[105], [106], [107] In this section, the electron density fluctuation is related to morphology. The perfect crystal lattice without thermal vibrations will have zero-density fluctuation. However, a lattice or system with defects will have density fluctuation. The following is an application of these concepts to EO copolymer system.

The EO copolymers may have a certain amount of defects in crystalline phase. These included defects make the electron density of crystalline phase irregular (as shown schematically in **Figure 4.4.3.1**). The more defects in a crystalline phase, the higher the electron density fluctuation the system must have. The zero-scattering vector intensity $I(0)$ should be increased with defect content due to the relation

$$I(0) = \rho^2 kT\beta_T \qquad (5.4.4.1)$$

where ρ and β_T are the mean-electron density of an object and the isothermal compressibility. k is the Boltzmann constant and T the absolute temperature. Experimentally, $I(0)$ can be determined from Vonk's method (**equation 4.4.3.2**) and Ruland's method (**equation 4.4.3.3**). **Figure 5.4.4.1** shows the observed background intensity and the calculated intensity by using both methods for LPE and EO copolymers. The observed intensity of M-LPE does not show the positive deviation unlike that of EO copolymers. An alternative method to estimate the electron density fluctuation component, Fl_e, is given by [108]

$$I_{obs}(q)\cdot q^4 = K_p \cdot H^2(q) + Fl_e \cdot q^4 \qquad (5.4.4.2)$$

The slope of $I_{obs}(q)\cdot q^4$ versus q^4 represents the electron density fluctuation. **Figure 5.4.4.2** shows that the slope becomes steeper as comonomer content increases representing the increase of electron density fluctuation. The three methods show similar results, as shown in **Figure 5.4.4.3**. The Vonk and Ruland methods cannot be differentiated from each other graphically.

Figure 5.4.4.4 shows the component Fl_e obtained from **Figure 5.4.4.2** as a function of defect content. If H-LPE without defects in system has constant electron density in crystalline phase, assuming the chain ends are expelled from crystal, we can subtract Fl_e from those of EO copolymers. By performing this procedure, at least we can remove the common Fl_e of H-LPE and EO copolymers. According to Rathje *et. al.*,[109], the electron density fluctuation depends on the crystallinity and temperature. Their data showed that as crystallinity decreases, Fl_e increases linearly. The sample of zero

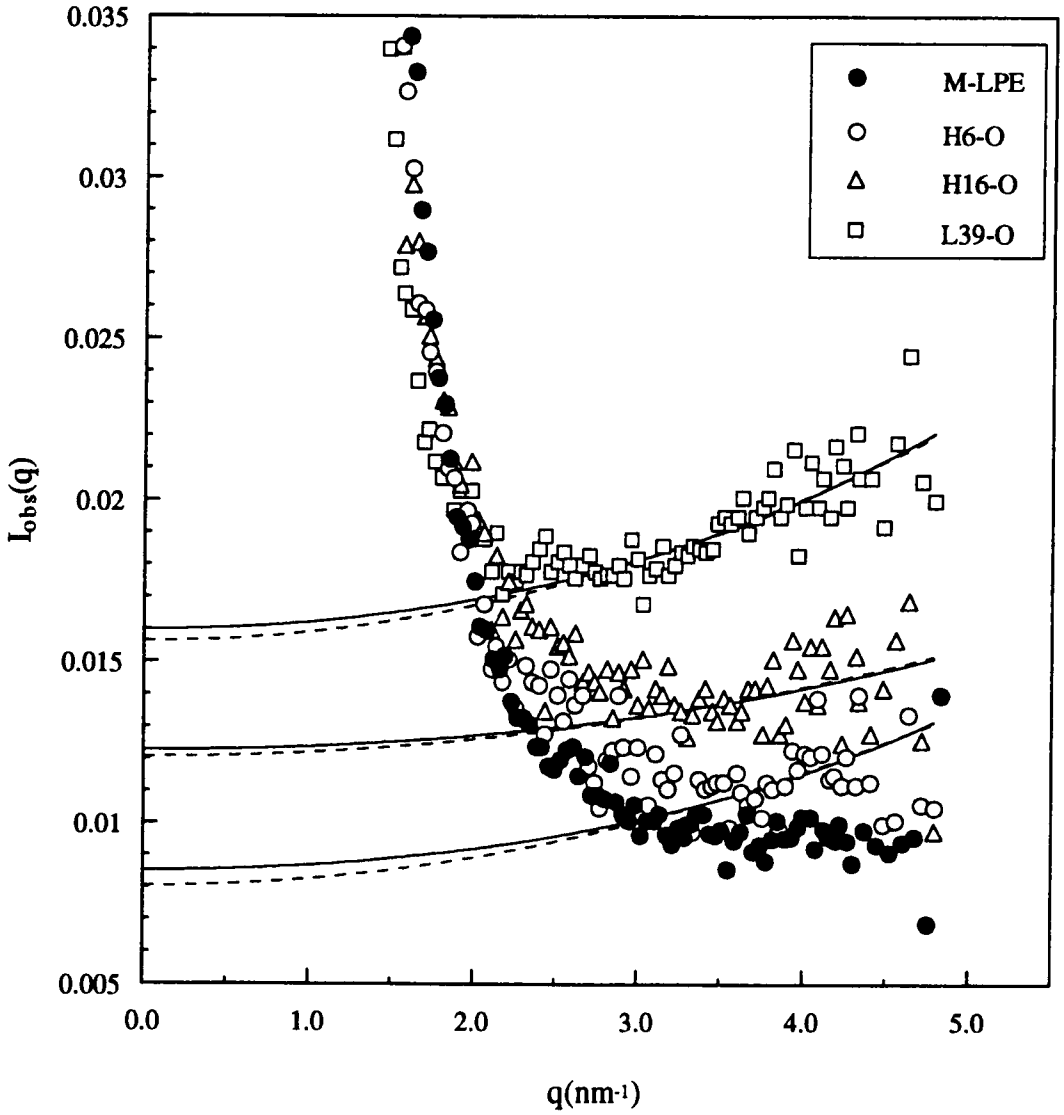


Figure 5.4.4.1. The observed and the background intensity obtained using Vonk(broken line) and Ruland(solid line) empirical equation for M-LPE and EO copolymers.

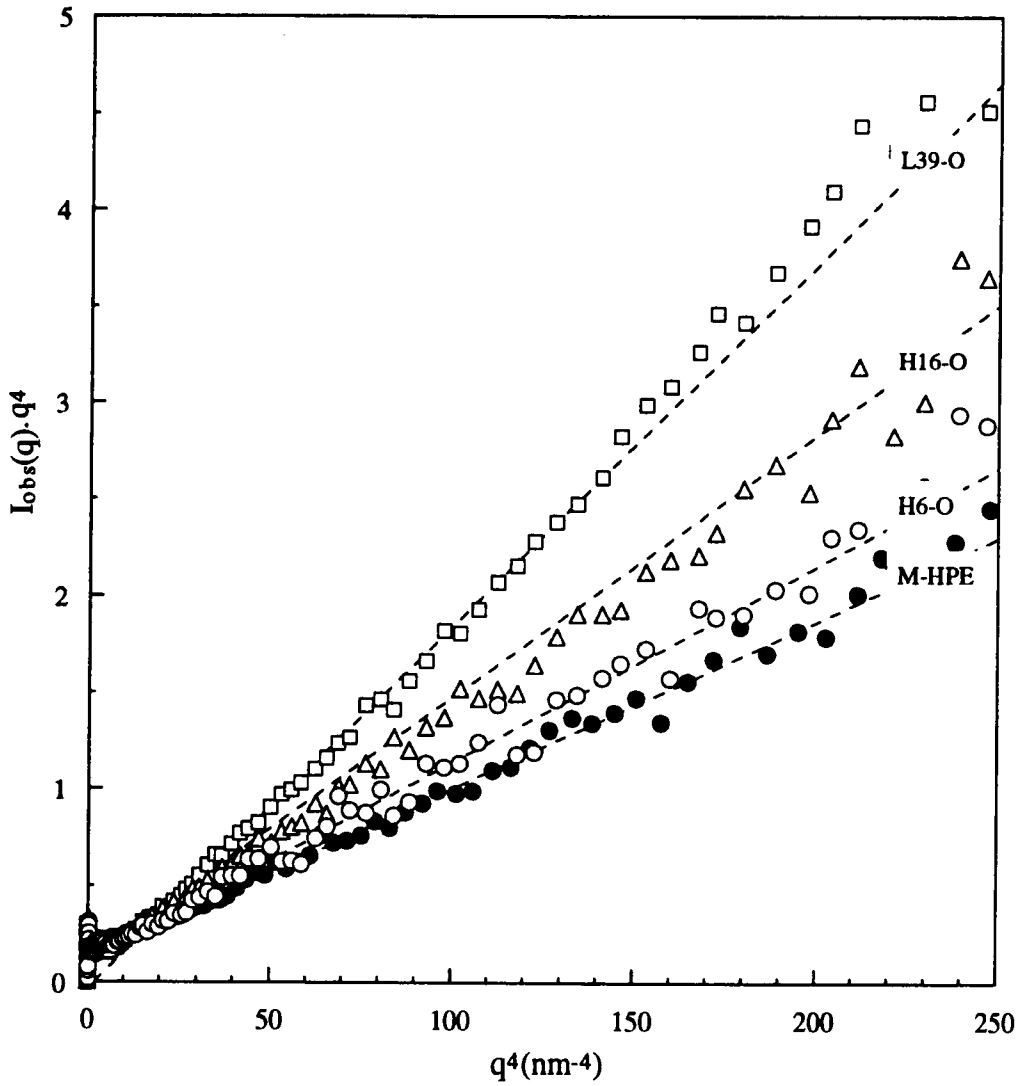


Figure 5.4.4.2. Alternative plot to estimate electron density fluctuation component (Fl) for LPE and EO copolymers.

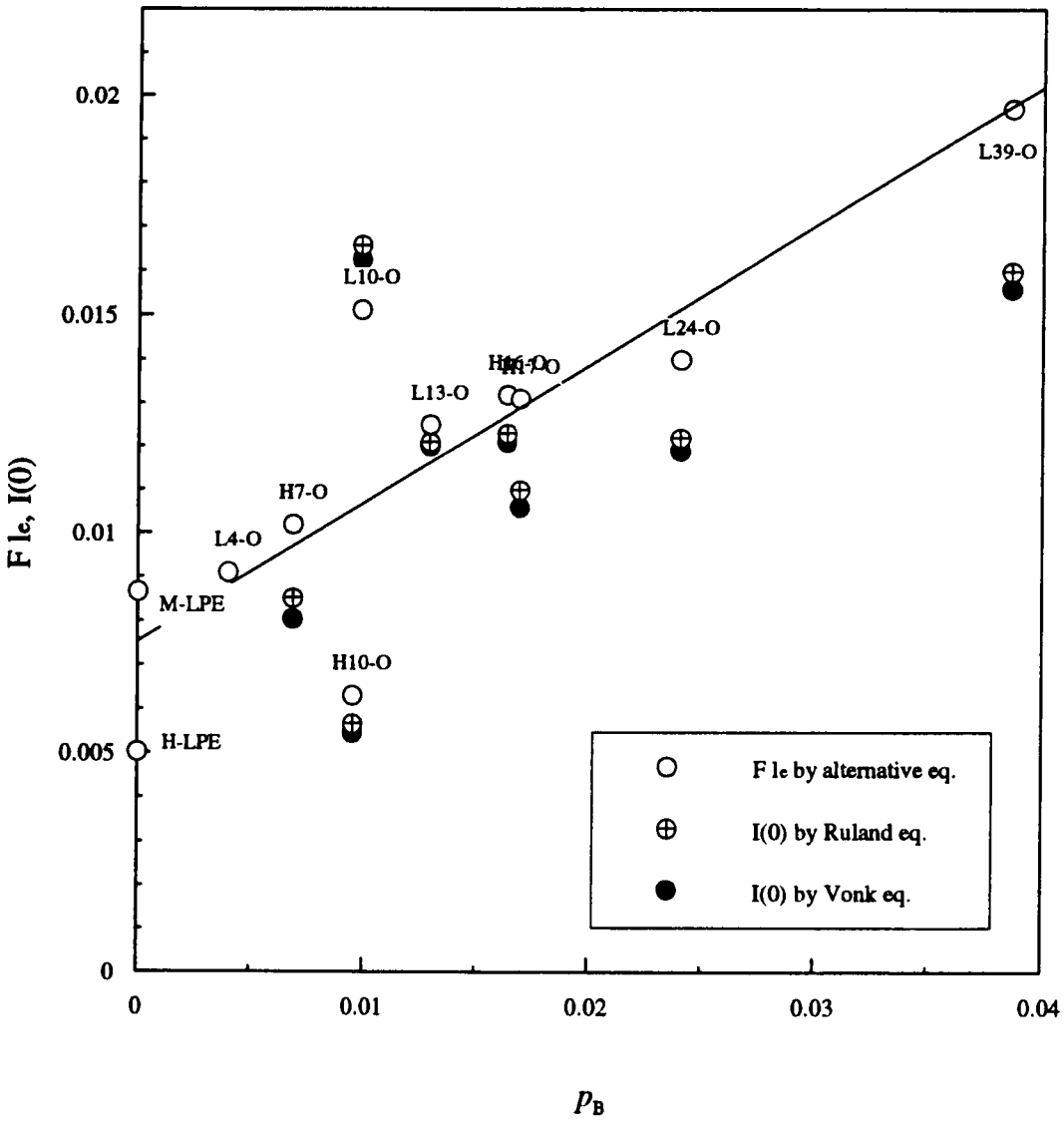


Figure 5.4.4.3. Electron density fluctuation components (Fle) of polymer systems by various empirical methods.

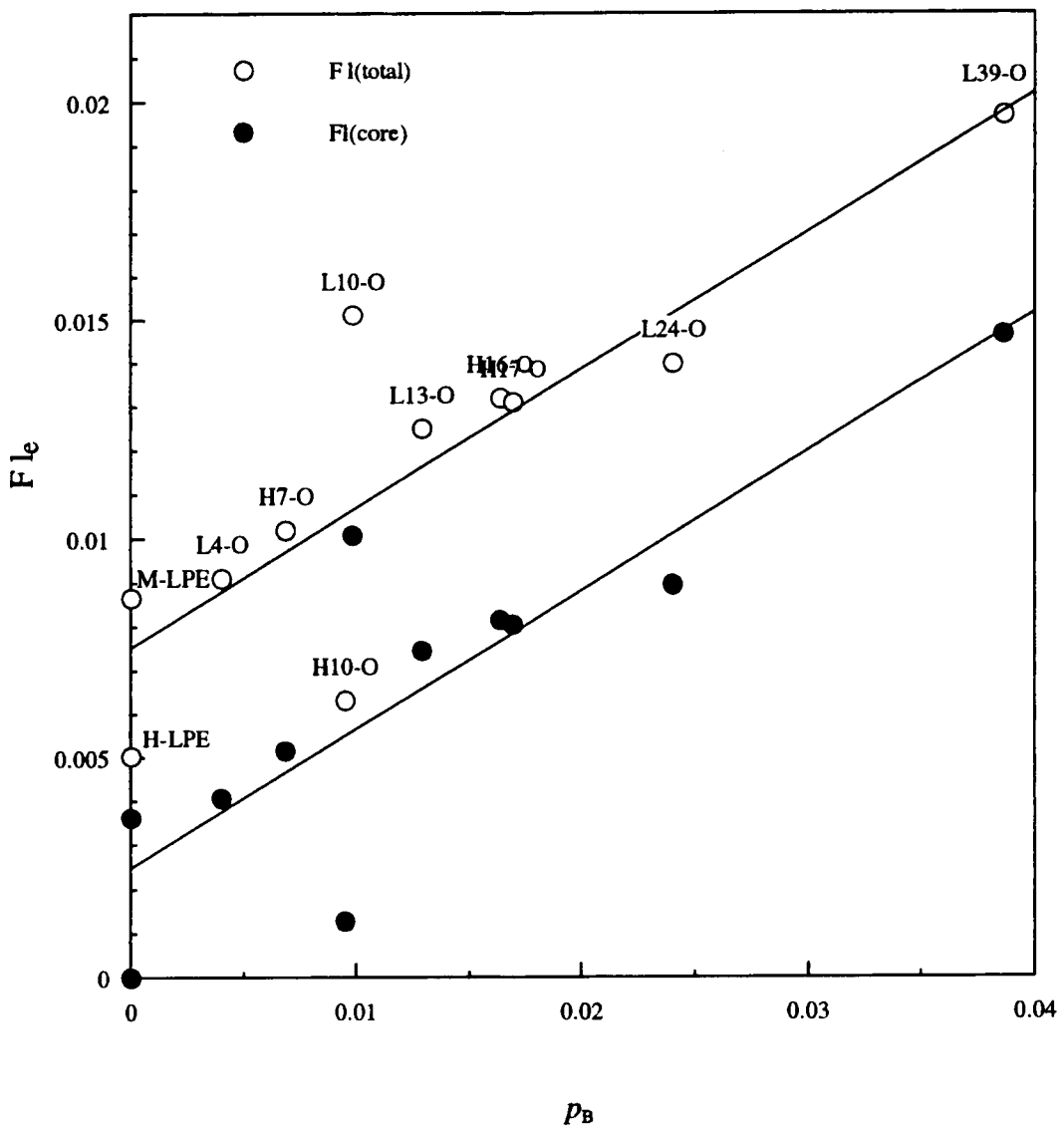


Figure 5.4.4.4. Electron density fluctuation components for LPE and EO copolymers without and with subtraction of Fl_e of H-LPE.

crystallinity showed the highest Fl_e. Their results have the same trend as **Figure 5.4.4.4.** It is not clear whether component Fl_e is dominated by defects in amorphous phase, by the crystalline phase with defects, by the interfacial layer or all of them. To solve this problem, the electron density difference between the amorphous and crystalline phases was obtained from invariant, density, and baseline analysis of 1-DCF.

The invariant as a function of defect content is shown in **Figure 5.4.4.5**. Since the electron density fluctuation was removed from the system, the calculated values can represent the mean square electron density deviation, $(\rho_c - \rho_a)^2$, of the sample. Since the calculation step to obtain electron density difference from the invariant duplicates work of Strobl [62], only calculated results are listed in **Table 5.4.4.1**. The electron density difference, $\rho_c - \rho_a$, decreases with comonomer content and similarly the density of the crystal core and the amorphous phase decreases with defect content as shown in **Figure. 5.4.4.6**. In fact both ρ_c and ρ_a decrease with defect content, but the decrease in ρ_c is larger than that in ρ_a. Qualitatively, a crystalline phase with defects contributes to high Fl_e. The decrease of ρ_c means that the crystalline phase is not perfect and has a certain degree of defects in crystal. The Fl_e of H7-O and H10-O is close to M-LPE and H-LPE, respectively, suggesting few defects in crystalline phase. This parallels the result of the Flory plot as the Flory copolymer equation that assumes exclusion of defects can apply up to $p_B = 1.0\%$ for homogeneous EO copolymers. The primary purpose of this section was to find a method to confirm the inclusion and exclusion result of **section 5.3.5**. Conclusively, the results of Fl_e and $\rho_c - \rho_a$ from SAXS correspond to the earlier result.

Temperature effect on Fl_e must be measured as a function of temperature for the sample quenched or crystallized at a particular temperature. However, Figure **5.4.4.7** constructed using H-LPE crystallized isothermally as a function of time and temperature

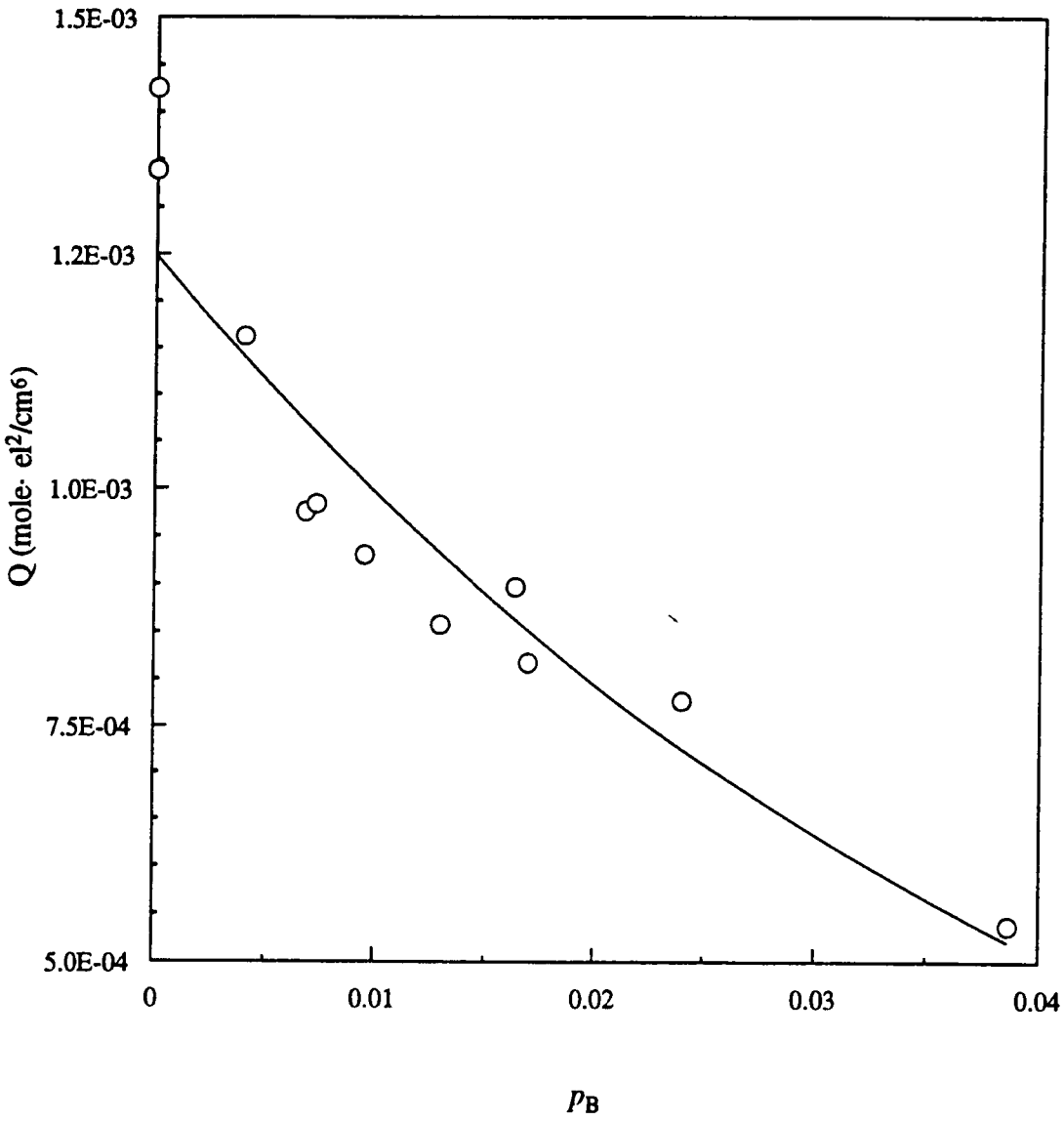


Figure 5.4.4.5. Invariant, $Q(mole \cdot el^2/cm^6)$, as a function of defect content for quenched LPE and EO copolymers.

Table 5.4.4.1. Electron and mass density of the crystalline and amorphous phase for the quenched LPE and EO copolymers.

Samples	mass density d (g/cm^3)	electron density ρ [a] (mole el/cm^3)	invariant $Q\times10^4$ (mole el^2/cm^6)	baseline $\times10^4$ (mole el^2/cm^6)	$\rho_c-\rho_a$ (mole el/cm^3)	ρ_a (mole el/cm^3)	ρ_c (mole el/cm^3)	d_a (g/cm^3)	d_c (g/cm^3)	d_c-d_a
H-LPE	0.9540	0.5451	14.259	5.3527	0.0848	0.5220	0.6068	0.9135	1.0619	0.1483
M-LPE	0.9510	0.5434	13.397	5.3527	0.0810	0.5203	0.6013	0.9105	1.0523	0.1418
L4-O	0.9365	0.5351	11.630	4.5322	0.0759	0.5139	0.5898	0.8992	1.0321	0.1329
H7-O	0.9180	0.5246	9.7592	4.7712	0.0665	0.5027	0.5693	0.8798	0.9962	0.1164
H7'-O	0.9180	0.5246	9.8430	4.7712	0.0669	0.5027	0.5696	0.8798	0.9969	0.1171
H10-O	0.9126	0.5215	9.3112	4.4809	0.0652	0.5003	0.5655	0.8756	0.9896	0.1140
L13-O	0.9110	0.5206	8.5834	4.3809	0.0598	0.4967	0.5565	0.8692	0.9738	0.1047
H16-O	0.9003	0.5145	8.9760	4.4809	0.0636	0.4933	0.5569	0.8633	0.9745	0.1113
H17-O	0.9003	0.5145	8.1800	3.7401	0.0616	0.4951	0.5568	0.8665	0.9743	0.1079
L18-O	0.9027	0.5158	-	-	-	-	-	-	-	-
L24-O	0.8975	0.5129	7.7787	3.8380	0.0593	0.4933	0.5526	0.8632	0.9670	0.1038
L39-O	0.8700	0.4971	5.3811	1.7171	0.0542	0.4840	0.5382	0.8471	0.9419	0.0948

a) ρ(mole el/cm^3) = d(g/cm^3)×8/14(mole el/g)

Table 5.4.4.1. (continued)

Samples	mass density d (g/cm^3)	electron density ρ (mole el/cm^3)	invariant $Q\times10^4$ (mole el^2/cm^6)	baseline $\times10^4$ (mole el^2/cm^6)	$\rho_c-\rho_a$ (mole el/cm^3)	ρ_a (mole el/cm^3)	ρ_c (mole el/cm^3)	d_a (g/cm^3)	d_c (g/cm^3)	d_c-d_a (g/cm^3)
L40-P	0.9046	0.5169	8.1364	2.8802	0.0649	0.4999	0.5649	0.8749	0.9885	0.1136
L93-P	0.8849	0.5057	5.3389	2.2736	0.0505	0.4906	0.5411	0.8585	0.9469	0.0884
L31-B	0.9048	0.5170	8.4813	3.6426	0.0635	0.4979	0.5615	0.8714	0.9826	0.1112

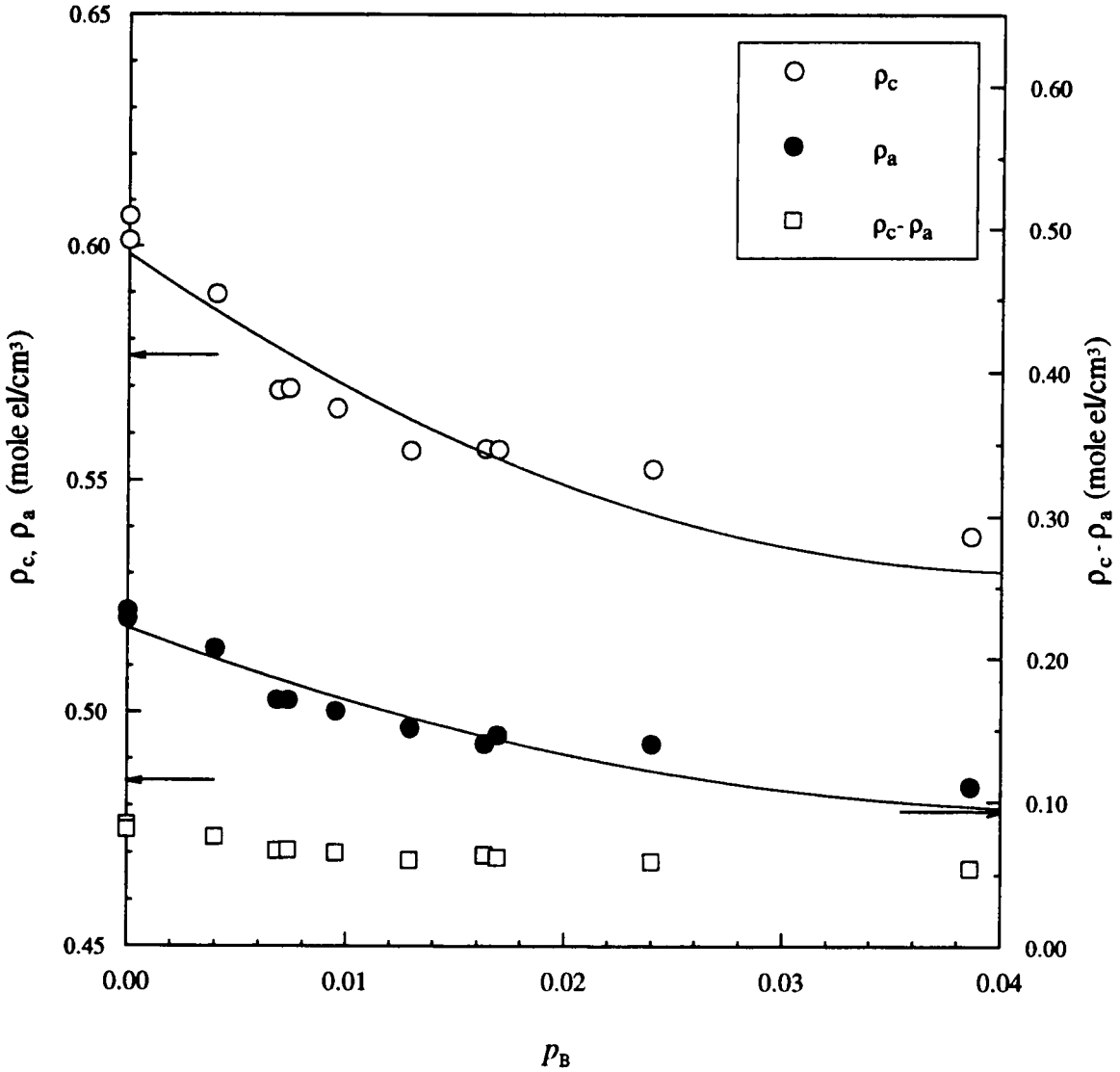


Figure 5.4.4.6. Electron density (mole el/cm ^{3}) of crystalline (ρ_c) and amorphous (ρ_a) phase for quecnhed LPE and EO copolymers as a function of defect content, assuming a two-phase model. Indicated arrows represent the corresponding theoreical values.

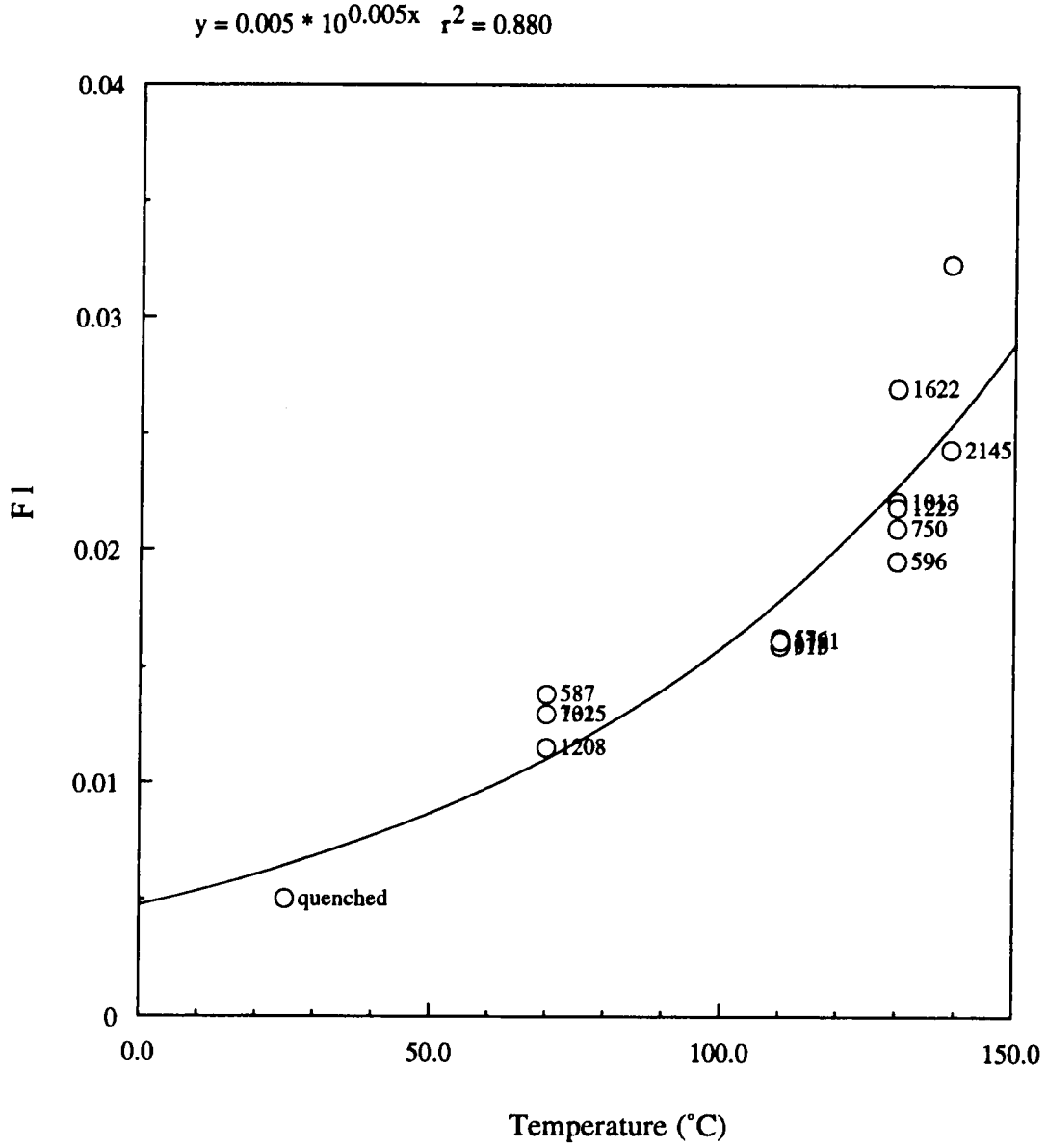


Figure 5.4.4.7. Electron density fluctuation component (Fl_e) as a function of temperature for H-LPE crystallized at various temperature.

can roughly demonstrate the temperature effect because Fl_e was measured in-situ. The increase of Fl_e of H-LPE with temperature may be due to the increasing amorphous part and thermal vibration of lattice.

5.4.5. Interfacial Layer (Diffuse Phase Boundary or Transition Layer) Thickness

It is of interest to study the possibility of the existence of the third phase in a semi-crystalline polymer system consisting of crystalline and amorphous phases. For this purpose, the SAXS intensity pattern was studied systematically. Detailed theoretical background was described in **Section 4.4.3**. In this section, the effects of background, defects, crystallization temperature, time and temperature of SAXS measurement on the interfacial layer thickness will be discussed.

5.4.5.1. The Effect of Background Correction

Figure 4.4.4.1 and **Figure 4.4.4.2** showed the change of negative slope with background correction. The numerical values of **Table 5.4.5.1** demonstrate the underestimation of the interfacial layer thickness when the background effect is not corrected. Although the Vonk and Ruland empirical equations cause a little different background intensity as shown in **Figure 5.4.3.2**, the correction by both methods does not affect the numerical values when values rounded off. Most EO copolymers, however, showed an underestimation less than 1.0 Å when the background was not corrected. The maximum underestimation observed in EO copolymer system was 1.5 Å. For example, L10-O ($T_c = 110\,^{\circ}C$, $t_c = 11$ days) showed $\Delta = 3.9$ Å and $\Delta = 5.4$ Å in the case

Table 5.4.5.1. Interfacial layer thickness and background effect due to the electron density fluctuation component for the quenched LPE, EO, EB, and EP copolymers.

Sample	$I(0)\times10^3$		Fl_e $\times10^2$	Δ (Å)[a] w/o correction	Δ (Å)[a] by Vonk or Ruland	Deviation (%) [b]	T (Å)[a] w/o correction	T (Å)[a] by Vonk or Ruland	Deviation (%) [b]
H-LPE	No Positive Deviation		0.504	7.9 ± 2.1	-	-	16.6 ± 1.8	-	-
M-LPE	No Positive Deviation		0.867	9.0 ± 2.4	-	-	18.2 ± 2.0	-	-
L4-O	No Positive Deviation		0.911	15.3 ± 0.7	-	-	28.3 ± 0.9	-	-
H7-O	5.47	5.67	1.02	14.3 ± 0.9	14.6± 0.6	2.1	23.7 ± 0.4	23.9 ± 0.5	0.8
H7'-O	-	-	0.632	14.3 ± 0.7	-	-	22.7 ± 1.4	-	-
H10-O	8.03	8.19	1.09	13.6 ± 1.0	14.5 ± 1.2	6.2	22.2 ± 0.7	22.4 ± 1.0	0.9
L13-O	12.0	12.3	1.25	12.2 ± 0.9	12.6 ± 0.9	3.2	21.3 ± 0.9	21.6 ± 0.8	1.4
H16-O	12.1	12.3	1.32	11.8 ± 1.1	12.3 ± 1.1	4.1	20.6 ± 0.9	21.0 ± 0.9	1.9
H17-O	10.6	11.0	1.31	11.6 ± 1.2	12.0 ± 1.2	3.3	20.5 ± 1.0	20.9 ± 1.0	1.9
L18-O	-	-	-	9.9	-	-	17.4	-	-
L23-O	11.9	12.2	1.40	10.8 ± 1.0	11.2 ± 0.9	3.6	19.5 ± 0.9	19.9 ± 0.8	2.0
L39-O	15.6	16.0	1.97	None	3.3 ± 3.3	-	None	7.6 ± 7.6	-
L40-P	9.46	9.63	1.05	14.5 ± 0.8	15.0 ± 0.8	3.3	26.5 ± 1.1	27.0 ± 1.4	1.9
L93-P	8.87	9.30	1.16	16.7 ± 0.6	16.7 ± 0.6	1.8	28.4 ± 0.4	29.1 ± 0.9	2.4
L31-B	9.91	9.93	1.02	11.5 ± 0.7	11.9 ± 0.7	3.4	20.2 ± 0.9	20.5 ± 0.9	1.5

a) Maximum error limit estimated for room and in-situ temperature is 10.0% and 15.0%, respectively except for L39-O and M-LPE.
b) Deviation(%) = (corrected - w / o corrected) × 100/corrected.
In the case of in-situ temperature, maximum deviation(%) was 28.0%. Therefore, background correction is recommended to obtain the accurate interfacial layer thickness.

without and with I_{bg} correction, which causes 28% underestimation. Despite its large percentage of underestimation, the difference of the absolute values is quite small and does not affect the physical interpretation of the interfacial layer thickness. With increasing interfacial layer thickness the degree of underestimation is reduced simply for numerical reasons. For example, an interfacial layer thickness higher than 10 Å tends to have less than 6% underestimation. Although the existence of transition layer, $\Delta = 3.3$ Å and $T = 7.6$ Å for L39-O is detected after background correction, the chosen slope is not clear compared to other samples (see **Figure 4.4.4.3** and **Figure 4.4.4.4**). Therefore there is a reliability problem and the value of $\Delta = 3.3$ Å is small enough to reflect a sharp phase boundary between crystal and amorphous phase. When the semi-sigmoidal model is applied to estimate transition layer thickness (T), the background correction effect is much reduced due to the relatively large value of T compared to Δ.

5.4.5.2. As a Function of Defects for Quenched Samples

The transition layer thickness of the quenched LPE and EO copolymers was determined as a function of defects at room temperature. **Figure 5.4.5.1** and **5.4.5.2** show the interfacial layer thicknesses Δ, T and E estimated with sigmoidal-gradient, semi-sigmoidal gradient and linear gradient models, respectively. These Δ, T and E values decrease with increasing defect content. However the interfacial layer thickness of LPE is lower than those of EO copolymers up to $p_B(\%) = 24$. Even if the background due to electron density fluctuation is corrected, the tendency does not change. The decrease of interfacial layer thickness is accelerated at high defect contents. Passing $p_B(\%) = 24$, the phase boundary of the highly branched EO copolymer, L39-O, becomes thinner than even that of LPE. This must mean that the boundary phase between crystalline and amorphous

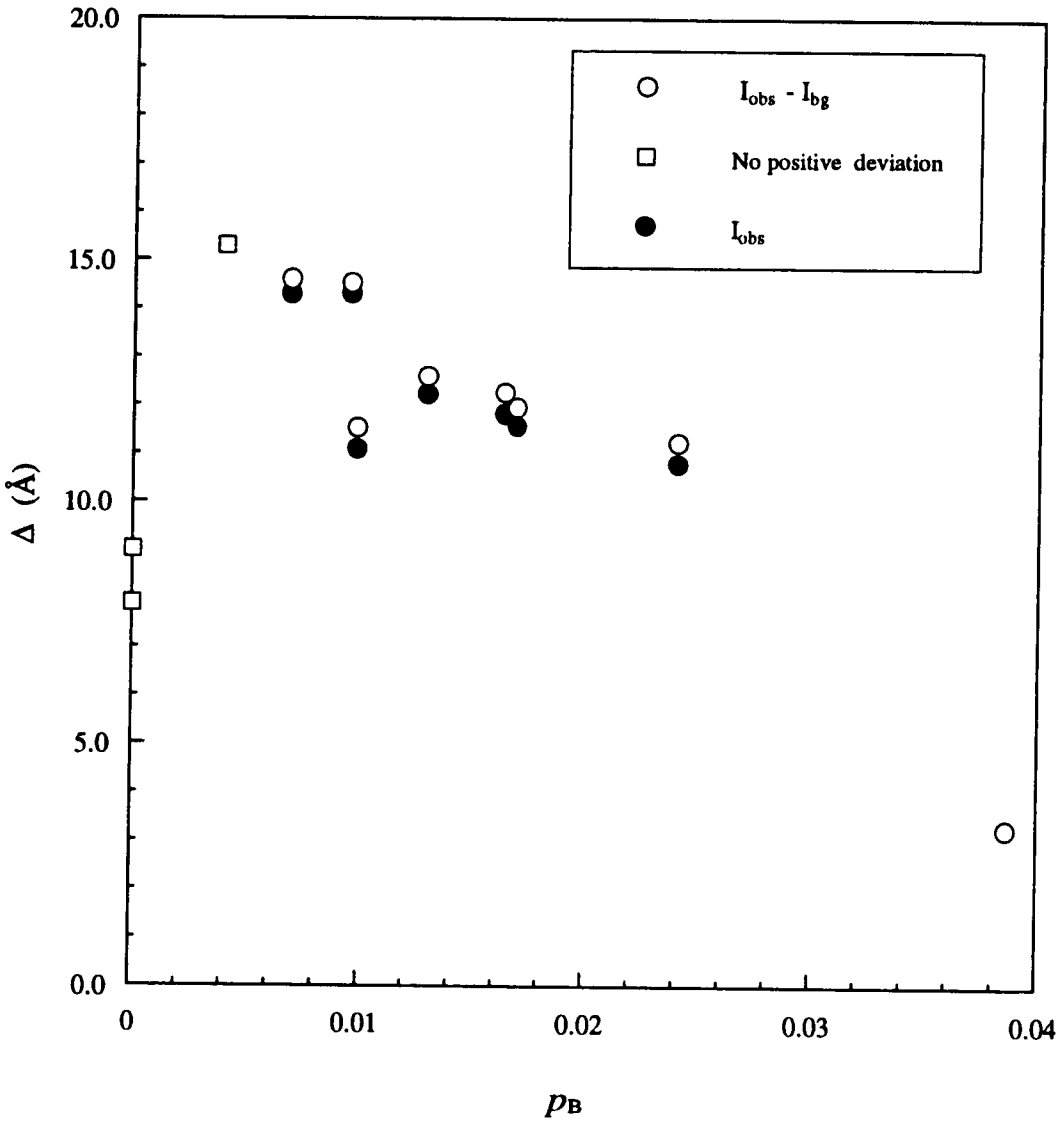


Figure 5.4.5.1. The effect of background intensity (I_{Bg}) correction on the interfacial layer thickness $\Delta(\mathring{A})$ assuming sigmoidal-gradient model.

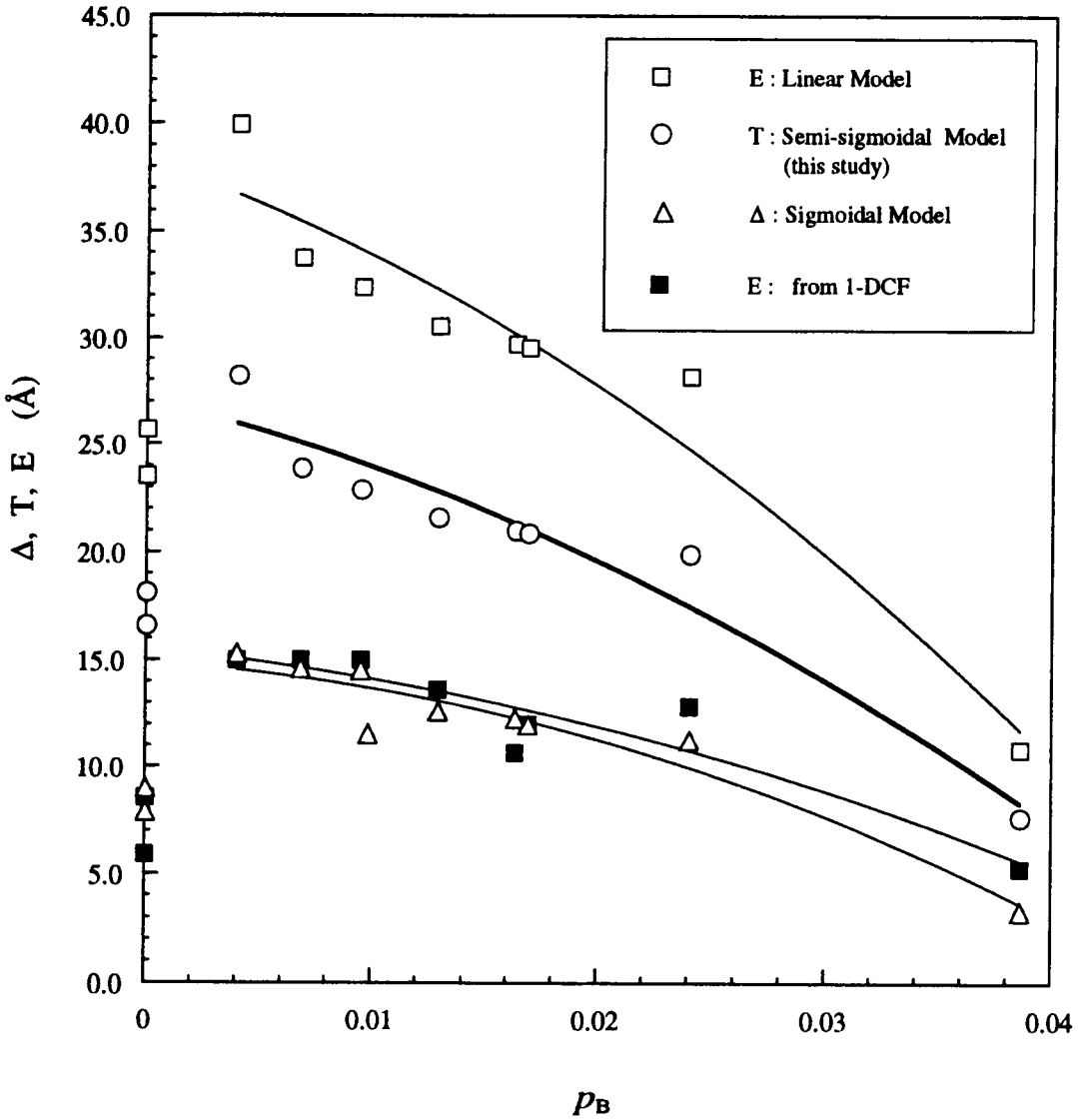


Figure 5.4.5.2. Interfacial layer thicknesses, Δ, T, E (Å) obtained by using various models, sigmoidal-, semi-sigmoidal- and linear gradient models, as a function of defect content for LPE and EO copolymers quenched in ambient temperature.

phase disappears as defects increase in the system, contrary to expectation. Moreover, the result of this study is an opposite trend compared to literature data for TREF fractions of a heterogeneous EO copolymer[110] For comparison the literature results of Defoor *et.al.*, the interfacial layer thicknesses, $E(\mathring{A})$ for quenched samples were obtained assuming the linear-gradient model of **Figure 4.4.4.3**. **Figure 5.4.5.3** shows the opposite behavior clearly between interfacial layer thickness of this study and Defoor *et.al.* Also the $E(\mathring{A})$ of this study is higher than that of their study. Why does this occur? They explained the effect in terms of crowding of defects rejected from crystalline phase causing the increase of the interfacial layer thickness due to packing, borrowing Alamo *et. al.*'s results that the relative interfacial content determined analyzing Raman internal modes increases rapidly with increasing defect content.[111]

The earlier results(see **Table 5.3.5.1**) of this study suggest that more defects are rejected from crystalline phase as well as increasing inclusion of defects with increasing the defect content of copolymers. Both this study and literature results (Alamo *et. al.*,[111]) support the accumulation of defects outside the crystalline phase. But there is a contradiction of interfacial layer thickness behavior between this study and literature in spite of the fact that the defects are expelled from the crystalline phase. The slope change in **Figure 4.4.4.3** and **Figure 4.4.4.4** is too distinct to be considered due to experimental error. An fundamental reason may come from the fact that both EO copolymers have a different defect distribution in a copolymer system. The EO copolymers of this study are homogeneous copolymers consisting of homogeneous B-counit distribution while those of Defoor *et. al.*, are the TREF fractions of heterogeneous copolymers still consisting of heterogeneous B-counit distribution (see **Figure 5.1.2.2**). Although Defoor *et.al.*, used the TREF technique to obtain more homogeneous chain microstructure based on their description, it is impossible to obtain a uniform intra-distribution of B-counit from a

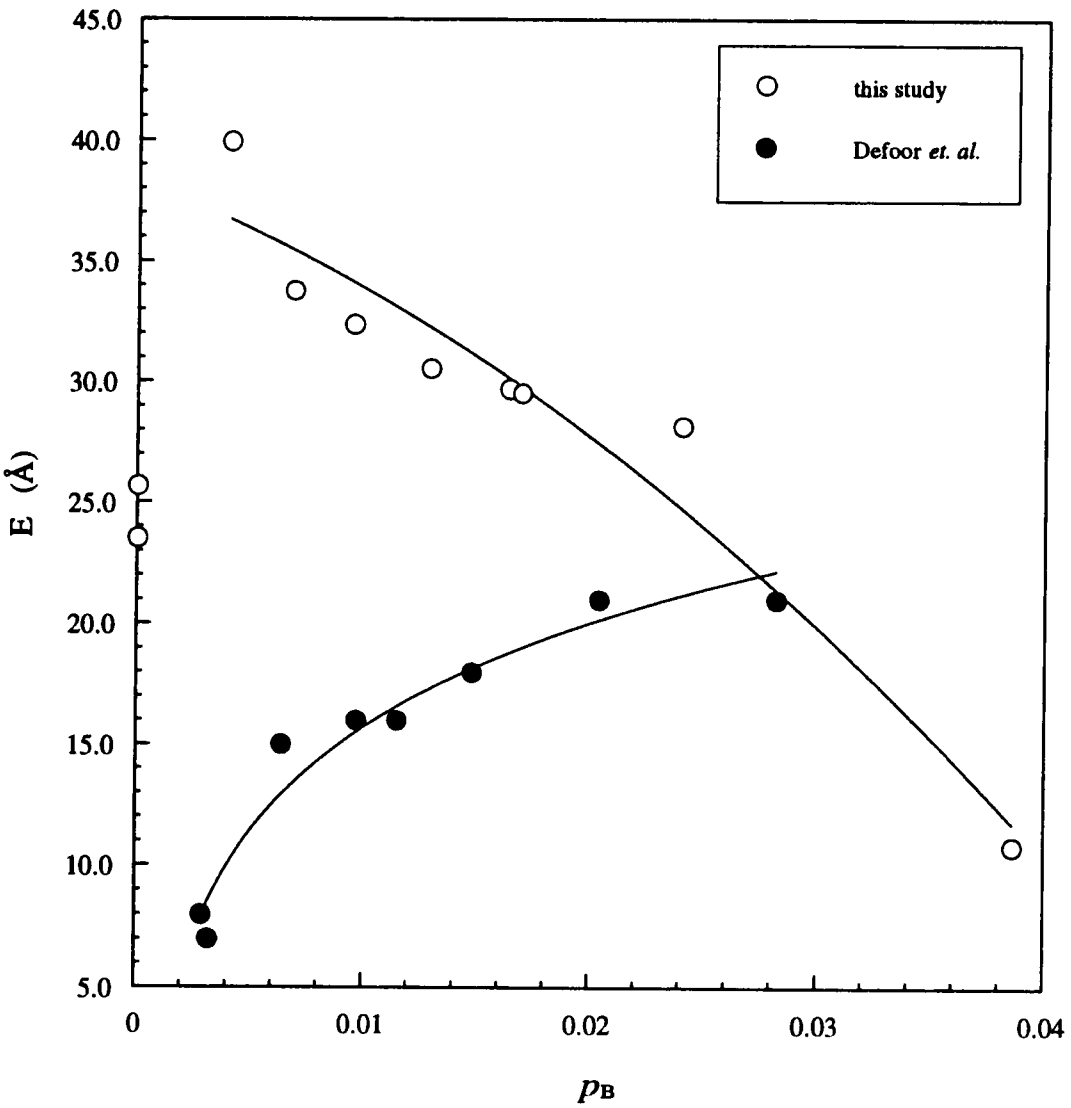


Figure 5.4.5.3. Interfacial layer thickness for homogenous (open circle) and heterogeneous (closed circle) EO copolymers assuming linear gradinet of electron density.

chain consisting heterogeneous intra- distribution although the heterogeneity of inter-distribution of defects can be reduced. The defect distribution may be the main reason for the oppositing transition layer thickness trend. We need to understand two experimental results shown in **Figure 5.4.5.3**, using defect distribution in the system if defect distribution is a main reason. First is to understand the result that the $E(\mathring{A})$ of homogeneous EO copolymers is higher than that of heterogeneous EO copolymers. And second is to understand the behavior that the $E(\mathring{A})$ of homogeneous EO copolymers decreases with defect content while that of heterogeneous EO copolymers increases with defect content. This behavior may be due to the statistical contribution of defects in the transition layer thickness. It is not suitable to generalize the explanation that crowding of defects at interfacial layer causes to increase transition length. Let us think about the case of homogeneous EO copolymers. The estimation of interfacial layer thickness using SAXS was developed assuming an electron density gradient from crystalline to amorphous phase. To satisfy this condition, the electron density of the transition layer must be higher than that of amorphous and lower than that of the crystalline phase. As defects increase in an imaginary transition layer, the entropy in this region increases but remains lower than that of amorphous phase. In this case the interfacial layer thickness increases. Further increasing of defects (hexyl branches, branches end or/and branch points) will give rise to an increase in the entropy as much as in the amorphous phase, making the electron density of the transition and amorphous phase ultimately identical. Therefore the system will have sharp phase boundary. Another morphological parameter governing interfacial layer is the lamellar thickness fluctuation at the crystal surface. As more defects are distributed outside the crystalline phase, the crystal thickening is restricted due to defects and may not occur at all. Therefore the homogeneous EO copolymers will have a uniform lamellar thickness as defects increase, accumulating defects outside the crystalline phase. For this reason, the interfacial layer thickness will

decrease with defect content. On the other hand, the heterogeneous EO copolymers have a localized distribution of defects having long crystallizable A-sequences. In this case, thickening occurs in the long A-sequence length but not in short A-sequence. At low branch content, most A-sequences are long enough to be considered similar to the chain length of linear polyethylene (LPE) and will be crystallized in the same manner as LPE. At high branch content, short A-sequences will be increased. The increased short A-sequence chain will cause the lamellar fluctuation with long A-sequence chains. If this explanation is reasonable, the interfacial layer thickness should as low as in LPE. As localized defect content increases, the interfacial layer thickness increases due to the severe lamellar fluctuation.

An unsolved problem is why the interfacial layer thickness of homogeneous EO copolymers is higher than that of heterogeneous ones at low contents. This beavior requires more study.

5.4.5.3. As a Function of Crystallization Time

Figure 5.4.5.4 and **5.4.5.5** illustrate the effects of crystallization time on the interfacial layer thickness, Δ and T, of EO copolymers, using SAXS profiles measured at room temperature. As crystallization time increases, the interfacial layer thickness decreases. However, the interfacial layer thickness of the low branched sample (e.g., H6-O) increases with crystallization time (t_c) in the case measured in-situ, while it decreases during room temperature measurement (**Figure 5.4.5.6** and **Figure 5.4.5.7**). This contrasting behavior may be due to the role of small crystal and lamellar thickening fluctuations. The rate of thickening must be different for chains with and without defects.

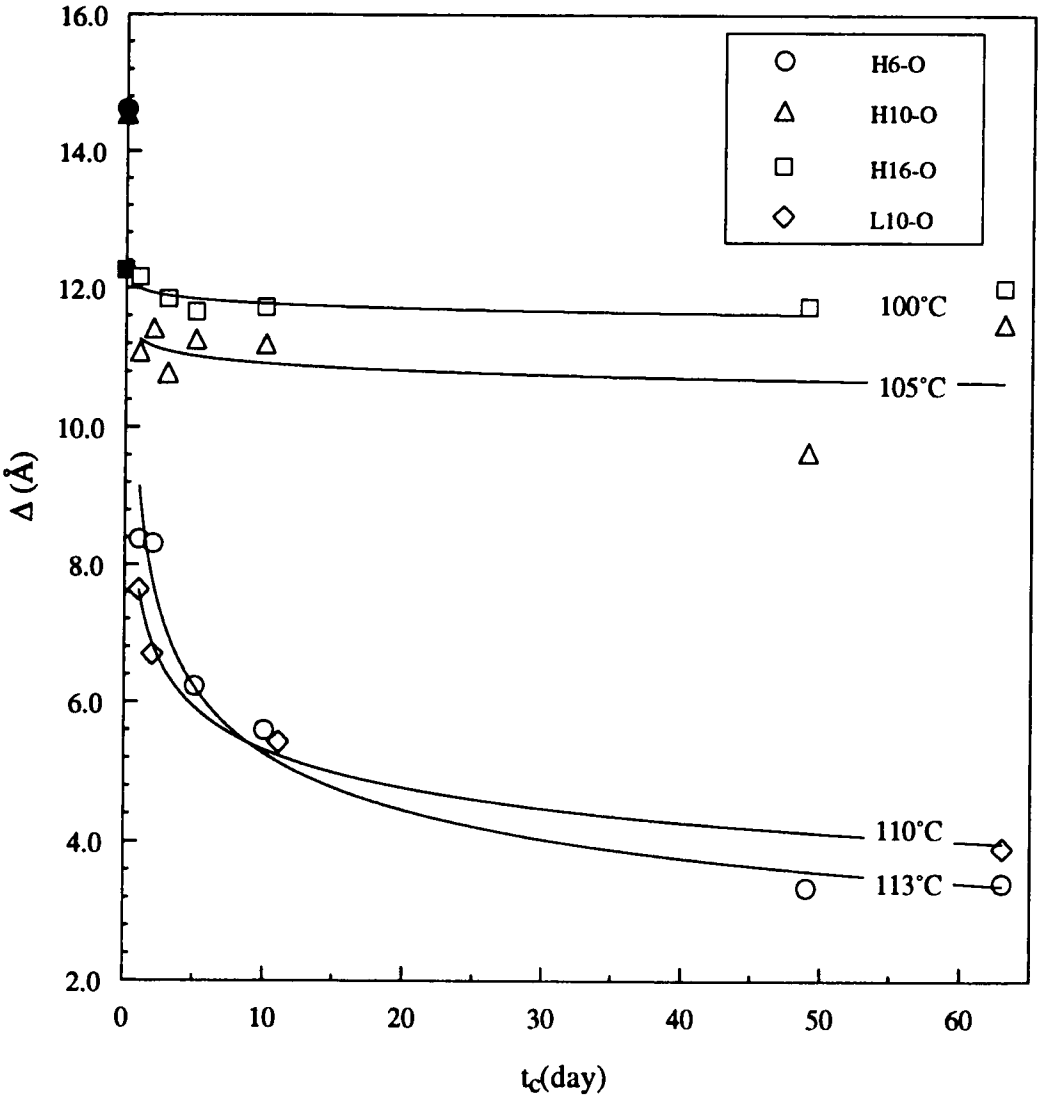


Figure 5.4.5.4. Interfacial layer thickness (Δ) determined at ambient temperature as a function of crystallization time for EO copolymers crystallized at indicated T_c. (closed symbol is the corresponding Δ quenched in ambient air).

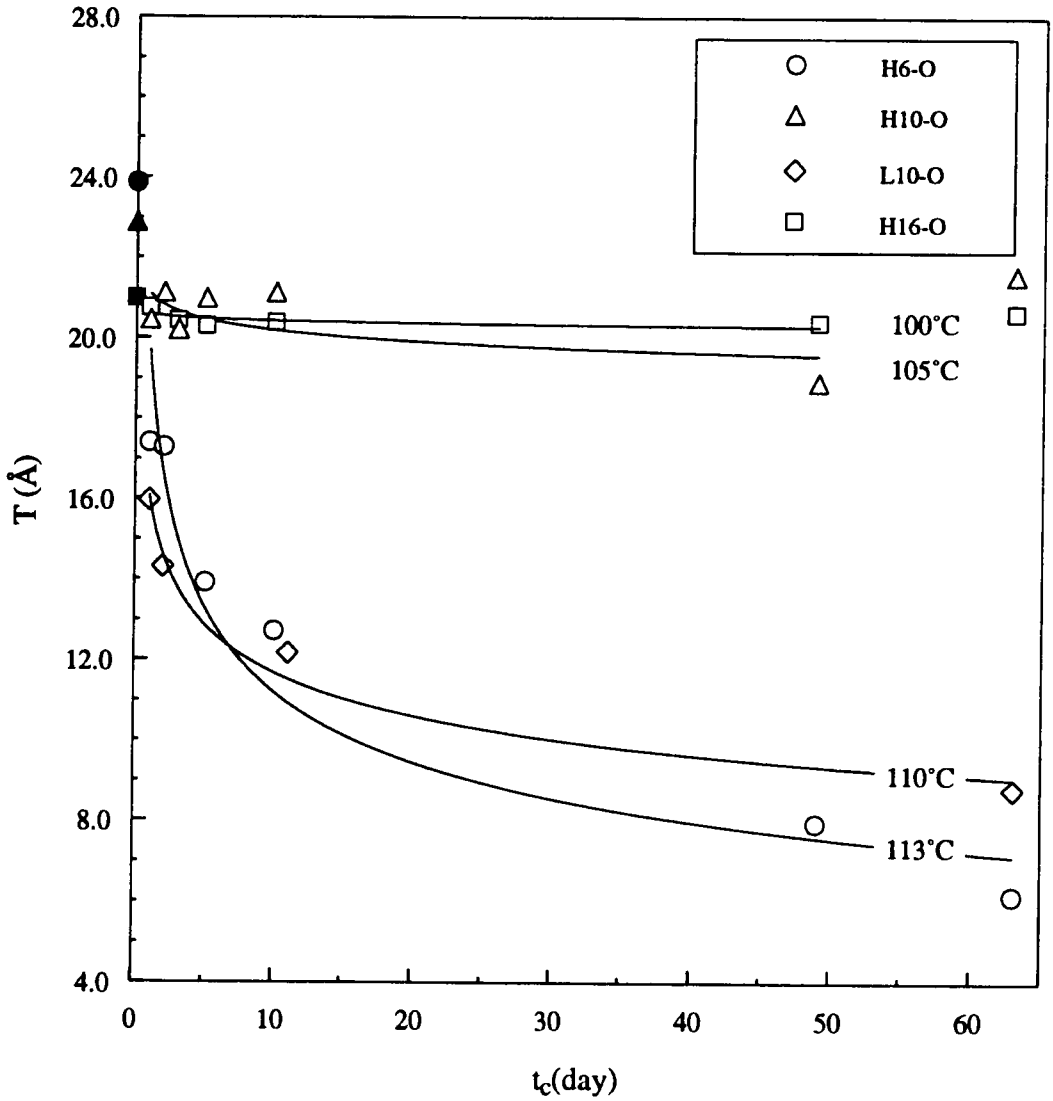


Figure 5.4.5.5. Interfacial layer thickness (T) determined at ambient temperature as a function of crystallization time for EO copolymers crystallized at indicated T_c.(closed symbol is the corresponding T quenched in ambient air).

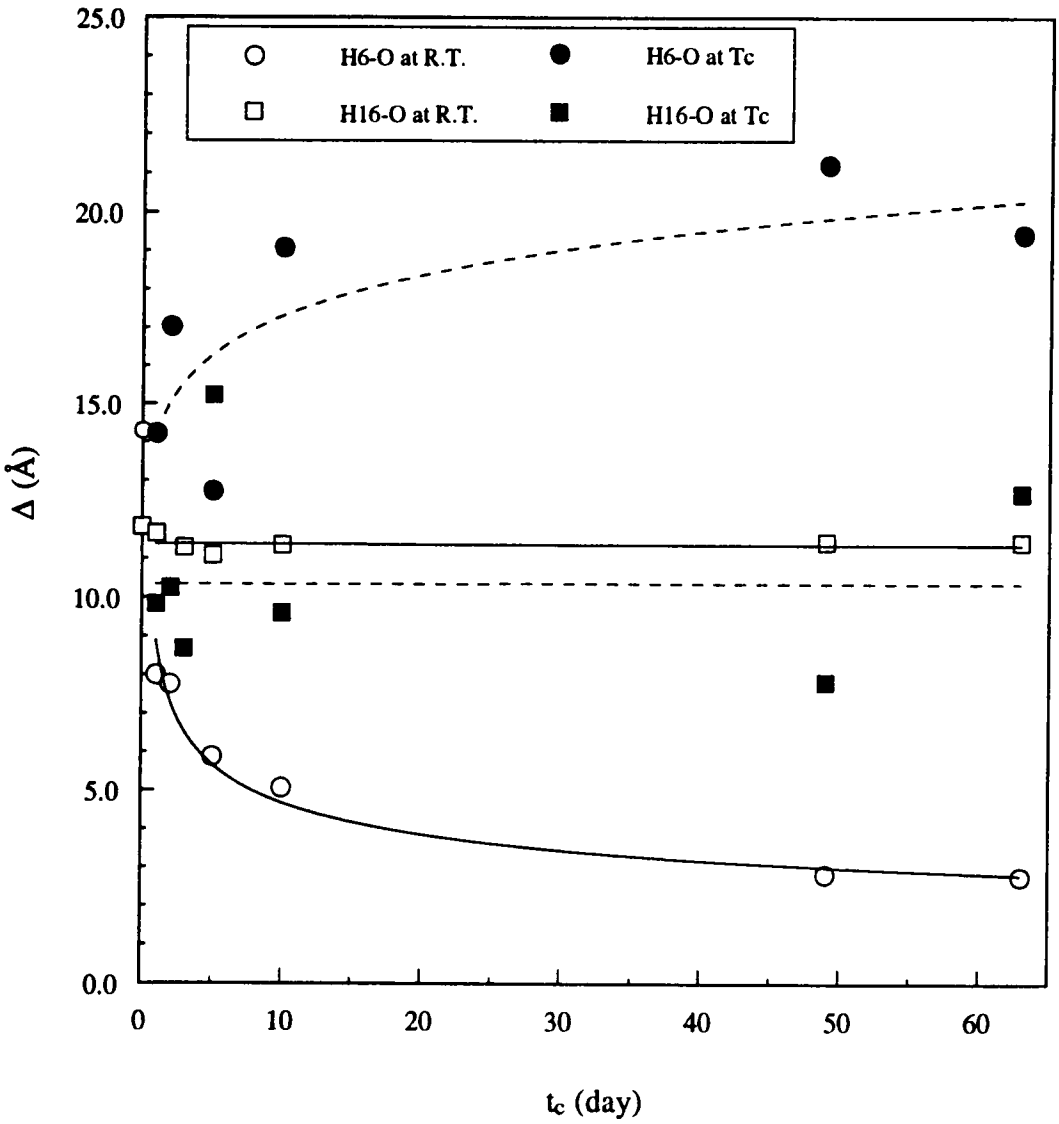


Figure 5.4.5.6. Interfacial layer thickness (Δ) as a function of crystallization time.H7-O and H16-O were crystallized at 113 °C and 100 °C, respectively. Open and closed symbols indicate the room and the in-situ measurement of SAXS intensity.

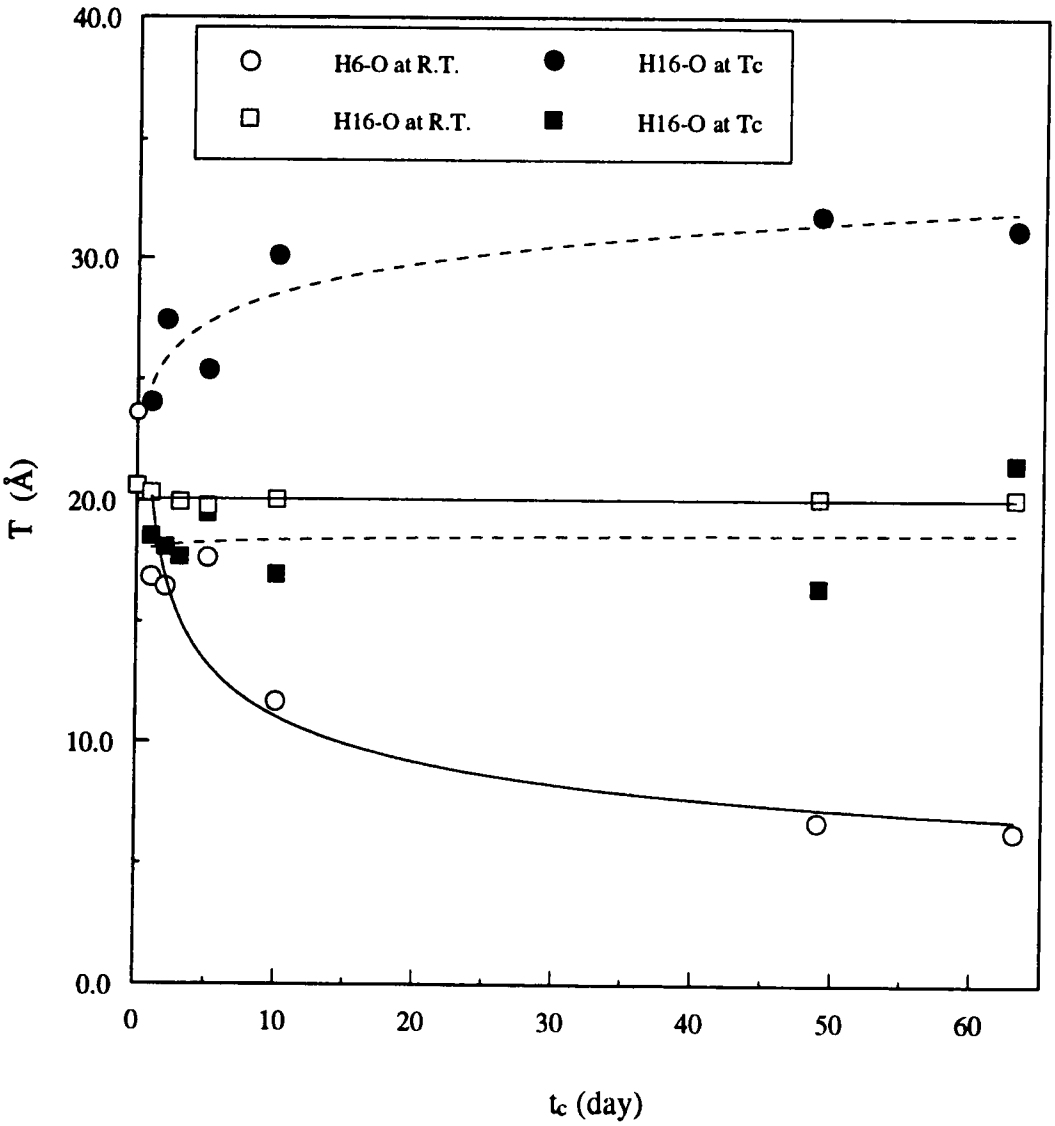


Figure 5.4.5.7. Interfacial layer thickness (T) as a function of crystallization time.H7-O and H16-O were crystallized at 113 °C and 100 °C, respectively. Open and closed symbols indicate the room and the in-situ measurement of SAXS intensity.

Certainly, the rate of thickening for a section of defect-free chains must be faster than that of chains with defects. This means that as crystallization time increases, the fluctuation of lamellar thickness increases producing deep niches and causing the interfacial layer to become thick when it measured in-situ. On the other hand, the samples in room temperature experiments have been cooled down after isothermal crystallization. During the cooling process, chains consisting of small A-sequence length will be crystallized in energetically favorite places such as niche. This filling process makes the deep niches, which are produced by long crystallization time, shallow, thus making the interfacial layer thin. However, when this filling process occurs in shallow niches, which produced by less thickening for short crystallization time, small chains will be extruded over niches, making the interfacial layer thick. This explanation is consistent with the experimental result that Δ and T of quenched samples are higher than those of isothermally crystallized samples.

On the other hand, the phase boundary of the highly branched sample, H16-O, shows a slightly lower interfacial layer thickness in-situ than at ambient temperature, but is less dependent on the crystallization time and in-situ temperature. The behavior can be understood as highly branched samples will thicken less with crystallization time due to the surrounded defects.

5.4.5.4. As a Function of Crystallization Temperature

Interfacial layer thickness depends on the crystallization temperature and measuring temperature of SAXS intensity as well as crystallization time. Assuming sigmoidal-gradient and semi-sigmoidal gradient model, the interfacial layer thickness, Δ and T, estimated without correcting electron density fluctuation is given in **Figure 5.4.5.8**

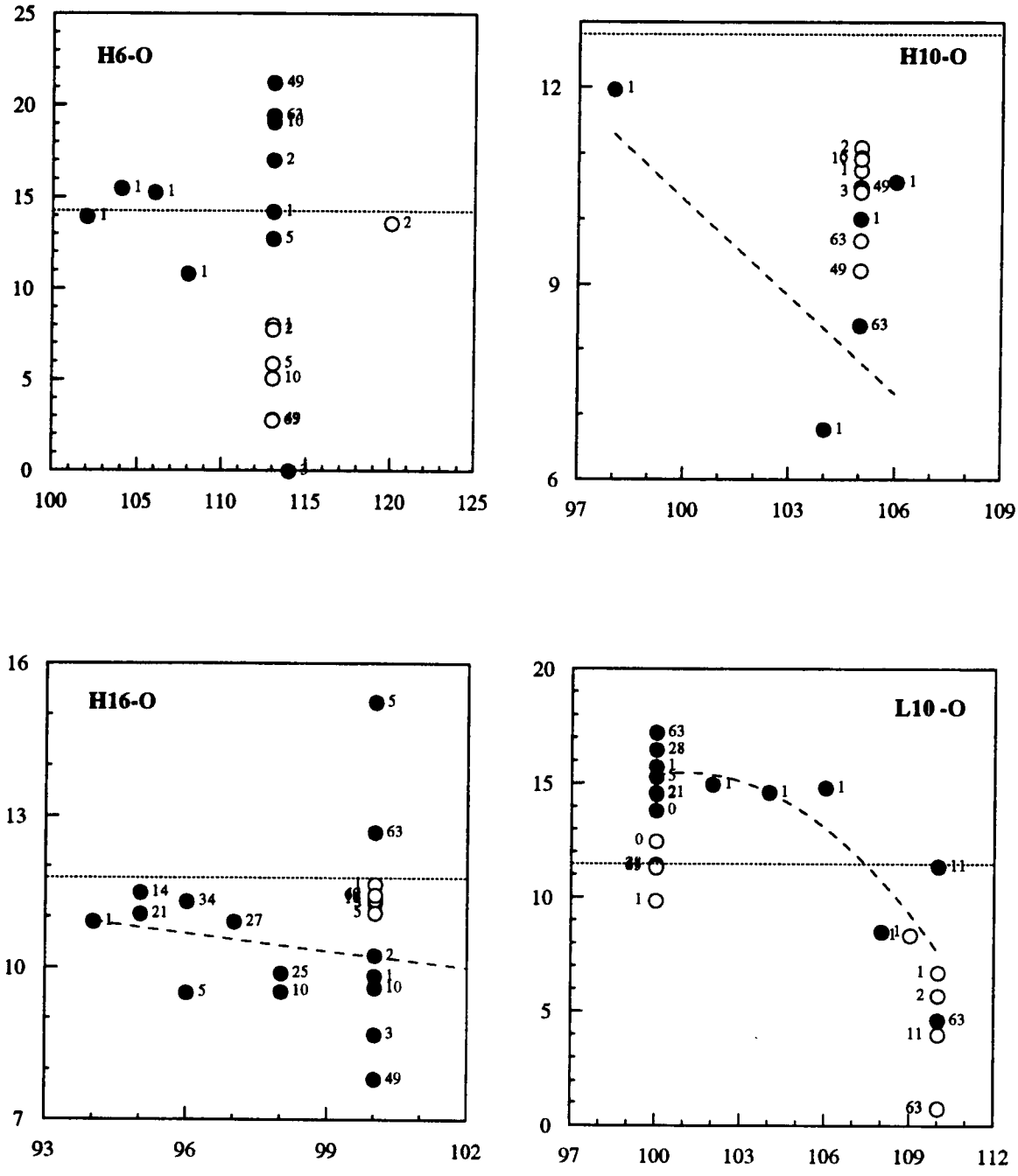


Figure 5.4.5.8. Interfacial layer thickness (Δ(Å) estimated from sigmoidal model) as a function of crystallization temperature (°C). Open and closed symbols represent the measurement at room and crystallization temperature, respectively. Dotted horizontal line is the Δ for quenched EO copolymers.

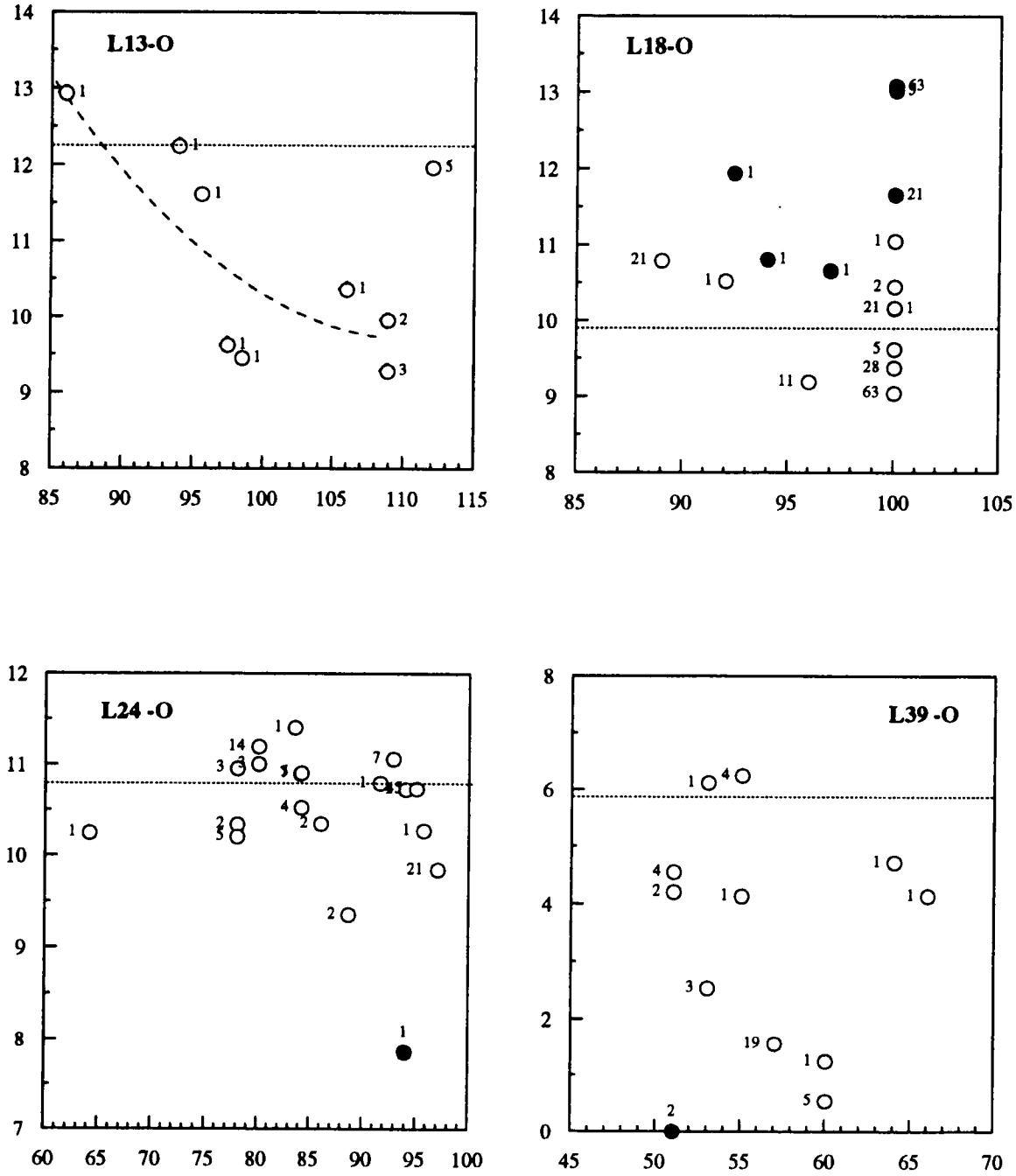


Figure 5.4.5.8. (continued)

and **Figure 5.4.5.9**, respectively. (Comments; Background correction does not affect the tendency although their contribution to Δ and T was observed small and large for room and in-situ temperature, respectively). These figures show many interesting manners of interfacial layer thickness as a function of crystallization temperature, measuring temperature and crystallization time: (i) the interfacial layer thicknesses (closed circle) of H6-O, L10-O and L18-O obtained at crystallization temperature are higher than those (open circle) from room temperature while H10-O and H16-O show the opposite tendency. (ii) The interfacial layer thicknesses (dotted line) of quenched EO copolymers are higher than those for isothermally crystallized samples at ambient temperature measurement except for Δ of L18-O. Although Δ of L18-O shows higher values, the T values shows the same tendency as other samples. (iii) On increasing the crystallization and measuring temperature, interfacial layer thickness decreases. Highly branched L24-O and L39-O show no negative slope even if background is corrected., which makes it impossible to determine Δ or T. (iv) Interfacial layer thicknesses of H6-O, L10-O and L18-O increase with crystallization time during in situ measurement while those measured at room temperature decrease with crystallization time. (Need explanation)

5.4.6. Morphology of H-LPE ($T_c = 130\ ^{\circ}C$, $t_c = 17$ days) with temperature

It is useful to study temperature effect systematically on the sample with the highest crystallinity (w_c = 94%) and highest melting temperature ($T_m = 138.9\ ^{\circ}C$) since such a simple and stable system without defects will give a general base for understanding a complicated system such as a copolymer. One-dimensional correlation function (**Figure 5.4.6.1**) for H-LPE ($T_c = 130\ ^{\circ}C$, $t_c = 17$ days) as well as intensity profiles (**Figure 4.4.1.5**) and Lorentz corrected intensity patterns (**Figure 4.4.1.6**) show constant long

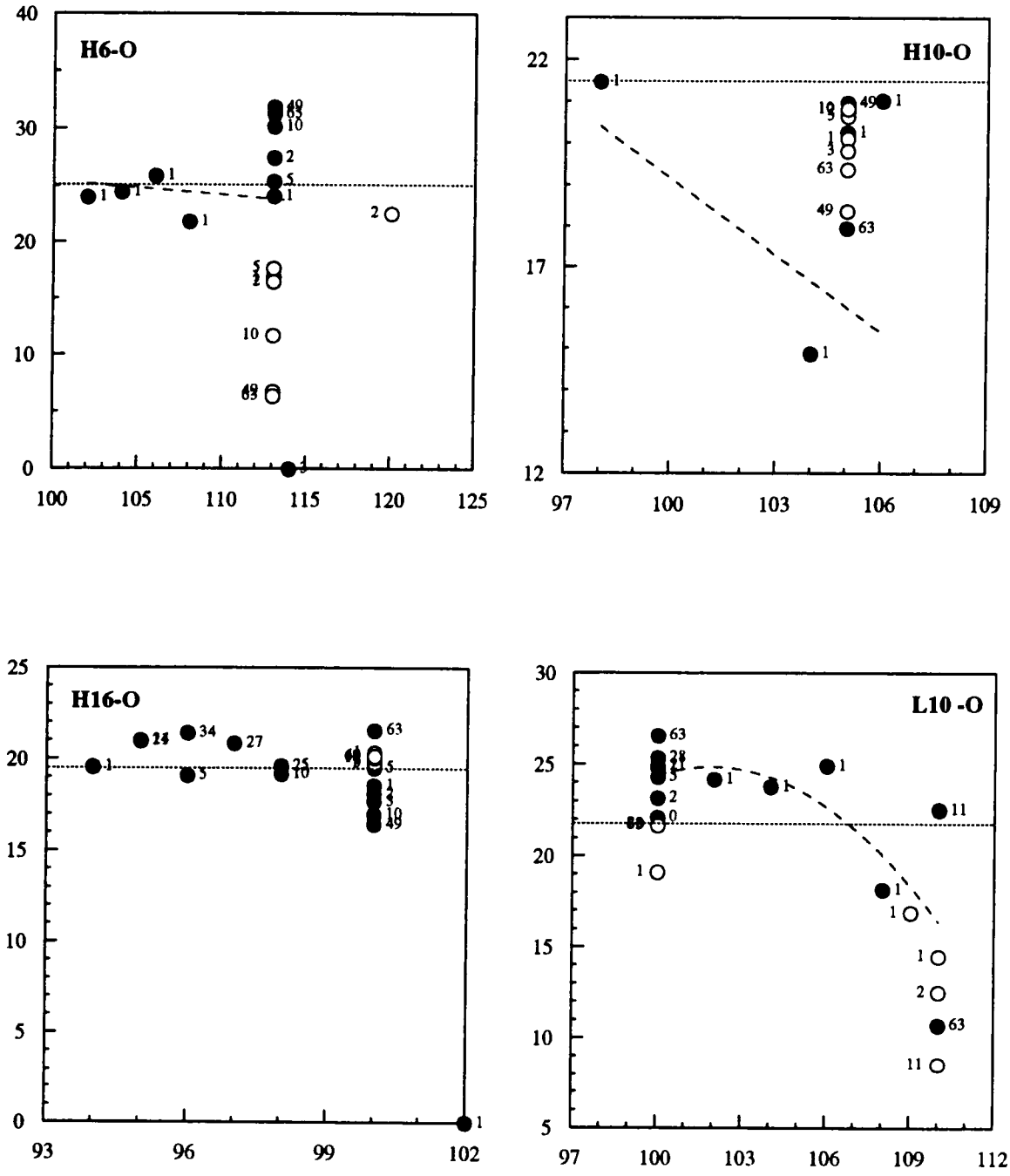


Figure 5.4.5.9. Interfacial layer thickness (T (Å) estimated from the graphical method of this study) as a function of crystallization temperature(°C). Open and closed symbols represent the measurement at room and crystallization temperature, respectively. Dotted horizontal line is the T for quenched EO copolymers.

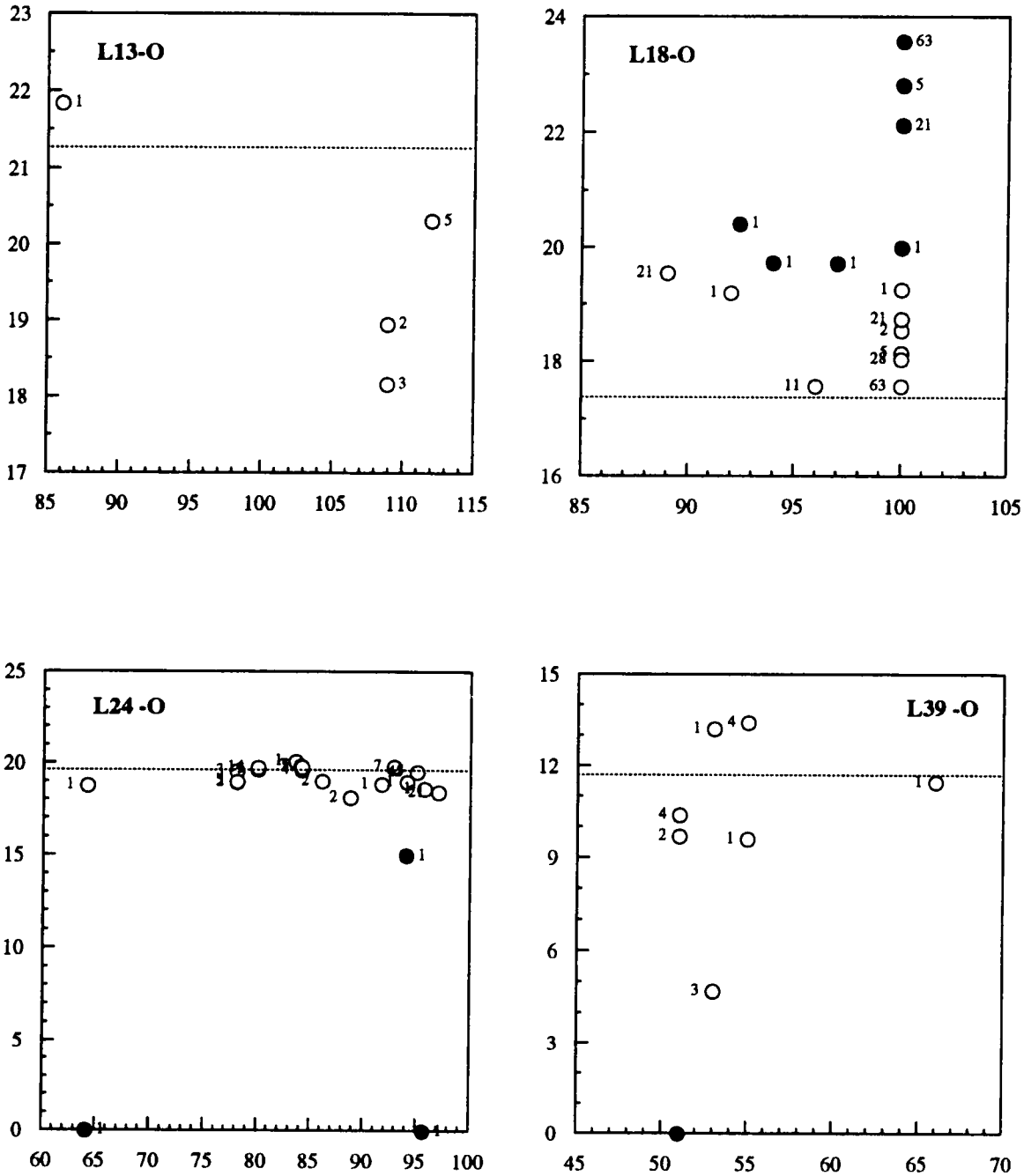


Figure 5.4.5.9. (continued)

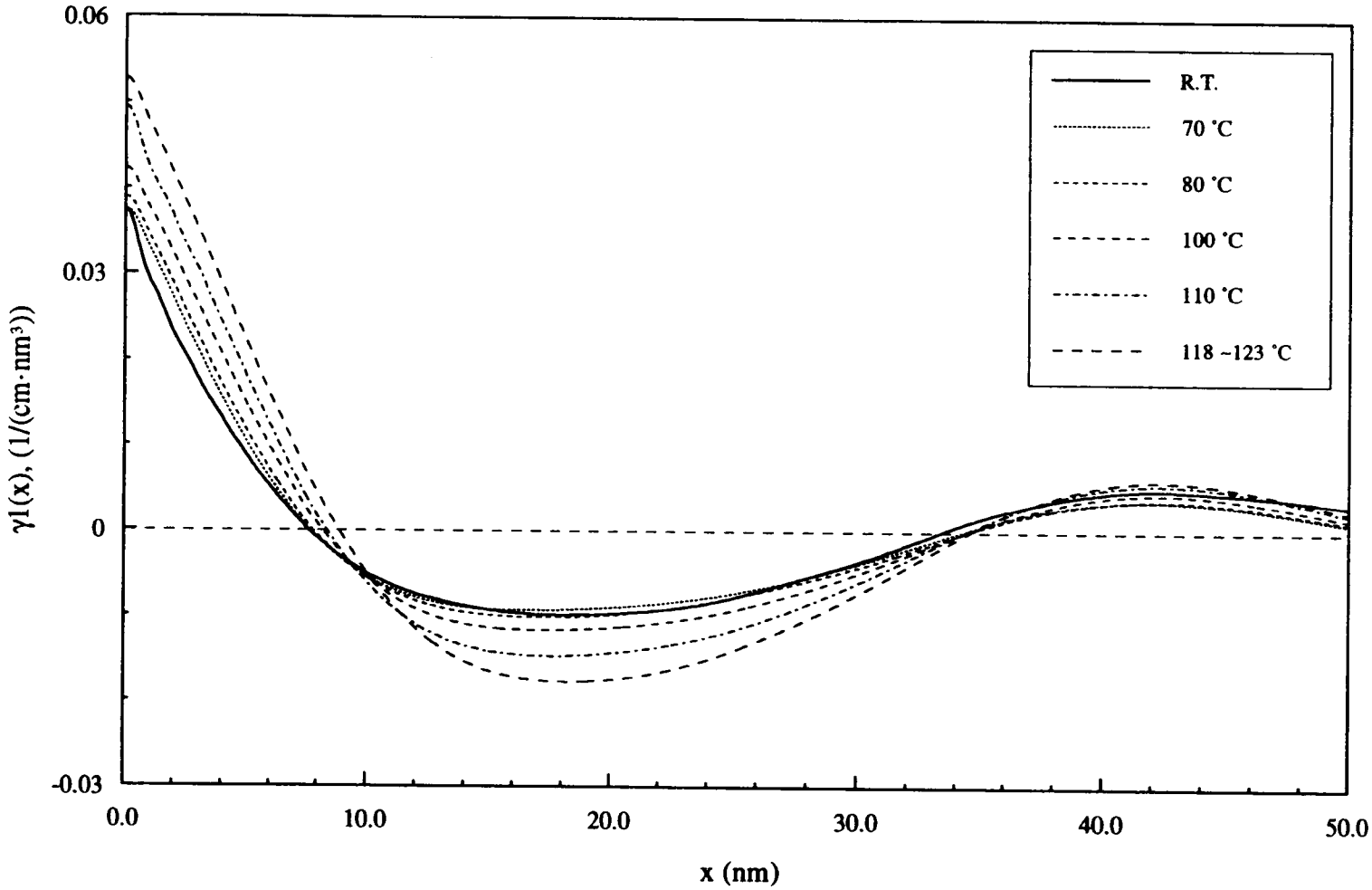


Figure 5.4.6.1. One dimensional correlation function behavior for H-LPE (Tc = 130 °C, t_c = 17 days) measured at different temperatures.

periodicity with temperature whereas the average lamellar thickness increases with temperature. This may be due to the effect of melting of small crystals in niche and thickening of small crystals formed during the quenching process, which causes increases of the average lamellar and crystalline core thicknesses. Better understanding comes when the phase boundary (interfacial layer) thicknesses (Δ) are measured as a function of temperature as shown in **Figure 5.4.6.2** and **Figure 5.4.6.3**. The increase of the interfacial layer thickness is a solid evidence of melting of small crystals in niches crystallized during quenching process. Melting of small crystal increases the fluctuation of lamellar thickness and simultaneously interfacial layer thickness. Morphological parameters are summrized in **Table 5.4.6.1**.

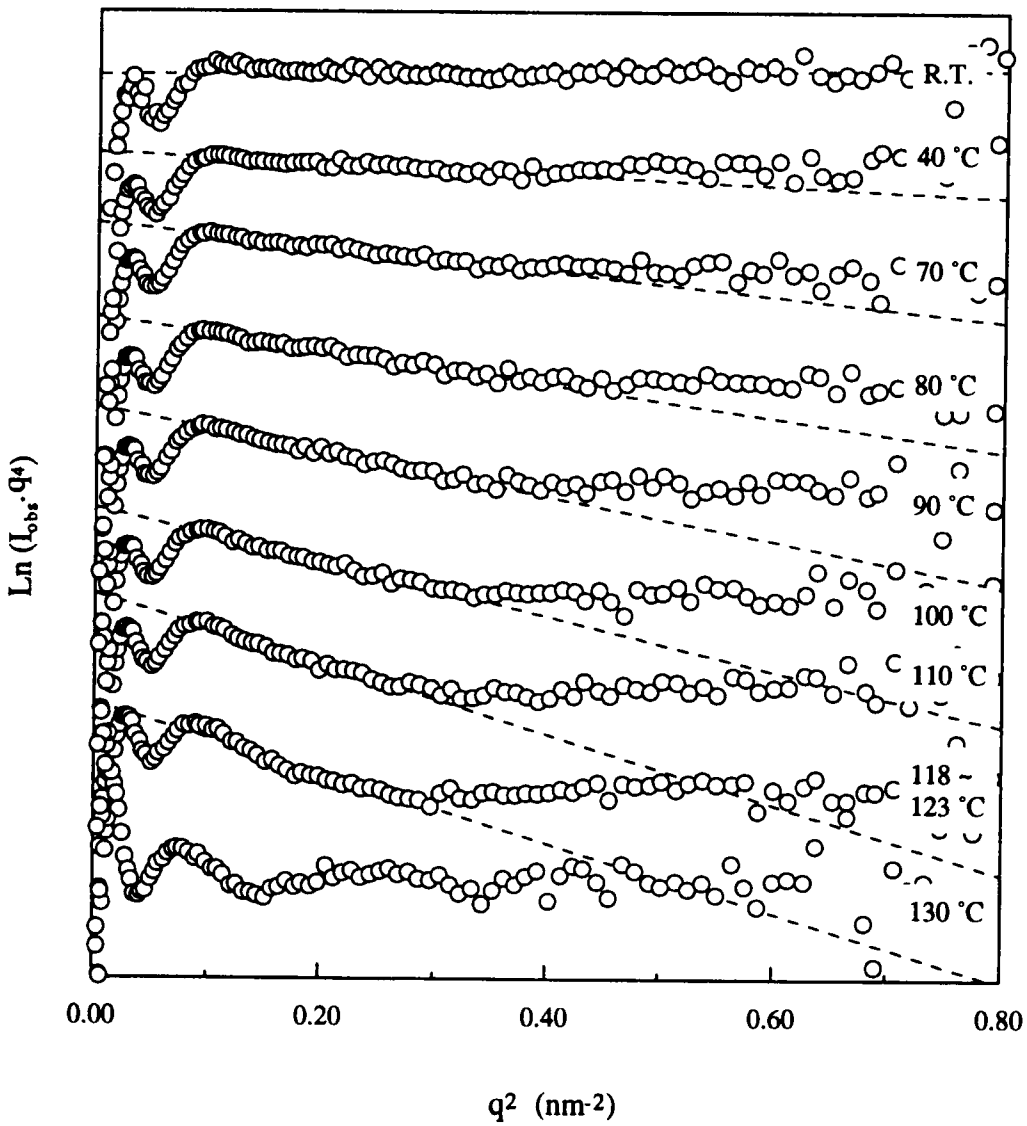


Figure 5.4.6.2. Ruland's plot to obtain Δ of H-LPE crystallized at 130°C for 17days, using SAXS profiles measured at indicated temperature.

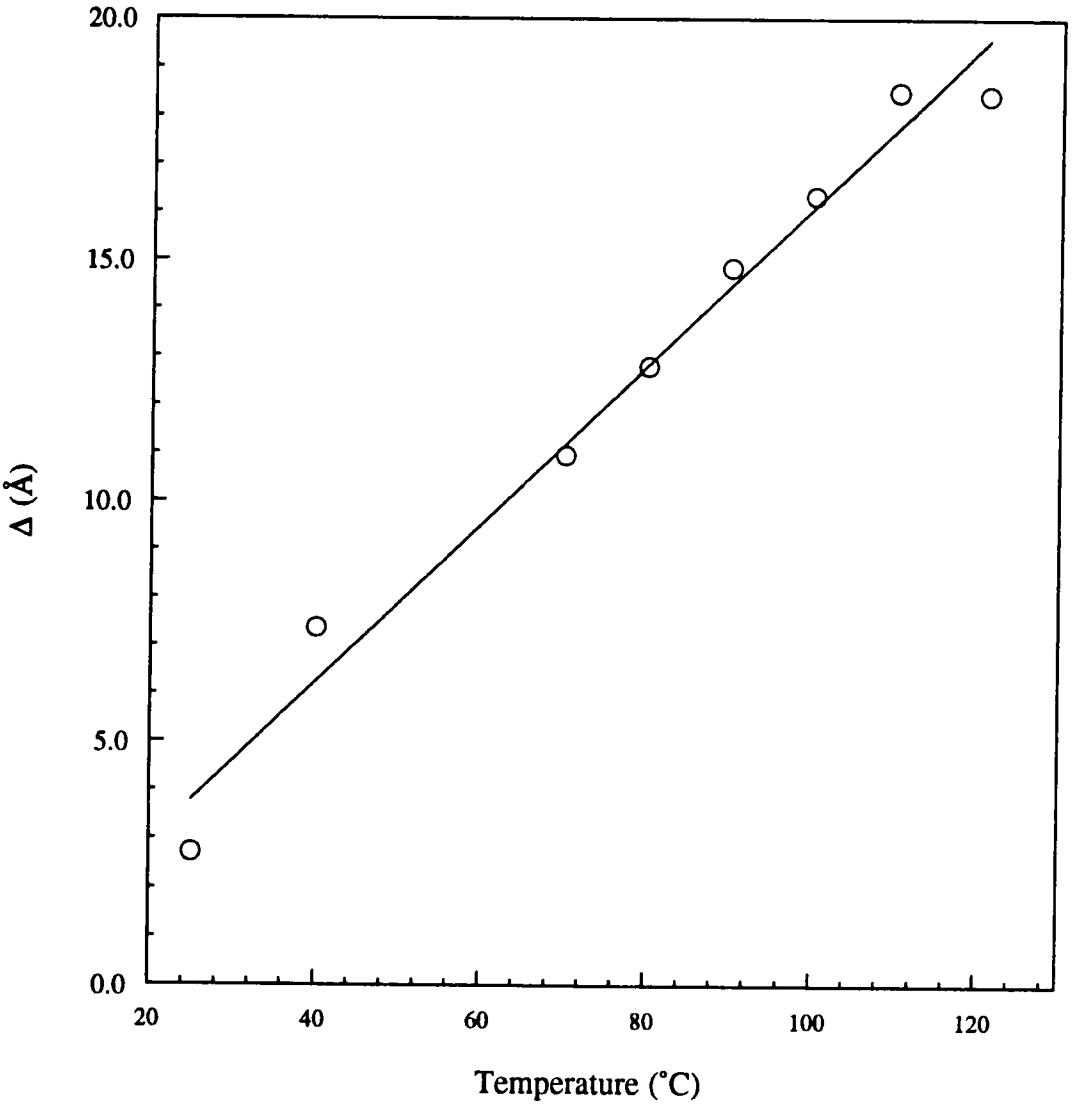


Figure 5.4.6.3. Interfacial layer thickness (Δ) against temperature for H-LPE (T_c=130°C, t_c = 17days).

Table 5.4.6.1. Morphological parameters obtained from SAXS analysis for H-LPE (Tc=130°C, t=17days).

Code	$Q \times 10^3$ (mole el^2/cm^6)	baseline $\times 10^4$ (mole el^2/cm^6)	$\rho_c - \rho_a$ (mole el/cm^3)	Δ (Å)	R_g (Å)	L (Å)	l_c (Å)	l (Å)[a]	Os$\times 10^3$ [b] (Å^{-1})	L'/L [c]
RT	1.30	3.45	0.08851	2.7	94.7	423.0	76.0	-		
40	1.10	2.42	0.08601	7.4	102	411.4	76.0	78.0	4.63	1.0
70	1.30	3.24	0.09012	11.0	101.5	419.7	76.0	85.5	4.67	1.0
80	1.35	3.53	0.09059	12.8	99.5	423.0	76.5	91.0	4.56	1.0
90	1.46	4.01	0.09314	14.8	100.3	423.0	78.5	92.0	4.67	1.0
100	1.47	5.81	0.08495	16.3	98.4	421.4	82.2	96.5	5.88	0.8
110	1.71	5.09	0.08452	18.5	99.9	422.0	84.5	100.5	4.56	1.0
118~123	1.83	6.13	0.09855	18.5	101.8	421.7	89.0	110.5	4.55	1.0

a) from self-correlation triangle analysis b) specific inner surface, c) lamellar planarity, $L' = O_s/2$

6. CONCLUSIONS

6.1. Thermal Analysis

1) As branch content increases in LLDPE, non-isothermal, isothermal, melting temperatures, and heat of fusion (or degree of crystallinity) are decreased. This behavior is explained as due to the decrease of lamellar thickness and formation of poor crystal structure, on the basis of the role of a branch as a defect.

2) Annealing phenomena were observed in all the LLDPE's including even highly branched EO copolymer (L39-O) and EP copolymer (L93-P).

3) There was some unevenness of branch distribution on main chain. The molecular segregation by heterogeneity of branch distribution rather than molecular weight was observed around 40 ~ 50 ℃.

4) There is branch length effect on melting point depression. Long branches cause more melting and crystallization temperature depression than short chain branches. Melting temperature depressions of EO random copolymers with long branches (hexyl) were larger than those of EB and EP random copolymers with ethyl and methyl branches, respectively.

5) Defect distribution in copolymer systems is a more important factor governing T_m of olefin type copolymers than branch content. The homogeneous random copolymers have always higher T_m than that of heterogeneous copolymers.

6.2. Bulk Crystallization Kinetics

1) The rate of crystallization ($1/t_{1/2}$) decreases with molecular weight and branch content.

2) The rate of crystallization ($1/t_i$) obtained with the reciprocal initial time gives similar behavior as ($1/t_{1/2}$) and the same regime transition behavior.

3) The regime I-II transition observed for the homogeneously branched copolymer is lower than that of the heterogeneously branched copolymer due to the short A-sequence length in spite of the same branch content.

4) Avrami exponent depends on the temperature and branch content.

6.3. Equilibrium Melting Temperature

1) The Thompson-Gibbs plot of melting temperature versus reciprocal lamellar thickness gives a reliable estimation of the equilibrium melting temperatures whereas the plot (Hoffman-Weeks plot) of T_m versus T_c can not be applied to obtain the equilibrium melting temperatures of ethylene/1-octene random copolymers.

2) Molecular weight dependence on equilibrium melting temperature of linear polyethylene has been determined and it does not correspond to the Flory-Vrij equation. An empirical **equation (5.3.3.1)** is more sensitive to molecular weight than the Flory-Vrij equation. The equilibrium melting temperature, $T_m^o(n \to \infty)$, for linear polyethylene at infinite molecular weight was found to be 144.42^oC.

3) The equilibrium melting temperature, $T_m^o(n, p_B)$, of ethylene/1-octene random copolymers is a function of the molecular weight and the defect at low defect content ($p_B\% \leq 1.0\%$). The $T_m^o(n, p_B)$ is a weak function of molecular weight and a strong function of the defect content at high defect content ($p_B\% \geq 1.0\%$).

4) The Flory copolymer equation can predict the equilibrium melting temperature for the ethylene/1-octene random copolymer at $p_B\% \leq 1.0\%$ when the molecular weight effect is corrected using **equation (5.3.3.1)**. In the range of high defect content, the experimental values are always higher than the calculated values obtained using the uniform inclusion model of Sanchez-Eby, which does give a prediction that is closer than that using the Flory equation.

6.4. Morphology Study using SAXS

1) The mathematical and graphical methods to estimate phase boundary thickness using SAXS were developed. The interfacial layer thicknesses, E, T and Δ, estimated from linear-gradient, semi-sigmoidal of this study and sigmoidal models have the following relationship: $E(=\sqrt{12}\Delta) > T(=\sqrt{6}\Delta) > \Delta$. (see **equation 4.4.3.16**, **equation 4.4.3.24** and **equation 4.4.3.20** for definition of E, T and Δ, respectively.)

2) With increasing defect content, the electron density fluctuation component increases and the electron density difference becomes smaller. Both results support the conclusion from equilibrium melting study that some defects are included in the crystalline phase.

3) Phase boundary thickness depends on defect content, distribution of defects in system, crystallization temperature, crystallization time as well as the temperature for measuring SAXS intensity.

(3.1) At room temperature, the interfacial layer thicknesses of the homogeneous EO copolymers are higher than those of LPE up to $p_B(\%) = 24$. The highly branched EO copolymer, L39-O, showed a thinner interfacial thickness than LPE due to the high entropy of the phase boundary.

(3.2) Phase boundary size in homogeneous EO copolymers decreases with defect content whereas that of heterogeneous EO copolymer increases. This opposite behavior was understood due to the differences of defect distribution.

(3.3) The interfacial layer thicknesses of LPE and EO copolymers at low in-situ temperature are higher than those at ambient temperature. With increasing in-situ temperature, the phase boundary becomes thin and finally disappears.

4) It was verified experimentally that there is a relationship between the morphological structure and the defects.

REFERENCES

1. L. D. Cady, *Plast. Eng.*, **43**, 25, (1987).
2. Debral L. Wilfong, G. W. Knight, *J. Polym. Sci. Phys. Ed.*, **28**, 861 (1990).
3. F. Defoor, G. Groeninckx, H. Reynaers, P. Schouterden, and B. Van Der Heijden, *J. Appl. Polym. Sci.*, **47**, 1839 (1993).
4. G.Odian, Principles of Polymerization, 2nd ed., Chapter 8 (1981).
5. A.D. Horton, *Trip*, **2(5)**, May, 158 (1994).
6. A. Wood, *Chemical Week*, July 1/8, 42 (1992).
7. H. Sinn and W. Kaminsky, *Adv. Organomet. Chem.*, **18**, 99 (1980).
8. V. K. Gupta, S. Satish, I. S. Bhardwaj, J.M.S.-Rev. *Macromol. Chem. Phys.*, **C34(3)**, 439 (1994).
9. D. Schwank, *Modern Plast. Inter.*, August, 40 (1993).
10. B. Wunderlich, Thermal Analysis, Chapter 3, Academic Press, Inc., CA (1990).
11. P. J. Phillips, *Reg. Prog. Phys.* **53**, 549 (1990).
12. J. D. Hoffman and J. I. Lauritzen, *J. Res. NBS* **A65**, 297 (1961).
13. J. D. Hoffman, G. T. Davis, J. I. Lauritzen, Jr., "Treatise on Solid State Chemistry", N.B. Hannay, Ed., Vol. 3, Plenum Press, NY., (1976).
14. B. Wunderlich, Thermal Analysis, Chapter 2, Academic Press, Inc. (1990).
15. P. J. Phillips and W. S. Lambert, *Macromolecules*, **23**, 2075 (1990).
16. P. J. Flory, *Trans. Faraday Soc.* **51**, 848, (1955).
17. P.J. Flory, *J.Chem.Phys.*, **17(3)**, 223, (1949).
18. P. J. Flory, A. Vrij, *J. Am. Chem. Soc.*, **85**, 3548, (1963).
19. E. Helfand, and J. I. Lauritzen, Jr., *Macromolecules*, **6(4)**, 631 (1973).
20. I. C. Sanchez, and R. K. Eby, *Macromolecules*, **8**, 639 (1975).
21. J. Martinez-Salazar, M. S. Cuesta, and F. J. Balta' Calleja, *Colloid & Polym. Sci.*

265(3), 239, (1987).

22. B. S. Morra and R. S. Stein, *J. Polym. Sci. Polym. Phys. Ed.*, **20**, 2243, (1982).
23. R. G. Alamo *et al.*, (equation 10 in *Macromolecules*, **25(24)**, 6381 1992) reported that this equation was given by Morra and Stein(equation (3) in the reference 22). Originally, this equation was derived by the J. D. Hoffman *et al* (equation (6) in the reference 13 and in *Kolloid-Z. u. Z. Polymere*, **231**, 564 (1969)).
24. L. Mandelkern, G. M. Stack, *Macromolecules*, **17**, 871, (1984).
25. L. E. Alexander, "X-Ray Diffraction methods in Polymer Science", Chapter 5, R. E. Krieger publishing Co. Fl., (1979).
26.. O.Kratky, I. Pilz, and P.J. Schmitz, *J. Collid and Interface Sci.*, **21**, 24, (1966).
27. F. J. Baltá-Calleja and C. G. Vonk, X-ray Scattering of Synthetic Polymers, Chapter 1, Elsevier Science Publishers B.V., (1989).
28. J. M. Schultz, "Diffraction for Materials Scientists", Chapter 1, Prentice-Hall, Inc. N.J. (1982).
29. A. Guinier and G. Fournet, Small Angle Scattering of X-rays, Chapter 2, John Wiley & Sons, Inc. N.Y., (1955).
30. B. Crist, *J.Polym. Sci., Polym. Phys.*, **11**, 463, 635 (1973).
31. B. Crist and N. Morosoff, *J. Polym. Sci., Polym. Phys.*, **11**, 1023 (1973).
32. P. Debye and A.M. Bueche, *J. App. Phys.*, **20**, 518 (1949).
33. P. Debye, H. R. Anderson, Jr. and H. Brumberger, *J. Appl. Phys.*, 28(6), 679 (1957).
34. C. G. Vonk, G. Kortleve, *Kolloid Z. Z. Polym.*, **220**, 19 (1967).
35. W. Ruland, *Colloid Polym. Sci.*, **255**, 417 (1977).
36. U. Siemann and W. Ruland,(Need Journal) **260**, 999 (1982).
37. N. Stribeck and W. Ruland, *J. Appl. Cryst.*, **11**, 535 (1978).

38. O. Glatter and O. Kratky, Small Angle X-ray Scattering, Chapter 13, Academic Press, N.Y. (1982).
39. O. Glatter, *J. Appl. Cryst.* **12**, 166 (1979).
40. A. Guiner, *Ann. Phys.* **12**, 161 (1939).
41. B. Stroll, J. F. Fellers, and J. S. Lin, *Mat. Res. Soc. Symp. Proc.* **79**, 105 (1987).
42. J. H. Magill, *Polymer*, **2**, 221 (1961).
43. R. S. Stein, *Polym. Sci., C*, **15**, 185 (1966).
44. P. J. Phillips and Y. H. Kao, *Polymer*, **27**, 1679 (1986).
45. R. W. Hendricks, *J. Appl. Cryst.* **11**, 15 (1978).
46. G. D. Wignall, J. S. Lin, S. Spooner, *J. Appl. Cryst.*, **23**, 241 (1990).
47. J. L. Matthews, H.S. Peiser, P.B. Richards, *Acta Cryst.*, **2**, 85 (1949).
48. D. Wilfong and G. W. Knight, *J. Polym. Sci. Polym. Phys. Ed.*, **28**, 861 (1990).
49. P. J. Phillips and A. Vatansever, *Polymer*, **30**, 711 (1989).
50. R. M. Gohil and P. J. Phillips, *Polymer*, **27**, 1687 (1986).
51. R. M. Gohil and P. J. Phillips, *Polymer*, 27, 1696 (1986).
52. Polymer Handbook, J. Bradrup and E. H. Immergut, 2nd Ed., (1975).
53. G. R. Strobl and W. Hagedorn, *J. Polym. Sci.*, B, 16, 1593 (1978).
54. R. G. Snyder, S. J. Krause and J. R. Scherer, *J. Poly. Sci.*, B, 16, 1593 (1978).
55. M. Glotin and L. Mandelkern, *Colloid Polym. Sci.*, 260(2), 182 (1982).
56. R. G. Alamo, E. K. M. Chan, L. Mandelkern and L. G. Voight-Martin, *Macromolecules*, **25(24)**, 6381 (1992).
57. C. G. Vonk, A. P. Pijpers, *J. Polym. Sci. Polym. Phys. Ed.*, **23**, 2517 (1985).
58. C. G. Vonk, *J. Appl. Cryst.*, **6**, 81 (1973).
59. G. R. Strobl, M. Schneider, *J. Polym. Phys. Ed.*, **18**, 1343 (1980).
60. J. T. Koberstein, B. Morra, R. Stein, *J. Apply. Cryst.* **13**, 34 (1980)

61. W. Ruland, *J. Apply. Cryst.* **4**, 70 (1971).

62. G. R. Strobl, M. J. Schneider, I. G. Voigt-Martin, *J. Polym. Sci. Polym. Phys. Ed.*, **18**, 1361 (1980).

63. A. Todo, T. Hashimoto, H. Kawai, *J. Appl. Cryst.*, **11**, 558, (1978).

64. R. Bonart, E. H. Müller, *J. Macromol. Sci. Phys.* **B10(1)**, 177 (1974).

65. R. J. Roe, *J. Appl. Cryst.* **15**, 182 (1982).

66. P. G. de Gennes, *J Chem Phys.*, **55**, 572 (1971).

67. J. D. Hoffman, C. M. Guttman and E. A. DiMarzio, *Disc. Faraday Soc.*, **68**, 198 (1979).

68. M. Doi and N. Y. Kuzuu, *J. Polym. Lett.* **18**, 775 (1980).

69. D. S. Pearson and E. Helfand, *Macromolecules*, **17**, 888 (1984).

70. J. D. Hoffman, L. J. Flory, G. S. Ross and J. I. Lauritzen, *J. Res. NBS (A)*, **79**, 671 (1975).

71. W. S. Lambert and P. J. Phillips, *Macromolecules*, **27**, 3537 (1994).

72. J. I. Lauritzen and J. D. Hoffman, *J. Appl. Phys.*, **44**, 4340 (1973).

73. J. D. Hoffman, G. T. Davis, and J. I. Lauritzen, Treatise Solid State Chem., **3** (1976).

74. J. H. Magill, Nature (London), **187**, 770 (1960).

75. H. T. Tseng, P. J. Phillips, *Macromolecules*, **18**, 1565 (1985).

76. F. J. Baltá Callejá, D. C. Bassett and A. Keller, *Polymer*, 4 (1963).

77. F. Gornick and J. D. Hoffman, *Ind. Eng. Chem.*, **58(2)**, 41 (1966).

78. J. D. Hoffman, L. J. Frolen, G. S. Ross, and J. I. Lauritzen, Jr., *J. Res. Nat. Bur. Stand. (U.S.)* **79A** (Phys. and Chem.), No 6, 671 (1975).

79. J. D. Hoffman and R. L. Miller, *Macromolecules*, **21(10)**, 3038 (1988).

80. R. G. Alamo, E. K. M. Chan, L. Mandelkern, and I. G. Voigt-Martin, *Macromolecules*, 25(24), 6381 (1992)

81. E. N. Dalal, K. D. Taylor and P. J. Phillips, *Polymer*, **24**, 1623 (1983).

82. E. Martuscelli and M. Pracella, *Polymer*, **306**, 15 (1974).

83. L. Mandelkern, G. M. Stack and P. J. M. Mathieu, *Anal. Cal.*, **5**, 223.

84. D. C. Bassett, A. M. Hodge and R. H. Olley, *Proc. Roy. Soc. London*, **A377**, 39 (1981).

85. K. H. Illers and H. Hendus, *Makromol. Chem.*, **113**, 1 (1968).

86. B. Wunderlich and G. Czornyl, *Macromolecules*, **10(5)**, 906 (1977).

87. D. C. Bassett et. al., *Proc. R. Soc. Lond.* **A377**, 25 (1981).

88. This index is named as degree of deviateion from molecular weight of pure polymer in this study.

89. M. G. Broadhust, *J. Res. Nat. Bur. Stand. (U.S.)* **70A** (Phys. and Chem.), No 4, 481, (1966).

90. J. D. Hoffman and Robert L. Miller, *Macromolecules*, **21**, 3038 (1988).
The constant 2.903 on the numerator of equation (5.3.3.6) is correct. In Hoffman and Miller's paper, this constant is written in 2.093.

91. M. G. Broadhust, *J. Res. Nat. Bur. Stand. (U.S.)* **70A** (Phys. and Chem.), No 4, 481, (1966).

92. J. N. Hay, *J. Polym. Sci., Polym. Chem. Ed.*, **14**, 2845 (1976).

93. L. Mandelkern and G. M. Stack, *Macromolecules*, **17**, 871 (1984).

94. M. G. Broadhurst, *J. Res. Nat. Stand. (U.S.)* **66A** *(Phys. and Chem.)*, No 3, 241, (1962).

95. B. Wunderlich and G. Czornyl, *Macromolecules*, **10(5)**, 906 (1977).

96. G. M. Stack, L. Mandelkern, C.Kröhnke, and G. Wegner, *Macromolecules*, **22**, 4531 (1989).

97. K. S. Lee, G. Wegner, *Macromol. Chem., Rapid Commun.*, **6**, 203 (1985).

98. G. M. Stack (1989)

99. J. N. Hay and Xiao-Qi Zhou, *Polymer*, **34(5)**, 1002 (1993).

100. S. Hosoda, H. Nomura, Y. Gotoh, and H. Kihara, *Polymer*, **31**, 1999 (1990).

101. B. S. Morra and R. S. Stein, *J. Polym. Sci. Polym. Phys. Ed.*, **20**, 2243 (1982).

102. H. Scherr, P. C. Hägele, H. P. Grossmann, *Colloid & Polym. Sci.*, **252**, 871 (1974).

103. B. L. Farmer and R. K. Eby, *Polymer*, **20**, 363 (1979).

104. J. Rathje and W. Ruland, *Colloid & Polymer Sci.* **254**, 358 (1976).

105. M.V. Smoluchowski, *Ann. Phys.* **25**, 205 (1908).

106. A. Einstein, *Ann. Phys.* **33**, 1275 (1910).

107. J. Rathe and W. Ruland, *Colloid Polym. Sci.*, **254**, 358 (1976).

108. W. Ruland, *J. Appl. Cryst.* **4**, 70 (1971).

109. R. J. Roe, *Macromolecules*, **14**, 1091 (1981).

110. F. Defoor, G. Groeninckx, H. Reynaers, P. Schouterden and B. Van der Heijden, *Macromolecules*, **26**, 2575 (1993).

111. R. Alamo, R. Domszy and L. Mandelkern, *J. Phys. Chem.*, **88**, 6587 (1984).

VITA

Man-Ho Kim was born in Cheon-An, Southern Choong-Chung Province, Korea on March 31, 1962. He graduated from the Mapo High School at Seoul in February 1981. In March of that year, he enrolled in the INHA University at Incheon. He received a Bachelor of Engineering degree in 1985 and a Master of Science degree in Polymer Engineering in 1987 studying on the effect of solvent on radical copolymerization of N-methylolacrylamide with styrene. After graduation, he entered the Military Academy in Young-Cheon, Northern Kyung-Sang Province, in the fall of 1987 and graduated as a second lieutenant in February 1988. In the April of 1988, he was employed as a research scientist of the functional polymer laboratory by the Korea Institute of Science and Technology (KIST). He performed the various synthesis and polymerization of materials relating to photolithography.

In August 1991, he enrolled at The University of Tennessee, Knoxville to pursue the Doctor of Philosophy Degree in Polymer Engineering. He received his doctoral degree with melting and small angle X-ray scattering study of homogeneous ethylene copolymers in May of 1996. He has accepted a postdoctoral position from Professor Leo Mandelkern and Dr. Rufina G. Alamo group in the Institute of Molecular Biophysics of Florida State University, Tallahassee.

The author is a member of Division of High Polymer Physics (DHPP) of The American Physical Society (APS).

He married Won-Sil Shin in December 1994. They have a proud son, Young-Wook, who was born on October 6, 1995.